Détection de l'interaction pastille-gaine (IPG) et de la fusion à cœur lors d'une irradiation de type transitoire de puissance dans le réacteur Jules Horowitz (RJH) : modélisation et méthode de mesure en temps réel des déformations d'un crayon combustible

V. d'Ambrosi

AIX-MARSEILLE UNIVERSITÉ
Commissariat à l'Énergie Atomique et aux Énergies Alternatives
ÉCOLE DOCTORALE 353
Laboratoire de Mécanique et d'Acoustique de Marseille
DES/IRESNE/DER/SPESI/Laboratoire de Dosimétrie Capteurs et Intrumentation

Thèse présentée pour obtenir le grade universitaire de docteur

Discipline: Sciences pour l'ingénieur : Mécanique, Physique, Micro et Nanoélectronique
Spécialité: Mécanique des Solides

Veronica D'AMBROSI

Détection de l'Interaction Pastille-Gaine (IPG) et de la fusion à cœur lors d'une irradiation de type transitoire de puissance dans le réacteur Jules Horowitz (RJH) : modélisation et méthode de mesure en temps réel des déformations d'un crayon combustible.

Soutenue le 02/06/2020 devant le jury composé de:

Amna REKIK	Maître de Conférence, Polytech Orléans	Rapporteur
Philippe COMBETTE	Professeur, IES Montpellier	Rapporteur
Elisabeth MASSONI	Professeur, MINES ParisTech	Examinatrice
Yann MONERIE	Professeur, Montpellier	Examinateur
Christelle REYNARD-CARETTE	Maître de Conférence, AMU/IM2NP	Examinatrice
Jean-Marie GATT	HDR, CEA Cadarache	Directeur de thése
Frédéric LEBON	Professeur HDR, AMU/LMA	Co-Directeur de thése
Rodrigue LARGENTON	Ingénieur Chercheur, EDF R&D	Invité
Christophe GARNIER	Ingénieur Chercheur, FRAMATOME	Invité
Christophe DESTOUCHES	Ingénieur Chercheur, CEA Cadarache	Co-encadrant
Jérôme JULIEN	Ingénieur Chercheur, CEA Cadarache	Co-encadrant

Numéro national de thèse/suffixe local: 2020AIXM0141/008ED353

Acknowledgements

This Ph.D. thesis has been a unique opportunity to grow, personally and professionally, but it would never have seen the light without the people who made it possible and those who supported me along the way.

First of all, I would like to thank Amna Rekik and Philippe Combette for agreeing to review the manuscript and for their pertinent comments. I would also like to thank Christelle Reynard-Carette, Elisabeth Massoni, Yann Monerie, Christophe Garnier and Rodrigue Largenton for agreeing to be part of the jury. Thank you for the time you devoted to my work and the interest you showed for it. Also, in these particular times, your understanding and willingness have been essentials.

During these three years, I had the opportunity to work with professionals for whom I have great esteem but also, and above all, with people of immense value. First of all, I would like to thank my thesis directors, Jean-Marie Gatt and Frédéric Lebon. You have been scientific and human guides for me, thank you for feeding my scientific curiosity and for supporting and encouraging me throughout the project. A big thank you to my supervisors, Christophe Destouches, Jérôme Julien and Daniel Parrat. Christophe, you believed in my skills and allowed me to develop new ones and to build a strong critical thinking. Above all, you encouraged me to improve every day. I thank you for the passion you put in your work. Jérôme, thank you for the willingness and the patience you showed me, for our discussions and for your constructive criticism that allowed me to find answers to my questions. Thank you for the support you have always offered me, for listening to me and for giving me renewed motivation and self-confidence when I needed it. General thanks to both of you, for teaching me that it is always better when a speech starts with the subject and its context. Special thanks go to Daniel: you believed in me since the internship and supported me in undertaking this journey and followed me along its achievement. Thank you above all for endorsing me with some of your knowledge, I will take care of it and feed it so that it grows and strengthens in the next years.

I would like to thank Guillaume Ricciardi for the scientific support and to all the DTN technicians and engineers for their help and collaboration, which allowed me to develop and complete my experiment. I would like to express my sincerest thanks to Frédéric Rey for the fruitful discussions and to Jean-Christophe Brachet, Nony Guillaume and the members of the DMN for providing us the essential claddings for the experiment. Also, I would like to express my gratitude to Olivier Howald and the LECA teams for your support and fundamental collaboration.

No man is an island and this project would have been impossible without the moral and professional support of the two teams that I was lucky to join. First of all, I would like

to thank the service heads, Mireille Bauer and Alain Moreau, for welcoming me into their services, for following my work and allowing me to complete it. My sincere thanks go to the laboratory heads, Fabienne Delage and Jean-François Villard, for the attention they pay to the people in their teams, for helping to create a welcoming atmosphere and for the perfect mix of professionalism, humanity and moral support you have always showed me.
I would like to thank all the members of the LDCI, the LEVA, the LM2C and the LECIM for your willingness, for the collaboration you have offered me over the years and for the time you have dedicated to answer my questions.
I would like to thank Stephane, first of all for the technical and scientific support in the design of IMPIGRITIA. Second, it is my duty to thank you for having willingly lent yourself to the role of spell checker: I give him credit if you have not noticed grammatical or spelling mistakes in my French emails. Thanks to Gregoire and Clement, for your culture, certainly vast and heterogeneous, sometimes bizarre but always surprising, and the spontaneity with which you share it. Thanks to Damien, Loic, Nicola, Gilles, Philippe and Maxime for being sincere and helpful colleagues and for having made, each in his own way, this journey unique. Special thanks go to Nathalie, Isabelle, Alexandra and Mireille, thanks for being the examples of strong and competent women. Thank you to Christophe, Jonathan and Hervé, for introducing me to the Argot of Provence, to the local cinema and in general, for your good mood and the joy you convey.
I would like to thank the wonderful secretaries who have helped me during these years: Régine and Christelle, I thank you for your daily kindness and for the smile with which you have always welcomed me.

Thanks to the Italian community of Cadarache and the fellow PhD students and friends with whom I shared this path: Daniela, Lidia, Joane, Thomas, Daria, Giorgio, Carla, Julien, Paolo, Serafina, Samuele, Lorenzo, Salvatore, Axel, Alix, Alexis, Corantin , Adrien and all those with whom I laughed, joked and created memories that I will jealously keep with me. Good luck to all those who are working for their thesis: enjoy every moment, even the tough ones.

Special thanks go to my family, to you who have supported my choices even though they have taken me far away from you, to you who always give me new strength and encourage me to achieve my goals.

A last thank you goes to you Luca; you have managed my psychological well-being in the last few months. You have always listened to me and supported me. Thanks for bringing me my 5 o'clock tea when I didn't have time to prepare it. A thank you is not enough, but it is a good start.

Résumé Étendu

Introduction à l'Interaction Pastille Gaine

Dans un réacteur nucléaire, le combustible est constitué de dioxyde d'uranium UO_2, sous forme de pastilles cylindriques empilées à l'intérieur d'une gaine pour former le crayon combustible. Dans un Réacteur de type à Eau Pressurisée (REP), la chaleur générée par les réactions de fission dans la pastille est transmise à la gaine et évacuée par le réfrigérant primaire, l'eau, à 155 bars et à environ 300°C. Le gradient de température dans la pastille se présente sous la forme d'un profil quasi-parabolique avec un maximum au centre de la pastille. La pastille de combustible, qui est une céramique, se fragmente dès la première montée en puissance du fait de sa fragilité à basse température (<900°C). Le gradient de température, entre le centre de la pastille et sa périphérie, induit une dilatation différentielle conduisant à la mise en diabolo des fragments. Cela se traduit par une déformation plus importante au niveau du plan Inter-Pastille (IP) par rapport au plan Médian de la pastille (MP) . Au cours de l'irradiation on observe une réduction du jeu entre la pastille et la gaine. En effet d'une part, le rayon des pastilles augmente en raison de la dilatation thermique et du gonflement (solide et gazeux) induit par la formation de produits de fission, et d'autre part, la gaine soumise à la pression externe du réfrigérant primaire vois son rayon diminuer par fluage. Le contact entre la pastille et la gaine s'établit d'abord au niveau du plan IP, en raison de la mise en diabolo de la pastille, puis s'étend axialement au fur et à mesure que la gaine se déforme pour épouser la forme de la pastille. Des sur-déformations au niveau de la gaine, appelées plis primaires, apparaissent au niveau du plan IP, caractérisant ainsi son interaction forte avec la pastille.

En conséquence du contact, les deux objets interagissent et leur comportement est mutuellement influencé : la pastille, en se dilatant, va déformer la gaine et générer des contraintes dans cette dernière ; la gaine, de son côté, s'oppose à la pastille ralentissant de ce fait la déformation de la pastille vers l'extérieur. Ce phénomène est connu sous le nom d'Interaction Pastilles-Gaine (IPG). Dans des situations incidentelles, les contraintes générées au cours de l'IPG peuvent entrainer un risque de rupture de la gaine, rupture qu'il faut prévenir et éviter puisque la gaine constitue la première barrière de confinement du combustible et donc des produits de fission radioactifs.

Aujourd'hui, en France où l'électricité provient principalement du nucléaire, le projet est d'intégrer l'apport intermittent des énergies renouvelables dans le mix énergétique et demande donc une plus grande flexibilité de la production d'électricité. Pour atteindre cette flexibilité, il est nécessaire d'augmenter la manœuvrabilité des centrales nucléaires afin de suivre la demande du réseau. Lors de ce suivi, une variation soudaine de puissance (transitoire de puissance) peut se produire, entraînant une augmentation de la température du combustible. Cette augmentation va créer une dilatation plus importante des pastilles.

Dans ces conditions, une déformation caractéristique au niveau du plan MP, appelée plis secondaires, peut avoir lieu générant des contraintes supplémentaires dans la gaine. Afin de garantir la sûreté des installations, l'Autorité de Sûreté Nucléaire (ASN) demande à l'exploitant des centrales (EDF dans le contexte français) de s'assurer de l'intégrité physique de la gaine et de l'absence de fusion au centre des pastilles de combustible lors de ces transitoires de puissance.

Pour mieux comprendre les phénomènes physiques liés à l'IPG dans ces conditions transitoires, des expériences d'irradiation spécifiques appelées rampes de puissance sont réalisées dans des réacteurs d'essais dédiés à ce type d'expériences : les Material Testing Reactors (MTR). A partir d'un crayon de combustible neuf ou pré-irradié dans une centrale, un nouveau crayon est fabriqué, pour répondre aux exigences géométriques du MTR, puis soumis à une séquence d'irradiation qui simule un transitoire, appelé rampe de puissance. Après l'essai, des Examens Post-Irradiation (EPI), sont alors effectués sur le crayon. Ils permettent d'étudier les mécanismes qui se sont produits pendant les différentes phases de l'essai, comme, par exemples, la déformation résiduelle et les modifications microstructurales de la gaine et du combustible.

Les données recueillies sont tout d'abord utilisées dans un cadre de démonstration de sureté mais aussi pour améliorer la compréhension des phénomènes mis en jeu, pour développer la modélisation et pour valider les simulations numériques en utilisant par exemple la mesure des plis primaires et secondaires. Aujourd'hui, la majorité des mesures sont effectuées avant et après l'expérience, ne donnant que l'état initial et final du système. L'apport de la simulation permet donc d'évaluer la cinétique des phénomènes d'intérêt. Cependant, peu d'expériences ont été réalisées en intégrant un dispositif d'instrumentation qui permettrait de suivre le comportement du crayon combustible au cours de l'expérience et ainsi d'obtenir des données plus complètes à comparer aux résultats des simulations. Aujourd'hui, il est essentiel de disposer de données sur la cinétique d'évolution des phénomènes d'intérêt pour mieux valider la modélisation et améliorer ainsi les outils de calcul.

Dans le futur réacteur expérimental Jules Horowitz (RJH), des séquences d'irradiation hautement instrumentées sont prévues pour mesurer en ligne le comportement du combustible et ainsi espérer combler l'écart existant entre les données expérimentales et les données issues de la simulation.

Le travail présenté ici constitue la première étape vers le développement d'une méthode de mesure en ligne pour améliorer la connaissance des phénomènes physiques pertinents associés à l'IPG. Ces améliorations sont nécessaires pour développer des produits toujours plus performants et étendre les marges opérationnelles afin de suivre la demande du réseau tout en garantissant le respect des critères de sûreté demandés.

Identification des paramètres

Pour sélectionner les paramètres observables les plus pertinents à mesurer, nous nous appuyons sur la simulation. L'outil de référence utilisé dans ce travail est le code multi-dimensionnel de performance du combustible ALCYONE de la plateforme de simulation PLEIADES, développée par le CEA en collaboration avec EDF et FRAMATOME. A partir d'un historique d'irradiation spécifique, le calcul thermo-hydraulique définit le coefficient d'échange à la surface du crayon. A partir de cette information, la température externe

de la gaine est calculée et imposée comme condition limite au calcul thermique dans le crayon de combustible. Les calculs thermomécaniques et physico-chimiques permettent d'évaluer le comportement, l'évolution microstructurelle et l'évolution macroscopique du combustible. ALCYONE permet trois types de modélisation : 1,5D, 2D et 3D. Dans notre étude, nous avons utilisé la simulation 1,5D (le crayon est découpé en tranches axiales, chaque tranche est modélisée en 1D. Un couplage via la thermo-hydraulique est pris en compte entre les tranches) pour évaluer le comportement global du crayon. Le modèle 3D permet, d'une part, une analyse plus fine et détaillée du comportement local d'un fragment, et d'autre part, de distinguer le comportement du crayon combustible au niveau du plan Inter-Pastilles et au niveau du plan Médian-Pastille.

A l'aide d'ALCYONE, nous avons étudié le comportement thermo-mécanique de l'élément combustible en simulant des conditions idéales de fonctionnement normal et des tests de rampe de puissance. Ces simulations nous ont permis d'identifier les paramètres d'intérêt pour l'étude de l'IPG et de la fusion à cœur. à ce stade des travaux, ALCYONE ne dispose d'aucun modèle pour tenir compte du début de la fusion dans la pastille de combustible, la modélisation et l'analyse se limitant au combustible solide.

Pour l'analyse, nous classons l'IPG selon deux catégories : l'IPG dite faible et l'IPG dite forte. L'IPG faible correspond au contact entre la pastille et la gaine en raison de la cinétique de déformation des deux objets, sans aucune influence sur le comportement de l'une sur l'autre. L'IPG forte implique que l'interaction mécanique induit une modification mutuelle des mécanismes de déformation des deux composants du crayon combustible.

Pour l'IPG faible, nous avons identifié les indicateurs directs observables suivants :

- Le contact pastille-gaine : il est nécessaire à l'IPG faible pour s'établir. C'est un résultat assez intuitif mais sa détection n'est pas trivial ;

- La température locale de la surface du combustible à l'IP, qui diminue en raison de l'amélioration de l'échange thermique entre les pastilles et la gaine à travers la fermeture du jeu.

L'IPG forte a des conséquences directes sur :

- Le diamètre externe de la gaine : le diamètre évolue pour s'adapter à la forme des pastilles, avec pour conséquence la cinétique de formation de plis primaires pendant le fonctionnement normal et des plis secondaires pendant les essais de rampe de puissance. L'amplitude de la modification induite étant de l'ordre du micromètre, les mesures sans contact sont ainsi préférées. La cinétique de la déformation de la gaine demande que l'investigation soit effectuée sur toute la longueur du crayon (si possible) sinon sur les pastilles centrales (de trois à cinq). La discrétisation spatiale requise est de l'ordre de 0,5 mm ;

- L'allongement axial de la gaine : la modélisation montre qu'une discontinuité dans la cinétique de l'allongement de la gaine se produit lorsque l'IPG est suffisamment forte le long de la colonne combustible. En effet, la colonne combustible s'allongeant davantage entraîne la gaine lorsqu'il y a accrochage et accélère l'allongement de la gaine (qui va par conséquence freiner l'allongement de la colonne combustible). Depuis ce moment, la déformation des deux objets est mutuellement influencée ;

– La température locale au centre du combustible et la température locale de la surface du combustible au plan MP : La modélisation montre une modification de leurs cinétiques après la fermeture complète du jeu sur la longueur de la pastille.

L'allongement de la colonne de combustible ne présente pas un comportement caractéristique associé à l'IPG forte, mais sa mesure est nécessaire pour évaluer le volume du plénum supérieur. En effet, ce dernier, avec le jeu radial, permet d'évaluer l'évolution du volume libre dans le crayon. Ce volume entre dans le calcul de la pression interne. Lorsque cette pression est linéairement corrélée avec la diminution du volume libre, alors on est en phase d'IPG faible. La mesure de l'allongement de la colonne combustible est donc un indicateur indirect de l'IPG faible.

De même, la pression interne des crayons est un indicateur indirect de l'IPG faible car elle permet de détecter la réouverture locale du jeu : en cas de réouverture du jeu. En effet, une augmentation soudaine de la pression interne peut se produire dans le plenum des crayons.

Les calculs effectués ont montré que la température de la surface externe de la gaine pilote les températures dans la gaine et dans les pastilles et donc la fermeture du jeu. Pour cela, la mesure de cette température doit être effectuée et si possible couplée à celle du diamètre extérieur de la gaine.

Faisabilité théorique pour détecter le début de la fusion à cœur à partir de la déformation de la gaine

L'absence d'un modèle permettant de tenir compte du début de la fusion de la pastille combustible dans ALCYONE a nécessité la mise au point d'un modèle thermomécanique, en mettant en œuvre des méthodes d'homogénéisation. L'objectif de ce développement est de calculer les effets mesurables sur la cinétique de déformation de la gaine dus à l'expansion caractéristique du changement de phase solide-liquide du dioxyde d'uranium.

Tout d'abord, nous avons examiné les caractéristiques thermophysiques du combustible REP au début de la fusion. Dans la littérature scientifique, il est communément admis que la température de fusion de l'UO_2 stœchiométrique non irradié s'élève à 2874°C ± 20°C. Sous irradiation, la fusion du dioxyde d'uranium ne se fait pas à température constante. L'intervalle de fusion est caractérisé par une température de solidus Tsol et une température de liquidus Tliq. Ces températures dépendent du taux de combustion, du rapport oxygène sur actinides et de la teneur en plutonium du combustible. Sur la base des connaissances actuelles, le taux de combustion réduit la température du solidus, la stœchiométrie et le plutonium réduisent les deux températures (solidus et liquidus). En fonction de la redistribution radiale de l'oxygène, de la partie chaude de la pastille (le centre) vers la région périphérique plus froide, nous avons défini l'intervalle de fusion pour le combustible irradié hypostœchiométrique en supposant une superposition linéaire des effets dus au taux de combustion et de l'écart par rapport à la stœchiométrie. Les effets dus à la présence de plutonium sont ici négligés car seul le dioxyde d'uranium a été considéré dans ce travail. Les combustibles MOX n'ont pas été étudiés.

Pour améliorer son intégration dans les modèles thermomécaniques d'ALCYONE, le modèle de fusion a été développé pour être piloté par la température locale et est basé sur les mêmes approches d'homogénéisation que celles utilisées pour modéliser le comportement

thermomécanique du combustible solide (description du comportement par des potentiels elliptiques pour le fluage diffusion et le fluage dislocation).

Pour développer le modèle de fusion, nous partons donc de la définition du comportement mécanique visqueux du combustible poreux défini par un potentiel thermomécanique elliptique. Du fait de l'état contrainte en compression dans le combustible à l'approche de la fusion, on considère que la porosité est nulle. Dans ce cas, la vitesse de déformation viscoplastique du combustible au début de la fusion est définie à partir d'un potentiel classique de Norton. Pour modéliser la fusion, on suppose que des inclusions liquides apparaissent progressivement et uniformément dans la région centrale, où la température locale dépasse le seuil de la température du solidus. Ce volume, dont la température est au-dessus de la température du solidus, est donc décrit comme un milieu hétérogène constitué de solide et d'une fraction volumique de liquide. Les propriétés élastiques macroscopiques du matériau équivalent sont évaluées en fonction de la fraction liquide par une approche auto-cohérente. La diminution de la masse volumique due à la fusion est prise en compte comme une dilatation isotrope, contribuant à la déformation totale de la pastille. Pour le comportement viscoplastique, la méthode d'homogénéisation dite de la sécante modifiée est utilisée pour obtenir le comportement macroscopique. La simulation montre que la déformation viscoplastique subit une forte accélération, due au fluage dislocation, conduisant à une forte diminution de la contrainte au centre de la pastille.

Pour analyser le comportement macroscopique du système, les propriétés du matériau UO_2sont implémentées dans l'outil MFRONT. Cet outil développé dans le cadre de la plateforme PLEIADES, permet de développer des lois de comportement pouvant être utilisées comme lois externes par Cast3m (logiciel muti-physique de calcul par éléments finis développé par le CEA). L'analyse sur un modèle simplifié (prenant en compte que la pastille) du déplacement en périphérie de pastille, fait apparaitre une discontinuité dès le début de la fusion. Une corrélation est ensuite clairement observée entre la progression de la fusion et la déformation de la gaine.

Au-delà de cette thèse, des travaux complémentaires seront nécessaires pour intégrer le modèle de fusion dans ALCYONE et coupler les contraintes associées au processus de fusion avec les phénomènes caractéristiques se produisant dans la pastille combustible (par exemple le gonflement gazeux). Nous ne pouvons donc pas calculer quantitativement l'effet d'une fusion partielle au cœur de la pastille combustible sur la cinétique de déformation de la gaine. Néanmoins, d'après les résultats obtenus sur le cas simple, nous pensons que la déformation macroscopique de l'élément combustible sera amplifiée dès le début de la fusion au centre de la pastille.

Méthode de mesure pour la caractérisation on-line de l'IPG et du début de la fusion dans le RJH

Dans la troisième et quatrième partie de la thèse, les paramètres identifiés et les critères de mesure associés guident un examen critique des solutions technologiques, disponibles et en cours de développement, les plus adaptées pour une application dans l'environnement du RJH.

Dans un premier temps, les solutions technologiques étudiées sont évaluées en fonction des derniers développements publiés. Nous examinons leurs principes de mesure, leurs

caractérisations expérimentales, les perturbations attendues du système associées à la présence du capteur et le niveau de maturité par rapport à l'application en milieu nucléaire. Cette dernière implique des rayonnements ionisants, une température et une pression élevées, une interaction chimique avec le réfrigérant, des contraintes opérationnelles imposant une fiabilité et une stabilité élevées.

Ensuite, nous prenons en compte la conception spécifique et les caractéristiques environnementales du dispositif ADELINE, qui est identifié comme le cadre d'application de la méthode de mesure, et nous sélectionnons les technologies retenues.

Dans ce cadre, nous proposons et développons une étude de faisabilité pour étudier si le contact pastille-gaine et sa progression le long de l'axe de l'élément peuvent être détectées par l'analyse des vibrations du crayon combustible induites par son interaction avec le fluide de refroidissement environnant.

Le RJH et le dispositif d'irradiation ADELINE

Le Réacteur de recherche Jules Horowitz (RJH) est une installation internationale sur le site du CEA Cadarache (France), conçue pour l'étude du comportement des matériaux et du combustible sous flux neutronique et pour les applications médicales de production de radio-isotopes. Actuellement en construction, il sera opérationnel avant la fin de la décennie.

Il s'agit d'un réacteur de 100 MWth dont le cœur compact est refroidi par un circuit primaire légèrement pressurisé, environ 10 bars. Des laboratoires chauds seront disponibles pour la préparation du dispositif d'essais et la réalisation d'examens pré et post-irradiation. Le cœur du RJH est conçu pour atteindre un flux thermique jusqu'à 5.10^{14}n/cm^2/s et un flux rapide jusqu'à 1.10^{15}n/cm^2/s. Ce réacteur permet d'accélérer le vieillissement des matériaux par rapport à un réacteur de puissance industriel. Nous pouvons ainsi étudier le comportement de nouveaux types de combustible, tester des protocoles d'exploitation étendus et les qualifier avant leur utilisation dans un réacteur de puissance industriel.

Pour permettre une large gamme de conditions d'irradiation, l'installation présente plusieurs emplacements d'irradiation parmi lesquels six boucles en eau installées sur des dispositifs de déplacement qui permettent de réaliser divers tests d'irradiation. La boucle ADELINE est un des dispositifs de test actuellement en cours de développement pour étudier le comportement des crayons combustible des réacteurs à eau légère. Ce dispositif permet de tester le comportement d'un échantillon jusqu'à ses limites de fonctionnement et pendant certaines séquences incidentelles ou accidentelles, y compris jusqu'au début de la fusion à cœur du combustible. C'est dans cette boucle que les études portant sur les limites opérationnelles liées à l'IPG sont envisagées dans notre étude en effectuant des tests de rampe de puissances dédiées.

La boucle ADELINE présente une section d'essai mono-crayon. Les types de crayon considéré sont de géométrie REP standard et sont constitués de pastilles en UO_2 ou MOX, neuves ou précédemment irradiés dans un réacteur de puissance.

La boucle se compose de deux parties principales : la partie en-pile, soumise au flux dans la piscine du réacteur, et la partie hors-pile, une section hors flux comprenant les composants pour le conditionnement du fluide caloporteur et les auxiliaires. La partie en-pile

est montée sur un système de déplacement qui permet de rapprocher ou d'éloigner le dispositif du cœur du RJH, selon la séquence d'irradiation, avec une vitesse de variation de puissance linéaire de 10 à 660 W/cm/min.

Dans cette section d'essai, les conditions thermohydrauliques représentatives du REP sont reproduites avec de l'eau de refroidissement à 155 bars, qui est injectée à partir de la partie hors pile. Cette eau en régime turbulent, pénètre dans le tube intérieur par le bas et refroidit le crayon. Selon la conception actuelle, le diamètre du tube intérieur est d'environ 20 mm au niveau de l'élément combustible et les dimensions enveloppes autorisées pour le crayon sont: un diamètre externe maximal de gaine de 9,5 mm et une longueur comprise entre 200 et 600 mm. Le crayon combustible est soutenu dans la section d'essai par un porte-échantillon, faisant une longueur totale d'environ 3 m. Son plan médian est aligné avec le plan médian du cœur du RJH. Les profils axiaux sont donc identiques : la puissance linéaire maximale est obtenue au Plan Médian (PM) du crayon d'essai avec une diminution de 20% aux deux extrémités situées à 30 cm du PM.

L'environnement et la conception de l'appareil d'irradiation ADELINE imposent des contraintes spécifiques pour l'instrumentation à mettre en œuvre :

- Espace radial disponible réduit (5 mm de rayon au niveau du crayon) et difficile d'accès en raison de la longueur du dispositif ;
- Les flux neutroniques et gamma sont élevés et fortement anisotropes. Ainsi, les capteurs doivent faire face à un fort gradient axial et radial. Le crayon présente une face chaude tournée vers le cœur du RJH qui subit un flux de neutrons 10% plus élevé que la face froide. Le profil de puissance du RJH a un maximum au niveau du plan médian de la tige et diminue de 20% aux extrémités. Les températures au centre du combustible peuvent atteindre environ 2800°C, lorsque la fusion est activée, mais la surface de la gaine externe est toujours maintenue autour de 300°C ;
- Les scénarii d'irradiation impliquent que les conditions environnementales imposées aux capteurs varient très rapidement, soumettant l'instrumentation à des chocs thermiques ;
- Les capteurs situés dans la section d'essai sont soumis à des vibrations induites par un écoulement turbulent.

Ces caractéristiques sont prises en compte dans l'étude des capteurs éligibles pour la caractérisation en ligne de l'IPG et la détection du début de la fusion.

Mesure de température

Nous recherchons la possibilité de suivre en ligne l'évolution des températures ce qui nous amène à ne pas prendre en compte les capteurs de température basés sur les matériaux eutectiques fusibles (cellules points fixes) et les capteurs SiC, qui permettent de récupérer la température locale maximale mais seulement par analyse post irradiatoire.

Deux technologies ont été considérées comme non adaptées pour la caractérisation de l'IPG :

- Le thermomètre à expansion, parce qu'il est trop intrusif ;

– Le thermomètre de Johnson à bruit thermique, incompatible en termes de dimensions mais qui pourrait servir au recalibrage des capteurs thermiques pendant le fonctionnement en réacteur.

Température de la gaine externe

Parmi les solutions technologiques étudiées, la conception du thermomètre à ultrasons fait que cette technologie n'est pas adaptée au contrôle de la surface de la gaine. Sa dimension n'est pas en effet compatible avec le crayon combustible.

Les thermocouples ont l'avantage d'être une solution technologique robuste, avec plusieurs applications validées dans l'environnement nucléaire. Plusieurs types de thermocouples permettent d'investiguer la gamme de température étudiée (autour de 300°C). Mais, ils permettent une mesure en un seul point (à l'extrémité du thermocouple).

Les réseaux de Bragg à fibres (FBG de l'anglais Fiber Bragg Gratings) sont une alternative intéressante aux thermocouples car ils permettent d'effectuer des mesures réparties avec un capteur unique. Ils nécessitent à l'heure actuelle des développements supplémentaires pour résister aux radiations. Les FBG, qu'ils soient de types régénérés ou femtosecondes montrent des résultats prometteurs pour étendre la plage de fonctionnement à des températures bien supérieures à celles qui caractérisent la surface de la gaine dans cette étude. En plus de la température, les FBG sont sensibles à la déformation, ce qui impose une compensation ou l'utilisation d'un mini-tube pour les protéger.

Tout comme les FBG, les capteurs optiques à lumière diffusée peuvent être appliqués à la surveillance répartie de la température de la gaine externe. Les solutions technologiques qui répondent à la résolution spatiale sont l'OFDR ("Optical Frequency Domain Reflectometry") basé sur Rayleigh, qui présente une intéressante précision de mesure de 0,1°C, le BOTDA ("Brillouin Optical Time Domain Analysis") basé sur l'émission Brillouin et l'OTDR ("Optical Time Domain Reflectometry") basé sur le Raman. Parmi ces capteurs optiques, le seul qui n'a pas besoin d'être compensé pour la contrainte est le capteur Raman. Cependant, ces technologies n'ont jamais été testées dans un réacteur nucléaire et leur résistance aux rayonnements neutroniques et gamma doit être étudiée.

Tous les capteurs susmentionnés doivent être en contact avec l'objet cible : la présence du capteur réduit localement l'échange thermique entre la gaine et le réfrigérant, ce qui entraîne une modification locale du comportement thermomécanique du système.

La pyrométrie optique est la technologie retenue car c'est la seule, parmi celles étudiées, qui permet de mesurer la température locale de la surface de la gaine par une mesure sans contact, ce qui est recommandé en raison des modifications micrométriques induites par l'IPG sur la surface de la pastille. La possibilité d'utiliser des fibres optiques permet de minimiser l'encombrement du capteur. Cependant, son efficacité dans la plage thermique de 300°C et ses performances sous irradiation doivent être étudiées. De plus, comme le capteur doit être placé devant l'objet cible, il faut mettre au point un dispositif de déplacement pour mesurer le profil thermique.

Température externe du combustible

Sur la base des solutions technologiques étudiées, la mesure de la température externe du combustible ne peut être effectuée sans introduire le capteur directement à l'intérieur de la tige d'échantillonnage, ce qui n'est pas compatible avec le phénomène de l'IPG. Nous avons dû conclure qu'aucune des solutions technologiques étudiées ne permet de surveiller la température externe du combustible dans le cadre de la caractérisation de l'IPG.

Température centrale du combustible

La plage de variation de la température du combustible de l'axe central, de 1000°C dans des conditions normales de fonctionnement, à environ 2900°C en cas de début de fusion, est très complexe à étudier. Parmi les technologies disponibles, les seules adaptées à cette plage de températures sont les thermocouples de type C, qui sont limités à 2000°C et peuvent supporter des radiations pendant un temps limité, et le thermomètre à ultrasons, qui permet d'atteindre des températures jusqu'à 2800°C et d'effectuer une mesure distribuée.

Une caractéristique de la température centrale est que la configuration géométrique du système rend le point d'intérêt dans la colonne de combustible difficile d'accès. Pour ce faire, la seule façon identifiée est de percer le centre de tout ou partie de la colonne de combustible pour y introduire le capteur. Dans le cadre de la détection et de la mesure PCI, de fortes modifications sont induites sur le comportement thermomécanique de la pastille par le trou central et doivent faire l'objet d'une étude spécifique pour analyser la représentativité des grandeurs mesurées et établir la fonction de transfert vers le système non perturbé.

Ces deux technologies sont probablement éligibles pour valider le code de calcul hors de la zone concernée par l'étude de l'IPG. Dans ce cadre, le thermomètre à ultrasons offre l'avantage d'une mesure distribuée.

Mesure de la pression interne

Le capteur de contre-pression s'avère être un dispositif robuste et fiable, pouvant être utilisé pour des séquences expérimentales dédiées à l'IPG. Il répond en effet aux critères de mesure identifiés concernant la pression interne : il permet de mesurer en ligne l'évolution de la pression interne jusqu'à 120 bar avec une précision démontrée de $\pm$ 0,325 bar (2σ). De plus, il a été conçu et qualifié pour fonctionner dans l'environnement nucléaire (expérience REMORA 3) avec un minimum de perturbation du système et sans dérive du signal collecté. Sa conception peut être adaptée pour être appliquée au dispositif ADELINE.

Le capteur acoustique constitue un développement intéressant car il permet théoriquement de doubler l'information collectée à partir d'une seule mesure : l'évolution de la pression interne et la modification de la composition du gaz. Le dispositif développé s'avère performant sous irradiation pour ce qui concerne la surveillance en ligne de la composition des gaz de fission libérés. Mais une caractérisation expérimentale et des recherches supplémentaires sont nécessaires pour vérifier la performance du capteur pour mesurer la pression par l'atténuation de l'amplitude du signal acoustique et que cette atténuation peut être séparée de l'atténuation du signal de sortie induite par l'irradiation.

Mesure des dimensions

Allongement axial

Les capteurs LVDT sont des solutions technologiques robustes et fiables pour les applications en pile, et les conceptions disponibles peuvent être optimisées pour s'adapter à la configuration d'ADELINE. Ils permettent de suivre l'allongement total de la gaine et du combustible pendant l'irradiation et, grâce aux récents développements sur l'autocompensation, ses performances permettent d'atteindre une précision de 9 µm dans la plage de mesure de 1 mm.

L'extensomètre Fabry-Perot constitue une technologie complémentaire prometteuse au LVDT : il permet en effet d'évaluer l'allongement local d'une partie de la gaine. Aujourd'hui, les performances de la solution technologique à haute température et sous irradiation n'ont pas encore été testées, mais les résultats intermédiaires donnent des résultats positifs. Un dispositif résistant aux rayonnements a été mis au point et les mesures à haute température ont montré une résolution de l'ordre du micromètre. En raison de la configuration géométrique des éléments de combustible, cette technologie n'est pas adaptée à la mesure de l'allongement de la colonne de combustible.

Diamètre extérieur de la gaine

L'un des paramètres les plus importants à caractériser pendant l'irradiation est la cinétique de déformation du diamètre extérieur de la gaine. Pour cela, nous avons étudié quatre solutions technologiques : l'interféromètre de type Michelson, la jauge de diamètre, la jauge de contrainte soudable et la microscopie confocale.

L'interféromètre de type Michelson et la jauge de contrainte permettent via un palpeur de réaliser des profils de la gaine avec une précision de l'ordre de quelques µm. Cependant, elles nécessitent le contact mécanique du palpeur avec la gaine ce qui entraine d'une part, un risque de détérioration de la surface occultée (rayure) et d'autres part, une perturbation locale des échanges thermiques risquant de biaiser la mesure effectuée.

Ces solutions technologiques sont donc moins adaptées à la caractérisation de l'IPG que les solutions envisagées ci-après.

La jauge de diamètre bénéficie des nombreux retours d'expérience des irradiations dans le réacteur de Halden, où le système a permis de réaliser la profilométrie des gaines. Mais, la conception originale de Halden n'est pas compatible avec la configuration géométrique d'ADELINE. La conception modifiée proposée par le CEA répond aux contraintes géométriques et, sur la base de la caractérisation hors pile, répond à la précision de mesure requise pour l'étude de l'IPG. Sa conception présente trois longs bras pour évaluer le profil de la tige d'échantillonnage. Cela rend le capteur sensible au profil thermique axial et aux vibrations induites par l'écoulement qui caractérisent la section d'essai ADELINE.

La microscopie confocale est la seule solution technologique identifiée qui permet de réaliser une mesure sans contact instantanée du diamètre local de la gaine. étant une mesure optique, elle permet d'effectuer des mesures avec une précision de l'ordre du micromètre, comme cela est requis pour l'étude de l'IPG. L'utilisation d'un capteur à fibre optique permet également de minimiser les dimensions caractéristiques du capteur. Aujourd'hui, des études sont menées pour étudier la possibilité de l'appliquer dans le contexte nucléaire.

Pour son application dans le dispositif ADELINE, il est nécessaire de développer un support mobile, pour permettre l'étude du profil du crayon testé. L'effet des vibrations induites par l'écoulement doit être étudié, même si la constante de temps des vibrations caractéristiques du crayon semble plus élevée que le temps caractéristique nécessaire pour une seule mesure.

Contact Pastille-Gaine

En ce qui concerne la détection du contact entre les pastilles et la gaine, nous avons présenté deux solutions technologiques qui font toutes deux l'objet d'une étude de faisabilité.

Tout d'abord, la microscopie acoustique a montré des résultats intéressants avec des matériaux représentatifs dans des conditions de laboratoire, mais il faut étudier sa capacité à effectuer la mesure sous des vibrations induites par l'écoulement et à distinguer l'IPG faible d'un contact local causé par un manque d'alignement des pastilles ou un fragment simplement délocalisé.

Deuxièmement, nous avons proposé d'étudier si le contact progressif entre les pastilles et la gaine et la diminution du mouvement relatif le long de l'axe de la colonne combustible induisent un effet mesurable sur les vibrations des éléments de combustible induites par leur interaction avec le liquide turbulent environnant. La présence du jeu local entre les pastilles et la gaine ainsi que l'excitation du crayon induite par l'écoulement du fluide externe provoquent un mouvement relatif entre les pastilles et la gaine : des chocs entre les pastilles et la gaine et du frottement entre les pastilles et la gaine. Ces mécanismes de dissipation contribuent à l'énergie totale dissipée dans la structure et amortissent les vibrations du système. L'établissement de la faible interaction réduit les mouvements relatifs, avec pour conséquence une réduction de l'énergie dissipée. Ceci devrait pouvoir être observé par une modification des fréquences du système, de son rapport d'amortissement visqueux ou de l'amplitude des vibrations.

Pour cela, nous avons réalisé une étude de faisabilité.

Étude de faisabilité pour détecter l'IPG par les vibrations de l'élément de combustible

Le banc d'essai IMPIGRITIA[1] est conçu et réalisé dans le cadre de cette thèse de doctorat pour étudier la faisabilité de la mesure de l'impact d'une faible interaction locale entre la gaine et les pastilles sur le comportement dynamique du crayon de combustible. La configuration géométrique est développée sur sa base et le circuit hydraulique est conçu pour soumettre le crayon à l'excitation représentative de celle d'ADELINE.

IMPIGRITIA fonctionne à température ambiante, à basse pression et hors flux de neutrons. Pour évaluer le débit représentatif à imposer à la barre d'échantillonnage, nous avons appliqué la similarité hydraulique imposant la conservation des fluctuations de pression de la paroi et le principe de Burgreen. Nous avons identifié une gamme de valeurs

[1] Acronyme de "Interaction Mécanique PastIlle Gaine : RéalIsation du Test vIbrAtoire", du latin impigritia, impigritiae ; signifie "zèle, dévouement"

équivalentes. La configuration géométrique a été simplifiée et la longueur totale du porte-échantillon est d'environ 1.5 m, ce qui augmente la rigidité du dispositif IMPIGRITIA par rapport à ADELINE. Les conditions limites sont les mêmes que pour le dispositif ADELINE : le porte-échantillon est fixé au sommet de la section d'essai et il est centré au moyen de quatre éléments annulaires, situés sur sa longueur. Le crayon est constitué d'une gaine en Zy4 supportant 33 pastilles de 15 mm de hauteur, pour une longueur totale de l'élément d'environ 50 cm. Pour des raisons d'exploitation, l'UO_2 n'a pas pu être utilisé pour les pastilles et celles-ci sont fabriquées en molybdène, représentatif en termes de masse volumique. Dans notre crayon, le jeu radial imposé par la fabrication s'élève à 80 µm. La faible IPG est induite dans le système par un système de dilatation locale : le gonflement d'un ballon. Le système est introduit par le haut du porte-échantillon, à travers des pastilles percées au centre, et est placé dans la région où l'on veut induire la fermeture du jeu. A cet endroit, les pastilles sont remplacées par deux demi-coquilles, qui sont déplacées au moyen du ballon gonflé, ce qui entraîne un contact entre les pastilles et la gaine.

La campagne expérimentale s'est déroulée en deux phases : une première phase en air, où le système est étudié au travers d'essais de vibrations libres. Cette phase permet de caractériser le système et de vérifier la faisabilité générale de la détection. Dans la seconde phase, la structure est immergée dans l'eau et est soumise à l'excitation représentative du dispositif ADELINE par une débit d'eau turbulent adapté. Les seuls mécanismes d'excitation sont les vibrations induites par le fluide. L'objectif de cette phase est de vérifier la faisabilité technologique de mesurer l'impact d'une IPG faible avec un système passif sans qu'il soit nécessaire d'exciter activement le crayon. Pour les deux phases expérimentales, le mouvement transversal de l'élément est mesuré par vibrométrie laser Doppler, même si cela n'est pas applicable dans ADELINE.

Tous les tests ont montré que le contact local ne peut pas être détecté par l'analyse des fréquences caractéristiques de la structure. Par contre, nous avons montré la faisabilité de la détection de l'IPG de type faible par analyse de son effet sur l'énergie dissipée dans le crayon, qui modifie le taux d'amortissement visqueux et l'amplitude des oscillations.

En effet, les essais de lâcher en air ont montré des résultats positifs sur la capacité à détecter le contact local entre les pastilles et la gaine sur environ 10 % de la longueur de la colonne de combustible (45 mm sur les 50 cm environ). Les investigations effectuées sous écoulement turbulent sont positives mais affectées par des incertitudes plus importantes.

Lors des tests, la variabilité du comportement des crayons en fonction de l'excitation externe et la manque de répétabilité des mesures nous portent à considérer l'intérêt d'une excitation active de la structure. Ceci permettrait d'explorer l'ensemble des fréquences et amplitudes de vibration de la structure afin d'identifier les zones de fonctionnement les plus propices à la probabilité de détection de l'IPG faible.

Scénario d'irradiation proposé pour détecter et caractériser l'IPG et le début de la fusion dans ADELINE

Enfin, sur la base des recherches effectuées, nous avons proposé le principe d'un scénario d'irradiation pour le futur dispositif ADELINE du réacteur RJH ainsi que la méthode de mesure correspondante afin d'améliorer la compréhension de l'IPG et détecter le début

de la fusion du combustible. Le scénario prévoit l'utilisation d'un élément de combustible neuf, constitué de pastilles en UO_2 et d'une gaine zyrcalloy, qui sera soumis à un test de rampe de puissance par palier. Le combustible neuf permet de connaître le seuil de fusion et de limiter les effets du comportement de l'élément de combustible induits par le gonflement gazeux et les effets de l'irradiation. La rampe par palier permet d'approcher le seuil de fusion en gérant les contraintes induites sur la gaine et en limitant le risque d'une perte non désirée de son intégrité physique.

La méthode de mesure associée propose l'utilisation des solutions technologiques, supposées développées et optimisées: thermomètre à ultrasons pour la température de l'axe, microscopie confocale pour le diamètre externe de la gaine, les LVDT pour l'allongement axial de gaine et combustible, capteur de type LVDT modifié pour solliciter périodiquement la structure et détecter le contact pastille-gaine via la mesure de vibrations et enfin, le capteur de contre-pression pour mesurer la pression interne du système étudié. Le couplage de la mesure discrète et de la mesure continue permet de définir un scénario d'irradiation qui peut être piloté en ligne pour optimiser le suivi de la phénoménologie étudiée. Il permet d'obtenir une grande quantité d'informations qui peuvent être comparées aux résultats du code de calculs pour sa validation et son éventuelle amélioration.

Perspectives

La faisabilité de la détection de l'IPG étant établie avec un bon niveau de confiance et le lien causal entre la fusion à cœur et la dynamique de déformation de la gaine mis en évidence sur la base d'un schéma de calcul très simplifié, l'intégration du modèle de fusion dans ALCYONE est fondamentale pour la qualification et la quantification de ces effets. Nous proposons que le modèle soit validé expérimentalement par un test spécifique, par exemple réalisé dans l'installation VERDON (CEA Cadarache).

Afin de comparer quantitativement les résultats de la simulation avec les résultats expérimentaux, il est important d'améliorer le degré de confiance du code de performance du combustible en quantifiant les incertitudes des quantités calculées. En effet, les paramètres calculés sont affectés par plusieurs sources d'incertitudes : les propriétés des matériaux, les paramètres du modèle, les conditions expérimentales (en particulier celles liées à la puissance linéaire à laquelle le crayon est irradiée et les mesures thermiques), les incertitudes sur les résultats expérimentaux qui sont utilisés pour valider le code (comme la mesure des gaz de fission relâchés) et les incertitudes de la modélisation. La propagation de ces incertitudes peut être effectuée via la plate-forme URANIE et/ou d'une technique de Monte-Carlo.

Dans le cadre de l'utilisation des vibrations du crayon pour la détection de l'IPG faible, d'autres études peuvent être développées sur la base des travaux réalisés dans le cadre de cette thèse sur l'essai de faisabilité IMPIGRITIA et l'utilisation des vibrations des crayons pour détecter l'IPG.

Tout d'abord, le développement d'un modèle dynamique de l'élément prenant en compte les dissipations internes et l'interaction avec le fluide environnant, en support de l'interprétation des phénomènes observés pendant l'expérience. Les résultats collectés au cours de l'expérience IMPIGRITIA peuvent être utilisés pour valider le modèle développé. D'autres mesures sont proposées, pour tester et qualifier l'intérêt d'une mesure active et d'un

relâchement de la force appliquée par le ressort qui bloque axialement les pastilles, afin de contrôler et d'accroître le mouvement interne des pastilles. Des tests effectués avec des pastilles en UO_2 sont également nécessaires car le molybdène a un coefficient de friction différent de celui de l'UO_2.

Le modèle développé et la deuxième campagne expérimental permettrons de donner des éléments pour l'optimisation du dispositif ADELINE afin d'améliorer la possibilité de détecter l'IPG faible par vibrations.

Concernant la méthode de mesure, les solutions technologiques identifiées doivent être développées ou optimisées pour être appliquées à l'appareil ADELINE. Ainsi, le scénario doit être détaillé et validé par de pré-calculs à l'aide d'ALCYONE.

Les LVDTs et le capteur de contre-pression demandent des adaptations pour leur application dans ADELINE. Il est important de vérifier la faisabilité de l'utilisation de la microscopie confocale dans un environnement hautement radiatif, à haute température et à haute pression à travers une couche de débit turbulent. La performance de la pyrométrie optique doit être confirmée dans la gamme des températures opérationnelles d'environ 300°C. D'autres essais dans un réacteur de recherche devraient être effectués pour étudier les performances des thermomètres à ultrasons et les comparer aux thermocouples de type C. La fonction de transfert liée à l'introduction de ce capteur au centre de la pastille doit être établie avec précision. Enfin, il serait nécessaire de concevoir le capteur pour la mesure des vibrations du capteur et permettant d'exciter activement le crayon.

En perspective, les résultats de cette thèse fournissent un faisceau d'éléments qui établissent la faisabilité de la mesure de l'IPG. Cependant, celle-ci ne sera établie que par la définition et la réalisation d'un véritable programme expérimental consacré à l'IPG. Pour cela, un scénario d'irradiation précis doit être développé et le comportement thermomécanique attendu du crayon de combustible calculé par ALCYONE, où chaque paramètre observable à mesurer est associé à sa plage d'incertitudes.

Detection of the fuel Pellet-Cladding Interaction (PCI) and of the fuel central melting during a power ramp test in the Jules Horowitz Reactor (JHR): modeling and real time measurement of the fuel element deformation

Abstract

In a nuclear reactor, the fuel is in the form of cylindrical pellets stacked in a cladding. The nuclear fission reaction within the fuel causes the temperature of the fuel to rise and thus cause the pellets to expand. The cladding surrounding the pellets is subjected to the external pressure of the coolant, leading to the decrease of its diameter by creep. The initial gap between the fuel and the cladding therefore gradually closes and a mechanical interaction between the two objects establishes, called the Pellet-Cladding Interaction (PCI).

In the frame of a greater flexibility in the maneuverability of nuclear power plants (to follow the grid demand according to the intermittent supply of renewable energies), a sudden power variation (power transient) may occur, leading to the increase of fuel temperatures. This increase induces a greater expansion of the pellets and generates additional stresses in the cladding. The Safety Authority requires the power plant operator to ensure the physical integrity of the cladding, which constitutes the primary containment barrier for radioactive materials, and the absence of central melting in the fuel pellets.

To better understand the physical phenomena related to PCI under these transient conditions, specific experiments called power ramps are carried out in dedicated research reactors. The data collected are used to increase our knowledge and thus improve modelling and validate numerical simulations. Today, the vast majority of measurements are performed before and after the experiment, giving only the initial and final state of the system and thus limiting the amount of available information.
The work of this thesis focuses on the development of a measurement method dedicated to the on-line characterization of the PCI kinetics as well as to the detection of the onset of central fuel melting.

The first part of the thesis deals with the identification of the set of relevant and observable parameters to be measured. For this, we use the multidimensional code ALCYONE, the reference fuel performance code of the simulation platform PLEIADES, developed by CEA in collaboration with EDF and FRAMATOME. The lack of a model to account for the onset of melting in the fuel pellet in ALCYONE required the development of a thermomechanical model, using homogenization methods. The objective of this development was to calculate the measurable effects on the cladding deformation kinetics due to the characteristic expansion of the solid-liquid phase change of uranium dioxide.

In the second part, the parameters identified and the associated measurement criteria guide the review of available technological solutions used in the nuclear field and the ongoing developments. The advantages and disadvantages of each measurement principle and their suitability for use in the nuclear field are discussed. We then take into account the specific environmental and geometrical constraints of the irradiation of the RJH test

reactor and its ADELINE device to identify the recommended technologies. An experimental study, called IMPIGRITIA, has been designed and carried out to state on the feasibility to detect the origin and evolution of the contact between the pellets and the cladding by means of fuel element vibrations. The initial results obtained are encouraging and further investigations are identified on this topic.

Finally, on the basis of the research carried out, we propose the principle of an irradiation scenario in the future ADELINE device of the JHR reactor as well as the corresponding measurement method in order to improve the understanding of PCI and fuel melting onset.

Key words: PCI, melting, incident, power ramp test, modeling, instrumentation, deformation, real time, vibrations, JHR, ADELINE

Résumé

Dans un réacteur nucléaire, le combustible se présente sous forme de pastilles cylindriques empilées dans une gaine. La réaction de fission nucléaire au sein du combustible va provoquer une élévation de la température de celui-ci et, donc, une dilatation des pastilles. La gaine entourant les pastilles est soumise à la pression externe du fluide caloporteur entrainant une diminution de son diamètre par fluage. Le jeu initial entre le combustible et la gaine va donc progressivement se fermer et une interaction mécanique va ainsi s'établir entre les deux objets, appelée Interaction Pastilles-Gaine (IPG).

Dans le cadre d'une plus grande flexibilité dans la manoeuvrabilité des centrales nucléaires (suivi du réseau en fonction de l'apport intermittent des énergies renouvelables), une variation soudaine de puissance (transitoire de puissance) peut se produire entrainant une augmentation des températures dans le combustible. Cette augmentation va créer une dilatation plus importante des pastilles et générer des contraintes supplémentaires dans la gaine. L'Autorité de Sûreté impose à l'opérateur des centrales d'assurer l'intégrité physique de la gaine qui constitue la première barrière de confinement des matières radioactives ainsi que l'absence de fusion au coeur du combustible.

Afin de mieux appréhender les phénomènes physiques de l'IPG dans ces conditions transitoires, des expériences spécifiques appelées rampes de puissance sont réalisées dans des réacteurs de recherche dédiés. Les données recueillies sont utilisées pour accroître nos connaissances et ainsi améliorer la modélisation et valider les simulations numériques. Aujourd'hui, la grande majorité des mesures sont effectuées avant et après l'expérience ne donnant qu'un état initial et final, limitant de ce fait la quantité d'informations disponibles.
Le travail de cette thèse se concentre donc sur le développement d'une méthode de mesure dédiée à la caractérisation en ligne de la cinétique de l'IPG ainsi qu'à la détection du début de la fusion à coeur.

La première partie de la thèse porte sur l'identification de l'ensemble des paramètres pertinents et observables à mesurer. Pour cela, nous avons utilisé le code multidimensionnel ALCYONE, code de référence pour la performance du combustible de la plateforme de simulation PLEIADES, développée par le CEA en collaboration avec EDF et FRAMATOME. Le manque d'une modélisation tenant compte du début de la fusion dans la pastille de combustible dans ALCYONE a nécessité le développement d'un modèle thermomécanique, au moyen de méthodes d'homogénéisation. L'objectif de ce développement était de déterminer numériquement les effets mesurables sur la cinétique de déformation de la gaine lors de la dilatation caractéristique du changement de phase solide-liquide du dioxyde d'uranium.

Dans la deuxième partie, les paramètres identifiés et les critères de mesure associés guident l'examen des solutions technologiques disponibles utilisées dans le domaine nucléaire et les développements en cours. Nous avons étudié les avantages et les inconvénients de chaque principe de mesure et leur aptitude à être utilisé dans le domaine du nucléaire. Nous avons ensuite pris en compte les contraintes environnementales et géométriques spécifiques de l'irradiation du réacteur d'essais RJH et de son dispositif ADELINE pour identifier les technologies recommandées. Une étude expérimentale, baptisée IMPIGRITIA, a été conçue et réalisée pour statuer sur la faisabilité de détecter l'origine et l'évolution du contact entre les pastilles et la gaine au moyen de vibrations de l'élément combustible. Les premiers résultats obtenus sont encourageants et des investigations complémentaires sont identifiées sur ce sujet.

Enfin, sur la base des recherches effectuées, nous proposons le principe d'un scénario d'irradiation réalisable dans le futur dispositif ADELINE du RJH ainsi que la méthode de mesure correspondante afin d'améliorer la compréhension de l'IPG et de la fusion à coeur.

Mots-clés : IPG, fusion à cœur, incident, rampe de puissance, modélisation, instrumentation, déformation, temps réel, vibrations, RJH, ADELINE

Contents

List of Figures

List of Tables

Introduction

Power variations and a flexible production from nuclear source has become a challenging subject in the last years. Indeed present days are characterized by a world attempt at moving to a more sustainable energy production. In France, where the electricity mainly comes from the nuclear source, the plan is to be realized by integrating in the energy mix the intermittent ones produced by renewable sources. The oscillating grid demand results into the need for nuclear power plants to ensure increased maneuvering. This involves the rise of stresses inside the fuel elements constituting the core of the nuclear reactor. Each fuel element is made of small cylindrical pellets stack inside a metallic tube, the cladding, which provides mechanical support and prevents the release of radioactive fission products out of the fuel element. During normal operation conditions, the pellets expand due to the thermal increase associated to power production. The gap existing between the pellets and the surrounding cladding by fabrication process progressively reduces up to its complete closure. Consequently to the contact, the two objects interact and their behaviors are mutually influenced: expanding pellets induce internal stresses on the cladding and drive its deformation while the cladding slows down pellets outward deformation. This phenomenon is known as **Pellet-Cladding Interaction (PCI)**. The integrity of the cladding ensures the confinement of radioactive fission products inside the fuel rod, so it has a fundamental role for safety. To improve the understanding of phenomena involved with PCI, dedicated experimental sequences are performed in material testing reactors and collected data are used to develop models and simulation code.

This work constitutes the first step towards the development of an on-line measurement method to better the knowledge of relevant physical phenomena associated to PCI. These improvements are required to extend operational margins to follow grid demand ensuring the cladding integrity and the absence of local melting inside the fuel material.

Modeling has become a fundamental tool to understand the macroscopic behavior of the fuel element and support the definition of technical specifications. Among the available simulation platforms, ALCYONE of the CEA computing environment PLEIADES is a reference tool that allows to assess the fuel rod thermal-mechanical behavior, at each time during normal and off-normal operations. ALCYONE development is based on data collected during irradiation experiments carried out in the past years in dedicated devices, installed in research nuclear reactors. The majority of data has been obtained from examinations carried out before and after the irradiation experiments. The harsh environmental conditions of the nuclear system strongly limits the number of instrumented irradiation permitting on-line measurements. Post Irradiation Examinations (PIE) allow to have a clear and accurate picture of the initial and final status of the system but are unsuited to study system evolution. Nowadays modeling, with its capability to describe the kinetics of

fuel rod behavior, needs data measured during the irradiation to define updated technical criteria to ensure the integrity of the cladding against pellet-cladding interaction and avoid local thermal increases leading to the onset of central fuel melting during power transients. To reach these objectives, dedicated irradiation sequences are foreseen in the next future Jules Horowitz research Reactor (JHR), under construction in Cadarache, France. A new measurement method specifically designed to assess PCI has to be defined and developed to permit the on-line detection and characterization of fuel behavior. For this, CEA is carrying out researches on the improvement of robust technological solutions and on the development of innovative ones to detect and measure the studied phenomena.

The PART I of this thesis concerns the identification of the set of relevant and observable parameters which measurements are needed to detect and to characterize PCI during normal and off-normal operation conditions.
What has to be measured? When measurements have to be performed to detect and characterize the PCI and the melting onset? Where do measurements have to be carried out?
To answer these questions, we use present modeling capabilities and build in ALCYONE code simulations describing the fine kinetics of fuel thermal-mechanical behavior to establish the physical links between the researched phenomena and the measurable effects.
Off normal conditions can possibly consist in power transients leading to really high temperatures in the fuel. Bearing in mind the safety requirements, we want to analyze the effects of the enhanced internal stresses on the cladding and verify the existence of a characteristic effect on PCI unequivocally due to the onset of central melting in the fuel.
Does a signature exists? Can it be measured?
ALCYONE does not present a model to account for fuel melting so, to identify this "signature" of fuel melting on PCI, we propose a thermal-mechanical model.
The PART II of this work concerns the development and implementation of this model to state on the theoretical feasibility to detect the onset of fuel melting.

The identified measurement requirements are the base to review present and on-going technological solutions that meet the required spatial and temporal resolution. In this PART III, both robust technologies resistant to the nuclear field and the most promising developments are investigated to evaluate the pro and cons of their measurement principles, their capability to respond to the measurement criteria and their readiness for use in the nuclear environment. The adaptation of a technology to the nuclear environment constitutes indeed a key challenge in the development of a technology: accuracy and reliability to meet scientific requirements, endurance to resist to the harsh nuclear environment and minimization to limit system perturbation and to cope with the reduced available space in the irradiation device.

The final PART IV concerns the application of the measurement method to detect and measure PCI to the JHR. Accounting for its specific environmental and geometrical constraints, we study the feasibility to detect the origin and the progression of PCI in an innovative way. From the results on feasibility study and accounting for the critical review performed, we propose an hypothetical irradiation scenario and the associated measurement protocol to characterize the PCI kinetics under irradiation during an off-normal operation condition which approaches the onset of fuel melting.
Lastly, the conclusions of this work are summarized and the identified perspectives are proposed.

Part I

Pellet-Cladding Interaction characterization

Chapter 1

Background and motivations

In this chapter we describe the phenomena leading to the Pellet-Cladding Interaction mechanism and discuss the related economical and safety concerns. In section 1.1 we introduce the nuclear context and describe the fuel element. Section 1.2 presents the origin and evolution of PCI mechanism in normal and off-normal operations and we give the definition of PCI that is used in the rest of the document. Finally, in section 1.3 we illustrate the safety and economical interests related to PCI that motivate the development of this thesis.

Contents

1.1 The nuclear context

Pellet Cladding Interaction is a phenomenon deeply linked to its environment and strictly influenced by the geometrical configuration of the system. To introduce the studied phenomenology, we first illustrate the environment and design of a nuclear power reactor and the main characteristics of the fuel elements constituting its core.

1.1.1 PWR - Pressurized Water Reactors

According to the 2016 French electrical review, 72% of the total electrical production comes from the clean and sustainable nuclear power [bilan16]. At present days, France has 58 operating Pressurized Water Reactors (PWR) subdivided in 19 nuclear sites. The primary source of the energy is the fission of an atom of U^{235} caused by its interaction with a thermal neutron[1]. The fissile material is part of the fuel, located in the reactor core within the reactor vessel. The energy produced by fission is transferred in the form of kinetic energy to the fission products produced by fission and transformed into heat as they slow down in the fuel. The produced heat is extracted by liquid pressurized water at 155 bars, with inlet temperature of about 290°C. All this occurs in the primary loop of the nuclear power plant, which scheme is presented in figure 1.1. At the steam generator, the water (coolant) transfers the heat to the secondary loop. The steam produced by the steam generator induces the rotation of the turbine. The mechanical work produced is converted in electricity at the electric generator and sent to the grid.

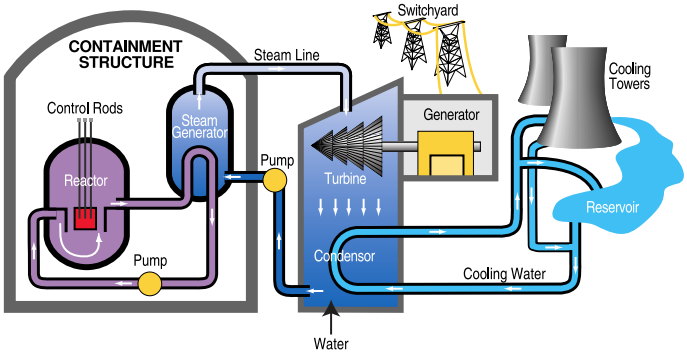

Figure 1.1 – Schematized view of a PWR nuclear power plant system: in purple the primary loop in dark blue the secondary loop and in light blue the condensation system

1.1.2 The reactor core

Within the PWR reactor vessel, the core consists of more than 150 fuel assemblies, which geometrical configuration is presented in figure 1.2. They present a square-mesh array and guarantee the mechanical support for the fuel rods, where energy is produced. The fuel assemblies also host the control rods, that are specific rods made of a neutron absorbant material like Gadolinium, which allow to manage the fission rate in the core. The structure of those assemblies presents an upper and a lower fitting, named the top and bottom nozzle, and the guide tubes, to which spacer grids are welded. The role of those spacer grids is twofold: support the fuel rods and improve the mixing of coolant, thus limiting the risk of local hot spots.

[1]We define thermal neutrons the neutrons having a kinetic energy of 0.025 eV. According the energy dependent fission cross section of U^{235}, those neutrons have the highest probability to interact with an atom of $U^{235}$and fission it

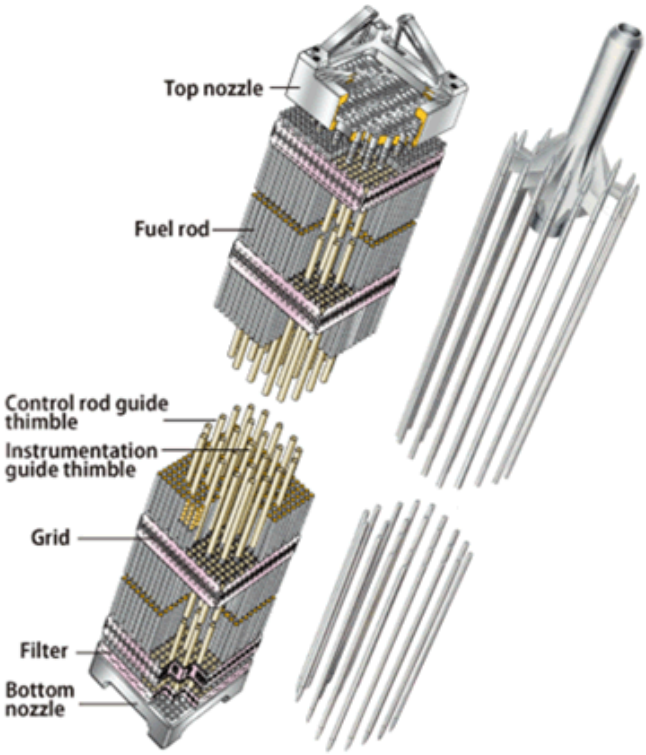

Figure 1.2 – PWR fuel assembly. On the left the different component mentioned in the text and on the right the control rod cluster [Bai96]

1.1.3 The fuel element

Figure 1.3 shows a schematic view of a PWR fuel rod, the fundamental component in a PWR reactor core: here, the fissile material is manufactured in cylindrical pellets which are stack inside a metallic tube. The figure 1.3 illustrates the sample rod geometry for a type of PWR: the external diameter of the cladding amounts to 9.5 mm and has a total length of 3.85 m. The active length, that corresponds to the total length of the fuel stack is 3.65 m. A spring is introduced in the top part to limit pellets movement during fuel rod handling before and after its life in the PWR core.

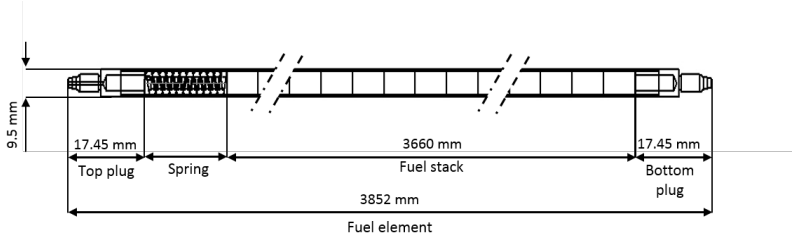

Figure 1.3 – Scheme of a PWR fuel rod showing the geometrical configuration and the characteristics dimensions

The internal atmosphere of the fuel element is pressurized at the beginning of life with helium at 30 bars (normal temperature and pressure). This process allows to limit the internal deformation of the system submitted to the coolant pressure (155 bars).
Two plugs welded on the top and bottom of the rod ensure the water-tightness of the element.

Figure 1.4 illustrates the geometrical characteristics of a PWR fuel pellet. It presents a diameter of 8.2 mm and a length of 13.8 mm and it is not a perfect cylinder: edges are eased (chamfer) to prevent their damage during fuel assembling procedures and a central dishing is introduced on the top and bottom section, generally having a diameter of about 6 mm. As it will be detailed in chapter 2, the dishing is used to accommodate fuel thermal expansion and allows an extra retention of fission products.

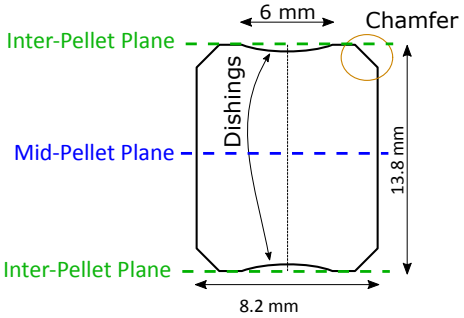

Figure 1.4 – Characteristic dimensions of a standard French PWR fuel pellet

To permit the assembly of the fuel element, a fabrication gap exists between the pellets and the cladding. Its radial thickness amounts by design to 80 µm. A synthesis of the mentioned characteristics is reported for practical use in table 1.1.

The fuel material: The usual fuel material in PWR reactors is uranium dioxide UO_2, which presents a low volume fraction of the fissile isotope of uranium, U^{235}, between 3% and 5%. Another type of fuel is the Mixed OXides (MOX fuel) which presents a higher percentage of fissile plutonium Pu^{239}, about 8%. From each fission event, an average of two to three fission products are produced. The kinetic energy transferred to fission products is dissipated into the fuel, leading to the volume heat generation.
The main goals of the nuclear fuel is:

- To produce the heat and deliver it to the coolant;
- For a safety concern, the fuel matrix has to confine as much as possible the FPs within itself, in normal operation conditions as well as in incident and accident (see section 1.3);
- To ensure the highest consumption of the fissile material to minimize the economical impact of the fuel cycle;

Length of the fuel element	3.85 m
Fuel stack length	3.66 m
Fuel pellet diameter	8.2 mm
Fuel pellet Length	13.8 mm
Dishing diameter	6 mm
Cladding internal diameter	8.36 mm
Cladding external diameter	9.5 mm
Radial fabrication gap	80 µm

Table 1.1 – Synthesis of useful geometrical characteristics of PWR fuel rod

– To guarantee a mechanical stability at high temperature and under ionizing radiation to preserve core geometry.

The porous ceramic UO_2 is the most performing material: chemically stable and compatible with water, this oxide presents very good resistance to high temperatures and irradiation. Moreover, it has a low parasitic neutron absorption caused by oxygen and a good retention capability of fission products in the fuel matrix.

The cladding material: The tube confining the fuel pellet stack has to ensure the mechanical support of the unit, guarantee the heat transfer from the fuel material to the external cooling and confine the radioactive fission products which would instead be released directly in the primary loop. **Thus, the cladding is the first barrier to prevent the release of radioactive fission products out of the fuel rod. Safety analysis pays specific attention to it.**
The material constituting the cladding has to show good transparency to neutrons, ensure the thermal exchange, present good mechanical strength even at high temperatures, limited degradation under ionizing radiation and good corrosion resistance in all situations, including accidental ones.
Nowadays, most of the claddings are made of zirconium alloys. This alloy has been chosen because it presents a low thermal neutron absorption, it satisfies mechanical properties, it is sufficiently stable under neutron flux and ionizing radiation and it shows a very high water corrosion resistance at high temperature.

1.2 PCI mechanism

We have defined the components playing a role in the Pellet-Cladding Interaction (PCI) phenomenon. We proceed now to the description of the fuel rod behavior in the reactor leading to the appearance and evolution of PCI in the system. For this we consider an usual PWR fuel rod has previously described, with UO_2 pellets and a specific zirconium based alloy cladding (Zy4) [Bai96].

1.2.1 Heat production and removal

The fission of an atom of U^{235} releases about 200 MeV. 80% of this energy is transferred to the Fission Products (FPs) in the form of kinetic energy which is dissipated in the fuel matrix by electrical excitation.
The power produced in the fuel stack is generally addressed in terms of a linear power production P_{lin} expressed in W/cm which is the heat produced in the unit of time in the unitary length of the fuel stack. Power production is maximum at the middle plan of the core and reduces towards the extremities. A simplified schematic view of the axial profile is illustrated in figure 1.5.

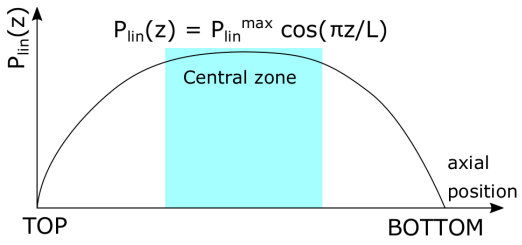

Figure 1.5 – Simplified schematic illustration of the axial power profile in a PWR core [Bai96]

The heat generation in the pellet volume can be considered to be uniform. In the radial direction, it is transferred to the cladding and removed by the coolant. A scheme of the system is reported in figure 1.6: during normal operation conditions, the central temperature does not exceeds 1100°C and the linear power production ranges at about 200 W/cm.

The thermal profiles are obtained by solving the conduction problem in the solid and the convection problem between the solid and the coolant [Bai96]. The resulting thermal profile in the fuel pellet presents a strong thermal gradient. This results from three main factors:

- The heat generation in the volume, uniform in first approximation;
- The presence of a forced cooling at the cladding external surface, constituting an heat sink for the generated heat;
- The low thermal conductivity characterizing the ceramic fuel matrix.

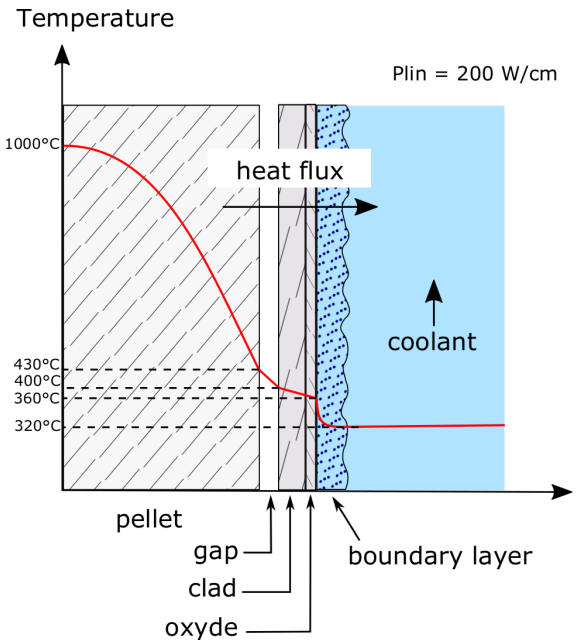

Figure 1.6 – Radial profile of the temperature in the fuel rod in normal operation conditions [Bai96]

1.2.2 Thermal-mechanical phenomena

Fuel densification: Porous UO_2 fuel pellets present by fabrication a target density of about 95%. A few percent porosity allows the pellet to accommodate its own swelling [CEA09]. Porous fraction can be subdivided in two types: small voids (order of µm) resulting from the powder metallurgy process and larger ones (> 10 µm) resulting from the pore forming product during fabrication.
During the first irradiation phase, the fuel stack undergoes a densification process. This results from the interaction of pores with produced fission products and leads to the disappearing of small size porous fraction. This induces a reduction of fuel stack length of 0.25% after 5-10 GWd/tU[2] [Bai96].

[2]The GWd/tU is the generally used measurement unit for the burn-up, which is a measure of how much energy is extracted from the nuclear fuel material

In order to verify the acceptability of densification process during irradiation, after fabrication pellets are submitted to thermal stability tests (24h at sintering temperature, 1700 °C).

Thermal expansion: The increase of system temperature leads to the expansion of the two fuel rod components. The expansion of the fuel and the cladding are different because of two reasons:

- The different thermal expansion coefficient α. At room temperature, this amounts to $9.7 \cdot 10^{-6}1/\mathrm{K}$ for the fuel and to $6.7 \cdot 10^{-6}1/\mathrm{K}$ for the cladding. So for the same thermal increase, the fuel has the tendency to expand more;
- The thermal range in the fuel pellet is far higher than in the cladding.

The fuel dilatation greater than the cladding leads to the decrease of the fabrication gap size. Table 1.2 presents a simplified estimation of the gap decrease, for normal operation conditions, on the average dilatation temperature in the component and assuming a constant thermal dilatation coefficient for the two objects. The radial modification is evaluated as:

$$\Delta(gap) = \Delta r_f - \Delta r_c^i = r_f \varepsilon_f - r_c^i \varepsilon_c \approx 20\mu m \tag{1.1}$$

with $\varepsilon_\mathrm{c} = \alpha_\mathrm{c}(\mathrm{T_{amb}})(\langle \mathrm{T_c} \rangle - \mathrm{T_{amb}})$ and $\varepsilon_\mathrm{f} = \alpha_\mathrm{f}(\mathrm{T_{amb}})(\langle \mathrm{T_f} \rangle - \mathrm{T_{amb}})$. The symbol $\langle . \rangle$ indicates the average.

Cladding	
$\langle \mathrm{T_c} \rangle$	340 °C
$\alpha_\mathrm{c}(\mathrm{T_{amb}})$	$6.7 \cdot 10^{-6}1/\mathrm{K}$
$\alpha_\mathrm{c}(\mathrm{T_{amb}})(\langle \mathrm{T_c} \rangle - \mathrm{T_{amb}})$	$2.1 \cdot 10^{-3}$
Fuel	
$\langle \mathrm{T_f} \rangle$	850 °C
$\alpha_\mathrm{f}(\mathrm{T_{amb}})$	$9.7 \cdot 10^{-6}1/\mathrm{K}$
$\alpha_\mathrm{f}(\mathrm{T_{amb}})(\langle \mathrm{T_f} \rangle - \mathrm{T_{amb}})$	$8.3 \cdot 10^{-3}$
Fabrication gap	80 µm
Hot condition gap	60 µm

Table 1.2 – Values taken from [Bai96]. The $\langle \mathrm{T_f} \rangle = \frac{2}{3}\mathrm{T_f^i} + \frac{1}{3}\mathrm{T_f^e}$ where T_f^i is the centerline fuel temperature and T_f^e is the fuel surface temperature

Fuel cracking: As it has been described in previous sections, the existence of a strong thermal gradient induces the appearance of strong internal thermal stresses. These stresses can be evaluated precisely by numerical calculation (finite element method for example) but a good approximation can be obtained analytically. We assume a constant thermal power and neglect the temperature dependency of material properties like Young's modulus, fuel conductivity and thermal expansion coefficient. Under these hypothesis, the maximum tensile stress σ_θ^{max} is reached at pellet surface and amounts to:

$$\sigma_\theta^{max} = \frac{E}{2(1-\nu)} \alpha (T_f^i - T_f^e) \tag{1.2}$$

where E is the fuel Young's modulus, α is the thermal expansion coefficient, ν is the Poisson's ratio, T_f^i is the central temperature and T_f^e is the temperature of pellet surface.

UO_2 is a brittle material, at least up to temperatures amounting to half of the melting threshold (2874 °C), the fuel cracks when the maximum tensile stress σ_θ^{max} exceeds the ultimate strength of the material R_{crack}:

$$\Delta T_{crack}^{min} = 2\frac{1-\nu}{E\alpha}R_{crack} \tag{1.3}$$

On average, the ultimate strength of UO_2 ranges between 100 and 150 MPa [Gue85]. By eq. (1.3), imposing E= 194 GPa, ν=0.3, the value of alpha given in the previous table 1.2 and R_{crack}=150 MPa, we find that fuel pellets start to fragment when the thermal gradient between the center and the pellet surface exceeds about 100 °C. The fuel consequently cracks since the first power increase at nominal conditions. Moreover, as the fragmentation energy of the uranium dioxide is small (some J/m^2), cracks form fragments. Figure (a) of 1.7 presents a picture of the section of an irradiated fuel pellet, obtained during a destructive Post Irradiation Examinations (PIE). It shows that 6 to 8 fragments are formed. Fragmentation of pellet is generally along the radial direction even though circumferential cracks also appear after some thermal cycles.
Those fragments slightly vibrate under the forced coolant external excitation.
As a consequence of the thermal gradient existing between the pellet center and its periphery, pellet fragments undergo differential expansion. From this pure thermal-elastic deformation of fragments under thermal stresses it results a stronger displacement of the external radius at the Inter-Pellet (IP) plane with respect to the Mid-Pellet plane (MP). The initial cylindrical pellet tends to an hourglass shape with convex faces, as represented in an amplified way in figure (b) of 1.7.

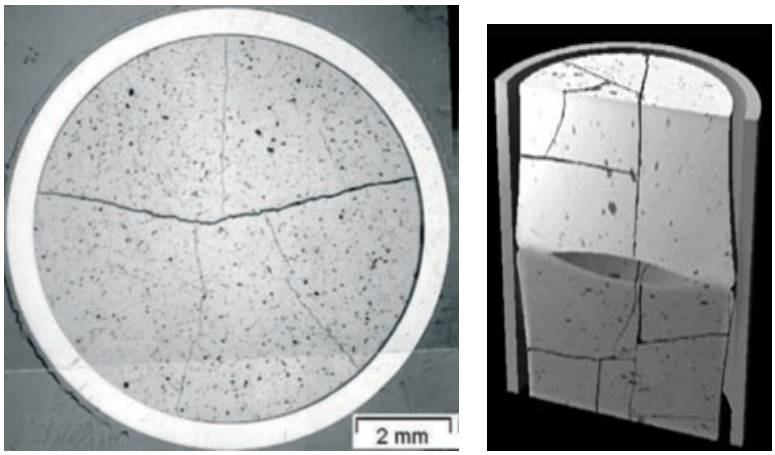

(a) (b)

Figure 1.7 – (a) Cross section photography of an irradiated fuel rod and (b) hourglass shape induced in the fuel pellet since the beginning of irradiation[CEA09]

Solid and Gaseous Swelling: Fuel swelling during irradiation is mainly due to fission products (FPs) atoms replacing heavy atoms. Most FPs are solid, and their contribution is commonly considered negligible. The vast majority of gaseous components are Xenon and Krypton, which are directly produced by fission.
Gaseous fission products produced in the fuel matrix have a very low solubility and thus tend to diffuse in the grains and coalesce into intra-granular bubbles. Those bubbles have a size of some micrometers. The concentration of gas in these bubbles varies according to the re-solution rate (by elastic collision with a fission fragment), the diffusion of other gaseous compounds and the coalescence between different bubbles. Bubbles migration within the

fuel matrix is mainly a thermal phenomenon: solid atoms tend to diffuse towards colder regions whereas gaseous compounds towards the hottest regions in the fuel pellet.
Solid and gaseous retention in the fuel matrix results in fuel swelling. This is attenuated by the mechanisms of gas release [Bai96]: the athermal diffusion, a diffusion mechanism that occurs at low temperature under irradiation; the direct ejection of the fission product from the pellet surface or by displacement cascade originated by a fission product slowing down in the matrix and the thermal diffusion, enhanced by the formation of open tunnels on grain-boundary.
Figure 1.8 shows the measured fractional release of gaseous fission products, produced in the fuel matrix, as a function of the burn-up, for UO_2 and MOX fuel. In this work, we are interested to UO_2 fuel, which shows a fractional release <1% up to about 40 GWd/tU to increase up to 7% at 70 GWd/tU [CEA09].

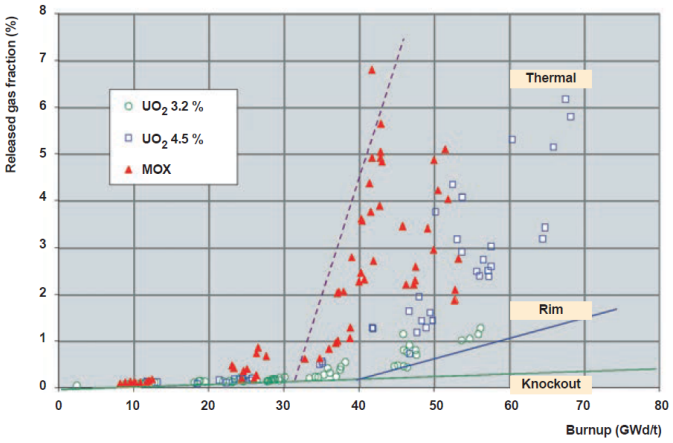

Figure 1.8 – Evolution of the fractional release of fission products as a function of the burn-up. Experimental results are reported for UO_2 and MOX fuel [CEA09]

Creep: Creep is an irreversible progressive deformation process which appears under the effect of stresses below the yield stress. It has different origins (mechanical, thermal, irradiation). Creep evolves in time according to the general evolution described in figure 1.9: (i) the primary creep induces a rapid plastic deformation with a high strain rate, decreasing in time; (ii) the secondary creep or stationary creep presents a quasi-constant strain rate; (iii) tertiary creep is characterized by an increasing strain rate leading to the failure of the material.

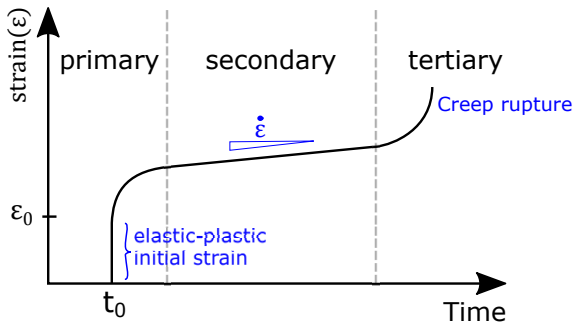

Figure 1.9 – Schematic representation of the evolution of creep deformation with time [Nuc15]

Creep is a fundamental mechanism in the deformation of UO_2 fuel pellets as it will be further detailed in the following chapters. It impacts the cladding deformation, which is submitted to the differential pressure between the external coolant at 155 bars and the internal fuel rod pressurization (30 bars in normal temperature and pressure condition).

1.2.3 PCI origin and evolution

Figure 1.10 schematically represents the geometrical evolution of the fuel rod system during its irradiation in the reactor.

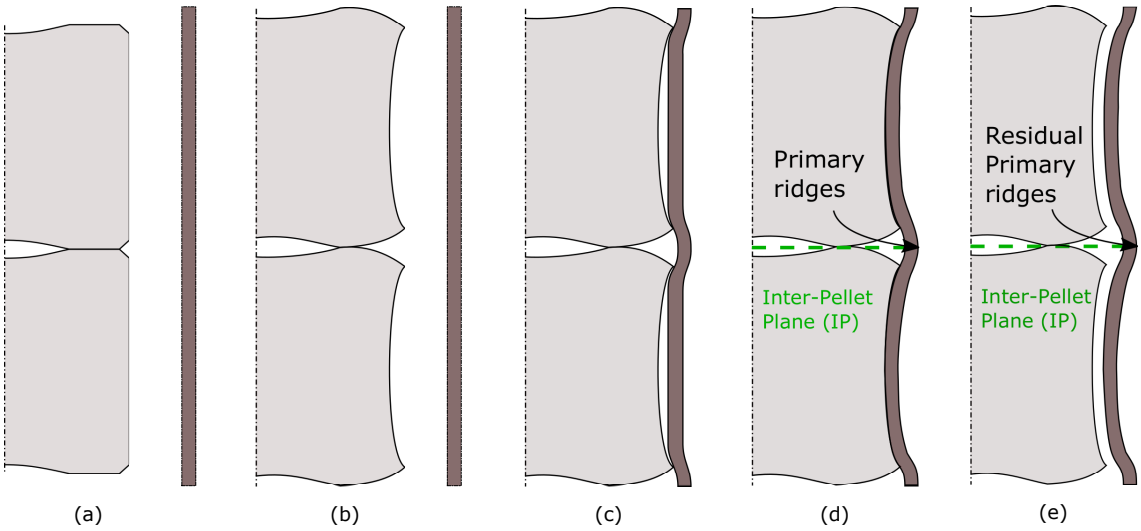

Figure 1.10 – Schematic view of pellet-cladding evolution during base irradiation: (a) rod after fabrication; (b) hourglassing since the first power increase (c) local closure of gap at the Inter-Pellet plane, formation of primary ridges (d) complete closure of the gap, (e) reopening of the gap after the end of the base irradiation.

Figure (a) presents the fuel rod geometry after fabrication: each pellet has cylindrical shape, with chamfers at the edges and a dishing at each extremity. Since the beginning of its life in the nuclear reactor, after the increase of power and temperatures, pellet cracks and the differential thermal expansion of the system leads to the hourglassing of pellet shape (b). Also, during the first days of irradiation, the densification decreases pellet diameter and increases the pellet-cladding gap. During irradiation, cladding creeps inward under the effect of the differential pressure between the inside of the fuel rod and the external coolant. Meanwhile, pellet undergoes solid and gaseous swelling which induce the increase of its diameter. The pellet-cladding gap progressively decreases. As a direct consequence of the hourglass shape, the closure of the gap first origins at the Inter-Pellet plane. From the contact, stresses are formed in the internal surface of the clad. As the cladding keeps on creeping inward, the gap progressively closes along the axial length of the pellet. It results that the last location where contact is created between a single pellet and the corresponding piece of cladding is the Mid-pellet plane.
The cladding undergoes irreversible deformation and modifies its shape according to pellet one. The strong Pellet-Cladding Interaction results in the formation of primary ridges on the cladding, at the Inter-Pellet plane (d), likewise visible after cooling (e).

If the linear power produced in the system is constant, the tensile stresses induced in

the cladding increase up to an equilibrium value, which depends on the external pressure and on the pellets swelling. Once equilibrium is reached, the system is defined "conditioned". In normal operation conditions, equilibrium hoop stress within the cladding is low (< 100 MPa) compared to the rupture strength (> 600 MPa). This means that there is no risk of cladding failure due to mechanical interaction.

During a **transient operation**, higher temperatures establish in the system. This enhances the hourglass shape of the fuel because a stronger thermal gradient origins. As a consequence of higher temperatures, swelling increases in the fuel and thermal creep mechanisms are activated. In the case of closed gap, as a consequence of the contact between pellet and cladding, stresses increase in the clad. The stress field is the highest at the Inter-Pellet plane. Here, the dishing, that characterizes pellet geometry at fabrication, plays an important role: during such transients it constitutes a reservoir for fuel deformation and stresses in the pellet can be relaxed towards the inside, leading to the progressive fulfillment of the dishing. The possibility of the pellet to deform towards the inside decreases the forces applied on the internal cladding surface.
During transient operations, a characteristic deformation origins on the clad: a secondary ridge appears at the level of the Mid-Pellet plane, as showed in figure 1.11.

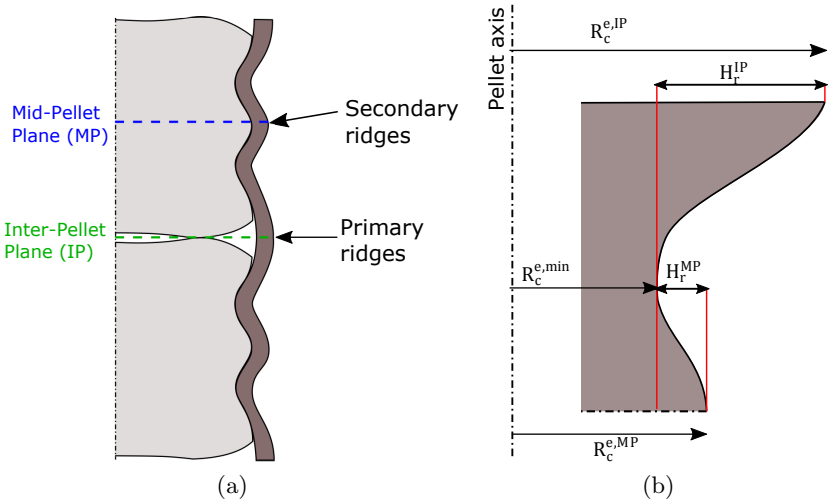

Figure 1.11 – Geometrical evolution of the fuel element after a power transient: (a) the characteristic deformation of the fuel pellet leads to the origin of the secondary ridge at the Mid-Pellet plane of the cladding; (b) evaluation of the height of primary and secondary ridges

The origin and evolution of this secondary ridge, as well as the evolution of the cladding profile, are a direct consequence of the superposed effect of swelling and creep mechanisms taking place in the pellet and of cladding creep.
A schematic representation of how primary and secondary ridges are evaluated is shown in figure (b) of 1.11. Their height is defined as a function of the local cladding diameter, at the Inter-Pellet for the primary ridge ($R^e_{c,IP}$), at the Mid-Pellet plane for the secondary ridge ($R^e_{c,MP}$), and of the minimum cladding radius ($R^e_{c,min}$):

$$H_{r,IP} = R^e_{c,IP} - R^e_{c,min} \tag{1.4}$$

$$H_{r,MP} = R^e_{c,MP} - R^e_{c,min} \tag{1.5}$$

The stresses induced on the cladding internal surface may lead to the formation of cracks and end in the loss of cladding integrity. Failures of the cladding related to the mechanical stress imposed by the pellet on the cladding are defined as **PCI induced failure**.

During the transient operation, the higher temperatures reached in the fuel pellets lead to an increase of the fractional release of fission products. Among the volatile released FPs, some are liable to chemically attack the cladding internal surface. Among the most corrosive volatile fission products for the internal surface of the cladding, is the iodine.
The release of volatile fission products preferentially occurs at cracks level, where also the mechanical stresses imposed by the pellet deformation are the highest.
A cladding failure which origins as a consequence of the mechanical interaction of pellet and cladding and on a cladding internally corroded by iodine is called Stress Corrosion Cracking in the presence of Iodine (SCC-I).

There are several processes which play an important role in the mitigation or worsening of PCI consequences:

Mitigation	(i) At high temperatures, a visco-plastic behavior appears in the central zone of the pellet. This leads to a realignment of radial fragments and attenuation of the pellet hourglass shape; (ii) The cladding creep reliefs internal stresses; (iii) After more than two cycles of irradiation (about 40 GWd/tU) the microstructure of the pellet periphery undergoes a strong evolution due to the combined effect of lower temperatures and an high fission product concentration, due to the formation of fissile Pu^{239} in this zone by neutronic capture of U^{238}. This evolution involves the formation of gas bubbles, occupying about the 10% of the external volume [CEA09]. This microstructure results into a relief on stresses applied by the pellet to the cladding.
Worsening	(i) The pellet undergoes outward swelling due to the progressive gas formation in the system. The amount of fission products increases with the power production and with the burn-up of the system.

From the superposition of these effects, it results that the most critical phase for cladding failure under PCI, during the entire life of the fuel rod, occurs when the fuel has a burn-up of about 30 GWd/tU [Pir17]. At this stage, the gaseous content in the fuel rod leads to a relevant contribution of gaseous swelling to the system deformation, stresses in the cladding are high due to the little relaxation through creep and the burn-up is still too low for high burn-up structure to appear and mitigate the pellet stresses on the cladding internal surface.

1.2.4 Definition of PCI

According to the aforementioned phenomenology, the PCI is related to the origin and the evolution of a stress and a strain field in the cladding due to its interaction with the pellet. To define a common glossary, we make a distinction between weak and strong PCI interaction. We talk about **weak PCI** when pellets and cladding get in contact as a consequence of the deformation kinetics of the two objects: pellet swelling and cladding inward creep. The deformation mechanisms of each component has no impact on the other one and the

two evolve in an independent way.
Pellet and cladding can be locally in contact with no PCI involved: a misalignment of pellets in the fuel stack at fabrication has no consequence on the initial interaction between the two components: as irradiation begins, pellets expand due to thermal dilatation in the preferential direction where stresses are lower, so towards the free gap. The resulting realignment of the pellet has no impact on cladding deformation mechanisms.

Fuel pellets and cladding present different thermal-mechanical behaviors. We talk about **strong PCI** when the behavior of one component modifies the behavior of the other one: the resulting kinetics of the fuel pellets and the cladding are mutually influenced. This phenomenon requires a strong adherence condition between the two. Contact achieved in the weak interaction is necessary but not sufficient.

Specific parameters are associated to the weak and the strong PCI, as we will see in chapter 3.

1.2.5 Relevant factors for PCI

Summarizing the elements given in previous sections, the PCI phenomenon is related to:

1. **Fuel Rod Design and Fabrication quality:** It results from previous description that the fuel rod design (definition of fabrication density and gap thickness over all) has a strong influence on the system response to deformation and swelling. An increased porous fraction in the fuel material fabrication phase leads to an increased capability to retain fission products but induces a reduced stability of the system with respect to the densification process. A stronger densification process under irradiation slows down the gap closure kinetics and induces a degradation of the thermal conductivity of the material, leading to higher temperatures and stresses to establish in the system. A higher porous fraction also reduces the volume fraction of fissile material, leading to an economic cost. The present design of the fuel rod is the result of an optimization process;

2. **Material susceptibility:** PCI mechanism is strictly connected to the material properties of each components, the evolution of their properties during irradiation and their thermal-chemical-mechanical compatibility during the whole life of the fuel in the reactor core;

3. **Operating conditions:** The local power production and the rate of change of global power production impact the contribution of PCI on a possible rod failure. Higher power production leads to a stronger pellet expansion resulting into a higher local stresses on the clad. The power rate modification instead impacts stresses relaxation thus modifying the cladding stress at the end of an operating process. The management and handling of a power reactor has to be carried out to avoid as much as possible the risk of an increase of stresses in the system leading to cladding failure. This results into strict limitations in the amplitudes and rate of power variations.

An effort is being done in recent years in the international community (OECD/NEA) to develop enhanced accident tolerant fuel, specifically designed to improve gas retention and limit as much as possible pellet-cladding interaction [OECD18]. Concerning the development of advanced fuel design, the French joint program carried on by CEA-EDF-FRAMATOME dedicated last years to the development of Cr_2O_3 doped UO_2. The

introduction of chromium indeed improves the retention of fission products by increasing the grain size and enhancing the viscoplastic behavior. These features induce a lower stress resistance capability of Cr_2O_3 doped $UO_2$with respect to present UO_2 pellet, which results to be beneficial as far as PCI cladding stresses are concerned [Del16] [Non04] [Non03].

1.3 Safety and Economical concerns related to PCI

Cladding has a primary role in safety analysis as it constitutes the first barrier to avoid the release of fission products in the primary loop and to limit the occurrence of possible contamination. Safety authority has identified four classes of operational conditions of the nuclear power plant [ASN]:

1. Class I operations: corresponds to the normal operation of the nuclear reactor, thus the base functioning and the eventual load following to cope with the variation in the electricity demand;
2. Class II operations: corresponds to the **incidental operations** having a low frequency of occurrence ($10^{-2} \leq f \leq 10^{0}$). It is required that the cladding integrity is ensured and that fuel melting is avoided;
3. Class III and IV operations: Corresponds to the accidents having very low frequency of occurrence ($10^{-4} \leq f \leq 10^{-2}$) and rare frequency of occurrence ($10^{-6} \leq f \leq 10^{-4}$). They lead to a progressive worsening of damages and radiological consequences.

In this work we focus on the operation conditions of class I and class II.

As a consequence of the increase in the renewable power production, industrial concern is meant to evolve towards the enhancement of reactor maneuverability to follow grid demand. Maneuverability of nuclear power plant during normal and transient operations has to be carried out always ensuring that the cladding integrity is preserved and that there is no central fuel melting. This is realized by limiting operations to respect safety criteria:

- Absence of centerline fuel melting: this is guaranteed by imposing a maximum linear power lower than the value power to melt threshold [IRS17];
- No cladding failure: Circumferential deformation of the zircaloy cladding has not to exceed 1%.

The technical specifications are based on the current knowledge of the PCI phenomenon and they are defined by imposing conservative safety margin.

Figure 1.12 schematizes a sample operation condition in which stresses induced on the cladding by Pellet-Cladding mechanical Interaction plays an important role in the stresses induced in the cladding.
At the beginning of irradiation, the pellet-cladding gap is open and pellet fragments are randomly located (a.). During the irradiation, the gap progressively closes as a consequence of inward cladding creep. Fragments are relocated to accommodate the gap closure and, after a certain time at constant linear power production, the system is conditioned thanks to stress relaxations (b.). Consequently to a decrease in the power produced by the reactor, the stronger thermal contraction of fuel pellet with respect to cladding leads

to a reopening of the pellet-cladding gap (c.).
During a possible extended operation of the reactor at reduced power production, the cladding undergoes inward creep as it is always submitted to the differential pressure between the external coolant and the internal pressurized rod. This inward creep reduces the dimension of the cladding and may lead again to the closure of the gap (d.) and, eventually, the conditioning of the system. In this conditions, stresses in the cladding have been relaxed bu the characteristic radial dimension of the sample rod is smaller that (b.).
Following a new increase of grid demand, power production is rose again. The temperature increase in the pellet impose the thermal expansion of UO_2 fragments expands. This expansion results into the origin of high stresses in the cladding (e.) which may lead to its failure.
If the cladding surveys this phase, stress relaxation takes place and the system is conditioned again (f.).

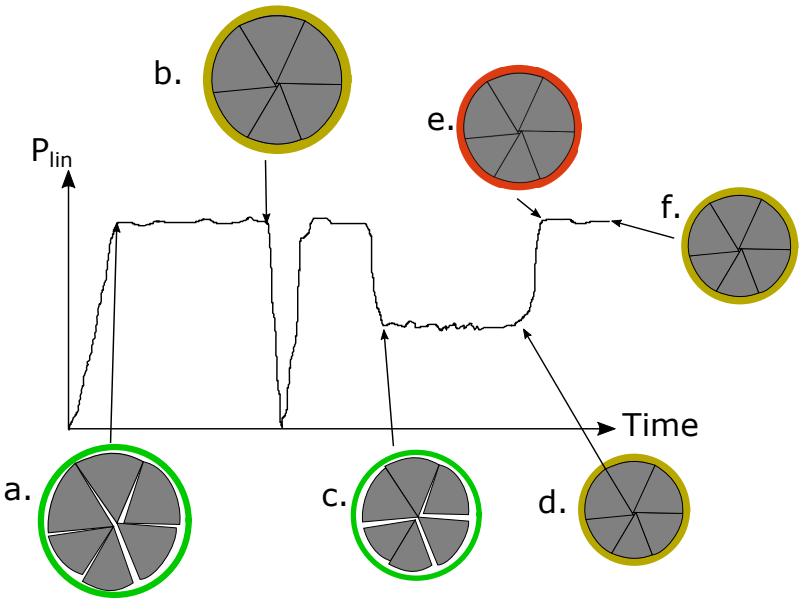

Figure 1.12 – Schematic and simplified representation of an extended operation at reduced power possibly leading to a critical PCI

The operator of power plants ensures the cladding integrity by limiting the amplitude and rate of power production variation. These limits are defined on the present knowledge of PCI phenomenology, that results from experimental studies and examinations, models and simulations of the fuel rod behavior. The gain of operational margins has to be supported by extensive scientific evidence of the respect of safety criteria. For this, there is the need to improve the understanding of phenomena, which can be achieved by dedicated experimental sequences and further validation and development of code simulations.

1.4 Concluding remarks

We have presented in this chapter the nuclear environment, the fuel rod system and discussed the different phenomena that play a role in the origin and evolution of PCI. The deformation mechanisms of the fuel stack and the cladding lead to the progressive closure of the fabrication gap existing between the two, with the consequent establishing of a weak PCI (pellet-cladding contact). A mutual influence origins after the contact and the deformation kinetics of both components is mutually modified. When the behavior of the single object is macroscopically influenced by the behavior of the other one, we talk about strong PCI.
By the strong PCI the plastic deformation on the cladding is induced, with the formation of primary and secondary ridges.

The mechanical interaction that takes place with the PCI is a phenomenon that origins in the fuel rod under normal operation conditions, with no risk for the integrity of the cladding. The cladding is indeed the first barrier to prevent the release of radioactive fission products in the primary loop and covers an important role in the safety analysis.
Depending on the operational protocol, the amplitude and the rate of power variation, the stresses induced by the PCI on the cladding can lead to its failure. Safety authority requires that during normal and incidental conditions the mechanical PCI does not origin any failure of the cladding, which is realized by limiting its circumferential deformation to 1% and that there is no centerline melting of the fuel pellet, guaranteed by imposing a maximum linear power lower than the power to melt threshold.
To achieve this, strict safety margins are imposed to the operator of power plant that limit the maneuverability of reactor to follow grid demand. The practical technical specification are defined on the base of present understanding of the PCI mechanism, that is the result of dedicated experimental sequences and development of fuel performance code to simulate fuel behavior.
To increase power plant maneuverability ensuring the respect of safety criteria, there is the need to improve the present understanding of the PCI mechanism, by simulation and by experimental characterization. In the following chapter we discuss the historical approach to study PCI mechanism, the state of the developed code capabilities to model it and define a new strategy to improve this knowledge.

Chapter 2

Modeling and experience to characterize PCI

In this chapter, we discuss the present state of the art of PCI modeling, which results from an experimental database developed in the research reactors. In section 2.1, we introduce the historical experimental procedure carried out to study PCI, the related pre and post irradiation examinations and the obtained parameters. Then, in section 2.2, we present the fuel performance code ALCYONE of the CEA computing platform PLEIADES. Based on the measured experimental data obtained by the historical procedure, it is now a reference tool for understanding and improving knowledge. In this code the physical phenomena leading to the origin of PCI are modeled and coupled to evaluate the thermal-mechanical behavior of the fuel during irradiation. Finally in section 2.3, we compare the present capacity of code simulations with the available results from experimental data. On this base, we define the new strategy to couple experiment and modeling which requires on-line monitoring of relevant parameters.

Contents

2.1 Historical approach

Present knowledge on PCI phenomenology has been acquired through the years by means of measured data collected during dedicated irradiation sequences, carried out in the so called Material Testing Reactors (MTR). This type of research reactors are fundamental to investigate and improve the knowledge of phenomena taking place during irradiation. Their specific design permits a large flexibility in terms of operating conditions (normal, incidental and accidental conditions) without any risk for safety.
MTR are complex and expensive research facilities so a few of them have been built in each country: e.g. SILOE, OSIRIS and JHR (in the next future) in France, HALDEN reactor in Norway, BR2 in Belgium. MTR can have different designs but they all present instrumented irradiation devices which use the neutronic flux produced by the reactor in separated and isolated loop system. The thermal hydraulic separation of device loops with respect to the reactor core one guarantees safe and flexible experimental management. In these devices, it is possible to reproduce different operational conditions tuning pressure and temperature parameters of the single cooling loop. For what concerns the study of PCI mechanism, the environmental conditions of the industrial power reactor are reproduced in order to recreate the representative fuel rod thermal-mechanical behavior.

The conventional procedure to study the fuel performance related to PCI in incidental conditions, consists in the following steps:

- **Refabrication process**: A fuel element previously irradiated in the nuclear power reactor is refabricated to meet the geometrical requirements of the MTR design;
- **Pre-Irradiation Examinations**: The refabricated fuel is submitted to preirradiation examinations to characterize its geometrical dimensions;
- **The irradiation sequence**: The rod is submitted to a dedicated irradiation sequence named the Power Ramp Test, designed to test the limits and the behavior of the fuel when experiencing a strong power transient;
- **Post-Irradiation Examinations**: In order to evaluate the effects of the power ramp test on the fuel, non-destructive and destructive examinations are performed.

The four meter long fuel rods used in the nuclear power reactor are not compatible with the geometry of MTR core, which generally has the dimensions of a common washing machine (60 cm x 60 cm). In France, the refabrication process consists in taking a fuel rod previously irradiated in a nuclear reactor, the mother rod, and re-fabricate it according to a qualified process known as the FABRICE process [Jos88].

The short rod is then submitted to an **irradiation sequence** designed to simulate class II transients occurring in PWR. Two types of these tests are represented in a schematic way in figure 2.1.
First, a conditioning phase is imposed to the short rod: this is characterized by a linear power equivalent to the one seen by the mother rod in the nuclear power reactor and it is meant at reestablishing the thermal-mechanical and chemical state of the rod at the end of the base irradiation.
The power transient is then imposed, with a power rate ranging from 10 to 100 W/cm/min. The power increase is generally obtained by moving the irradiation device closer to the MTR reactor core.

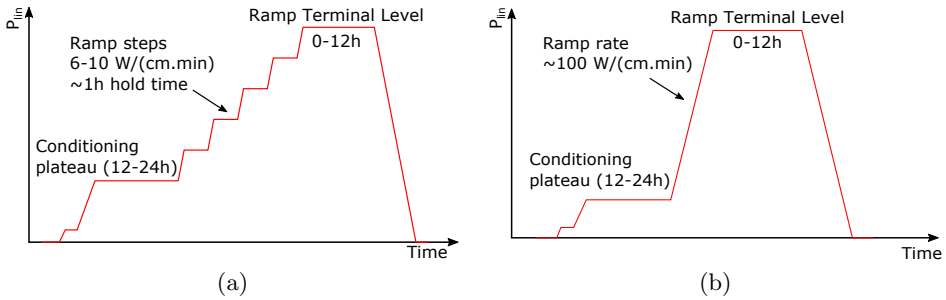

Figure 2.1 – Schematic view of typical ramp test sequences: (a) the "staircase" type; (b) the single-step type

Two main types of experimental sequences exist: the "staircase" ramp or the single-step power ramp. With the first one, PCI mechanism is approached by leaving the time to the fuel rod to relax stresses during the holding time at each step. The second type is of course much more aggressive.
Once reached the Ramp Terminal Level (RTL), an holding time can be foreseen or not, depending on the test objectives: zero holding time is imposed to study the effects of the transient phase on the sample rods while the holding time is required to study the effects of gaseous swelling, which takes place on longer periods.
In order to evaluate PCI limits for different fuel rods having different power history in reactors, fuel rods characterized by a wide range of burn-up values are tested.
At the end of the irradiation sequence, the linear power experienced in the sample rod is brought to zero by moving the irradiation device far from to MTR core and out of the neutron flux.

Data from irradiation are mostly obtained before and after the irradiation sequence, from **Pre and Post Irradiation Examinations (PIE)**, carried out in controlled and isolated environmental conditions, the hot cell laboratories. From the analysis of such examinations we can identify the phenomena which took place in the power transient and deduce their effects on the fuel system, like the residual deformation and microstructural modifications. Some sample results are reported in figure 2.2.
The set of PIE generally associated to a power ramp test is the following:

- **Fuel rod optical profilometry**: meant at measuring the residual evolution of cladding diameter, the amplitude of primary and secondary ridges on cladding surface. From the comparison of pre and post irradiation examinations, information can be obtained of the resulting macroscopic impacts due to gaseous swelling and fuel creep which took place during the transient.
- **Optical microscopy** is applied to cross sections and longitudinal ones. This destructive analysis is carried out after the irradiation and leads to assess the pellet fragmentation, the residual dish filling resulting from fuel creep and dilatation, the evolution of microstructure and gas behavior and the thickness of the gap after irradiation in cold conditions.
- **SEM, EPMA, SIMS**: the Scanning Electron Microscope, the Electron Probe MicroAnalyser and the Secondary Ion Mass Spectrometry respectively, allow to access the fuel restructuring, the fission product distribution and to observe the inner surface of the cladding;

– **X and Gamma inspections**: they allow to perform gamma spectrometry to measure the distribution of gamma emitters in the sample rod, and photon based tomography. If the spatial resolution is sufficient (order of 100 µm) the cracks on the cladding surface can be detected;

– **Neutron imaging**: complementary to the X and Gamma inspections due to the

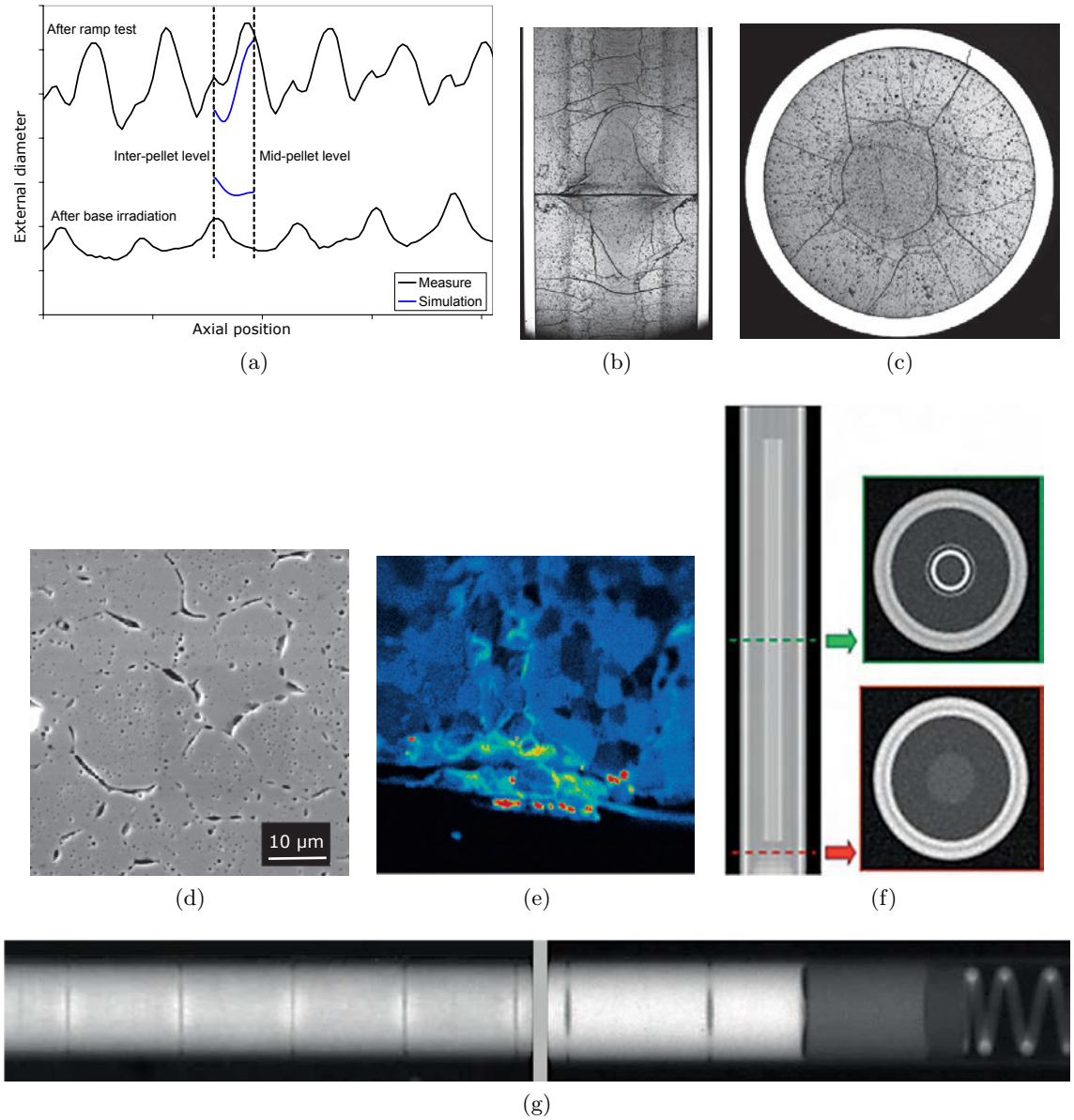

(a) (b) (c)

(d) (e) (f)

(g)

Figure 2.2 – Examples of examinations results on a pressurized water reactor fuel rod before and after a ramp test. Images from [MicB13],[Ser13] and [CEA18]: (a) Cladding profilometry before and after the ramp; (b) Optical microscopy on longitudinal section; (c) Optical microscopy on the cross section; (d) SEM image of the fuel microstructure in the pellet center; (e) SIMS image of iodine taken in the are of the pellet-cladding gap; (f) axial radiography and cross sectional tomographies of a cylindrical object which diameter amounts to 40 mm and length 700 mm; (g) example of neutron imaging: on the left from a detection of moisture in the sample rod, on the right isotopic contrast between MOX pellets (light grey) and natural uranium (dark grey)

different sensitivity of materials with respect to thermal neutrons and high energy photons, it allows to highlight the presence of neutron absorbing material. It is used to detect defects in the structure, detect the presence of water inside the sample rod to identify a loss of integrity of the cladding and can reveal fuel relocation.

PIE permit to have a clear image of the residual effects resulting from the superposed phenomena occurring during irradiation and have been a fundamental source of information to develop the present knowledge of PCI mechanism.

On the basis of experimental data obtained by PIE, models have been developed through the years and coupled between each other to describe the physical processes leading to the measured effects:

- Neutronic model to evaluate the generated power in the system;
- Thermal-hydraulic model to evaluate the heat exchange between the fuel rod and the external coolant and define the thermal field in the system;
- Thermal-mechanical model to evaluate the macroscopic deformation and the microstructure modifications of the components;
- Physico-chemical model to analyze the physics behind the chemical evolution in the components.

These complex and generally non linear models have been numerically implemented and permit now to follow the system evolution, from its base irradiation, through the refabrication process, up to the end of the power ramp test. The calculated effects resulting from modeled phenomenology are then compared to available measured data to validate the code. Figure 2.3 presents a schematic simplified view of the historical approach to improve the knowledge on fuel behavior.

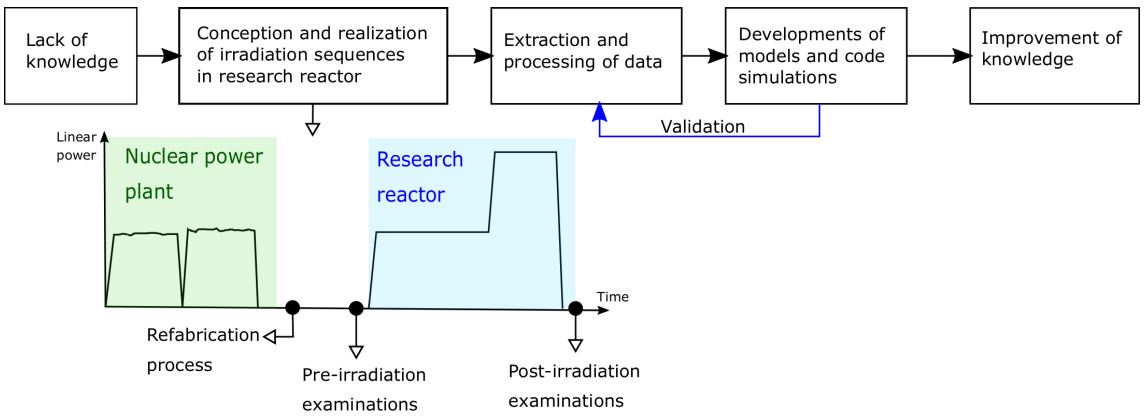

Figure 2.3 – Historical approach to improve the knowledge of fuel performance

In this work, we use the multidimensional fuel performance code ALCYONE of the computing platform PLEIADES, developed by CEA in collaboration with EDF and FRAMATOME. It is the reference code for the analysis of the thermal-mechanical behavior of the fuel element during normal and off-normal operating conditions. Its development is based on experimental data obtained from irradiation sequences carried out in the past and more recent years in different research reactors (e.g. SILOE and OSIRIS in France,

HALDEN reactor in Norway, BR2 in Belgium).

In the following sections, we present the structure and main features of ALCYONE code to then discuss the experimental results available that can be compared with simulations and define the methodology proposed is this work to further improve the understanding of PCI by both experiment and modeling.

2.2 ALCYONE: the reference tool for fuel performance analysis

ALCYONE has been developed by CEA, EDF and FRAMATOME in the context of the PLEIADES fuel computation platform [MicB13] and it is the reference simulation tool for the multi-dimensional analysis of the thermal-mechanical behavior of the fuel rod used in PWR. Figure 2.4 shows the multi-physics problem to be addressed to simulate the macroscopic behavior of the fuel element under irradiation [MicB13].

For a specific irradiation profile history, the thermal-hydraulic computation evaluates the force cooling conditions on the fuel rod external surface and defines the thermal exchange between the fluid and the solid wall, in single phase as well as in two-phase flow regime. From this, the cladding external temperature is evaluated which is one of the boundary

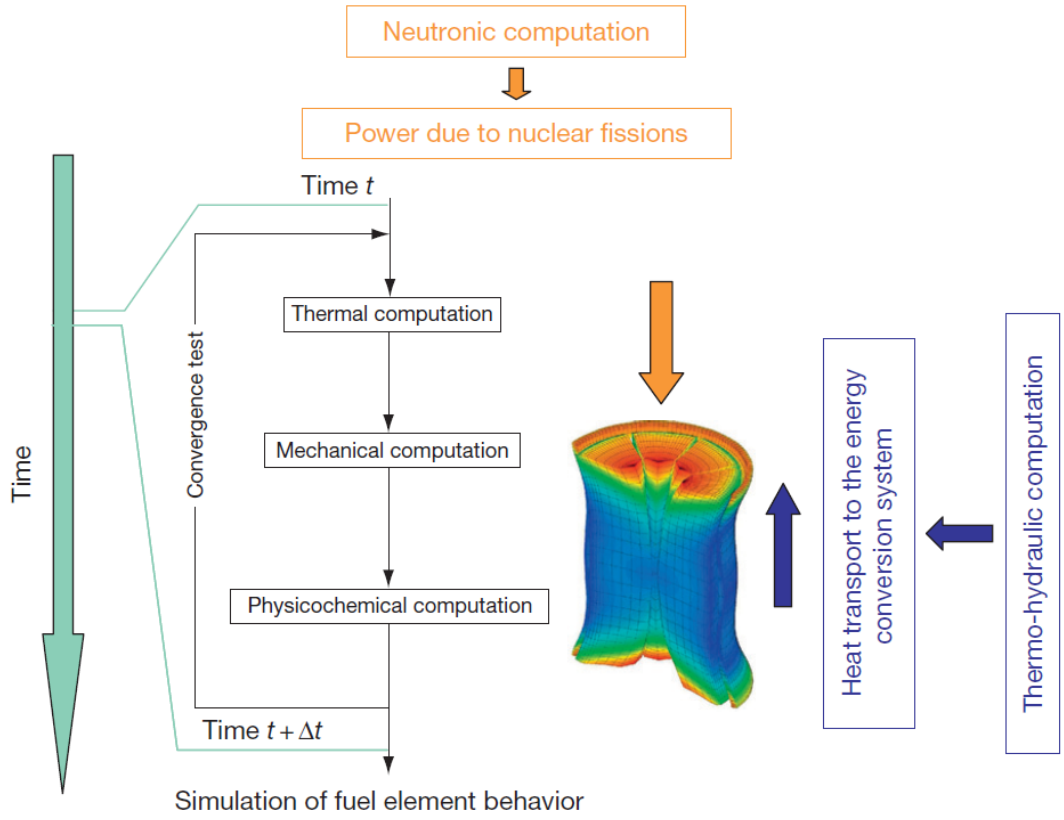

Figure 2.4 – Multiphysics problem to be solved to simulate the macroscopic behavior of the fuel system under irradiation [MicB13]

conditions for the thermal computation. For the same irradiation sequence, the local power produced in the fuel pellet is obtained by neutronic computation. Then, the thermal, mechanical and physico-chemical computations permit to evaluate the fuel behavior from the microstructural changes up to its macroscopic behavior. The different models constituting ALCYONE are widely presented in literature [MicB13]. In the following we present the ones which are fundamental for our study: the thermal model, the fission gas model and overall the mechanical computation, with a specific attention to the modeling of the fuel material.

2.2.1 Thermal model

To evaluate the temperature distribution in the fuel rod, energy conservation is applied:

$$\frac{\partial H}{\partial t} + div\boldsymbol{\lambda}\vec{\nabla}T + \boldsymbol{q}_v = 0 \tag{2.1}$$

Where $H = \rho h$ is the volume enthalpy, λ is the thermal conductivity of the component, T the local temperature and $\boldsymbol{q}_v$ the local power produced. ALCYONE is based on a temperature resolution. So the first term in eq. (2.1) is replaced by:

$$\frac{\partial H}{\partial t} = \frac{\partial}{\partial t}(\rho h) = \rho\frac{\partial h}{\partial t} + h\frac{\partial \rho}{\partial t} \simeq \rho\frac{\partial h}{\partial t} = \rho c_p\frac{\partial T}{\partial t} \tag{2.2}$$

Which results from the hypothesis that $\rho\frac{\partial h}{\partial t} \gg h\frac{\partial \rho}{\partial t}$. The boundary condition for the resolution of the thermal problem is imposed by the thermal flux exchanged with the coolant Φ. In general terms, it depends on the thermal difference between the solid wall and the bulk temperature of the fluid $(T_e - T_\infty)$ and on the wall exchange coefficient h

$$\Phi = h(T_e - T_\infty) \tag{2.3}$$

A similar condition is applied to the internal surface of the clad, where the thermal exchange is evaluated accounting for gap conductance in the case of an open gap and thermal contact resistance when the gap is closed.

2.2.2 Fission gas model

Even though it is not the focus of this work, it is important to mention the relevance of a precise model to describe the behavior of fission gasses in the fuel. This is accomplished by the comprehensive research code MARGARET [Noi11] and the industrial version CARACAS [Jom14], introduced in the PLEIADES platform and used in ALCYONE. The basic behaviors to be modeled are: gas bubbles nucleation, their growth by atomic migration of fission atoms to existing bubbles, re-solution of the gas in the matrix, bubble migration depending on temperature and stress gradients, coalescence of bubbles and their interaction with crystal defects and finally the release of fission gases to external surfaces, like cracks and the pellet-cladding gap, and to internal surfaces, like grain boundaries.
In our work, we focus on the deformation of the fuel rod, thus a fundamental aspects to be considered is that the fission gas production leads to an additional contribution to the fuel deformation. This is a temperature dependent mechanism that depends on material properties and burn-up. This deformation doesn't need to be coupled to the mechanical behavior of the fuel as long as stresses keep low [MicB13].

2.2.3 Mechanical model

The mechanical resolution is carried out by integrating the static equilibrium equation 2.4 according to a weak formulation with the finite element method:

$$div\boldsymbol{\sigma} = 0 \tag{2.4}$$

We detail in the following the model of fuel mechanical behavior, which is the base in Part II for the development of the thermal-mechanical model of the fuel undergoing melting onset.
A brief description of the cladding behavior and the pellet-cladding interface constitutive equations are then given.

Notations

It is useful to recall here some definitions which are used in the following mechanical description as well as further in this document. For the second order stress $\boldsymbol{\sigma}$ and strain $\boldsymbol{\varepsilon}$ tensors we define for each one two invariants:

- The first invariant is defined in the following way:

$$\varepsilon_H = \frac{tr(\boldsymbol{\varepsilon})}{3} \quad ; \quad \sigma_H = \frac{tr(\boldsymbol{\sigma})}{3} \tag{2.5}$$

- The second invariant is defined as a function of the deviatoric component of the tensor, $\mathrm{e} = \boldsymbol{\varepsilon} - \varepsilon_{\mathrm{H}}\mathbb{I}$ and $\mathrm{s} = \boldsymbol{\sigma} - \sigma_{\mathrm{H}}\mathbb{I}$:

$$\varepsilon_{eq} = \sqrt{\frac{2}{3}\boldsymbol{e} : \boldsymbol{e}} \quad ; \quad \sigma_{eq} = \sqrt{\frac{3}{2}\boldsymbol{s} : \boldsymbol{s}} \tag{2.6}$$

  with $\mathbb{I}$ the identity tensor

The fuel

The fuel is a porous material which presents at high temperature an elasto-visco-plastic mechanical behavior.
Assuming after Leclerc [Lec98] the additivity of macroscopic strains under the hypothesis of small strains for nuclear pellet, the creep-fracture coupled formulation is expressed using the Hooke's law as reported in the following expression:

$$\dot{\boldsymbol{\sigma}} = \mathbb{C} : \dot{\boldsymbol{\varepsilon}}^e = \mathbb{C} : \left(\dot{\boldsymbol{\varepsilon}} - \dot{\boldsymbol{\varepsilon}}^{in}\right) \tag{2.7}$$

Where $\mathbb{C}$ is the 4^{th} order elastic tensor, $\dot{\boldsymbol{\varepsilon}}^e$ is the elastic strain rate, which is equal to the difference of the total strain rate of the component $\dot{\boldsymbol{\epsilon}}$ and of the inelastic strain rates $\dot{\boldsymbol{\epsilon}}^{in}$. Inelastic strain rates account for the cracking induced damage $\dot{\boldsymbol{\epsilon}}^{\text{crack}}$, the creep mechanism $\dot{\boldsymbol{\epsilon}}^{\text{vp}}$, the thermal strain rate $\dot{\boldsymbol{\epsilon}}^{\text{th}}$ and the gaseous swelling $\dot{\boldsymbol{\epsilon}}^{\text{g}}$ resulting from the previously introduced fission gas model.

$$\dot{\boldsymbol{\epsilon}}^{in} = \dot{\boldsymbol{\epsilon}}^{crack} + \dot{\boldsymbol{\epsilon}}^{th} + \dot{\boldsymbol{\epsilon}}^{vp} + \dot{\boldsymbol{\epsilon}}^{g} \tag{2.8}$$

According to Frost and Ashby [Fro82], uranium dioxide presents two creep mechanisms which are activated once temperature overcomes about 1000°C. The strain rate generally presents two phases: a first one, defined primary creep, characterized by a decrease of the velocity of deformation, and a second one, the secondary creep, where the strain rate is approximately constant. This secondary creep mechanism is strongly influenced by the thermal and stress fields. We can identify two secondary creep mechanisms: one associated to the diffusion of vacancies[1] (diffusion creep or scattering creep), and a second

[1] Vacancies are a type of point defect in which an atom is missing from one of the lattice sites.

one associated to the motion of dislocations (dislocation creep). The prevalence of one mechanism or of the other depends on the temperature and the stresses applied to the material.
For example, when the fuel material is in compressed state by the application of 20 MPa, the tilting temperature between diffusion and dislocation creep is in the order of 1700°C; if the applied pressure increases to 200 MPa, the tilting temperature reduces to 1000°C[Ser07].
During normal irradiation operations, as we previously saw, central temperature in the pellet ranges at about 1000°C while it ranges at about 500°C at its external surface. Under this thermal field, the driving mechanism is the diffusion creep.
During a power ramp tests instead, temperatures increase in the system and the dislocation mechanism is activated.
Primary creep is the main mechanism during the start-up and the cooling down.

Monerie and Gatt in 2006 [Mon06] proposed a mechanical model to describe the poro-elasto-viscoplastic behavior of the fuel: the material is considered at the miscoscopic scale to be made of:

- An incompressible matrix having elasto-viscoplastic behavior;
- A porous fraction, isotropically distributed in the matrix, which is meant to evolve during irradiation as a consequence of mechanical and thermal stresses and the interaction with radiation and FPs. It is defined as the ratio between the volume of voids and the total volume of the system, given by the sum of void volume V_v and the volume occupied by the matrix V_m.

$$f = \frac{V_v}{V_v + V_m} \tag{2.9}$$

The general creep mechanism of a solid incompressible matrix can be described by a Norton dissipative potential:

$$\psi_i^{vp}(\boldsymbol{\sigma}, n_i) = \psi_i^{vp}(\boldsymbol{s}, n_i) = \frac{\sigma_0 \dot{\varepsilon}_0}{n_i + 1} \left(\frac{\sigma_{eq}}{\sigma_0} \right)^{n_i+1} \tag{2.10}$$

with:

- n is the Norton exponent for the "i$^{\text{th}}$" non linear mechanism ($n \to \infty$ for stiff plasticity, n=1 for linear behavior);
- σ_0, ε_0 are material constants.

We just say here that the following mechanical behavior of the total system has been proposed in 2006 by Monerie and Gatt [Mon06], on the basis of the homogenization technique proposed by Michel and Suquet in 1992 [MicJC92]. Further details on this type of approach are given in Part II, where we discuss the development of the mechanical model for the fuel material at melting onset.
The i$^{\text{th}}$ creep mechanism of the porous material is thus described by the following elliptical dissipative potential:

$$\Psi^{vp}(f, n_i, \boldsymbol{\sigma}) = \frac{\sigma_0 \dot{\varepsilon}_0}{n_i + 1} \left(A(f, n_i) \left(\frac{3}{2} \frac{\sigma_H}{\sigma_0} \right)^2 + B(f, n_i) \left(\frac{\sigma_{eq}}{\sigma_0} \right)^2 \right)^{\frac{n_i+1}{2}} \tag{2.11}$$

where:

$$A(f,n_i) = \left[n_i\left(f^{-1/n_i}-1\right)\right]^{-2n_i/(n_i+1)} \quad ; \quad B(f,n_i) = \left(1+\frac{2}{3}f\right)(1-f)^{-2n_i/(n_i+1)} \tag{2.12}$$

An extensive description about the derivation and definition of function $A(f,n_i)$ and $B(f,n_i)$ can be found in [Mon06]. For our purpose, it is sufficient to know that the $A(f,n_i)$ function is obtained analytically by the hollow sphere model imposing a pure hydrostatic problem, while the $B(f,n_i)$ function is evaluated by means of the Hashin and Shtrikman method associated to the modified secant linearization technique [MicJC92].
The two potentials describing the creep mechanisms are coupled by means of a temperature and stress dependent function $\theta(T,\boldsymbol{\sigma})$:

$$\Psi^{vp}(\boldsymbol{\sigma},T) = [1-\theta(T,\sigma)]\Psi_1^{vp}(\boldsymbol{\sigma},n_1) + \theta(T,\sigma)\Psi_2^{vp}(\boldsymbol{\sigma},n_2) \tag{2.13}$$

where subscript 1 stands for the linear diffusion creep ($n_1 = 1$) and 2 stands for the non linear dislocation mechanism ($n_2 = 8$).
The $\theta(T,\boldsymbol{\sigma})$ function is described by the following expression, as reported in [Jul08]:

$$\theta(T,\boldsymbol{\sigma}) = \frac{1}{2}\left[1+tanh\left(\frac{T-\bar{T}(f,\boldsymbol{\sigma})}{h}\right)\right] \tag{2.14}$$

The temperature $\bar{T}$ corresponds to the tilting temperature from the linear diffusion creep mechanism to the non linear dislocation one. At the beginning, this temperature used to depend only on the second invariant of the stress tensor, which lead to the fact that for a pure hydrostatic case the $\bar{T}$ was not clearly defined. Nevertheless, the fuel material finds itself submitted to a mainly hydrostatic mechanical loading and as reported in [Jul08], a new expression for the tilting temperature is proposed, which accounts for the porous volume fraction and the second stress invariant:

$$\bar{T}(f,\boldsymbol{\sigma}) = \bar{\omega}\left(\sqrt{\frac{4B(f,n_1)}{4B(f,n_1)+A(f,n_1)}\sigma_{eq}^2 + \frac{9A(f,n_1)}{4B(f,n_1)+A(f,n_1)}\sigma_H^2}\right)^{-q} \tag{2.15}$$

with $\bar{\omega}$ and q material parameters.
The constitutive equations of the mechanical model finally are:

$$\begin{cases} \dot{f} = (1-f)tr(\dot{\boldsymbol{\varepsilon}}^{vp}) \\ \dot{\boldsymbol{\varepsilon}}^{vp} = \frac{\partial\Psi}{\partial\boldsymbol{\sigma}} \end{cases} \tag{2.16}$$

The description of mechanical behavior of the equivalent solid material is completed by accounting for the elastic strain, which takes us back to equation (2.7). Martin [Mar89] initally derived correlations to express the material properties involevd in the elastic tensor as a function of the temperature, which were then used in 3D numerical simulations carried out by Gatt [Gat05] to derive the equivalent Young's modulus and shear modulus as functions of both temperature and porosity fraction $E(f,T)$ and $G(f,T)$ for the solid material having porosity f$\leq$ 0.3:

$$\begin{cases} E(f,T) = (1-2.5f)(a_1+b_1T+c_1T^2) \\ G(f,T) = (1-2.25f)(a_2+b_2T+c_2T^2) \end{cases} \tag{2.17}$$

where (a_i,b_i,c_i) are material parameters, experimentally defined.

The cladding

The cladding presents two types of behavior depending on the imposed external environment:

- During normal irradiation conditions, as already mentioned in the first chapter, stresses in the cladding are low. The cladding consequently creeps under the effect of the differential pressure. In this phase irradiation affects the creep mechanism accelerating cladding deformation and hardening the material;
- When strong stresses origin in the component, the system, hardened under irradiation, deforms according to a thermal creep.

When zircaloy cladding are used, the anisotropy in mechanical behavior of this alloy is taken into account by using the Hill's equivalent stress instead of the Von Mises one.

2.2.4 The pellet-cladding interface

As reported by Michel in [MicB13], friction is a primary importance phenomenon when evaluating the stress and strain concentrations on the cladding and the fuel cracking evolution. Friction which origins at the pellet-cladding interface is accounted by an unilateral contact low assessed by the Lagrangian multiplier method of the Cast3m Finite Element code [Hel15]. Friction is modeled according to a Coulomb model reported in the following:

$$F_{if} = \begin{cases} 0, & \text{if } \|F_t\| \leq \mu \|F_n\| \\ -cF_t, & \text{if } \|F_t\| > \mu \|F_n\| \end{cases} \tag{2.18}$$

Where F_{if} is the friction force created at the interface, F_t is the tangential force and F_n the normal one; c is a material depending parameter. μ is the friction coefficient between the fuel material and the cladding. For the UO_2-Zy4 system, non irradiated, this parameter ranges between 0.4 and 0.7 [Nak81] [Shc84]. It has been shown that contact pressure and temperature have no substantial impact of this parameter [Shc86] while irradiation seems to enhance friction.

2.2.5 Multi-D PCI computation schemes

ALCYONE code allows to simulate fuel rod thermal-mechanical behavior according to three computational models: 1.5 D, 2D(r, θ) and 3D.
Figure 2.5 represents the 2D model, which allows to study the local mechanical behavior of the system with a lower computational cost with respect to 3D.
Simplifications with respect to the 3D model are done: 2D(r, θ) allows to account for pellet fragmentation but leads to the impossibility to differentiate between the Inter-Pellet and the Mid-Pellet plane.
As for this study the computation cost of the analysis is not of primary importance, we decide to focus on the 3D simulation rather than the 2D ones.
In the following sections, we present the 3D and the 1.5D.

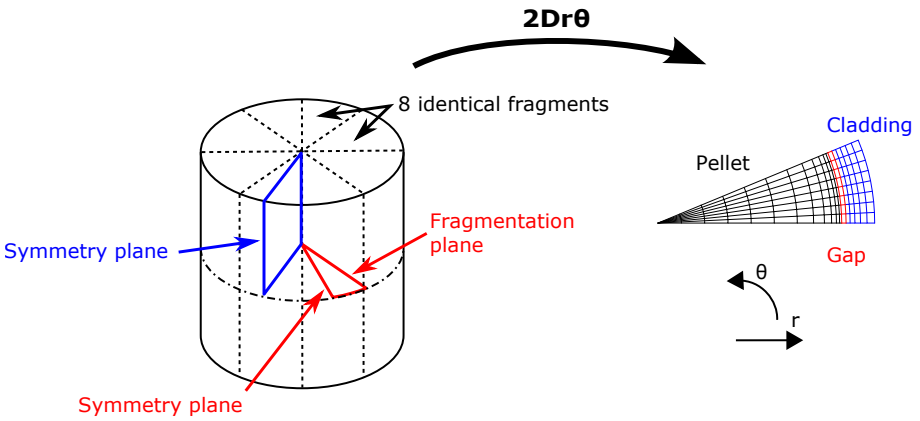

Figure 2.5 – Representation of the 2D computational models for the pellet-cladding system

1.5D simulation

Figure 2.6 shows the schematic view of the 1.5D simulation approach: the whole fuel rod (about 200 pellets for the PWR mother rod) is subdivided in a certain number of axial slices (30 in the figure), each one being representative of the behavior of all the pellets constituting the slice itself.
Each slice is modeled purely along the radial direction (1D simulation), as represented in the top right of figure 2.6, by assuming a certain number of hypothesis:

- Axisymmetry of the fuel rod;
- Generalized plain strain in the axial direction.

Under this hypothesis, the displacement of elements within the slice can be expressed as follows:

$$\boldsymbol{u}(r,\theta,z) = u(r)\boldsymbol{e}_r + \varepsilon_{zz} z \boldsymbol{e}_z \tag{2.19}$$

The mechanical interaction between slices is accounted by making an axial balance of forces (weight of pellets, effect of the internal pressurization of the fuel rod) whereas slices are coupled from a thermal point of view through the coolant temperature profile.

When pellet-cladding gap closes and contact is established between the two, it is considered that no interpenetration takes place between the two, this results into the fact that pellet

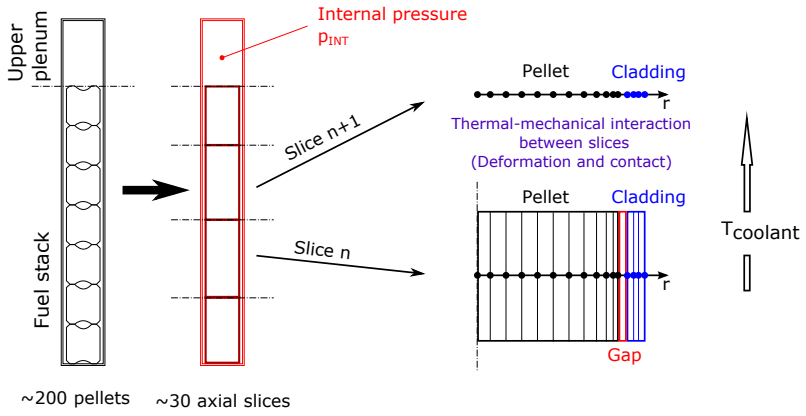

Figure 2.6 – Representation of the 1.5D computational model for the pellet-cladding system

radius can never be greater that cladding one. A second hypothesis is that when the contact is established, the two element are completely attached each other. Consequently the axial displacement of pellet and cladding is numerically imposed to be equal.
We define a quantity to be global when it applies to the fuel rod as a whole while local quantities are evaluated for each slice. The 1.5D simulation allows to evaluate global as well as local quantities. Among the global ones, which are fundamental for the 3D simulation as we will see in the following section, we obtain:

- Upper and lower plenum free volume;
- The release of fission gas;
- The internal pressure within the fuel rod;
- The elongation of the fuel stack and of the cladding tube.

For what concern the local quantities, 1.5D simulation allows to evaluate for each slice the average fuel and cladding deformation and the thickness of the external corrosion layer.

With this model we cannot distinguish between the Mid-Plane and the Inter-Pellet plane of the fuel rod system and we cannot assess a local precise behavior. This motivates the fact that, in our analysis, we use 1.5D simulation outputs for what concerns global quantities but we rather focus on the detailed local results of 3D simulation to study the observable effects associated to local PCI.

3D simulation

The 3D simulation assumes that fragmentation instantaneously takes place in the fuel pellets at the really beginning of the irradiation. It is supposed that cracking leads to the formation of 8 fragments, perfectly identical each other. Taking advantage of the symmetry of the fragment, the simulation can be carried out on just one fourth of it, strongly reducing the time cost of the simulation. Figure 2.7 shows a schematic simplified view of the pellet where the symmetry and fragmentation planes are highlighted. On the right side of the figure is illustrated the resulting mesh of the one fourth of the pellet fragment that is actually modeled.
The defined pellet fragment angle (22.5°) has been chosen as to maximize the magnitude of the fragment hourglass shape during normal irradiation conditions [MicB13].
As previously mentioned, it is found by Post Irradiation Examinations that axial fragmentations appear in the fuel pellet. Those fragmentations are not considered as it was shown by Bentejac [Ben04] that they have negligible impact on the hourglass shape of the system.

The boundary conditions imposed in the 3D calculations are showed in figure 2.8:

- At the MP plane, the axial displacement $u_{z,f}$ and $u_{z,clad}$ of the pellet and the cladding respectively are imposed to be the same for all nodes in the pellet and the same for all nodes in the cladding. This ensures the respect of the symmetry of behavior. The two components are free to deform independently up to pellet-cladding contact. A mid-pellet locking condition resulting in common axial displacement is imposed when the gap is closed at least at one point;
- At the IP plane, displacement $u_{z,f}$ and $u_{z,clad}$ are imposed to be larger or equal to 0 which ensures no interpenetration of two neighbor pellets;

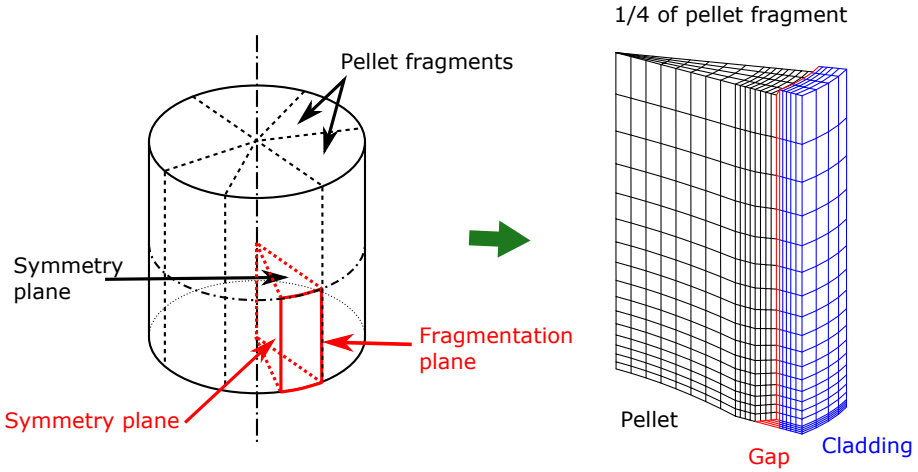

Figure 2.7 – Representation of the 3D computational models for the pellet-cladding system

- When contact appears, the pellet-cladding interaction is managed via the contact friction as previously described;
- The spring located at the top of the fuel rod is accounted by considering a supplementary stress applied on the MP plane of the pellet. This, with the internal pressurization of the fuel rod and coolant pressure, contributes to a background effect imposed to the local system;
- The internal pressure in the fuel rod is implemented as a force applied on the pellet surface and cladding internal wall;
- In the same way, the external coolant pressure is accounted via a stress applied on the cladding external wall.

It is clear that 3D simulation is the most adapted to study the PCI mechanism, as it allows to account for geometrical specifies (chamfers, dishing, hourglass shape), to model the local behavior of the system, taking into account axial gradients, and thus to distinguish between phenomena appearing at the IP plane and the MP plane (dishing filling, stress field in the pellet and in the cladding, gaseous swelling...).

Before to realize a 3D simulation, it is necessary to evaluate the evolution of the global variables defined before by means of a 1.5D simulation: the external temperature of the cladding and its evolution during the power history constitutes a boundary condition for the thermal computation carried out in 3D.

2.3 Comparing code simulation and experimental results

We have presented in section 2.1 the historical approach which lead us to the present state of comprehension of phenomena and of code development. Nowadays, the ALCYONE code allows to calculate and assess the system evolution at each time during the simulated irradiation history. For its validation, the experimental data resulting from PIE are largely used.
The measured parameters used for the 1.5D validation process are the following:

- Residual cladding external diameter;

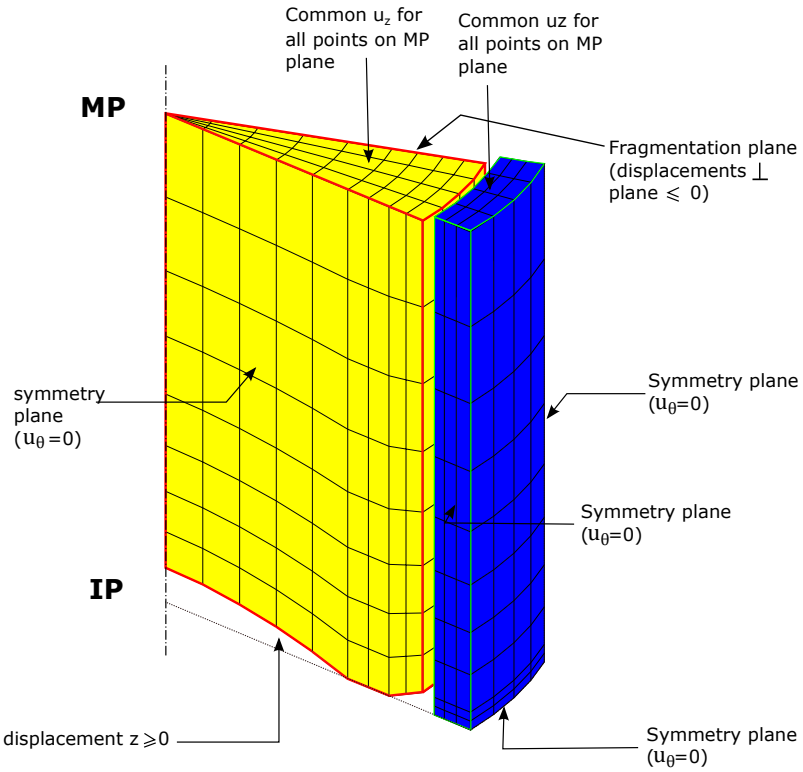

Figure 2.8 – Representation of boundary conditions imposed for the 3D calculation

- The residual fuel and the cladding axial elongation;
- The corrosion thickness on the cladding surface;
- The fission gas release;
- The internal pressure in the sample rod;
- The residual free volume.

As reported by Marelle at TOPFUEL 2017 [Mar17] calculations are in good agreement with the corresponding measured parameters obtained by post irradiation examinations. The main published results are summarized in figures 2.9 and 2.10. The first set of graphs in figure 2.9 presents the comparison between the calculated effects and the available experimental measures resulting from several base irradiation sequences. Dashed lines corresponds to measurement uncertainties and each point is related to a single PIE for a precise irradiation sequence. Figure (a) of 2.9 shows that the calculated residual variations of the cladding diameter are in agreement with the measurements performed in hot cell laboratories, once the experimental uncertainty is taken into account. Also, the ratio Calculated/ Measured (C/M) for the internal free volume, that is illustrated in (b), is approximately 1 and data dispersion are within the experimental uncertainty. In figure (c) and (d) are illustrated the C/M values for the release of fission gas and the internal pressure. We observe that the code has the tendency to overestimate both values with respect to the quantities measured by PIE.

The second set of graphs presented in figure 2.10, show the comparison of calculated and measured parameters after the power ramp, extracted by [Mar17]. The calculated external cladding diameter variation (a) is accurately evaluated for the M5 cladding while a

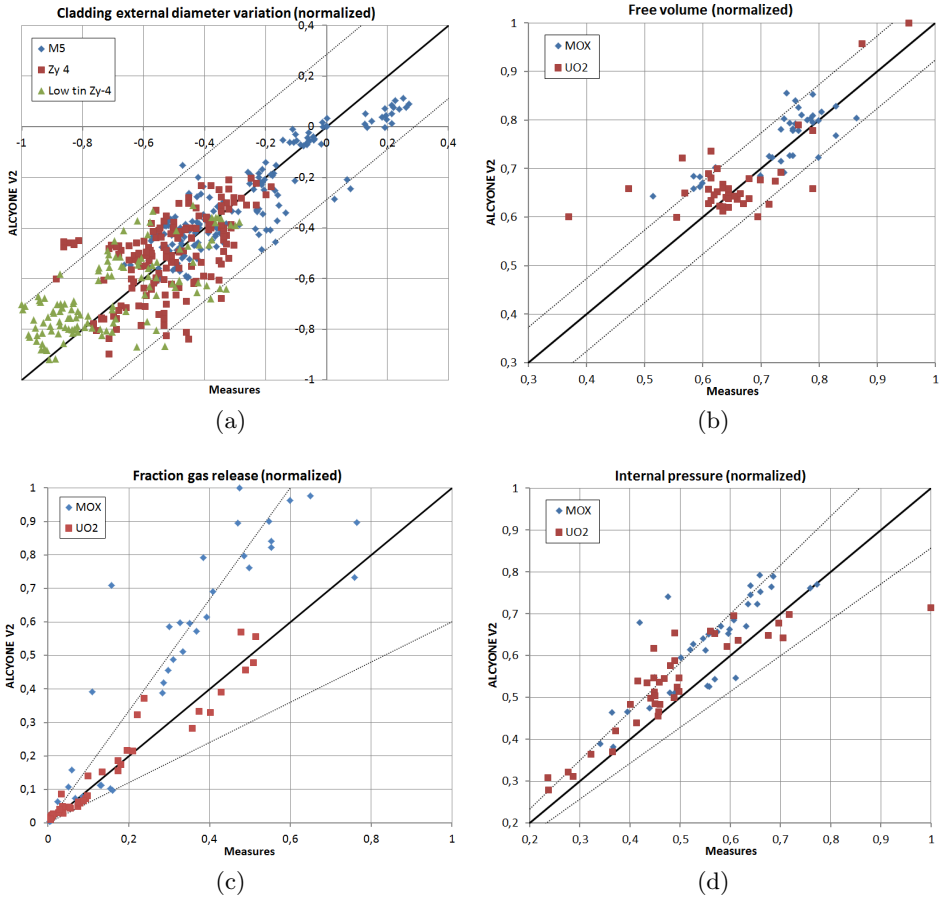

Figure 2.9 – Comparison of calculated and measured parameters for 1D validation process after base irradiation: (a) Cladding external diameter, (b) the free volume; (c) the fractional release, (d) the internal pressure [Mar17]

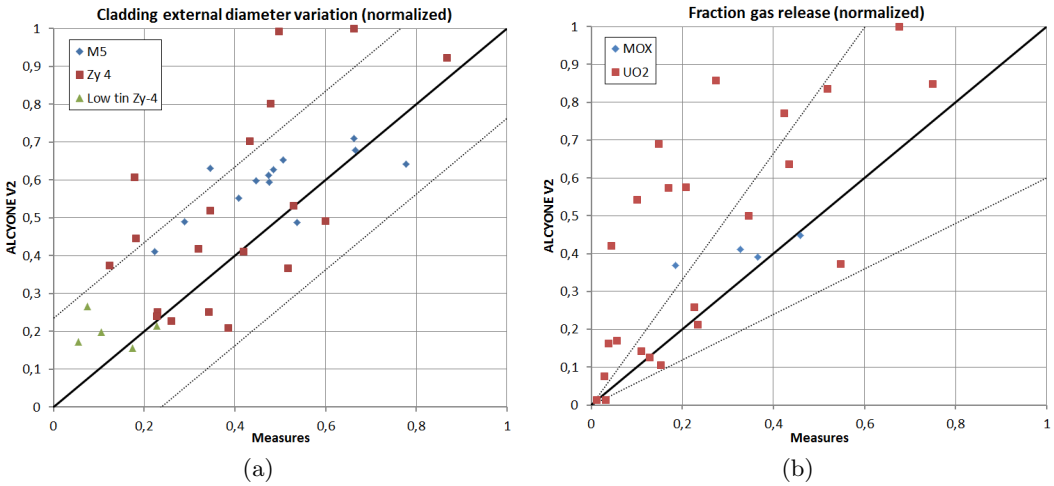

Figure 2.10 – Comparison of calculated and measured parameters for 1D validation process after power ramp test: (a) cladding external diameter, (b) fractional release [Mar17]

higher dispersion characterizes the Zy4 type cladding. For what it is concerned with the fractional release of fission products, the calculated values results to be overestimated.
As we detailed in the previous section 2.2.5, the global quantities resulting by 1D computation (external cladding temperature and internal pressure) are input data for the 3D simulation, which means that calculated errors are propagated to the 3D simulation.

For the 3D computation, Sercombe presents the validation process in [Ser13]. Most of the considered tests have been carried out in the OSIRIS reactor. PIE include measurements of the radial diameter of the cladding tube, of the amplitude of primary and secondary ridges after base irradiation and after the power ramp and the estimation of dish filling through optical microscopy. These are compared to the calculated values.
Figure 2.11 illustrates the C/M values of parameters after base irradiation. Specifically, the fuel rod diameter (a) after the base irradiation is estimated with an error within the range of measurement uncertainty ($\pm 5\mu m$), the amplitude of primary ridges (b) is evaluated with an average error of 1 μm, which falls within the measurement uncertainties of $\pm 3\mu m$ [Ser13].

Figure 2.12 illustrates the C/M values of parameters after a power ramp test. We observe that lager discrepancies arise between the calculated and the measured values of the residual variation of the cladding diameter before and after the power ramp test, at the Mid-Pellet plane (a) and at the Inter-Pellet Plane (b). The dispersion increases when we focus on the C/M height of primary (c) and secondary (d) ridges.

The increase of the difference between calculated and measured quantities after a power ramp test is partially affected by the propagation of errors from the base irradiation resolution. But, it is difficult to further analyze the reasons leading to this discrepancy by means only of the residual deformations measured after the test.
Indeed the experimental database is today largely based on post-irradiation measures that limit the further improvement of code simulation. As the code is capable to calculate the system kinetics along the entire irradiation sequence, on-line measurements constitute a huge source of information. Only a small amount of tests, devoted to R&D purposes, have been carried out integrating on-line measurements to follow the kinetics of relevant mechanisms and their coupling during the irradiation.
Among this kind we can mention, within the French research context:

- The GONCOR experiment [Hel04]: it has been performed in the past years in the SILOÉ reactor (Grenoble) and used the DECOR system to provide the deformation kinetics of the cladding external diameter and study the effects of gaseous swelling. A sample result of the experiment is presented in figure 2.13 which illustrates the measured evolution of the cladding diameter (blue) and the comparison with calculated results (red);
- The REMORA 3 experiment [Lam11]: realized in the OSIRIS reactor, it aimed at improving the knowledge of nuclear fuel behavior in the frame of the kinetics of fission gas and helium releases and to acquire data on the degradation of the fuel conductivity. For this, by a highly instrumented in-pile system it was measured the evolution of the internal pressure within the fuel rod, assessed the composition of the gas fulfilling rod plenum and measured the central temperature in the fuel pellet;

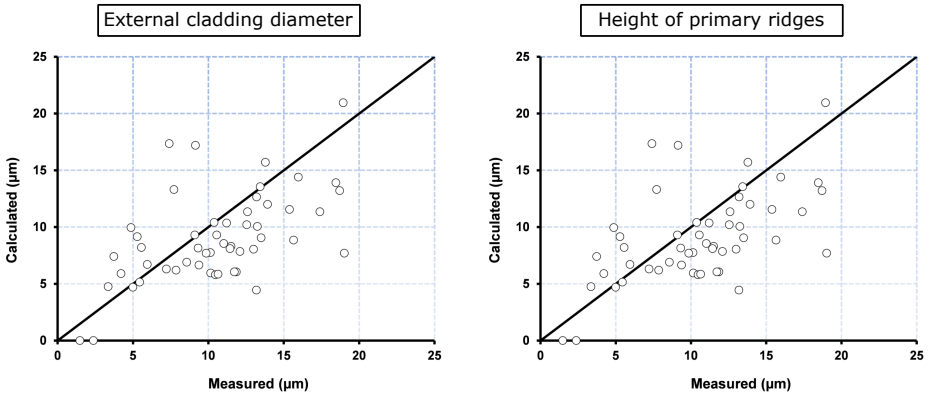

(a) (b)

Figure 2.11 – Comparison of calculated and measured parameters for 3D validation process after base irradiation: (a) residual cladding deformation and (b) residual height of primary ridges after base irradiation[Ser13]

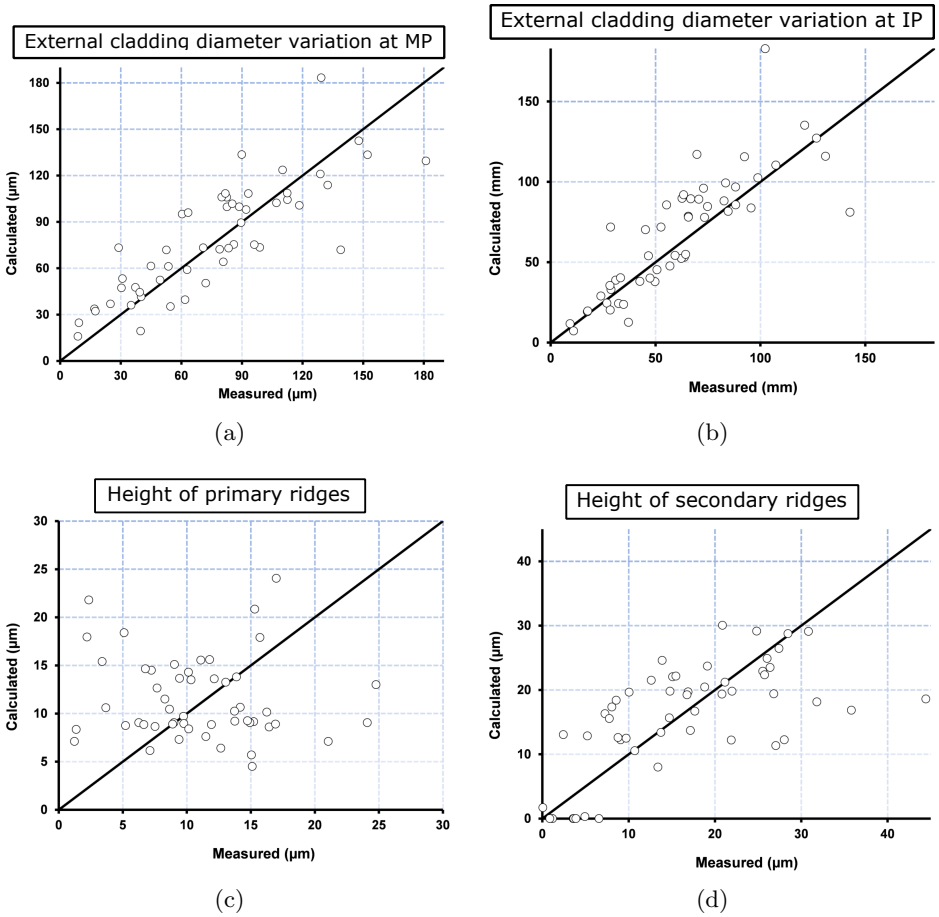

(a) (b)

(c) (d)

Figure 2.12 – Comparison of calculated and measured parameters for 3D validation process after power ramp test: (a) Mid-Pellet External Cladding Diameter and (b) Inter-Pellet Cladding External diameter before and after the ramp test, (c) Height of Primary ridges and (d) Height of secondary ridges after power ramp test [Ser13]

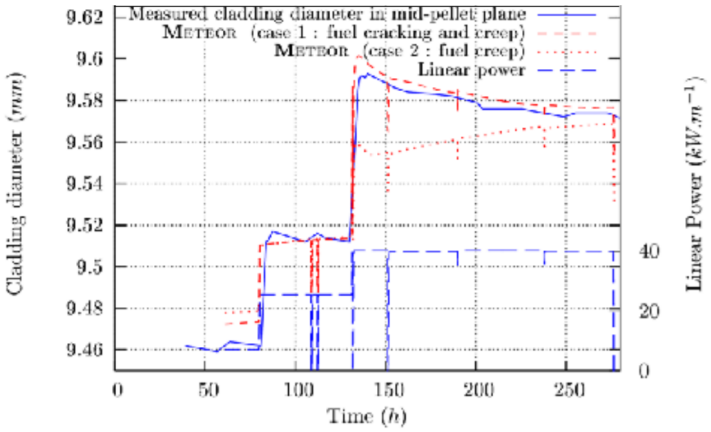

Figure 2.13 – In-pile evolution of the cladding diameter under irradiation during the GONCOR experiment. The measured evolution (blue) is compared to the calculated one by METEOR code (red). METEOR has been the base for the development of the ALCYONE code [Hel04]

– Several experiences have been performed in the HBWR reactor of Halden, specifically instrumented to follow the evolution of the central temperature of the fuel pellet, the internal pressure in the fuel rod and the fuel stack and cladding axial elongation.

As one may notice, no details are given about the instrumentation used in these experimental sequences. We prefer to stay focused on the phenomenology and its parameters, coherently with the purpose of the next chapter that is to identify the set of relevant parameters to be measured under irradiation. The discussion of the instrumentation used is reported to the Part III of this thesis.

The kinetics of phenomena that can be only assessed by on-line measurements and in-pile instrumentation are nowadays fundamental to allow the improvement of code simulation and increase the number of parameters that can be compared with calculated quantities.

In the next future MTR Jules Horowitz Reactor (JHR), highly instrumented irradiation sequences are foreseen to measure on line fuel behavior and bridge the existing gap between experiments and simulations. Figure 2.14 represents the approach to be used in JHR to design and realize an irradiation sequence: in black are reported the steps which are already part of the conventional understanding process and which allowed present code capability. The red steps are the needed ones to integrate simulation and experience to maximize the useful outputs of an irradiation sequence.

The methodology proposed in this work consists in using present code capabilities to define the measurement criteria by the identification and characterization of missing experimental data. This constitutes the base to review present instrumentation technologies in order to find the ones matching the theoretical specifications. Modeling capabilities is the driver to push for improvement of present technologies and the development of innovative solutions. Their implementation in dedicated highly instrumented irradiation sequence result into an extended database to permit code development and further understanding of PCI phenomenology.

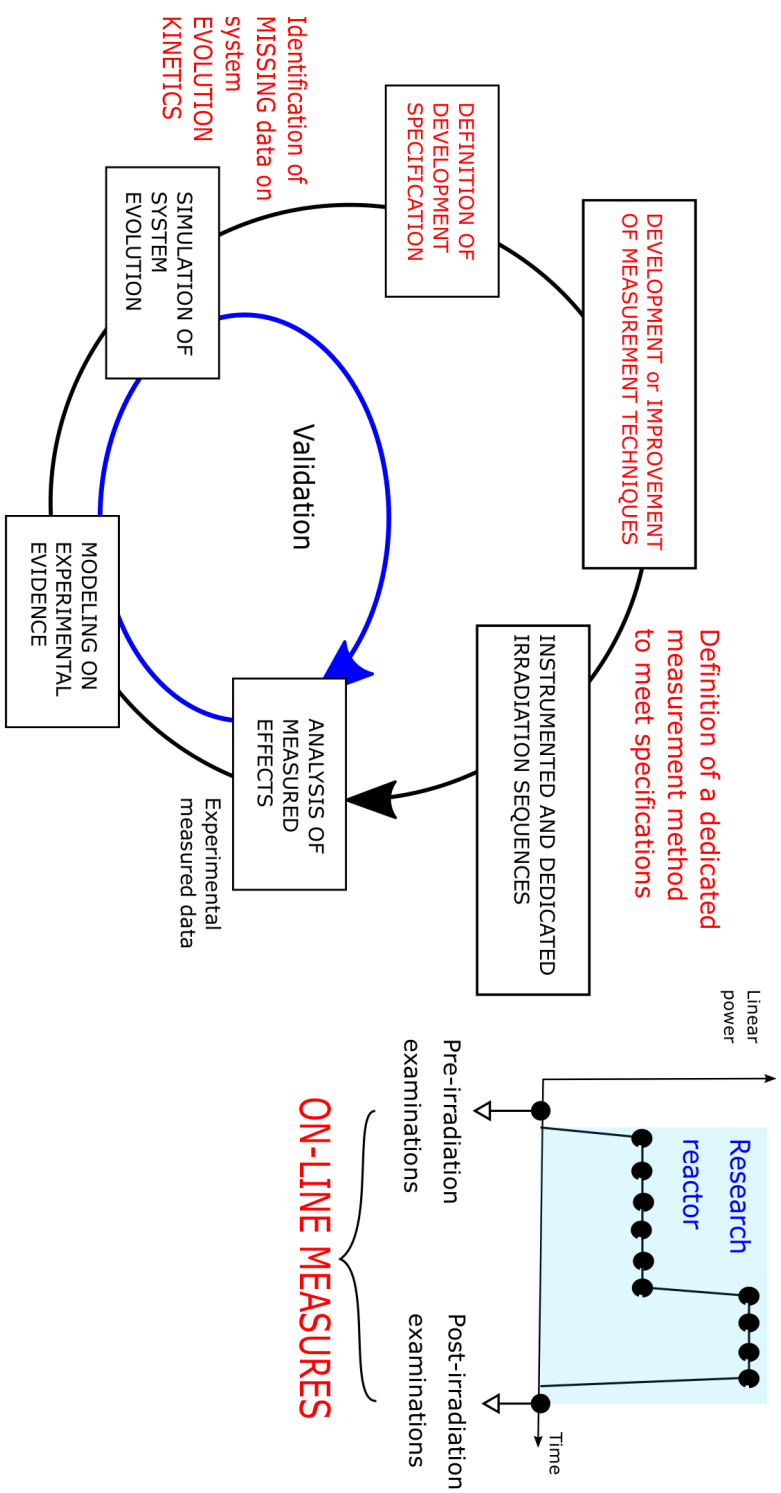

Figure 2.14 – Bridging the gap between experience and modeling for knowledge improvement of fuel performance

Chapter 3

Identification and characterization of relevant parameters

In this chapter we analyze the thermal-mechanical behavior of the fuel rod during normal irradiation condition and during power ramp test type transients to identify the set of of relevant and observable parameters for the detection and characterization of PCI. In section 3.2 we define the methodology used to perform the analysis. Section 3.3 is devoted to the analysis of the observable parameters to identify the relevant ones for PCI detection and measurement. The conclusions of the analysis are reported in section 3.4

Contents

3.1 Definition of useful labels to qualify parameters

We have introduced with the definition of PCI in 1.2.4 the distinction between the **weak** PCI, that corresponds to the local pellet-cladding contact, and the **strong** PCI, which implies that the different deformation kinetics of a component impacts the other one in a mutual way. Specific parameters are associated to the weak and the strong PCI and it is fundamental to exhaustively identify them. These parameters contribute in different way to PCI detection and for this we have defined some labels that are used further in this work:

- **Direct / Indirect**: A direct parameter implies that its modification is a straightforward consequence of the phenomena playing a role in PCI while an indirect marker presents a behavior which is related to one of the fundamental phenomena listed before in chapter 1. This latter contributes to the origin and evolution of the weak and/or the strong PCI but cannot allow its direct characterization. It may be associated to a complementary phenomenon influencing PCI. It generally needs to be synchronized to the evolution of another parameter;
- **Local / Integral**: PCI can result into a local modification of an observable parameter or it effect on the parameter can be the result of a cumulated effect along the fuel rod;
- **Detection / Measurement**: the detection of a parameter is the capability to recognize the occurrence of the weak or strong PCI while its measurement is related to the quantification of the effects induced by the PCI.

3.2 Methodology

We have relied on ALCYONE to simulate the fuel behavior under hypothetical irradiation sequences and to analyze the origin and the evolution of PCI to identify the relevant parameters related to the different activated mechanisms.
For the analysis, 1.5D model is performed to evaluate the behavior of the fuel rod system and to calculate the global quantities, like axial elongation and internal pressure. Also, the 1.5D resolution is required to perform a 3D simulation. This latter is used to analyze the local effects induced by PCI. In the following, we define the sample rod configurations and the irradiation sequences considered for the study.

3.2.1 Materials

To identify the exhaustive set of parameters describing PCI, we consider UO_2 fuel pellets with a M5 cladding. The pellets present the geometrical characteristics of french PWR pellets as described in chapter 1, enriched with a low percentage of U^{235}(about 4.5 %). The M5 has been chosen because it presents and enhanced resistance to external corrosion, with respect to zirconium alloys [CEA09]. The thickness of external corrosion is an important parameter in the choice of the most adapted fuel rod design to study PCI. Indeed, we deal with mechanisms leading to micro-metric changes in the rod surface thus it is important to reduce as much as possible the external corrosion thickness to increase the measurement accuracy of cladding external deformation.
For the base irradiation sequences, we consider a fuel stack of about 3.6 m made of pellets having radius of 4.1 mm and height 13.8 mm. The surrounding cladding has an internal radius of 4.18 mm and external diameter of 9.5 mm, for a total axial length of about

3.8 m and a radial gap of 80 μm. The upper plenum has a length of about 16 cm and it is pressurized at 30 bars. This rod is called the "long" rod, to distinguish it from the "short" rod used in the power ramp tests.
The short rod is obtained, according to a FABRICE process, from a long rod made of UO_2 pellets withing a cladding made of M5 and presents at the end of base irradiation a total average burn-up of about 30 GWd/tU. This burn-up is chosen because it corresponds to the most critical phase for PCI soliciting the cladding surface, as we said in chapter 1. The short fuel stack has a length of about 40 cm and an upper plenum length of 3.5 cm, where a spring occupies the 16% of the upper plenum volume and the internal gas is pressurized at about 30 bars.

3.2.2 Irradiation sequences

For this study, we define ideal base irradiation histories, to study the origin and evolution of PCI in normal operation conditions. Then, we define a series of power ramp tests imposed to the short rod in order to assess the mechanisms activated and the PCI kinetics in incidental conditions.

Normal operating conditions: The long rod is ideally submitted to a single irradiation cycle, lasting 3 years (1095 days). The duration of the irradiation is imposed sufficiently long to activate all the mechanisms involved in PCI, while all the intermediate sample conditions can be easily extracted by simulation.
In those ideal irradiation profiles we neglect the inter-cycles, that are the periodic return to zero power production characterizing the fuel rod history in the PWR. Inter-cycles are necessary in PWR to permit the periodic fuel management and recharge but can be neglected in our analysis as they have no consequences on rod behavior.
The linear power produced in the rod defines the thermal field in the system and drives the activation of different phenomena. We decided to study fuel rod behavior imposing a constant power production during the entire duration of the irradiation. According to a separate effect approach, the change in the amount of power produced is separately evaluated by comparing the same fuel rod performance in three different irradiation histories:

- $P_{lin} = 150$ W/cm
- $P_{lin} = 200$ W/cm
- $P_{lin} = 250$ W/cm

Power Ramp Test: To study the evolution and the macroscopic effects marking the PCI phenomenon in off-normal conditions, we simulate single-step power ramp tests, which configuration is illustrated in figure 3.1.
First of all, the conditioning plateau is reached with a power rate increase of 20 W/cm/min. This phase is highlighted in red in the figure. The linear power is maintained constant at about 200 W/cm for a total period of time of 15 h. Then, the power is increased at a rate of 100 W/cm/min up to the Ramp Terminal Level (RTL), in green in figure 2.1. The RTL is then kept constant for an holding period of 12 h. After the end of the holding period, the power is rapidly reduces to zero (in orange in the figure).
We considered that the same short rod is hypothetically submitted to different power ramp tests. Those different power ramp tests are characterized by their RTL level. We studied the evolution of mechanisms related to PCI between 450 W/cm and 665 W/cm. All the RTL levels are reached with the same power rate increase, fixed at 100 W/(cm.min). This

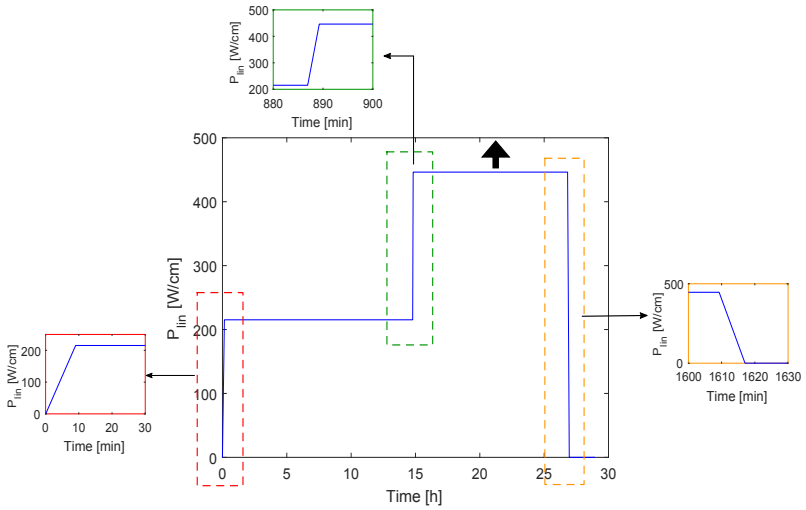

Figure 3.1 – Sample power ramp profile imposed to the short rod: the conditioning phase is reached with a rate of 20 W/(cm.min) and kept for 15 h (red). The transient phase is performed at fixed rate of 100 W/(cm.min) (green) up to variable Ramp Terminal Levels comprised between 450 W:cm and 665 W/cm.

leads to the fact that the transient phase lasts longer as the RTL level increases: about 2 minutes to reach 450 W/cm, the double to get to 650 W/cm.
The maximum tested RTL amounts to 665 W/cm which corresponds to the maximal linear power that can be reached by ALCYONE code with a 30 GWd/tU fuel rod. This is imposed by the validity range of fuel mechanical properties, which is limited to a maximal temperature below 2600°C.

3.3 Identification of relevant parameters for PCI characterization

Now that we have defined a common glossary to classify the relevant parameters and defined the methodology of analysis, we can proceed to discuss the evolution of the macroscopic parameters studied.
The analysis of the sample rod behavior and the evolution of parameters is always performed at a constant linear power. Calculated and measured results are always related to an exact linear power and a precise time at which they occurs. During the transient phase, the power variations along the sample rod are too rapid and it is extremely difficult to make use of these measured values to be compared to calculated ones for code validation.

First of all, we focus on the geometrical evolution of the fuel rod: for this, we discuss the effects of PCI on the radial deformation and the axial elongation of the fuel rod components. Second, we analyze the main temperatures of the system, so the fuel centerline and surface one and the cladding surface temperature. Finally, we discuss the dependency of the internal pressure on the mechanisms related to PCI.
In the following we focus on the calculated macroscopic consequences resulting from the coupled phenomena taking place during the difference irradiation sequences modeled. Further details on the phenomenology behind these macroscopic effects are reported in appendix A.

3.3.1 Geometrical evolution

On the basis of the phenomenology presented in the previous chapters, the Pellet-Cladding Interaction origins from the local contact between the pellet and the cladding. It first occurs at the mid-rod plane because the linear power profile has a maximum at this location, and then evolves towards the extremities of the rod. For this, our analysis focuses on the central pellets. We have analyzed the radial and axial deformation of the sample rod during normal operation conditions and during the power ramp tests. The radial deformation is extracted from the 3D simulation because, as we have already said, this representation permits to assess the local behavior of the fuel pellet, to take into account the geometrical characteristics of the system like chamfers, dishing and to study the different kinetics at the Inter-Pellet (IP) and the Median-Pellet (MP) plane.
The axial elongation of the fuel and of the cladding are global quantities and thus result of the 1.5D simulation.

Radial deformation

Normal operation conditions
Figure 3.2 illustrates the evolution during a base irradiation at 200 W/cm, constant linear power, where the complete closure of the gap along the length of the analyzed pellet is reached.
Since the beginning of the irradiation, the pellet undergoes instantaneous thermal dilatation. As a consequence of the strong thermal gradient and the fragile nature of the material, the pellet takes the hourglass shape: the $D^{e}_{f,IP}$ (orange) is greater than the $D^{e}_{f,MP}$ (green). After the initial dilatation, pellet diameter decreases as a consequence of the densification process that takes place in the component.
Once the densification ends, the pellet undergoes solid and gaseous swelling, which progressively increases the radial dimension of the pellet.
Meanwhile, the cladding undergoes an instantaneous thermal dilatation, largely smaller than the one in the pellet, because of the lower temperatures established in this components, as it has already been detailed in chapter 1. Then, the cladding undergoes inward creep and the gap thickness progressively decreases.
As a consequence of the hourglass shape, the gap closes first at the IP plane, where the weak PCI is first established (superposition of the orange and of the red curves) and then at the MP plane. In the interaction, the local deformation kinetics of both cladding and fuel results to be modified: when the contact is established at the IP, the expanding pellet slows down the inward creep of the cladding. At the MP, this latter is free to continue to deform up to the contact at the MP (superposition of the blue and green curves), which corresponds, for symmetry reasons, to the complete closure of the gap. Since this moment, the pellet expansion prevails.
The deformation mechanisms taking place inside the sample rod are reflected on the outer surface of the cladding (magenta and cyan curves). When the contact establishes at the IP, the deformation kinetics of the $D^{e}_{c,IP}$ is slowed down while the $D^{e}_{c,MP}$ keeps on accommodating the pellet hourglass shape. When the contact is established along the entire pellet length, the expansion of the fuel pellet internally prevails and imposes a directional switch of the cladding deformation, which starts expanding. The range of absolute variation of the cladding is in the order of ± 300 µm.
After the end of the base irradiation, the residual deformation consists of a $D^{i}_{j,IP} > D^{i}_{j,MP}$ for the i surface of the j component. Among these, the grater deformation of the $D^{e}_{c,IP}$ with respect to the $D^{e}_{c,MP}$ appears as a ridge on the cladding surface, the primary ridge, as we

said in chapter 1. Calculation shows that the primary ridges origin from the strong PCI at the IP, grow during the closure of the gap between the IP and the MP and remain approximately constant since the closure of the gap at the MP. Through their deformation of the cladding external diameter, they allow to detect and measure the evolution of the strong PCI. A single point measurement is not sufficient to characterize the deformation kinetics of the cladding and characterize the evolution of primary ridges, which height and deformation kinetics depend on the local evolution of the cladding portion. Multiple measurements need to be carried out, with a spatial resolution sufficiently small to reconstruct the ridge shape. This should be at least 0.5 mm to follow the ridge shape along the pellet length (13.8 mm).
The amplitude of the primary ridges ranges in the tens of micrometers which imposes a relative accuracy for the measurement in the order of 1 µm.
The calculated time evolution shows that the kinetic of ridge formation is slow, in the order of several days to deform of a micrometer, and depends on the local linear power. This results in a loosening of constraints related to the duration of a single measurement to be performed along a certain axial extension: the evolution of clad deformation during the measurement time can be considered to be negligible, as long as the linear power is kept constant during the measurement time.

Power ramp
At the end of the conditioning plateau, calculations show that in the central pellet the contact is established at the IP but a residual gap exists between the pellet and the cladding. This gap closes during the transient phase by thermal dilatation and the strong PCI is induced.
Figure 3.3 illustrates the macroscopic evolution of the cladding radial profile during the power ramp test for three samples, characterized by different values of maximum linear power, the Ramp Terminal Level (RTL). Calculation show that depending on the characteristics of the power ramp test, the radial deformation of the cladding can be highly or slightly not uniform along the axial direction, with a strong variability in the deformation kinetics of primary and secondary ridges.
The deformation kinetics of the cladding is strictly linked to the mechanisms that are activated in the fuel depending on the thermal range and on the way they superpose during and after the transient phase: thermal dilatation and creep mechanisms, solid and gaseous swelling and dish fulfillment kinetics. Indeed, thermal dilatation and gaseous swelling contributes to expand the pellet that deforms and accommodates stresses creeping towards the outside (and the cladding). At the IP, the pellet can creep also towards the inside, fulfilling the dish. This acts like a reservoir and locally reduces the tendency of the pellet to deform towards the cladding.
These mechanisms superpose in different ways depending on the local linear power, to the rate of increase of this power. They can lead to the non uniform deformation kinetics of the cladding and contribute to the evolution kinetics of the primary and secondary ridges during the power ramp.

Thus, simulation results show that by measuring the evolution of the cladding deformation kinetics we can extract information on the mechanisms taking place in the pellet, that propagate to the cladding through the mechanical interaction between the two. The non uniform deformation of the cladding and the different evolution of the primary and secondary ridges impose the need to measure the evolution of the entire, or at least a part of, the cladding. Considering the calculated profile of the clad, a spacing of 0.5 mm or less allows to reconstruct the ridges profile.

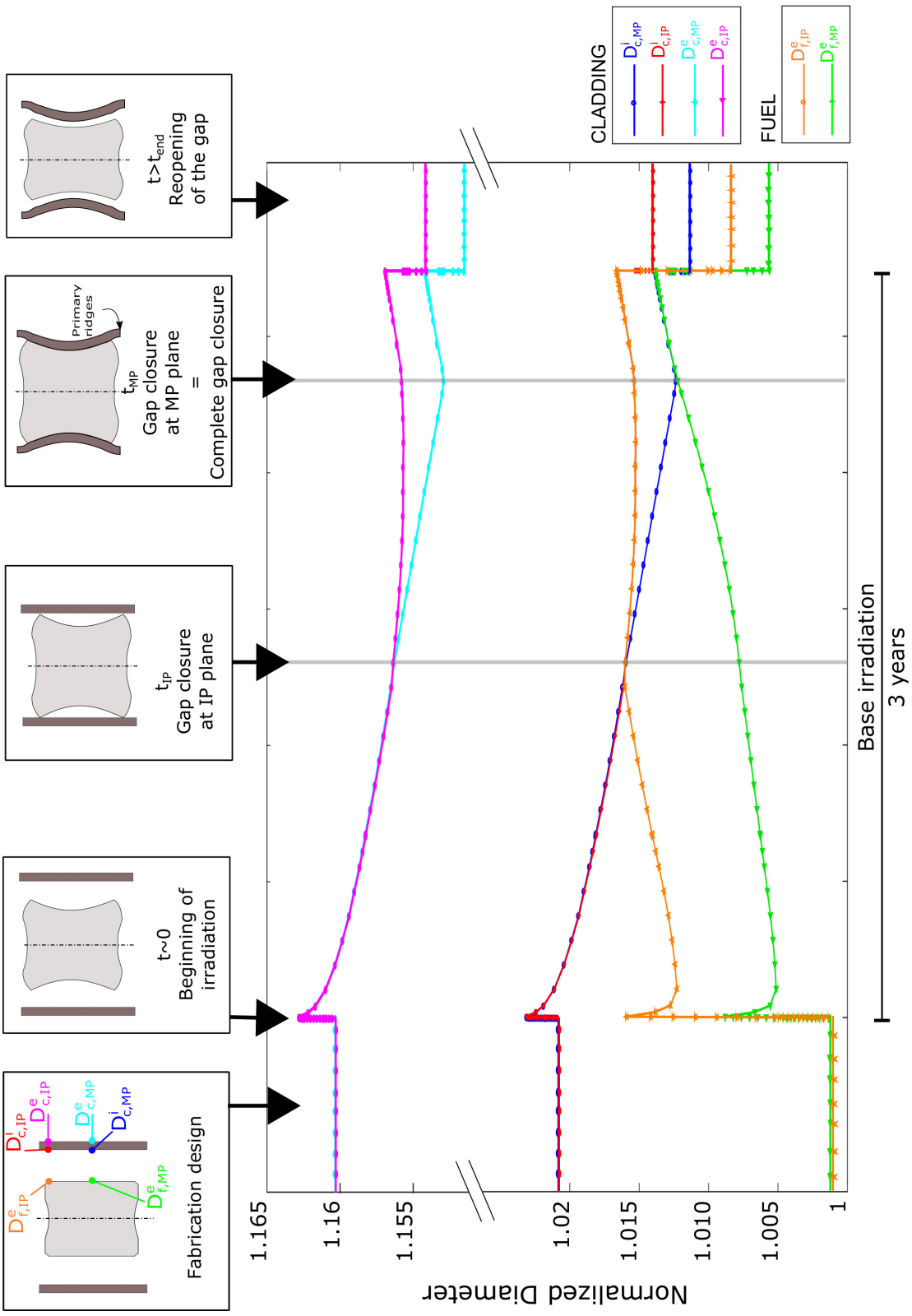

Figure 3.2 – Normalized evolution of the cladding and fuel diameter during base irradiation: the evolutions are obtained with ALCYONE 3D simulation, $P_{lin} = 200W/cm$, duration = 3 years.

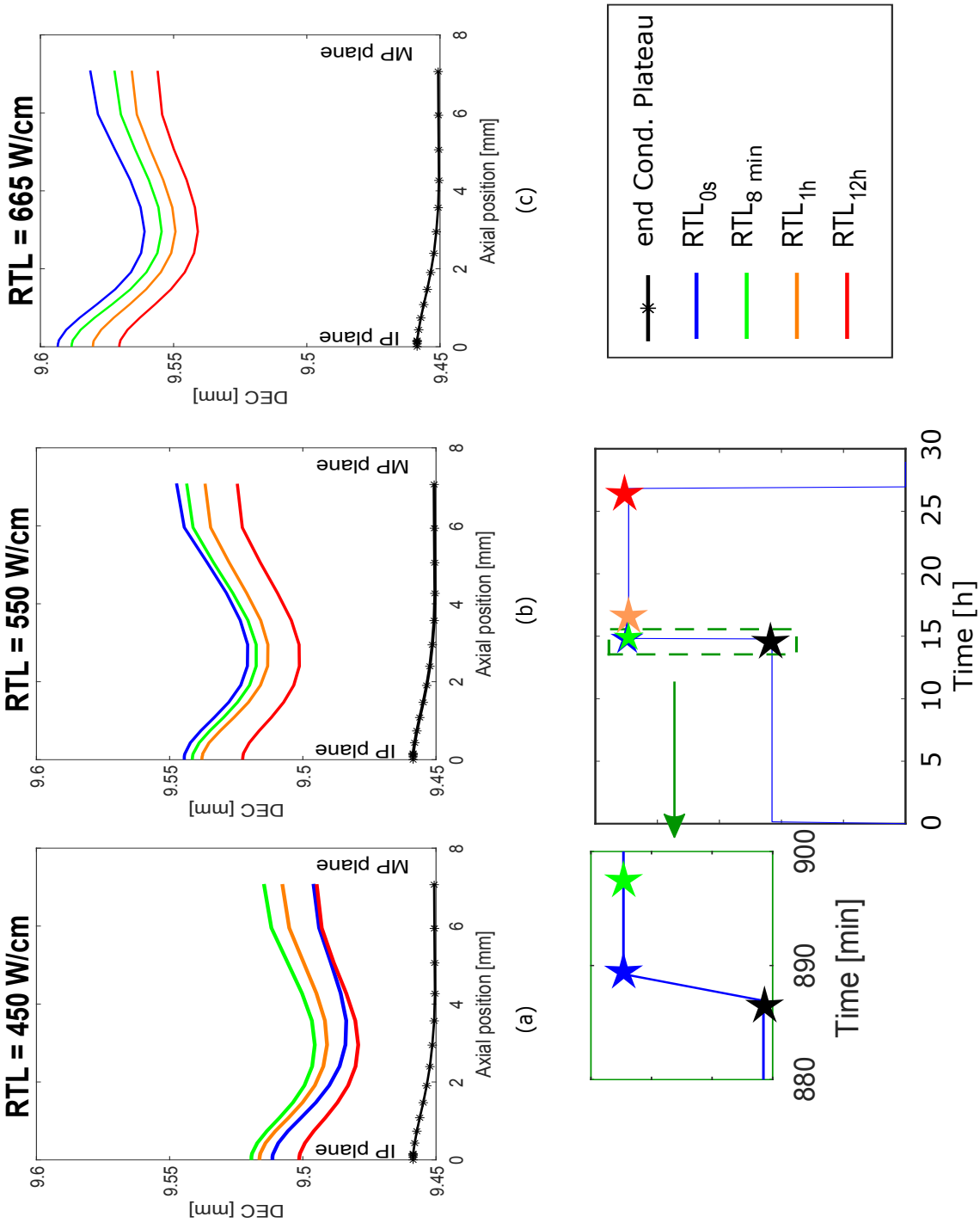

Figure 3.3 – Evolution of the cladding profile during three power ramp tests having different Ramp Terminal Level (RTL) (a) 450 W/cm; (b) 550 W/cm and (c) 665 W/cm. The calculated profiles are extracted at the end of the conditioning phase (black) at the beginning of the Terminal level plateau (blue), after 8 minutes at constant power (green) after 1h (orange) and at the end RTL (red).

The amplitude of these deformation is small, in the order of the tens of micrometers. The deformation kinetics is accelerated with respect to normal operation conditions because of the higher temperatures: calculations show that the kinetics evolves faster in the first phases after the transient (order of minutes) and slows down during the holding time at constant power, releasing the requirements in the terms of sampling frequency of measurements (order of hours).

Axial elongation

Normal operation conditions

The mechanical interaction that establishes in the radial direction evolves along the rod axis according to the axial profile of the linear power (c.f. figure 1.5). Figure 3.4 illustrates the relative axial evolution of the fuel stack (blue) and the entire cladding (red) during base irradiation at 200 W/cm. Considering the cladding, after the increase of the linear power production and the rise of the internal temperatures, it undergoes instantaneous thermal dilation. Then, during the base irradiation, it creeps to relax internal stresses, which results into an axial elongation.
Meanwhile, the fuel stack undergoes an instantaneous thermal dilatation stronger than the one occurring in the cladding because of the higher temperatures. The thermal dilatation is then followed by a decrease of the length due to the densification process. After some days in the irradiation, it creeps to relax internal stresses and its length increases. The different material properties of the two components, the higher temperatures in the fuel stack and the presence of solid and gaseous swelling in the pellets, lead to a stronger creep mechanism of the fuel with respect to the cladding. When the mechanical interaction between the pellets and the cladding establishes along a sufficient portion of the axial length, the cladding deformation is accelerated by the fuel. The two component deform according to the same mutually impacted kinetics.
It is important to stress that the discontinuity that origins when the fuels starts driving the cladding creep does not coincide with a local interaction but is the result of the cumulated strong mechanical interaction along a portion of the fuel stack.

The detection of this discontinuity and the characterization of the modified elongation kinetics have fundamental interest for the study of PCI. This can be obtained from a local measurement of the integral elongation of the fuel and the cladding, which vary in the range of the few tens of millimeters.

Power Ramp

Figure 3.5 presents the calculated evolution of the fuel and clad axial elongations during the power ramp test with RTL at 450 W/cm
The power increase from the room temperature to the conditioning phase induces the thermal expansion of the system. The system is conditioned at that power and no deformation occurs during the 12 hours holding period. The transient imposes a thermal dilatation to the system, proportional to the maximum linear power produced. The maximum axial elongation for each component is reached at the end of the transient. Then, during the holding period, the two components relax internal stresses through creep and the macroscopic dimensions reduce.
The strong PCI, which has been observed and discussed during base irradiation, takes place from the beginning of the conditioning phase: the cladding deformation is driven by the fuel stack and the two components deform according to the same kinetics.

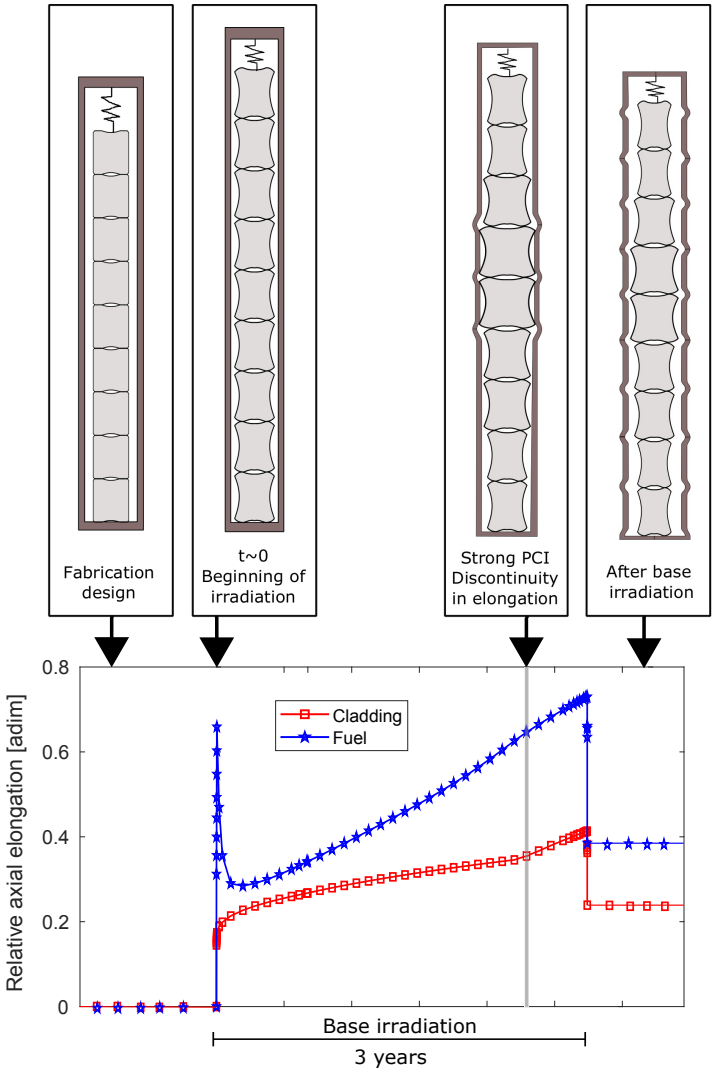

Figure 3.4 – Relative axial elongation of the cladding and the fuel during base irradiation, result obtained by ALCYONE 1D simulation, P_{lin} = 200W/cm, duration = 3 years.

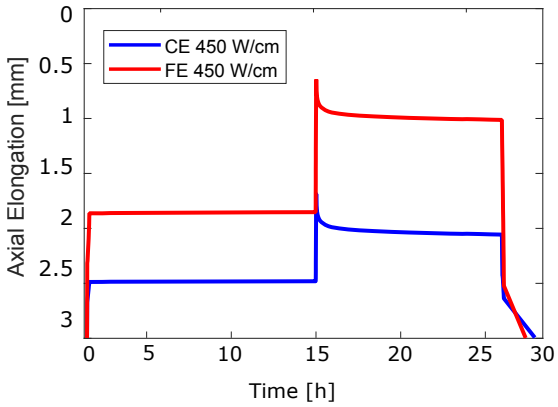

Figure 3.5 – Time evolution of the fuel stack and cladding axial elongation during the power ramp test with ramp terminal level at 450 W/cm

3.3.2 Temperature evolution

The local temperatures in the fuel pellets and in the cladding depend on the linear power production, on the material properties and their evolution under irradiation, the presence of the external coolant and, globally, on the radial heat exchange from the pellet, through the cladding, to the coolant. During normal and incidental conditions, like the ones considered in this work, single phase liquid coolant is imposed to the system, to collect the heat produced in the fuel rod. The correct cooling is ensured with no chance of failure during the calculated operation conditions, as required by the safety authority.
In the following we discuss the calculated effects of the progressive closure and contact between the two components (weak PCI) on the centerline fuel temperature, on the fuel surface temperature and on the cladding external surface temperature. The quantities are extracted from 3D modeling as to distinguish between the IP plane and the MP plane.

Normal operation conditions
Figure 3.6 shows the evolution of the temperatures in the fuel and in the cladding during the calculated base irradiation at constant linear power production of 200 W/cm.
In the fuel, the capability of the fuel to transfer the heat produced evolves with the thermal conductivity of the UO_2, which degrades under irradiation [Bai96]. This tends to increase the thermal field in the pellet. Also, the progressive release of fission gases in the gap decreases the gap conductance, also pushing for an increase of the fuel temperatures. Calculations show that, because of the superposed effects of these phenomena, the local closure of the gap at the IP doesn't result into a characteristic effect on the central fuel temperature. When the pellet-cladding contact establishes along the whole pellet, only the mechanisms inducing a degradation of the thermal exchange take place. This results into a global increase of the fuel temperatures, both at the IP, in red, and at the MP, in blue.

The graph shows that the temperatures of the fuel surface linearly decrease with the reduction of the gap and the improve of the thermal exchange. This decrease stops when the gap locally closes. The $T^{e}_{f,IP}$ remains constant since the local contact at the IP while the $T^{e}_{f,MP}$ continues to decrease up to the complete closure of the gap.
This leads us to conclude that the local contact at the Inter-Pellet plane (weak PCI) induces a characteristic modification of the local $T^{e}_{f,IP}$ while the complete closure of the gap modifies the local $T^{e}_{f,MP}$ and both $T^{i}_{f,IP}$ and $T^{i}_{f,MP}$. By their local measurement we can thus detect the establishing of the weak (local contact at IP) and strong (complete closure of the gap along the pellet) PCI, respectively. The calculated thermal modification are in the order of the tens of degrees, which imposes an accuracy of the relative measurements of about 1°C.

We observe from the graph that the improve in the thermal exchange that results into a decrease of the fuel pellet surface temperature has no effects on the calculated cladding surface temperature. For each analyzed base irradiation, the T^{e}_{c} is approximately constant during the whole irradiation, with a maximum variation between the beginning and the end of the irradiation smaller than 5°C for all the three cases.
We stress that the temperature of the external cladding is the same for the IP and the MP place as it is a global quantity, it results from the thermal-hydraulic resolution and it constitutes an input for the thermal-mechanical calculation of the sample rod behavior done by ALCYONE.

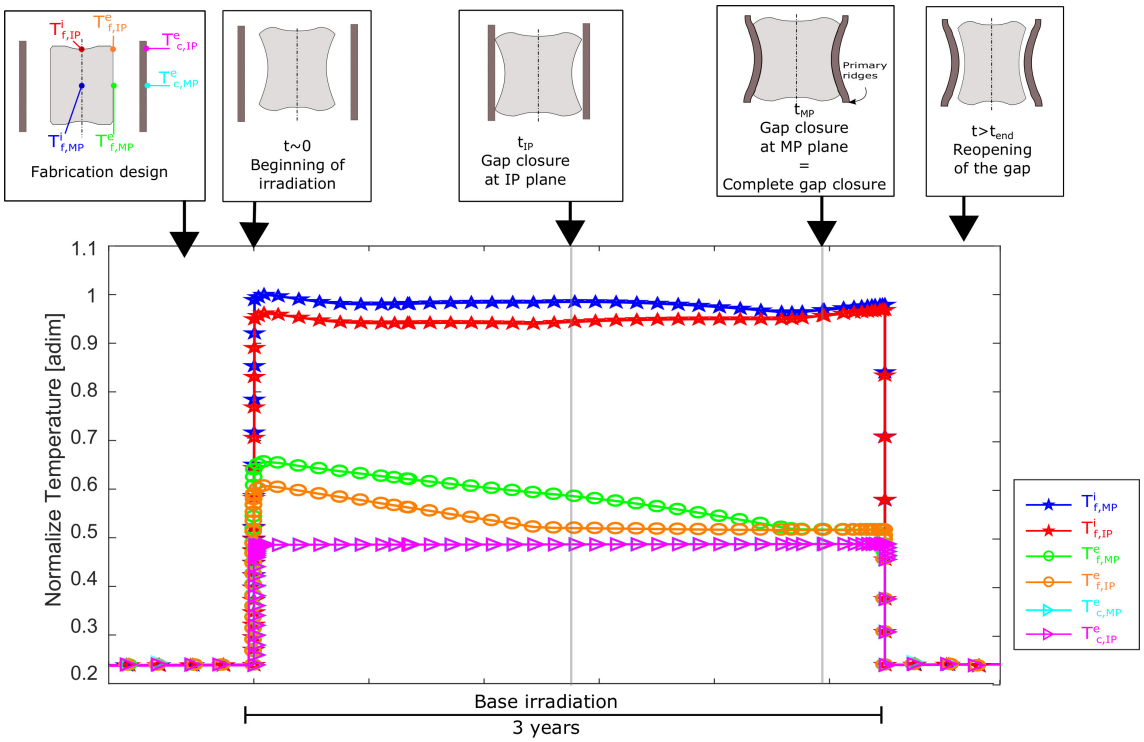

Figure 3.6 – Normalized evolution of temperatures in the cladding and in the fuel pellet during base irradiation, results with ALCYONE 3D simulation, P_{lin} = 200W/cm, duration = 3 years.

Power Ramp test

The temperatures are eligible parameters to detect the local occurrence of the weak or strong PCI while they do not allow to measure its evolution. For the power ramp tests under analysis, the weak PCI and the strong PCI locally occurs since the beginning of the irradiation or during the transient phase so that they are not relevant parameters to detect PCI in these operation conditions.

3.3.3 Internal rod pressure evolution

We focus in this section on the evolution of the internal rod pressure during base irradiation and during power ramp test, to identify the existence of a characteristic behavior to be associated to PCI. The internal pressure is a global quantity so it results from 1.5D simulation. It is evaluated according to the ideal gas law:

$$p_{int} = \frac{nR}{\sum_i \frac{V_i}{T_i}} \tag{3.1}$$

The internal pressure depends through the ideal gas constant R on:

- The total number of gas moles n present in the fuel rod is given by the initial quantity of gas introduced to pressurize the system and the quantity produced by fission during the nuclear reactor operation and that is released from the fuel. This value increases during the life of the fuel rod;
- The volume where the gas or a portion of gas is stored V_i;

– The temperature in that free volume T_i.

The free volumes considered by Alcyone are the following:

– The volume of the pellet-clad gap at the average temperature of the gap;

– The volume of dishings at the average temperature of each dishing;

– The volume of chamfers at the average temperature of each chamfer;

– The volume of cracks at the local temperature in the fuel;

– The volume of open porosity at the temperature of the external surface of the fuel;

– The volume of the upper and lower plenum, at the average temperature of the coolant corresponding to the first or last axial slice.

We are interested in the evolution of the internal pressure to discuss its dependency on the volume of the pellet-clad gap, and identify if the local and progressive closure of the gap along the fuel rod axis leads to a characteristic increase of the p_{int}. Such a characteristic evolution would define the internal pressure as a direct indicator of the PCI.
To understand the evolution of the internal pressure, we need to consider also the release of fission products and the evolution of the internal free volume. The three are reported during normal operation conditions and during a power ramp test operation.

Normal operation conditions
Figure 3.8 shows the calculated evolution of the internal rod pressure in the upper plenum (a), of the fractional release of fission products (b) and of the internal free volume (c) for the three base irradiations considered: 150 W/cm in blue, 200 W/cm in green and 250 W/cm in red.
We observe that the internal rod pressure evolves according to the decrease of the internal free volume. This is clear because the change in its kinetic is related only to the increase of the release of fission products for the base irradiation at 250 W/cm.
The evolution of the internal free volume is the sum of different contribution, as we previously saw. At the beginning of the irradiation, the thermal expansion imposes a sudden decrease to the free volume, which then increases because of the fuel densification phenomenon. Then, its evolution is constant and driven by the progressive closure of the radial gap along the axial length of the fuel stack. There is no characteristic impact that can be associated to the the local or integral effects of PCI but rather an indirect effect that drives its evolution during the entire irradiation. The pressure in the upper plenum slowly increases and ranges in the orders of the tens of bar and undergoes a slow evolution during base irradiation.

Power Ramp We focus now on the evolution of the internal pressure during the power ramp test. As before, we report its kinetics with the evolution of the internal free internal volume and of the release fraction of fission products. Figure 3.8 shows the calculated evolution of the three parameters for three power ramp tests: in blue for an RTL of 450 W/cm, in green of 550 W/cm and in red of 665 W/cm.
The graphs report only the last 5 hours of the conditioning phase: the concerned phenomena take place with a characteristic time longer than the 12 hours holding time imposed so the three parameters are constant in this phase.
The power transient induces a sudden increase of the internal pressure, that varies between 70 bars during the conditioning phase up to 120 bars during the RTL. Its evolution

is initially related to the instantaneous increase in the free volume resulting from the thermal increase associated to the transient. During the holding period, the evolution of the internal pressure is driven by the release kinetics of fission product. The modification of the internal volume is a minor contributor to the total behavior.

Monitoring the internal rod pressure during a power ramp test does not allow the direct characterization of PCI but it is important to characterize the release kinetics of fission product. The reason is twofold: first, as we see in the central figure of 3.8, the reopening of the gap results into an increase of the released fraction, that can lead to a sudden increase of the internal pressure; second, the release of fission products is part of the model that describes the gaseous swelling in the fuel, which plays an important role in the PCI kinetics during incidental conditions. The pressure is thus an indirect indicator of the integral effects of weak PCI along the rod axis.

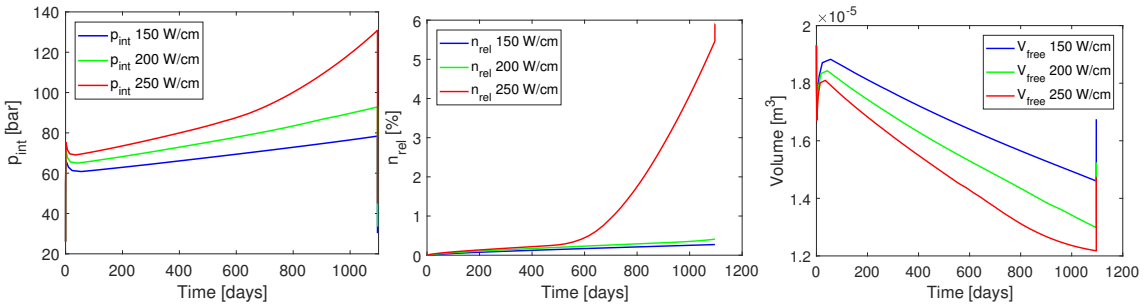

(a) (b) (c)

Figure 3.7 – Time evolution of the internal pressure in the upper plenum (a) of the released fraction of fission products from the fuel (b) and of the free volume within the fuel rod during the three base irradiation considered: 150 W/cm in blue, 200 W/cm in green and 250 W/cm in red.

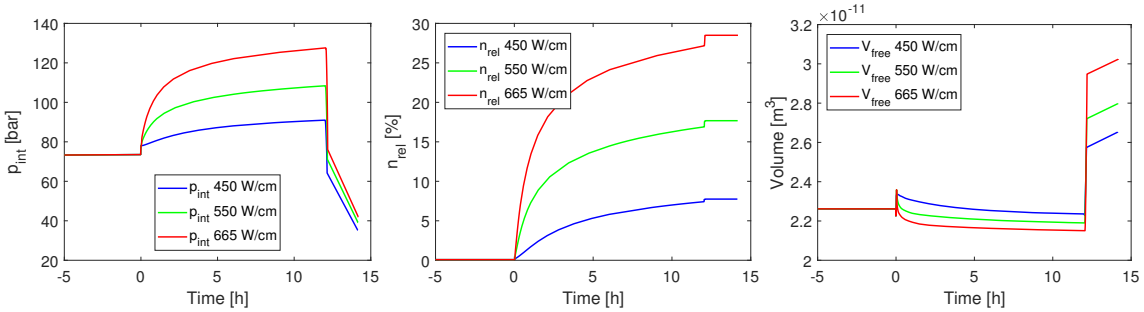

(a) (b) (c)

Figure 3.8 – Time evolution of the internal pressure (a) of the released fraction of fission products from the fuel (b) and of the free volume within the fuel rod during the three power ramp tests considered: RTL= 450 W/cm in blue, RTL= 550 W/cm in green and RTL= 665 W/cm in red.

3.4 Conclusions of the analysis

We have discussed in this chapter the observable effects of the weak and strong PCI. For this we have used the 1.5D and 3D representations of ALCYONE to model fuel performance during base irradiation and during power ramp test. The analyzed parameters are the following:

- Radial deformation;
- Cladding temperature;
- Fuel temperatures;
- Axial elongation;
- Internal pressure.

Table 3.2 summarizes the main characteristics of identified parameters.
A trivial direct indicator of the local weak PCI is the **Pellet-Cladding Contact**, which progresses from the Mid-Rod plane toward the extremities of the rod.

The **radial deformation of the cladding** shows to be directly impacted by the local mechanical interaction with the pellet, with the formation of primary and secondary ridges. Their formation and coupled evolution are strongly related to the mechanisms taking place in the fuel rod and leading to cladding deformation. By measuring the radial deformation over a portion of the fuel rod or over the entire fuel rod, it is possible to detect and characterize the evolution of the strong PCI. The radial deformation of the clad is thus a direct indicator of the local weak and strong PCI. The amplitude of the induced deformation is small, in the order of the micrometer. To reduce as much as possible the perturbations of the system during the measurement, a remote monitoring is recommended.

In the previous discussion we highlighted the interest of coupling this measurement with the evolution of the **Cladding Elongation**. Calculations show that a characteristic discontinuity occurs in its elongation kinetics, when the strong PCI establishes along a certain portion of the fuel stack. Since this stage of interaction, the fuel stack drives the cladding deformation, accelerating it. It is thus a direct indicator of the integral effect of the strong PCI.
To obtain a complete characterization of the internal strong mechanical interaction which origins the discontinuity in clad creep rate, it is fundamental to couple these measurements with the monitoring of the radial deformation.

The **Internal Rod Pressure** is an indirect indicator of the PCI because it can detect the local reopening of the gap, if it is related to a sudden release of fission products that increases the pressure in the upper plenum.
On a second order, when the release of fission products is low, the internal pressure evolves according to the reduction of the internal free volume. This latter depends on the differential elongation of the cladding and of the fuel and the radial closure of the gap along the rod axis. For this the **Fuel Elongation** is considered an indirect indicator of the weak PCI. Calculations shows that the interaction with the cladding results into a negligible modification in its elongation kinetics. By the synchronized measurement of the fuel and cladding elongation and the internal rod pressure we could indirectly characterize the progressive reduction of the pellet-cladding gap along the axis of the rod .

For what it is concerned with temperatures, calculations show that the **Temperature of the External surface of the Cladding** is not modified by the interaction of the pellet with the cladding. From a physical point of view, this temperature is indeed defined by the thermal exchange with the coolant. Actually, this temperature is the boundary condition for the evaluation of the thermal-mechanical model in the fuel rod, that describes the origin and evolution of the PCI. It thus constitutes a fundamental input parameter for the numerical simulation. For this, we shall analyze in the following parts of this thesis the technological solutions adapted to its measure.
Temperatures in the fuel are locally impacted by the improvement of the heat exchange that results from the reduction and closure of the gap. The local **Fuel External surface Temperature** allows to directly detect the weak PCI and the strong PCI while the **Fuel Centerline Temperature** allows to detect the local complete closure of the gap along the pellet length. It is thus a direct indicator of the strong PCI.

The PIRT (Phenomenon Identification Ranking Table) diagram illustrated in figure 3.9 resumes the information about each parameter and its relevancy for the characterization of the PCI mechanisms. It also gives the present state of comprehension and experimental characterization related to the parameter.

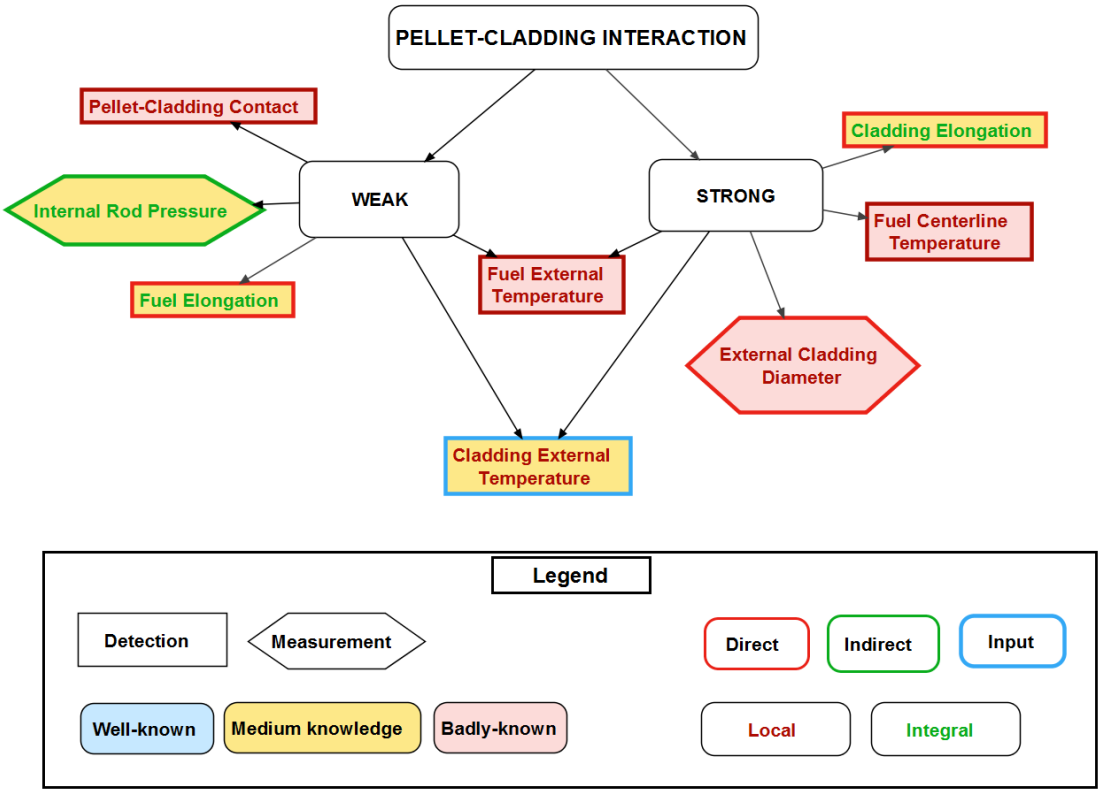

Figure 3.9 – PIRT resulting from the analysis on the identification of the observable parameters to detect and measure the PCI during normal conditions and power ramp tests.

Parameter	**PCI**	**Type of indicator**	**Type of measurement**	**Range of variation**	**Order of relative accuracy**	**Comments**
Pellet-Cladding contact	Weak	Direct - Local	Detection	Fuel stack	1 pellet	
Cladding External Diameter	Strong	Direct - Local	Measurement	±300 µm	1 µm	Recommended remote measurements
Cladding Elongation	Strong	Direct - Integral	Detection	±2.5% of rod length	0.1 mm	Synchronization: External Cladding Diameter, Fuel Elongation, Internal Pressure
Fuel Elongation	Weak	Indirect - Integral	Measurement	±2.5% of rod length	0.1 mm	Synchronization: External Cladding Diameter, Cladding Elongation, Internal Pressure
Internal Rod Pressure	Weak	Indirect - Integral	Measurement	[60-120] bars	1 bar	Synchronization: External Cladding Diameter, Cladding and Fuel Elongation
Fuel Centerline Temperature	Strong	Direct - Local	Detection	∼[900-2800] °C	∼1°C	
Fuel External Temperature	Weak and Strong	Direct - Local	Detection	∼[300-600] °C	∼1°C	
Cladding External Temperature	Weak and Strong	Input	Measurement	∼300 °C	∼1°C	

Table 3.2 – Synthesis of the characteristics of relevant indicators for PCI detection and measurement

Outcomes of Part I

We have started this thesis by introducing the context and motivations of the research. We have presented the nuclear context, characterized the fuel element and then discussed the origin and evolution of the Pellet-Cladding Interaction: during normal operation condition, the coupled mechanisms of pellet expansion under solid and gaseous swelling and cladding inward creep under differential pressure lead to the progressive closure of the fabrication gap between the two objects. Due to the thermal dependency of the driving mechanisms, the phenomena occur first at the mid-rod plane, where temperatures are the highest, and then evolves towards the rod extremities. The cladding progressively accommodates the shape of the pellet and the fuel element deforms according to the mutual impact of the behavior of one component to the others. We talk about strong PCI. During a transient operation, the efforts imposed by the larger expansion of the pellets increase the mechanical stresses formed in the cladding and lead to PCI induced failure of the latter.

The cladding plays a fundamental safety role as it is the first barrier to avoid the release of radioactive products in the primary loop of the nuclear reactor system. The operator (EDF in the French context) must guarantee to the safety authority that during normal and incidental conditions, the cladding remains tight and no melting is locally induced. To respect these safety criteria, strict safety margins are imposed to the technical specification that define the maneuverability of the power reactor.
The understanding of phenomena involved with PCI is based on dedicated experimental sequences, the power ramp tests, that are performed in material testing reactors. The vast majority of available data comes from post-irradiation examinations and they have been used to develop models and simulation codes that permit to access the kinetic of the phenomena of interest. Few experiments have been performed integrating an instrumentation set-up allowing the on-line monitoring of the fuel element behavior, which constitute a huge source of information to improve the accuracy of the simulation tools.

This work is the first step towards the development of an on-line measurement method to better the knowledge of relevant physical phenomena associated to PCI. This is required to gain operational margins to follow grid demand always respecting the aforementioned safety criteria.

To select the relevant parameters to be detected and measured on-line, we relied on simulation. The reference tool used in this work is the multidimensional fuel performance code ALCYONE of the simulation platform PLEIADES, developed by CEA in collaboration with EDF and FRAMATOME. We have presented the code with a specific attention to the thermal-mechanical model of the fuel, that is further used in the next part, and the different computational model applied in the study: the 1.5D simulation that allows to calculate the global quantities in the sample rod, and the 3D model, that permits a fine

and detailed analysis of the local behavior.

We have studied the thermal mechanical behavior of the fuel element by simulating several normal operation conditions and power ramp tests and identified the parameters that show a characteristic behavior related to PCI. At this stage of the work, ALCYONE has no model to account for the onset of melting in the fuel pellet so that the analysis is limited to the solid fuel.
For the weak PCI we identified the following observable direct indicators:

- The pellet-cladding contact: it is required for the weak PCI to establish. This is quite a dummy result but its detection is not a trivial topic;
- The local fuel surface temperature at the IP, which decreases because of the improved thermal exchange between the pellets and the cladding through the closed gap.

The strong PCI shows to have direct consequences:

- The external cladding diameter evolves to accommodate the pellet shape with the consequent formation kinetics of the primary ridges during normal operations and of secondary ridges during power ramp tests;
- The axial elongation the cladding: modeling shows that a discontinuity occurs when the PCI is sufficiently strong along the fuel stack that the fuel elongation drives the cladding one;
- The local fuel centerline temperature, that increases since the complete closure of the gap along the pellet length;
- The local fuel surface temperature at the MP, which modifies its kinetics after the complete closure of the gap along the pellet length.

The internal rod pressure and the fuel elongation are not mentioned among the direct indicators of PCI, indeed calculations show that they are not impacted by the origin and evolution of the weak or strong PCI. But, we have rather identified them as indirect indicators the integral, weak PCI. The internal rod pressure is indeed suddenly increased if the reopening of the gap is related to a release of fission gasses.
The fuel and the cladding elongation kinetics define the evolution of the upper plenum volume. This latter and the radial gap drive the evolution of the internal pressure, when the fractional release of fission product is negligible. By the synchronized measurement of the fuel and cladding elongation and the internal rod pressure we could indirectly characterize the progressive reduction of the pellet-cladding gap along the axis of the rod.
The external surface temperature of the cladding is not impacted by the gap closure but it is the boundary condition for the resolution of the thermal-mechanical computation that allows to model the origin and evolution of the PCI. Its measurement has thus great importance.

Part II

Theoretical feasibility to detect melting onset in the fuel material

Chapter 4

Thermo-physical properties of nuclear fuel material at melting onset

In this chapter we define the thermo-physical properties of interest for the development of the thermal-mechanical model which is the object of chapter 6. For this, we first define the non-congruent melting interval for the nuclear fuel material and then we define the enthalpy of fusion and discuss the discontinuity in material density appearing at melting onset.

Contents

4.1 Introduction

This part of the work aims at evaluating the theoretical effect of a partial fuel melting on the deformation of a fuel rod. The frame of the study is the same as before: a PWR fuel rod made of UO_2 pellets presenting a burn-up of about 30 GWd/tU, so in the critical range for PCI analyses, submitted to a power transient. But in this case the hypothetical power variation leads to very high temperatures in the fuel, the centerline temperature exceeds melting points and the material starts melting.
The subject of melting fuel material is not new in the nuclear context. Several studies have been carried out in the past 60 years to define the melting point of the fuel material and to characterize the effect of influencing parameters: fuel composition, stoichiometry and burn-up. The thermal and mechanical implication of molten fuel originating in the case of severe accidents have been largely investigated for safety purpose [All85] [Cam87] [Sil79]. None of these studies takes into account the existence of a molten phase. Recently, the non congruent melting of the fuel material has been studied by Welland [Wel09] for an hyperstoichiometric fuel. All the aforementioned researches considered the case of a defective cladding, where the loss of integrity lead to the reaction of the coolant with the UO_2. From the reaction it results a strong oxidation of the fuel material. The first peculiarity of our study is that we assume that the power transient does not induce the loss of integrity of the cladding, so the oxidation reaction doesn't drive the oxygen redistribution in the system. Secondly, the aforementioned research use the Phase Field model to evaluate the thermal behavior of melting fuel material but there is no available model in the open literature which accounts for the presence of liquid on the mechanical performance of the fuel.

Before to introduce the homogenization approach which has permitted the development of the thermal-mechanical model to describe the behavior of the nuclear material undergoing central melting, we need to define the main thermophysical properties of interest in the process which will be used as starting point in chapter 6: the definition of the melting interval, the enthalpy of melting and the characteristic expansion appearing at melting onset. This latter peculiarity has a first order importance in our study has it may be the driver for a signature, measurable behavior.

4.2 The melting temperature of UO_2

The melting point of UO_2 has been the object of various studies in the past 60 years. Its measurement is not a trivial problem as a consequence of the very high temperature to be characterized, the several investigation techniques which have been used and the chemical interaction of the compound with the containment or with the surrounding atmosphere. Figure 4.1 is extracted from the work of Baichi [Bai06]: it presents the historical evolution of experimental data on the measure of the melting temperature of UO_2 and highlights the strong data dispersion resulting from the mentioned difficulties.

In the early 2000's, the experts of International Atomic Energy Agency (IAEA) [IAEA05] stated as recommended value for the melting point of stoichiometric UO_2 the one proposed by Rand in [Ran78] on the basis of his set of experiments. The recommended temperature is 3120 K $\pm$ 30 K.

Then, Baichi proposed a critical review of the phase-diagram data of the U-O system in the U-UO_2 composition range in order to select the most reliable set of data. They

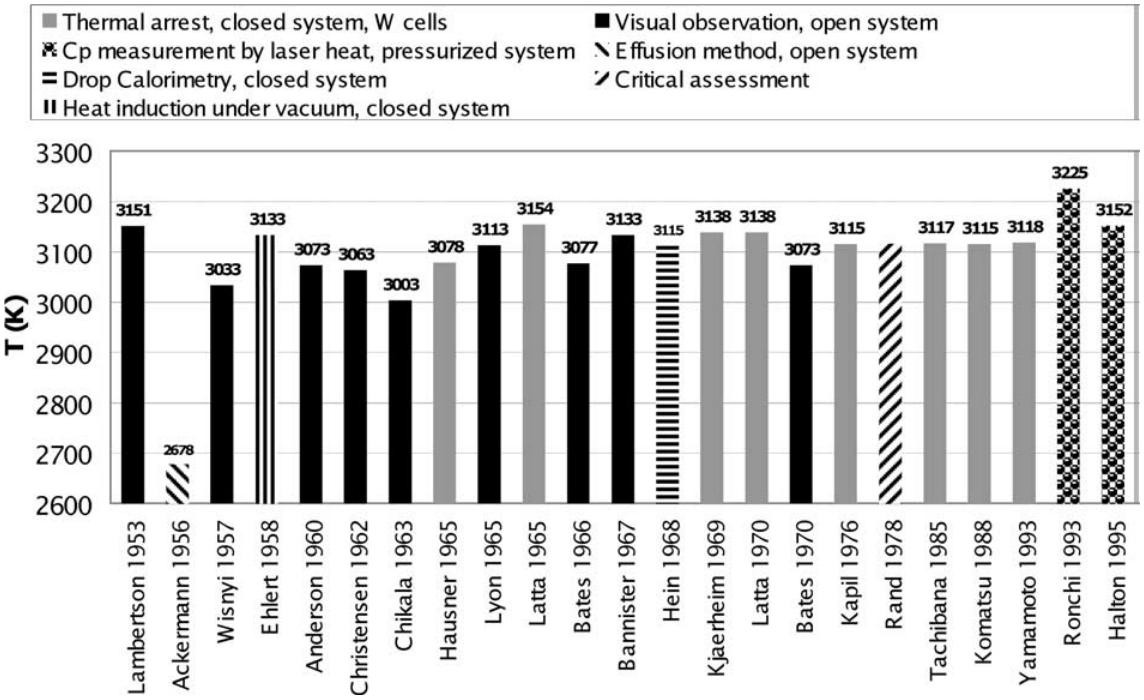

Figure 4.1 – Historical evolution of experimental data for the melting temperature of U-UO_2. The large data dispersion observed is due partly from difficulties in temperature measurements and partly from the chemical behavior of UO_2 compound, vaporization and reactivity with the containment or the atmosphere [Bai06].

retained the results obtained by a conventional investigation technique: closed systems, tungsten containers and black body pyrometry conditions [Bai06] ultimately retaining the melting temperature of Latta and Fryxell: 3138 K ± 15 K. Manara in [Man05] reexamined this value proposing to use a modern measurement technique: first, to use a subsecond pulse-heating in order to limit the time at with the investigated material is submitted to the highest temperature and undergoes enhanced reactivity; secondly, avoid the possibility of the sample interaction with the container material by means of container-less techniques, such as levitation. Also, the entire experiment took place under inert gas pressures. This technique guaranteed absence of contamination, suppression of non-congruent evaporation and appearance of influencing phenomena compromising the result. Rejecting the critics from Baichi [Man07], Manara supports a congruent melting temperature for UO_2 of 3147 K ± 20 K.

For our scope, it is important to highlight that the proposed recommended values are in good agreement with each others once the uncertainties are taken into account. In the following, we consider the melting point for congruent melting proposed by Manara and obtained by a precise modern measurement technique so:

$$T_m = 3147K \pm 20K \tag{4.1}$$

During its life in the reactor, irradiated nuclear fuel in no more a pure material and solid-liquid phase transition occurs over a melting interval characterized by a lower melting temperature, the "solidus temperature" T_{sol}, and an upper melting temperature, the "liquidus temperature" T_{liq}. During the phase transition, fuel material is an heterogeneous composition of the two phases.

According to literature [Pop00], the melting interval of the generic nuclear fuel material essentially depends on three parameters:

1. The burn-up BU, expressed in GWd/tU;
2. The ratio oxygen/metallic actinides (O/M) present in the fuel;
3. The fuel composition and especially in the case of MOX fuels, the volume fraction of PuO_2, generally identified with the symbol "y".

Those parameters impact the value of the solidus and liquidus temperatures during irradiation. The resulting melting interval is defined by the following equations:

$$T_{sol} = T_m + \Delta T_{sol} \tag{4.2}$$

$$T_{liq} = T_m + \Delta T_{liq} \tag{4.3}$$

We detail in the following how each of those parameters impact the melting process of non stoichiometric uranium dioxide imposing a modification of the solidus or liquidus temperatures.

4.2.1 Effect of the Plutonium content

The volume fraction of plutonium present in the nuclear fuel material after fabrication evolves considerably depending on the fuel material type, from 0% up to 25%. The correlation describing the evolution of melting interval of $(U,Pu)O_2$ material with the composition dates back to experimental measurements carried out in the 70's by Leon and Bailly [Lyo67] and by Aitken and Evans [Ait68]. The melting temperature of stoichiometric plutonium dioxide has been recently re-evaluated by De Bruycker [DeB10] who highlighted a difference with previous experimental characterizations of approximately 300 K. Previous measurements lead to the determination of the congruent melting point of PuO_2 of 2701 K±35 K, Carbajo and al. [Car01], and 2660 K, Guéneau and al. [Gue08]. De Bruyker discusses in his article that the previous measurements are affected by an error induced by the conventional measurement technique, which is affected by extensive interaction between the PuO_2 samples and the tungsten containment. For the characterization of the melting point of PuO_2 the experimental difficulties are the same as for UO_2. De Bruycker used the same technological solution proposed by Manara [Man07] and obtained a melting temperature for stoichiometric PuO_2 of 3017 K ± 20 K . The available recommended solidus and liquidus curves for a stoichiometric fresh fuel containing a certain volume fraction "y" of plutonium result from detailed analysis [Ada85] of experimental data [Lyo67] [Ait68] obtained previous to De Bruycker study and reported in [Pop00]:

$$\begin{cases} \text{solidus}: & \Delta T^y_{sol} = -388.1y + 30.4y^2 \\ \text{liquidus}: & \Delta T^y_{liq} = -655.3y - 336.4y^2 - 99.9y^3 \end{cases} \tag{4.4}$$

where y corresponds to the volume fraction of plutonium. This correlations are thus not completely reliable after the recent results on the melting of congruent plutonium oxide.

4.2.2 Effect of Burn-up

The effect of burn-up on the melting interval has been largely investigated in past years by [Ada85] [Yam88] [Kom88] [Kon99] and recently by Carbajo [Car01]. Carbajo critically reviewed the thermophysical properties of UO_2 and MOX fuels and reported the comparison figure 4.2 of synthesis for data from these references, taken from [Pop00].

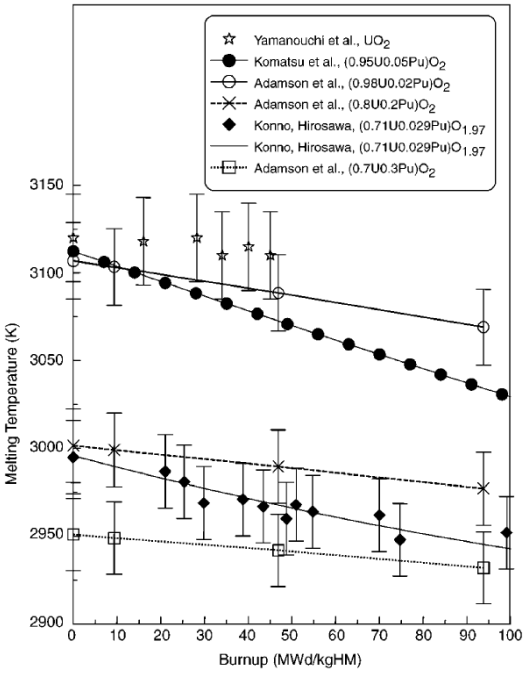

Figure 4.2 – Influence of burn-up on the melting temperature of UO_2 and of MOX fuels [Pop00].

From the figure, and in agreement with the final recommendation proposed in [Pop00], he recommended to correct the melting point of the nuclear fuel by decreasing the T_{sol}. of 0.5 K each GWd/tU:

$$\Delta T_{sol}^{Bu} = -0.5BU \tag{4.5}$$

4.2.3 Effect of oxygen to actinides ratio

According to past studies [Man05] [Kon99] and more recent analysis carried by Gueneau [Gue11], the evolution of T_{sol} and T_{liq} as a function of O/M are showed in figure 4.3. The oxygen to actinides ratio O/M of the fuel material is a highly influencing parameter: the deviation from stoichiometry induces a decrease in T_{sol} and T_{liq}. Also it progressively increases the difference between the two, thus leading the melting interval to occur over a wider range of temperatures.

The non congruent melting of UO_2 is presented in figure 4.3: for the hyperstoichiometric region we retained the experimental results obtained by Manara with the container-less measurement technique. In the hypostoichiometric region, the recommended correlations, valid in the range of $1.94 \leq O/M \leq 2.00$ are the following [Kon99]:

$$\begin{cases} \text{solidus :} & \Delta T_{sol}^{0/M} = -10^3(2.00 - O/M) \\ \text{liquidus :} & \Delta T_{liq}^{0/M} = -280(2.00 - O/M) \end{cases} \tag{4.6}$$

We have said in the introduction to this chapter that we consider for our study that melting onset in the fuel material during a very high power transient but this takes place without the failure of the cladding, which preserves its integrity during the whole transient. In a recent paper on ramped Cr-doped fuels, Riglet-Martial [Rig16] showed that the oxygen potential decreases significantly along the pellet radius during the holding period at Ramp

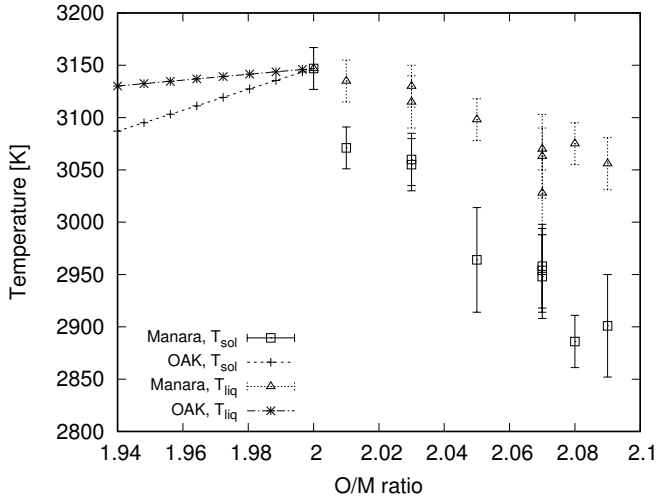

Figure 4.3 – Evolution of T_{sol} and T_{liq} as a function of the oxygen to actinides ratio in the UO_2 nuclear fuel. Data from [Man05] for hyperstoichiometric UO_2 and from [Kon99] for hypostoichiometric. The deviation from stoichiometry reduces the melting temperature and progressively increases the melting interval

Terminal Level (RTL). This phenomenon has been attributed to the oxygen thermodiffusion from the hot pellet center to the cold pellet rim region, a phenomenon which has already been observed in other type of reactors (Sodium Fast Reactor SFR and BWR power ramped fuels). Konarski in [Kon19] implemented in ALCYONE code a model to account for thermochemistry and oxygen transport in the pellet during power ramp test. From the analysis of a power ramp with 12 hours of holding period at RTL=420 W/cm he shows that the oxygen distribution is driven by the thermal gradient and during the first minutes withing the holding period the thermodiffusion induces a decrease of the O/M ratio in the central zone of the pellet. An RTL at 420 W/cm induces a maximum temperature reached in the fuel of about 2000°C. The higher temperatures reached in the case of melting onset enhances the oxygen redistribution, leading to a stronger decrease of the central stoichiometry. As the scientific community agrees that the maximum temperature is always reached in the pellet center, we can conclude that for our case, we focus on the hypostoichiometric region of the $UO_{2\pm x}$ system.

4.2.4 Definition of the melting interval

According to the previous discussion, we expect the central melting region to have an hypostoichiometric composition (O/M<2.00). The correlations to describe the evolution of solidus and liquidus temperatures as a function of the composition and of material irradiation have been proposed by [Kon99]. Under the hypothesis that the three effects can be linearly superposed, the melting interval can be expressed as follows:

$$T_{sol}(y, O/M, BU) = T_f + \Delta T^{y}_{sol} + \Delta T^{Bu}_{sol} + \Delta T^{O/M}_{sol} \tag{4.7}$$

$$T_{liq}(y, O/M, BU) = T_f + \Delta T^{y}_{liq} + \Delta T^{Bu}_{liq} + \Delta T^{O/M}_{liq} \tag{4.8}$$

where all the symbols have already been defined.

4.3 Enthalpy of melting

The enthalpy of melting UO_2 is proposed by Fink in [Fin00] at the temperature of 3120 K and amounts to 70 ± 4 kJ/mol. A difference is reported from the previous recommended value of 74.8 kJ/mol proposed in a previous review in 1981 [Fin81] and recommended by Harding in [Har89] even though the two values are coherent if uncertainties from the experimental characterization are accounted.

4.4 Thermal discontinuity at melting

Solid-liquid phase transition of UO_2 is characterized by a discontinuity in material density. According to the critical review recently proposed by Fink in [Fin00], the recommended equations to evaluate the linear thermal expansion of solid UO_2 are the ones proposed by Martin in [Mar88]:
For 273 K ≤ T ≤ 923 K

$$L(T) = L(T_0)(9.973 \cdot 10^{-1} + 9.082 \cdot 10^{-6}T - 2.705 \cdot 10^{-10}T^2 + 4.391 \cdot 10^{-13}T^3) \quad (4.9)$$

For 923 K ≤ T ≤ 3120 K

$$L(T) = L(T_0)(9.9672 \cdot 10^{-1} + 1.179.10^{-5}T - 2.429 \cdot 10^{-9}T^2 + 1.219 \cdot 10^{-12}T^3) \quad (4.10)$$

The $L(T)$ and $L(T_0)$ are the length at the generic temperature T and at $T_0 = 273\ K$, respectively.
The density of the solid UO_2 as a function of temperature can be calculated from:

$$\rho_s(T) = \rho_s(T_0)\left(\frac{L(T_0)}{L(T)}\right)^3 \quad (4.11)$$

where $\rho_s(T_0)$ is the density of stoichiometric solid UO_2 at 273 K, amounting to $10.963{\cdot}10^3$ kg/m^3.

For what it is concerned with the liquid UO_2, Fink recommended the equation given by Breitung and Reil [Bre90], obtained from in-pile measurements from 3120 K to 7600 K:

$$\rho_l(T) = 8.860 - 9.285 \cdot 10^{-4}(T - 3120) \quad (4.12)$$

where $\rho_l(T)$ is obtained in Mg/m^3 and the temperature T is in Kelvin. The recommended density at melting point, amounting to 8.86 Mg/m^3 is the one initially recommended by Drotning [Dro81] and confirmed by Fink.

According to the presented recommended correlations, density of solid UO_2 at melting temperature amounts to 9560 kg/m^3± 40 kg/m^3 and the discontinuity at melting point for a stoichiometric uranium dioxide amounts to 700 kg/m^3± 40 kg/m^3.
This decrease of about the 8% of material density taking place at melting has fundamental importance in our research because it results into a local volume expansion $\frac{\Delta V}{V}_m$ corresponding to:

$$\frac{\Delta V}{V}_m = -\frac{\Delta\rho}{\rho_m} \quad (4.13)$$

where $\Delta\rho = \rho_{sol} - \rho_{liq}$ is the difference in density between the solid and liquid UO_2 at melting temperature and $\rho_m = \rho_{sol}$. The characteristic expansion occurring at melting and associated to the discontinuity in material density, amounts to about 7.32% ± 0.39% according to Fink recommendation.

4.5 Concluding remarks

In this chapter we have presented the fundamental aspects to be taken into account to model the solid-liquid phase transition in the nuclear fuel material. The melting temperature for stoichiometric fuel material which shall be retained in this work is the one resulting from the most recent works carried out by Manara [Man05]: 3147 K ± 20 K.
Taking into account the lack of reliability in present available correlations for the effect of plutonium content in the melting point and as we focus on UO_2 type fuel, we can assume that the PuO_2 volume fraction is negligible. Even though the plutonium composition is considered null in this work, the deviation from stoichiometry and the burn-up induce the appearance of a non-congruent melting point: the fuel does not melt at a constant temperature but a melting interval can be identified. This is characterized by a solidus T_{sol} and a liquidus T_{liq} temperatures. The stoichiometry acts on the melting interval in a different way if the region where melting takes place has a hypostoichiometric or hyperstoichiometric composition. The oxygen distribution during irradiation is strongly temperature dependent. Researches [Rig16] [Kon19] showed that the central zone of the pellet, which experiences the highest temperatures, is concerned by a hypostoichiometric composition. For this, in the following we retain the correlation equations for T_{sol} and T_{liq} valid for O/M<2.00.
We have then introduced the enthalpy of fusion and discussed the discontinuity in material density which appears at melting onset. This shoot in density from solid to liquid generates a characteristic isotropic expansion which shall be considered in the following definition of the thermal-mechanical model.

Chapter 5

Methodology: Homogenization approach

The melting fuel material is considered in the following as an heterogeneous material where liquid inclusions nucleates in the solid matrix. To develop the thermal-mechanical model of the melting fuel material we have applied the homogenization approach.
In the following we focus on the analytic and static homogenization methods which will be later applied to the nuclear fuel material. As we said, the solid matrix presents at high temperatures an elasto-viscoplastic behavior. Considering separately the elastic and the viscoplastic contribution to the total deformation, we shall thus start from introducing the homogenization approach to linear elastic system and than discuss the non linear behavior. The both are presented in general terms and shall be applied in the next chapter to the nuclear fuel.

Contents

5.1 The homogenization principle

A composite materials is an heterogeneous system made of a matrix and a second phase, or more. This may be introduced during the fabrication process to improve the performance of the material (increase tightness, flexibility etc...) or it may result from a thermal process, like in our case the melting process. We can distinguish at least two scales: the macroscopic scale, the one of the material as a whole, and the microscopic one, where the heterogeneity of the material is clearly visible. At the heterogeneity scale, each phase presents specific properties determining its peculiar behavior. The deriving macroscopic thermal-mechanical behavior depends on the complex interactions between the constituting phases.
In this frame, the homogenization approach allows to move from the heterogeneous real material to an equivalent homogeneous one, which behaves at the macroscopic scale just like the real one. The scheme shown in figure 5.1 represents the mentioned principle: from the real component Ω we identify a representative volume $\mathcal{V}$, which behavior is representative of the macroscopic material. This is made of two phases, the matrix (1) and the inclusions (2), having different behaviors $(\mathbb{C}_1, \mathbb{C}_2)$ each being characterized by a specific spatial distribution (x_1, x_2). By homogenization, an equivalent material is defined, having an effective macroscopic behavior $\mathbb{C}^{hom}$ equivalent to the real one.

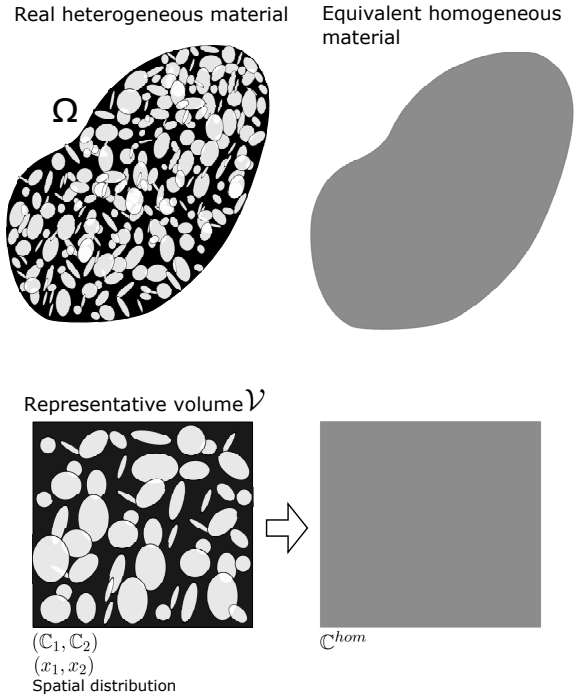

Figure 5.1 – Homogenization principle

The homogenization theory is based on three steps:

- **Representation**: Determine the representative volume $\mathcal{V}$ which behavior is representative of the whole heterogeneous structure;
- **Localization**: Determine the mechanical response of the representative volume $\mathcal{V}$ in terms of stress and strain fields;
- **Homogenization**: Determine the behavior of the equivalent homogeneous material.

In this document we suppose to a priori know the distribution of heterogeneities, their shape, their mechanical and thermal characteristics and we look for the macroscopic mechanical response of the material by determining its effective (or homogeneous) properties.

Our aim is not to present an exhaustive synthesis of the homogenization theory, for this we please the reader to refer to the mentioned references, but we focus on the theoretical knowledge on the homogenization of the mechanical behavior of porous material which is later applied to the elasto-viscoplastic nuclear fuel material. For this, we first recall some fundamental knowledge on the theory of effective behavior for linear elastic material and then we resume some fundamental principles in the evaluation of the effective behavior on non linear materials.

5.1.1 Theory of effective behavior

The macroscopic stress generated in a body $\tilde{\boldsymbol{\sigma}}$ and the associated macroscopic strain $\tilde{\varepsilon}$ result from a local stress $\boldsymbol{\sigma}(\boldsymbol{x})$ and strain field $\varepsilon(\mathbf{u}(\mathbf{x}))$, the latter associated to the microscopic displacement $\boldsymbol{u}(\boldsymbol{x})$, calculated in the representative volume $\mathcal{V}$. The local problem is defined by taking into account the equilibrium equation, the mechanical behavior of the material and the local boundary conditions.
If the mechanical behavior of the medium is elastic and isotropic, the constitutive equation is expressed as a function of the stiffness modulus $\mathbb{C}$ which can be written in the following form:

$$\mathbb{C} = 3K\mathbb{J} + 2G\mathbb{K} \tag{5.1}$$

where K and G are the bulk and shear modulus, respectively; $\mathbb{J} = \frac{1}{3}\delta_{ij} \bigotimes \delta_{ij}$ and $\mathbb{K} = \mathbb{I} - \mathbb{J}$ with $\mathbb{I}$ the 4^{th} order identity tensor. $\mathbb{J}$ and $\mathbb{K}$ are the projections of 4^{th} order tensors along the isotropic and deviatoric direction.
Imposing the condition of homogeneous stress on the surface of $\mathcal{V}$, for an heterogeneous elastic body having modulus $\mathbb{C}$(x), varying in the system, the local problem can be written in to following form:

$$(P_{CH}) : \begin{cases} div(\boldsymbol{\sigma}(\boldsymbol{x})) = 0, \quad \boldsymbol{\sigma}(\boldsymbol{x}) = \mathbb{C}(x) : \varepsilon(\boldsymbol{u}(\boldsymbol{x})) \quad in\ \mathcal{V}, \\ \boldsymbol{\sigma}(\boldsymbol{x}) \cdot \boldsymbol{n}(\boldsymbol{x}) = \tilde{\boldsymbol{\sigma}} \cdot \boldsymbol{n}(\boldsymbol{x}) \quad on\ \partial\mathcal{V} \end{cases} \tag{5.2}$$

Where $\boldsymbol{n}(\boldsymbol{x})$ is the normal vector to the boundary of volume $\mathcal{V}$ and $\mathbf{x} = (x_1, x_2, x_3)$ a generic point located in $\mathcal{V}$. We can also impose at the boundary the condition of homogeneous strain, so that the local problem can be written as follows:

$$(P_{DH}) : \begin{cases} div(\boldsymbol{\sigma}(\boldsymbol{x})) = 0, \quad \boldsymbol{\sigma}(\boldsymbol{x}) = \mathbb{C}(x) : \varepsilon(\boldsymbol{u}(\boldsymbol{x})) \quad in\ \mathcal{V}, \\ \boldsymbol{u}(\boldsymbol{x}) = \tilde{\boldsymbol{\varepsilon}} \cdot \boldsymbol{x} \quad on\ \partial\mathcal{V} \end{cases} \tag{5.3}$$

With $\boldsymbol{\sigma}$ and $\boldsymbol{u}$ being solutions of (P_{CH}), the **effective flexibility tensor** $\tilde{\mathbb{L}}$ links the macroscopic average strain $\tilde{\boldsymbol{\varepsilon}}$ to the macroscopic average stress $\tilde{\boldsymbol{\sigma}}$ [Bor01]:

$$\tilde{\varepsilon} = \langle \varepsilon(\mathbf{u}) \rangle = \tilde{\mathbb{L}} : \langle \sigma \rangle = \tilde{\mathbb{L}} : \tilde{\sigma} \tag{5.4}$$

where the symbol $\langle . \rangle$ notes the average on volume $\mathcal{V}$.

With $\boldsymbol{\sigma}$ and $\boldsymbol{u}$ being instead solutions of (P_{DH}), the **effective stiffness tensor** $\tilde{\mathbb{C}}$ links the macroscopic average stress $\tilde{\boldsymbol{\sigma}}$ to the macroscopic average strain $\tilde{\boldsymbol{\varepsilon}}$ [Bor01]:

$$\tilde{\sigma} = \langle \sigma(\mathbf{u}) \rangle = \tilde{\mathbb{C}} : \langle \varepsilon \rangle = \tilde{\mathbb{C}} : \tilde{\varepsilon} \tag{5.5}$$

There exist two main categories of methods to evaluate the effective moduli $\mathbb{C}$ and $\mathbb{L}$: the mean-field methods and the full field methods. The full field methods require a complete and extensive knowledge of the microstructure: mechanical properties of phases, geometry of inclusions and their spatial distribution. This permits to calculate the stress and strain field in every point of the microstructure by means of numerical methods (finite elements, FFT methods, etc). The mean-field methods are analytical and statistical approaches which permits to obtain an approximated or estimated evaluation by the effective behavior of the heterogeneous medium without the need to know its microstructure in detail. In this work, we have focused on the mean-field approach to propose the model to describe the mechanical behavior of melting fuel material.

5.1.2 Voigt and Reuss limits

Voigt approximation is based on the hypothesis that strains are uniform in $\mathcal{V}$, so that the tensor of effective moduli is approximated as follows:

$$\mathbb{C}^V = \langle \mathbb{C} \rangle \tag{5.6}$$

This rarely leads to accurate evaluation of the effective behavior of the heterogeneous system but it can be demonstrated that [Bor01]:

$$\frac{1}{2}\tilde{\varepsilon} : \mathbb{C} : \tilde{\varepsilon} \leqslant \frac{1}{2}\tilde{\varepsilon} : \mathbb{C}^V : \tilde{\varepsilon} \tag{5.7}$$

Where $\frac{1}{2}\tilde{\varepsilon} : \mathbb{C} : \tilde{\varepsilon}$ is the elastic strain energy of the equivalent system. This means that **the Voigt approximation is an upper limit for the evaluation of the effective stiffness modulus**.

On the other hand, **Reuss approximation is an upper limit for the equivalent flexibility tensor**. By imposing that stresses are uniform in the volume $\mathcal{V}$, it result that the effective flexibility tensor is:

$$\mathbb{L}^R = \langle \mathbb{L} \rangle \tag{5.8}$$

And it can be demonstrated that the elastic energy associated to the equivalent stress respects the following inequality:

$$\frac{1}{2}\tilde{\sigma} : \mathbb{L} : \tilde{\sigma} \leqslant \frac{1}{2}\tilde{\sigma} : \mathbb{L}^R : \tilde{\sigma} \tag{5.9}$$

Voigt and Reuss approximations result from a simple hypothesis about the distribution of stress and strain in the body and lead to little accuracy in the derived behavior. They are important because they define the limit for the existence and evolution of more fine estimations which we shall define in the following paragraph.

In the case of an heterogeneous material having two isotropically distributed phases, where we can define f_1 the volume fraction of the matrix and f_2 the volume fraction of inclusions, so that $f_1 + f_2 = 1$, the limit value for the equivalent bulk modulus $\tilde{K}$ and equivalent shear modulus $\tilde{G}$ are the following:

$$\begin{aligned} \tilde{K}^V &= f_1 K_1 + f_2 K_2 \\ \tilde{G}^V &= f_1 G_1 + f_2 G_2 \\ \frac{1}{\tilde{K}^R} &= \frac{f_1}{K_1} + \frac{f_2}{K_2} \\ \frac{1}{\tilde{G}^R} &= \frac{f_1}{G_1} + \frac{f_2}{G_2} \end{aligned} \tag{5.10}$$

5.1.3 Statistical approach

Based on the fundamental resolution of the single inclusion problem proposed by Eshelby [Esh57], **the Hashin and Shtrikman model** is based on the evaluation of the equivalent behavior of a model structure, named the Hashin assembly of composite spheres, which is meant to be representative for a medium made of two phases. The composite spheres are heterogeneous spheres having two components, each identical to the others, having internal inclusion of radius a_1 and external radius b_1. The volume fraction of inclusions is $f = (a_1/b_1)^3$. The hypothetical structure has representative volume $\mathcal{V}$ and it is fulfilled with composite spheres of progressive smaller dimensions (e.g. $b_{i+1} < b_i$) up to the complete fulfillment of $\mathcal{V}$, all being characterized by the same volume fraction f. In the model developed by Hashin, each composite sphere is made of a linear elastic material [Has63].

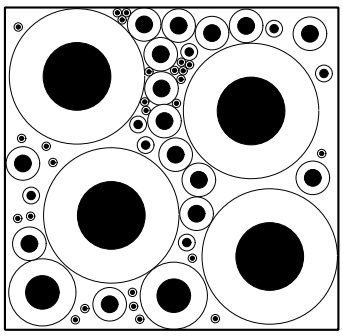

Figure 5.2 – Representation of the Hashin assembly of composite spheres [Has63]

The estimation is obtained by taking as fundamental hypothesis that phase distribution in the medium is known only in statistical terms.
They showed that the equivalent behavior of a two-phase material where phases are isotropically distributed is expressed as follows:

$$\tilde{\mathbb{C}}^{HS} = \left[\sum_{r=1}^{2} f_r(\mathbb{C}^* + \mathbb{C}_r)^{-1}\right] - \mathbb{C}^* \tag{5.11}$$

where $\mathbb{C}^*$ is the reference material. The result of the estimation depends on this choice.
When the two phases are isotropic and the reference material is consequently isotropic, the Hashin and Shtrikman tensor is isotropic and can be expressed as a function of the equivalent shear modulus $\tilde{G}$ and of the equivalent bulk modulus $\tilde{K}$:

$$K^{HS} = \left[\sum_{r=1}^{2} \frac{f_r}{K^* + K_r}\right]^{-1} - K^* = K_1 + f_2 \frac{K_2 - K_1}{1 + f_1 \dfrac{K_2 - K_1}{K^* + K_1}} \tag{5.12}$$

$$G^{HS} = \left[\sum_{r=1}^{2} \frac{f_r}{G^* + G_r}\right]^{-1} - G^* = G_1 + f_2 \frac{G_2 - G_1}{1 + f_1 \dfrac{G_2 - G_1}{G^* + G_1}} \tag{5.13}$$

where K^* and G^* are the mechanical properties characterizing the reference medium. Noting with index "0" the reference medium, they are defined as follows $K^* = \dfrac{4}{3}G_0$ and $G^* = \dfrac{G_0}{6}\dfrac{9K_0 + 8G_0}{K_0 + 2G_0}$.

The Hashin and Shtrikman limites are defined as the largest values that properties can have for a two phase medium so that:

$$\tilde{\mathbb{C}} \leqslant \tilde{\mathbb{C}}^{HS+} = \tilde{\mathbb{C}}^{HS}(\{3\ sup(K_1, K_2), 2\ sup(G_1, G_2)\}) \tag{5.14}$$

$$\tilde{\mathbb{C}} \geqslant \tilde{\mathbb{C}}^{HS-} = \tilde{\mathbb{C}}^{HS}(\{3\ inf(K_1, K_2), 2\ inf(G_1, G_2)\}) \tag{5.15}$$

Under the hypothesis that $K_1 > K_2$ and $G_1 > G_2$, the equivalent homogeneous properties are restricted by the following **limits**:

$$K^{HS-} \leqslant \tilde{K} \leqslant K^{HS+}$$

$$with: \begin{cases} K^{HS+} = K_1 + \dfrac{f_2}{\dfrac{1}{K_2 - K_1} + \dfrac{3f_1}{3K_1 + 4G_1}} \\ K^{HS-} = K_2 + \dfrac{f_1}{\dfrac{1}{K_1 - K_2} + \dfrac{3f_2}{3K_2 + 4G_2}} \end{cases} \tag{5.16}$$

$$G^{HS-} \leqslant \tilde{G} \leqslant G^{HS+}$$

$$with: \begin{cases} G^{HS+} = G_1 + \dfrac{f_2}{\dfrac{1}{G_2 - G_1} + \dfrac{6f_1(K_1 + 2G_1)}{5G_1(3K_1 + 4G_1)}} \\ G^{HS-} = G_2 + \dfrac{f_1}{\dfrac{1}{G_1 - G_2} + \dfrac{6f_2(K_2 + 2G_2)}{5G_2(3K_2 + 4G_2)}} \end{cases} \tag{5.17}$$

Mori-Tanaka scheme

The Mori-Tanaka scheme is defined for an heterogeneous medium where the elastic inclusions are istropically distributed in the linear elastic matrix and behave as each of them was totally isolated in an infinite matrix, as represented in figure 5.3. In this case, the equivalent homogeneous stiffness tensor $\tilde{\mathbb{C}}^{MT} = (3\tilde{K}^{MT}, 2\tilde{G}^{MT})$ is obtained from the Hashin and Shtrikman evaluation by imposing as reference medium the matrix. The following equations are obtained [Mor73]:

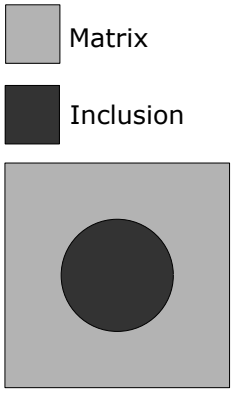

Figure 5.3 – Schematic representation of the MT estimation

$$K^{MT} = K_1 + \frac{f_2(K_2 - K_1)(K^* + K_1)}{K^* + K_1 + f_1(K_2 - K_1)} \tag{5.18}$$

with $K^* = \dfrac{4}{3}G_1$

$$G^{MT} = G_1 + \frac{f_2(G_2 - G_1)(G^* + G_1)}{G^* + G_1 + f_1(G_2 - G_1)} \tag{5.19}$$

with $G^* = \dfrac{G_1}{6}\dfrac{9K_1 + 8G_1}{K_1 + 2G_1}$.

The basic hypothesis of the model requires that the volume fraction of inclusion is small. It derives that this scheme is only valid as long as the volume fraction of inclusions is sufficiently small for this hypothesis to stand. Generally the Mori-Tanaka scheme is applied for a maximum volume fraction of inclusions at $f_2 = 20\%$.

Self-Consistent scheme

The self consistent scheme is based on the fundamental hypothesis that inclusions are surrounded by the equivalent medium that wants to be evaluated, so that the reference medium is the equivalent one, as represented in figure 5.4. The effective stiffness modulus is obtained through the Hashin and Shtrikman model solving the following implicit problem:

$$\mathbb{C}^{SC} = \mathbb{C}^{HS}(\mathbb{C}^{SC}) \tag{5.20}$$

The stiffness tensor being solution of the problem is the Self-Consistent estimation of the effective behavior.
We take as example a two phase isotropic medium, which phases are isotropic and incompressible. From the resolution of equation 5.20 we obtain that the shear modulus results from resolution of the second order equation:

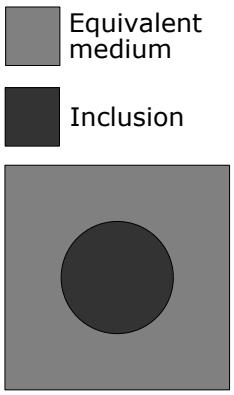

Figure 5.4 – Schematic representation of the AC estimation

$$\left(\frac{\tilde{G}^{SC}}{G_1}\right)^2 - \left(\frac{5f-2}{3}\frac{G_2}{G_1} - \frac{5f-3}{3}\right)\frac{\tilde{G}^{SC}}{G_1} - \frac{2}{3}\frac{G_2}{G_1} = 0 \tag{5.21}$$

where we imposed $f_2 = f$ ans $f_1 = 1 - f_2 = 1 - f$.
When the inclusions are pores fulfilled with incompressible liquid, $G_2 \to 0$ and the $\tilde{G}^{SC} = \left(1 - \frac{5}{3}f\right) G_1$ when $c < 3/5$ and it goes to zero for volume fraction $c \geqslant 0$.
In the case when the inclusions are made of a stiff material for which $G_2 \to +\infty$, the Self-Consistent estimation result into $\tilde{G}^{SC} = 2G_1/(2-c)$ when $c < 2/5$ while it goes to $+\infty$ for $c \geqslant 2/5$.
These two examples, which will be useful is our case, show that the Self-Consistent estimation evaluates two percolation thresholds. When more than 60% of pores fulfilled with incompressible liquid appear in the material , the heterogeneous material loses the capability to resist to a macroscopic loading (incoherent behavior). Besides, 40% of stiff inclusions is sufficient to make the material resist to any macroscopic strain [Bor01].

5.2 Application to non linear materials: the non linear extension

In the previous section we have discussed the homogenization approach for the behavior of an heterogeneous material made of linear elastic components. In this section we present the theoretical background about the effective mechanical behavior of an heterogeneous medium having non linear components. In this case, it is useful to describe the behavior of components in terms of a thermodynamic potential, generally convex. As the nuclear fuel material presents a viscoplastic behavior, we shall present here only the general theory related to the creep law. Then, we present the approach applied in the following chapter, the non linear extension of a linear model. For this, we introduce the classical secant method, which shows to be insufficient for the several studies. So, we move to the modified secant method which is the selected approach to develop the melting model in the nuclear fuel material.
For an exhaustive dissertation about the homogenization of non linear composites, the reader shall find the main references on the topic in the mentioned bibliography.

5.2.1 Microscopic and macroscopic thermodynamic potential

The mechanical behavior of a non linear material can be described in terms of a convex thermodynamic potential ϕ linking the stress field to the strain or strain rate field so that:

$$\boldsymbol{\sigma} = \frac{\partial \phi}{\partial \varepsilon}(\varepsilon) \tag{5.22}$$

This equation can be turned in terms of a dual expression of the thermodynamic potential, which is expressed as follows:

$$\varepsilon = \frac{\partial \psi}{\partial \sigma}(\sigma) \tag{5.23}$$

The thermodynamic potential $\psi(\sigma)$ is the complementary energy of the material. Indeed the thermodynamic potential $\phi(\varepsilon)$ is the area "under the curve" in the (ε, σ) diagram. In a similar way, the dual dissipative potential $\psi(\sigma)$ is the area below the curve in the (σ, ε) diagram. Figure 5.5 represents the reciprocal relation linking the two potentials, which is expressed in the following terms:

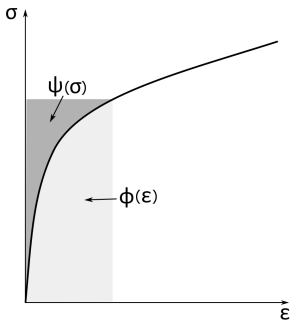

Figure 5.5 – Non linear mechanical behavior of a material, representation of the dissipative thermodynamic potential $\phi(\varepsilon)$ and its dual form $\psi(\sigma)$.

$$\psi(\sigma) + \phi(\varepsilon) = \sigma : \varepsilon \tag{5.24}$$

For a viscoplastic material the mechanical behavior is generally expressed in terms of a strain rate, for which the previous relations are valid, it is sufficient to replace to strain field with the strain rate one.
In the case of an heterogeneous material, the mechanical behavior of the phase r within the representative volume $\mathcal{V}$ is locally defined by a local thermodynamic potential ϕ_r and its dual form ψ_r. In the case under analysis for this thesis, the system is submitted to a macroscopic loading $\tilde{\sigma}$, homogeneous at system boundary as defined in section 5.1.1. The local problem to be solved is the following:

$$\begin{cases} div(\boldsymbol{\sigma}(\boldsymbol{x})) = 0 \quad in\ \mathcal{V} \\ \boldsymbol{\sigma}(\boldsymbol{x}) = \dfrac{\partial \phi_r}{\partial \dot{\boldsymbol{\varepsilon}}}(\boldsymbol{x}, \dot{\boldsymbol{\varepsilon}}(\boldsymbol{x})) \quad \forall\ \boldsymbol{x} \in \mathcal{V}_r, \\ \dot{\boldsymbol{u}}(\boldsymbol{x}) = \dot{\tilde{\varepsilon}} \cdot \boldsymbol{x} \quad on\ \partial\mathcal{V} \end{cases} \tag{5.25}$$

Where $\mathcal{V}_r$ is the volume within $\mathcal{V}$ occupied by the generic phase r. The local strain rate field meets the compatibility condition:

$$\dot{\boldsymbol{\varepsilon}} = \frac{1}{2}(\nabla \dot{\boldsymbol{u}} + \nabla \dot{\boldsymbol{u}}^T) \tag{5.26}$$

The solution of the local problem $\dot{\boldsymbol{u}}$ and $\boldsymbol{\sigma}$ has the following variational properties [Bor01]:

$$\langle \phi(\dot{\boldsymbol{\varepsilon}}(\dot{u})) \rangle = \inf_{\dot{\mathbf{v}} \in \mathcal{K}(\dot{\tilde{\boldsymbol{\varepsilon}}})} \langle \phi(\dot{\boldsymbol{\varepsilon}}(\dot{v})) \rangle \tag{5.27}$$

where

$$K(\dot{\tilde{\varepsilon}}) = \{ \dot{\mathbf{v}} = \dot{\tilde{\varepsilon}} \cdot \boldsymbol{x}\ on\ \partial\mathcal{V} \} \tag{5.28}$$

Alternatively, imposing the boundary condition of uniform traction, the variational properties are the following:

$$\langle \psi(\sigma) \rangle = \inf_{\dot{\tau} \in \mathcal{S}(\dot{\tilde{\boldsymbol{\sigma}}})} \langle \psi(\tau) \rangle \tag{5.29}$$

where

$$S(\tilde{\boldsymbol{\sigma}}) = \{\tau, div(\tau) = 0 \ in \ \mathcal{V}, \ \tau \cdot \boldsymbol{n} = \tilde{\boldsymbol{\sigma}} \cdot \boldsymbol{n} \ on \ \partial\mathcal{V}\} \tag{5.30}$$

The macroscopic behavior of the composite is also governed by two macroscopic potentials defined as follows:

$$\Psi(\tilde{\boldsymbol{\sigma}}) = \inf_{\dot{\tau} \in \mathcal{S}(\tilde{\boldsymbol{\sigma}})} \langle \psi(\tau) \rangle \quad \Phi(\dot{\tilde{\varepsilon}}) = \inf_{\dot{\boldsymbol{v}} \in \mathcal{K}(\dot{\tilde{\boldsymbol{\varepsilon}}})} \langle \phi(\dot{\boldsymbol{\varepsilon}}(\dot{v})) \rangle \tag{5.31}$$

Then the macroscopic behavior of the material is defined [Lem01]:

$$\dot{\tilde{\varepsilon}} = \frac{\partial \Psi}{\partial \tilde{\sigma}}(\tilde{\sigma}), \quad \tilde{\sigma} = \frac{\partial \Phi}{\partial \dot{\tilde{\varepsilon}}}(\dot{\tilde{\varepsilon}}) \tag{5.32}$$

5.2.2 Principle of the non-linear extension

We have seen that the evaluation of the macroscopic behavior of the heterogeneous medium is based on the resolution of the local problem at the scale of the representative volume $\mathcal{V}$. The exact resolution of this problem is not a trivial subject even in the linear case but in the case of non linear behavior of components, this is more complex particularly because of the non validity of the superposition principle. In order to take advantage of the knowledge developed in the linear domain, it is fundamental to make a linear approximation of the non linear local behavior of the material. The aim of this operation is to replace the non linear relations in $\mathcal{V}$ with linear ones, always defined in $\mathcal{V}$, to which the linear homogenization approach can be applied to determine the effective behavior of the medium. The linear local problem resulting from the linearization step is strictly equivalent to the homogenization problem of a linear equivalent material, named the "comparison linear composite material".
The linearization introduces complementary equations which define the non linear nature of the material behavior. The number of variables in these complementary relations is strongly reduced and they can generally be solved by numerical iterative methods. In some, simple cases, even an analytical method can be used to obtain a solution.
The principle of the non linear extension is represented in figure 5.6.

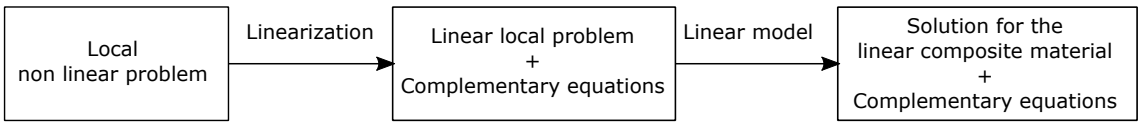

Figure 5.6 – General principle of non linear extension [Bor01]

5.2.3 Linearization methods: the secant method

The relation between stress and strain can be locally defined in each point $\boldsymbol{x} \in \mathcal{V}$ in the following form:

$$\boldsymbol{\sigma}(\boldsymbol{x}) = \mathbb{C}^{sct}(\boldsymbol{x}, \dot{\boldsymbol{\varepsilon}}(\boldsymbol{x})) : \dot{\boldsymbol{\varepsilon}}(\boldsymbol{x}) \tag{5.33}$$

where the $\mathbb{C}^{sct}$ it the local secant stiffness tensor, which depends on the local strain $\dot{\boldsymbol{\varepsilon}}(\boldsymbol{x})$ in the considered point $\boldsymbol{x}$ through the potential of the local phase. It exist a second family of linearization methods which is not used in this work: the affine one.
According to the classical extension of the secant method, the secant stiffness tensor

is related to the average strain field in the comparison linear material obtained by the retained linear model. In this frame we have:

$$\forall\ r \quad \mathbb{C}_r^{sct} = \mathbb{C}_r^{sct}(\langle\dot{\boldsymbol{\varepsilon}}\rangle_r) \tag{5.34}$$

This approach is particularly adapted for materials where the strain is homogeneous in the phase r but in general terms heterogeneity in the phase cannot be neglected [Bor01] and can lead to unrealistic solution of the problem.
A good measure of the heterogenity of the material is expressed by the second order moment of the equivalent strain field in the phase [Bor01]. By means of this characterization of the local heterogeneous behavior in the phase, the classical secant method can be modified in the following form. In the case of isotropic components, the complementary relation of equation (5.34) is expressed in the form:

$$\forall\ r \quad \mathbb{C}_r^{sct} = 3K_r\mathbb{J} + 2G_r^{sct}(\langle\dot{\boldsymbol{\varepsilon}}\rangle_r)\mathbb{K} \tag{5.35}$$

According to the modified secant method [Suq95], this relation is replaced by:

$$\forall\ r \quad \mathbb{C}_r^{sct} = 3K_r\mathbb{J} + 2G_r^{sct}(\sqrt{\langle\varepsilon_{eq}^2\rangle_r})\mathbb{K} \tag{5.36}$$

where the second order moment of the equivalent strain fiels $\sqrt{\langle\varepsilon_{eq}^2\rangle_r}$ can be evaluated by the following relations [Bor01]:

$$\langle\varepsilon_{eq}^2\rangle_r = \frac{1}{3f_r}\tilde{\varepsilon}_H^2\frac{\partial\tilde{K}}{\partial G_r} + \frac{1}{f_r}\tilde{\varepsilon}_{eq}^2\frac{\partial\tilde{G}}{\partial G_r} \tag{5.37}$$

$$\langle\sigma_{eq}^2\rangle_r = \frac{3}{f_r}\tilde{\sigma}_H^2\frac{\partial(1/\tilde{K})}{\partial(1/G_r)} + \frac{1}{f_r}\tilde{\sigma}_{eq}^2\frac{\partial(1/\tilde{G})}{\partial(1/G_r)} \tag{5.38}$$

5.3 Conclusions

We have presented in this chapter the general homogenization approach to be applied to a composite material presenting two phases in order to define the behavior of a homogeneous material, macroscopically equivalent to the composite one. We have focused on the analytical means field methods which are the ones which shall be used for the development of the thermal-mechanical model for the melting fuel material. We have considered the composite material to present an isotropic macroscopic behavior and we have assumed that the localization d representation phases are a priori known. The first part has concerned two phases presenting a pure elastic behavior and we have discussed the limits and estimations to evaluate the effective behavior of the equivalent medium. Then, in the second part, we have considered the case in which one of the components presents a non linear behavior. For this we have used the non linear extension method and the secant linearization approach to evaluate the effective behavior of the non linear composite material. The presented theory is applied in the following chapter to the evaluation of the equivalent behavior of the melting fuel material.

Chapter 6

The thermal-mechanical model of fuel at melting onset

This chapter focuses on the development of the thermal-mechanical model for a hyposto-ichiometric uranium-dioxide irradiated in a PWR reactor. In section 6.1 we define the basic hypothesis of the model. Then, once we have defined the problem in section 6.2, we evaluate the equivalent thermal-elastic behavior in 6.3 and the equivalent viscoplastic behavior in 6.4. Finally, we propose to validate the modeling principle by defining a simple test case and analyzing the macroscopic physical behavior obtained solving the problem by means of the finite element code Cast3m in 6.5.

Contents

6.1 Hypothesis

We have discussed in the previous chapter 4 that melting onsets in the fuel pellet center, where the temperature is the highest and the oxygen distribution leads to an hypostoichiometric composition. For the development of the following model we made some general hypothesis which are reported in the following:

1. A porous fraction is present in the solid fuel material, as it has been described in part I, chapter 2.2. We assume as a first order approximation that, due to the high temperatures reached by the fuel at melting onset, porosity in the central region can be neglected. This results into the fact that the solid material can be modeled like an isotropic incompressible material having elastic and viscoplastic behavior;

2. Pellet has cracked since the beginning of the irradiation. Since the high temperatures originating at the melting onset, we consider that in the central zone there are no fissures that could permit the displacement of the liquid fraction;

3. The liquid progressively appears in the solid matrix in the form of spherical inclusions, randomly distributed in the latter. The composite melting material can be thus assumed to be isotropic and the liquid phase can be completely described by its volume fraction, named x_{liq};

4. We consider that the liquid UO_2 has elastic behavior, that can be described by a stiffness modulus $\mathbb{C}_{liq} = (3K_{liq}, 2G_{liq})$. Also, we suppose that it can be considered as an ideal Newtonian fluid. Its bulk modulus $K_l \to \infty$ and the shear modulus $G_{liq} \to 0$.

It can be easily verified that this last hypothesis is in agreement with material properties of stoichiometric liquid UO_2 at melting point: by the equation proposed by Woodley and presented by Fink in [Fin00] we evaluate the shear viscosity of uranium dioxide at melting temperature, which is related to the tendency of a fluid to deform when submitted to a shear stress, for instance. For liquid UO_2 at melting point it amounts to 4.32 mPa.s:

$$\mu_l(T_f) = 0.988e^{4620/T_f} = 4.32 \quad [\text{mPa.s}] \tag{6.1}$$

where T_f is the melting temperature of stoichiometric UO_2, 3147 K. Solid material shear modulus is evaluated at melting onset by equation (2.17). At the congruent melting point this $G_{sol}(T_m)$ is in the order of the GPa.

The thermal-mechanical behavior of the solid has been exhaustively described in the previous sections: we consider its elastic properties, obtained according to equation (2.17), to remain constant and equal to the value obtained at T_{sol} during the melting process.

Liquid fraction x_{liq} is expected to vary according to the composition of material undergoing melting, which is temperature dependent. A linear dependency on temperature is postulated by Lainet in [Lai18] for the volume fraction of liquid during melting:

$$x_{liq} = \begin{cases} 0 & \forall T \leq T_{sol} \\ \dfrac{T - T_{sol}}{T_{liq} - T_{sol}} & \forall T_{sol} < T < T_{liq} \\ 1 & \forall T \geq T_{liq} \end{cases} \tag{6.2}$$

We propose instead to derive it from the composition of the heterogeneous material. For the generic temperature $T \in [T_{sol}; T_{liq}]$, the composition c of the material can be expressed in terms of the solidus and liquidus compositions c_{sol} and c_{liq} respectively, weighted on the volume fraction of each phase:

$$c(T) = [1 - x_{liq}(T)]c_{sol} + x_{liq}(T)c_{liq} \tag{6.3}$$

We propose to derive the liquid fraction expression from correlations of liquidus and solidus temperatures through the lever rule which principle is represented in figure 6.1: for the generic temperature T in the melting interval the liquid volume fraction x_{liq} is function of solidus and liquidus temperatures previously expressed in equations 4.7 and 4.8.

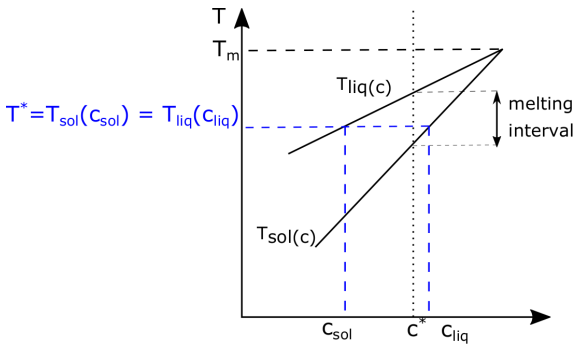

Figure 6.1 – Schematic view of the lever rule applied to the melting transition

For the generic stoichiometry O/M and burn-up Bu, the liquid fraction $x_{liq}(T, Bu, O/M)$, valid for $\forall T \in [T_{sol}; T_{liq}]$, can be expressed as follows:

$$x_{liq}(T, Bu, O/M) = \frac{10^3(O/M - 2.00) - 0.5Bu + T_f - T}{2.57(T - T_f) - 0.5Bu} \tag{6.4}$$

Figures 6.2 show the evolution of the liquid fraction depending on the Burn-up and stoichiometry respectively: we observe that an increase in Burn-up induces an increase of the amplitude of the melting interval by moving the solidus threshold at lower temperatures. Variation from stoichiometry in the hypostoichiometric domain leads instead to the displacement of the melting interval to lower temperatures, without modifying its amplitude.

6.2 Definition of the problem

Homogenization approach is used to evaluate the behavior of macroscopic heterogeneous materials and consists in replacing the real heterogeneous one with an homogenized medium whose behavior is macroscopically equivalent to the real one. Coherently with the appraoch described in chapter 5, we define a Representative Volume $\mathcal{V}$, which is large enough to consider the melting UO_2 nuclear fuel as an isotropic matrix including the liquid fraction, being characterized just by its volume fraction as defined in eq (6.4). The macroscopic stress field $\tilde{\boldsymbol{\sigma}}$ and the macroscopic strain field $\tilde{\boldsymbol{\varepsilon}}$ of the equivalent material are obtained by averaging on $\mathcal{V}$ the microscopic stress tensor $\boldsymbol{\sigma}$ and the microscopic strain tensor $\boldsymbol{\varepsilon}$, which

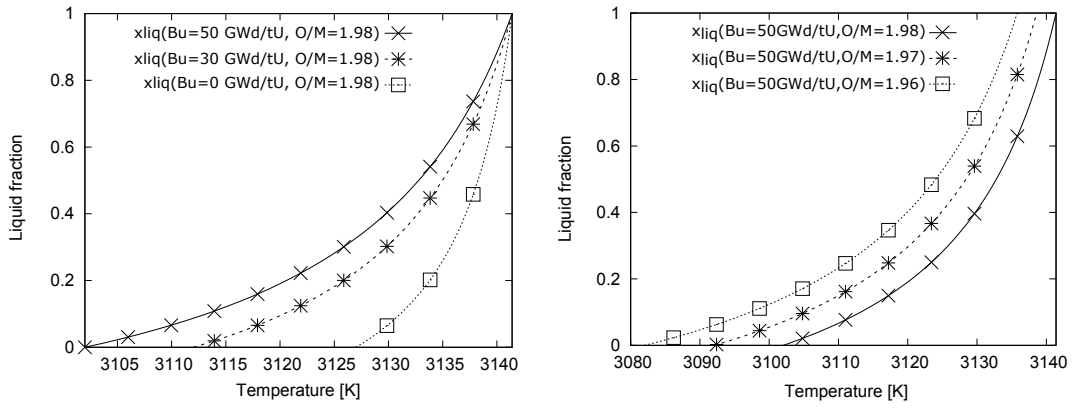

(a) (b)

Figure 6.2 – Evolution of liquid fraction in the melting interval. (a) x_{liq} depending on Bu for a fuel material having fixed hypostoichiometric composition: fission products formations and neutronic irradiation induce the increase of melting plateau and melting onset occurs at lower temperatures; (b) x_{liq} for a 50 GWd/t fuel depending on stoichiometry: the melting interval is moved to lower temperatures but its amplitude is not affected

are space dependent:

$$\tilde{\boldsymbol{\sigma}} = \langle \boldsymbol{\sigma} \rangle = \frac{1}{|\mathcal{V}|} \int_{\mathcal{V}} \sigma dv \tag{6.5}$$

$$\tilde{\boldsymbol{\varepsilon}} = \langle \boldsymbol{\varepsilon} \rangle = \frac{1}{|\mathcal{V}|} \int_{\mathcal{V}} \varepsilon dv \tag{6.6}$$

$$\tag{6.7}$$

Where $\tilde{\boldsymbol{\sigma}}$ and $\tilde{\boldsymbol{\varepsilon}}$ account for the presence of liquid in the material.

Under the hypothesis of small strains and according to the approach used by Monerie in [Mon06], we assume the additivity of macroscopic strains to stand. The thermal-mechanical strain for the equivalent melting material can be thus expressed as the sum of the elastic strain $\tilde{\boldsymbol{\varepsilon}}^e$, the viscoplastic strain $\tilde{\boldsymbol{\varepsilon}}^{vp}$, the thermal dilatation $\tilde{\boldsymbol{\varepsilon}}^{th}$. We have seen in chapter 4 that a characteristic discontinuity in material density occurs at the melting onset. To account for this strain we introduce $\tilde{\boldsymbol{\varepsilon}}^m$ as a characteristic strain related to the density reduction. The total strain $\tilde{\boldsymbol{\varepsilon}}$ is:

$$\tilde{\boldsymbol{\varepsilon}} = \tilde{\boldsymbol{\varepsilon}}^e + \tilde{\boldsymbol{\varepsilon}}^{vp} + \tilde{\boldsymbol{\varepsilon}}^{th} + \tilde{\boldsymbol{\varepsilon}}^m \tag{6.8}$$

The equivalent homogenized stress tensor can be thus expressed as:

$$\tilde{\boldsymbol{\sigma}} = \mathbb{C}^{hom} : \tilde{\boldsymbol{\varepsilon}}^e = \mathbb{C}^{hom} : [\tilde{\boldsymbol{\varepsilon}} - (\tilde{\boldsymbol{\varepsilon}}^{vp} + \tilde{\boldsymbol{\varepsilon}}^{th} + \tilde{\boldsymbol{\varepsilon}}^m)] \tag{6.9}$$

where $\mathbb{C}^{hom} = (3\tilde{K}, 2\tilde{G})$ is the effective elastic tensor, $\tilde{K}$ and $\tilde{G}$ are the effective bulk modulus and the effective shear modulus of the equivalent material, respectively.

6.3 The thermal-elastic behavior

According to classic writing the thermodynamic potential Ψ of the equivalent material can be written as follows:

$$\Psi = \frac{1}{\rho} \left[\frac{1}{2} \left(3\tilde{K}\tilde{\varepsilon}_H^2 + 2\tilde{G}\tilde{\mathbf{e}} : \tilde{\mathbf{e}} \right) - 3\tilde{K}\tilde{\alpha}(T - T_0)\tilde{\varepsilon}_H \right] - \frac{\tilde{C}_p}{2T_0}(T - T_0)^2 \tag{6.10}$$

Where ρ is the material density, $\tilde{\varepsilon}_H = \frac{1}{3}tr(\tilde{\boldsymbol{\varepsilon}})$ is the hydrostatic component of the strain tensor, $\tilde{\boldsymbol{e}} = \tilde{\boldsymbol{\varepsilon}} - \tilde{\varepsilon}_H\mathbb{I}$ is the deviatoric component of the strain tensor and $\mathbb{I}$ the 4^{th} order identity tensor, $\tilde{\alpha}$ is the macroscopic dilatation coefficient for the equivalent homogenized material, $\tilde{c}_p$ is the equivalent heat capacity of the homogenized material, T_0 is the reference temperature.
In addition to the usual terms of elastic deformation and thermal dilatation, during fuel melting due to the discontinuity in material density, the thermal-elastic strain presents an additional contribution due to the characteristic decrease in density at melting $\tilde{\boldsymbol{\varepsilon}}^m$. Under the hypothesis of isotropic strain, we can express this term under the form of an equivalent thermal dilatation coefficient which will be further detailed in section 6.3.3:

$$\tilde{\boldsymbol{\varepsilon}}^m = \tilde{\boldsymbol{\alpha}}^m(T - T_0) \tag{6.11}$$

The thermodynamic potential Ψ is modified as follows:

$$\Psi = \frac{1}{\rho}\left[\frac{1}{2}\left(3\tilde{K}\tilde{\varepsilon}_H^2 + 2\tilde{G}\tilde{\mathbf{e}} : \tilde{\mathbf{e}}\right) - 3\tilde{K}(\tilde{\alpha} + \tilde{\alpha}^m)(T - T_0)\tilde{\varepsilon}_H\right] - \frac{\tilde{c}_p}{2T_0}(T - T_0)^2 \tag{6.12}$$

The macroscopic mechanical behavior of the equivalent material $\tilde{\boldsymbol{\sigma}}$ can be obtained by deriving the potential with respect to the strain tensor:

$$\tilde{\boldsymbol{\sigma}} = \rho\frac{\partial\Psi}{\partial\tilde{\boldsymbol{\varepsilon}}} = 3\tilde{K}\tilde{\varepsilon}_H\mathbf{I} + 2\tilde{G}\tilde{\mathbf{e}} - 3\tilde{K}(\tilde{\alpha} + \tilde{\alpha}^m)(T - T_0)\mathbf{I} \tag{6.13}$$

The specific entropy of the system results from the derivative of the potential by the temperature T. Taking into account the dependency of material properties with respect to temperature T we have:

$$\begin{aligned} s = -\frac{\partial\Psi}{\partial T} = -\frac{1}{2}\left[\frac{\partial}{\partial T}\left(\frac{1}{\rho}\right)\left(3\tilde{K}\tilde{\varepsilon}_H^2 + 2\tilde{G}\tilde{\mathbf{e}} : \tilde{\mathbf{e}}\right) + \frac{1}{\rho}\left(3\frac{\partial\tilde{K}}{\partial T}\tilde{\varepsilon}_H^2 + 2\frac{\partial\tilde{G}}{\partial T}\tilde{\mathbf{e}} : \tilde{\mathbf{e}}\right)\right] \\ + \left\{\frac{\partial}{\partial T}\left(\frac{1}{\rho}\right)3\tilde{K}(\tilde{\alpha} + \tilde{\alpha}^m) + \frac{1}{\rho}\left[3\tilde{K}\left(\frac{\partial\tilde{\alpha}}{\partial T} + \frac{\partial\tilde{\alpha}^m}{\partial T} + 3\frac{\partial\tilde{K}}{\partial T}(\tilde{\alpha} + \tilde{\alpha}^m\right)\right]\right\}(T - T_0)\tilde{\varepsilon}_H \\ + \frac{1}{\rho}3\tilde{K}(\tilde{\alpha} + \tilde{\alpha}^m)\tilde{\varepsilon}_H + \frac{\tilde{c}_p}{T_0}(T - T_0) + \frac{\partial\tilde{c}_p}{\partial T}\frac{(T - T_0)^2}{2T_0} \end{aligned} \tag{6.14}$$

In other studies, where it is generally considered that the derivative with respect to time of material properties are negligible, this assumption leads to obtain the usual form of the specific entropy:

$$s = \frac{1}{\rho}3\tilde{K}(\tilde{\alpha} + \tilde{\alpha}^m)\tilde{\varepsilon}_H + \frac{\tilde{c}_p}{T_0}(T - T_0) \tag{6.15}$$

where $\tilde{c}_p$ is the equivalent heat capacity of the melting material, defined as a function of specific heat capacity of the solid at solidus temperature $c_{p,s}(T_{sol})$, liquid fraction and latent heat L:

$$\tilde{c}_p(T) = c_{p,s}(T_{sol}) + L\frac{\partial x_{liq}}{\partial T}(T) \tag{6.16}$$

In the generic case, we can indeed consider the thermal balance for the unitary melting mass in a closed system:

$$\frac{dh(t)}{dt} = q \tag{6.17}$$

where $h(t)$ is the enthalpy of melting material at time t during transition process and q the specific heat actually inducing the melting process. By taking advantage of the extensive nature of enthalpy we can say that:

$$h(t) = h_{sol} + x_{liq}(t)L \tag{6.18}$$

where h_{sol} is the enthalpy of the material at solidus temperature and L the latent heat as previously mentioned. Thus replacing in eq. (6.17) and taking advantage of the relation between enthalpy and temperature through specific heat capacity we can easily obtain eq. (6.16).

6.3.1 The equivalent elastic strain

According to previously stated hypothesis, the effective elastic tensor of the melting fuel material $\mathbb{C}^{hom} = (3\tilde{K}, 2\tilde{G})$ is obtained considering a newtonian incompressible liquid phase having $K_l \to \infty$ and $G_l \to 0$ and a solid phase whose properties are obtained according to eq. (2.17), evaluated at T_{sol}.

$$G_s = G(T_{sol}) \tag{6.19}$$

$$K_s = \frac{E(T_{sol})G(T_{sol})}{3[3G(T_{sol}) - E(T_{sol})]} \tag{6.20}$$

Figure 6.3 shows the evolution of effective properties for dense UO_2. Graphs are normalized with respect to the solid property for what concerns the shear modulus, with respect to the liquid property for the bulk modulus. They are obtained according to the different approaches previously introduced: Voigt and Reuss upper and lower bound respectively are evaluated to identify the region in which we expect the evaluation to vary, then the Hashin and Shtrikman (HS) approach is applied according to the Mori-Tanaka (MT) and Self-Consistent (SC) schemes [Bor01]. The general formula proposed by HS for the evaluation of bulk and shear modulus is proposed as follows:

$$\tilde{G} = G^{HS} = \left(\sum_{p=1}^{2} \frac{x_p}{G^* + G_p} \right)^{-1} - G^* = \frac{G^* < G > + G_l G_s}{G^* + x_{liq} G_s + (1 - x_{liq}) G_l} \tag{6.21}$$

$$\tilde{K} = K^{HS} = \left(\sum_{p=1}^{2} \frac{x_p}{K^* + K_p} \right)^{-1} - K^* = \frac{K^* < K > + K_l K_s}{K^* + x_{liq} K_s + (1 - x_{liq}) K_l} \tag{6.22}$$

where p stands for the generic phase, solid or liquid, $< . >$ referes to the average, K^* and G^* refer to the reference medium and are defined as follows $K^* = \frac{4}{3}\tilde{G}$; $G^* = \frac{G}{6}\frac{9\tilde{K}+8\tilde{G}}{\tilde{K}+2\tilde{G}}$. To apply the MT scheme, the reference medium corresponds to the solid matrix, whereas the SC is based on the hypothesis that the reference medium is the homogenized system itself.

As showed in figure (a) of 6.3, the MT and SC estimations are coherent as long as liquid fraction $x_{liq} < 0.1$. The self-constistent scheme based on the estimation of Hashin and Shtrikman as reported in [Bor01] is retained for the evaluation of the effective properties as it is better adapted for higher liquid fractions. Once solved eq. (6.21) and (6.22) the elastic properties for the equivalent elastic material are the following:

$$\tilde{K}(K_s, x_{liq}, \tilde{G}) = \frac{K_s}{1 - x_{liq}} + \frac{4}{3}\frac{x_{liq}}{1 - x_{liq}}\tilde{G} \tag{6.23}$$

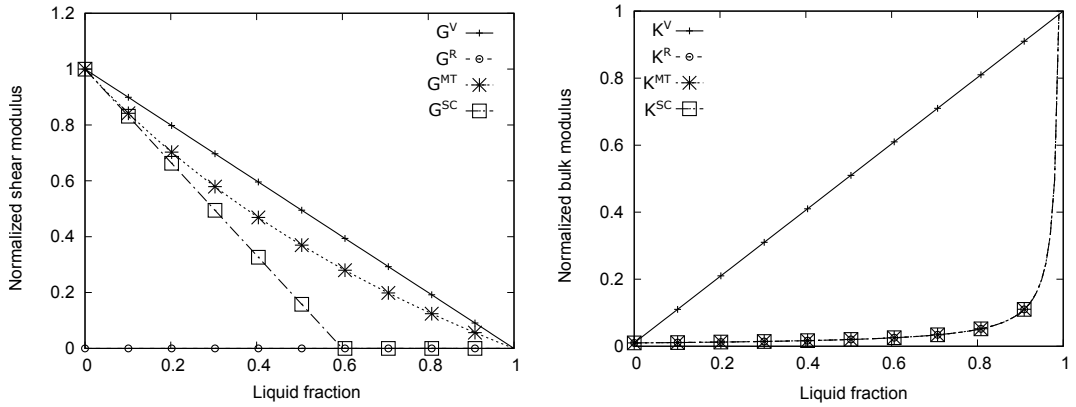

(a) (b)

Figure 6.3 – Evolution of effective shear modulus (a) and of the effective bulk modulus (b) as a function of the liquid fraction: comparison between the Voigt and Reuss limits and the Mori Tanaka and Self-Consistent approaches.

$$\tilde{G}^2 + \left(\frac{9}{4}\frac{K_s}{(2+x_{liq})} + \frac{4x_{liq}-2}{2+x_{liq}}G_s\right)\tilde{G} + \frac{3}{4}\frac{(5x_{liq}-3)}{(2+x_{liq})}K_sG_s = 0 \tag{6.24}$$

We observe that $\partial\tilde{G}/\partial x_{liq} \leq 0$ and is null for $x_{liq} = 0.6$, which is the well known solution for an heterogeneous material having incompressible matrix and an internal incompressible void fraction [Bor01]. Even though the bulk modulus $\tilde{K}$ following homogenization depends on the equivalent shear modulus, the fact that $K_s >> G_s$ induces no relevant dependencies. If we had a different case, we would have a non monotonous function of the liquid fraction as we immediately see once considering its derivative with respect to x_{liq}:

$$\frac{\partial\tilde{K}}{\partial x_{liq}} = \underbrace{\frac{1}{(1-x_{liq})^2}K_s}_{\geq 0} + \underbrace{\frac{4}{3}\tilde{G}\frac{1}{(1-x_{liq})^2}}_{\geq 0} + \underbrace{\frac{4}{3}\frac{\partial\tilde{G}}{\partial x_{liq}}\frac{x_{liq}}{1-x_{liq}}}_{\leq 0} \tag{6.25}$$

Thus we have a maximum of the bulk modulus for $x_{liq} < 0.6$ and for $x_{liq} > 0.6$ it increases as the square of x_{liq}.

6.3.2 The equivalent thermal strain

Under the hypothesis of isotropic mechanism, the thermal dilatation impacts the hydrostatic behavior of the medium:

$$\tilde{\boldsymbol{\varepsilon}}^{th} = \tilde{\varepsilon}^{th}\boldsymbol{I} \tag{6.26}$$

According to Levin relation as reported in [Tor02], the equivalent dilatation coefficient of an heterogeneous material can be expressed as a function of the equivalent bulk modulus $\tilde{K}$:

$$\tilde{\alpha} = \langle\alpha\rangle + \frac{\alpha_l - \alpha_s}{1/K_l - 1/K_s}\left(\frac{1}{\tilde{K}} - \left\langle\frac{1}{K}\right\rangle\right) \tag{6.27}$$

where $\langle\alpha\rangle = (1-x_{liq})\alpha_s + x_{liq}\alpha_l$ is the average dilatation coefficient.

6.3.3 The characteristic melting expansion

Still assuming the occurrence of an isotropic phenomenon, the characteristic strain due to density reduction impacts the hydrostatic term of the macroscopic behavior

$$\tilde{\boldsymbol{\varepsilon}}^m = \tilde{\varepsilon}^m \boldsymbol{I} \tag{6.28}$$

Volume expansion associated to discontinuity in density concerns just the melted volume fraction. The linear strain can be expressed as:

$$\tilde{\boldsymbol{\varepsilon}}^m = \left[1 + x_{liq}\left(\frac{\Delta V}{V}\right)_m\right]^{1/3} - 1 \cong \frac{1}{3}\left(\frac{\Delta V}{V}\right)_m x_{liq} \tag{6.29}$$

Figure 6.4 shows the evolution of $\boldsymbol{\varepsilon}^m$ with respect to the liquid fraction.

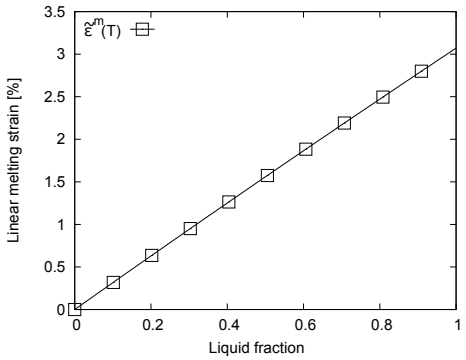

Figure 6.4 – Evolution of the linear expansion with the liquid fraction

The corresponding melting thermal expansion is obtained according to eq. (6.11):

$$\tilde{\alpha}^m = \frac{\tilde{\varepsilon}^m}{T - T_0} \tag{6.30}$$

6.4 The viscoplastic mechanical behavior

As presented in chapter 2.2, the total viscoplastic behavior of the system is given by the diffusion and the dislocation mechanism, modeled and coupled according to equations (2.11) and (2.13). The non linear strain rate for viscous solid material is obtained by deriving eq. (2.13) with respect to the macroscopic stress tensor [Mon06]:

$$\dot{\boldsymbol{\varepsilon}}^{vp} = (1-\theta)\dot{\boldsymbol{\varepsilon}}_1^{vp} + \theta\dot{\boldsymbol{\varepsilon}}_2^{vp} + (\Psi_2^{vp} - \Psi_1^{vp})\frac{\partial\theta}{\partial\tilde{\boldsymbol{\sigma}}} \tag{6.31}$$

The solid material is incompressible by hypothesis and its behavior is obtained imposing $A_i(f) = 0$ in eq.(2.11). Under this assumption the i^{th} creep mechanism can be expressed according to a Norton potential. The resulting strain rate of the solid matrix at melting onset is in the form:

$$\dot{\boldsymbol{\varepsilon}}_i^{vp} = \frac{\partial\Psi_i^{vp}}{\partial\boldsymbol{\sigma}} = \frac{3}{2}H(n_i)\sigma_{eq}^{n_i}\frac{\boldsymbol{s}}{\sigma_{eq}} \tag{6.32}$$

According to the nonlinear extension method, before to evaluate the behavior of the equivalent homogeneous melting material, linearization of the creep law is obtained by applying

the modified secant method as presented by P. Suquet in [Bor01]. The strain can be locally described for each point $x \in \mathcal{V}$ as a function of the local stress:

$$\boldsymbol{\varepsilon}(x) = \mathbb{L}^{sct}(x, \boldsymbol{\sigma}(x)) : \boldsymbol{\sigma}(x) \tag{6.33}$$

where $\mathbb{L}^{sct}(x, \boldsymbol{\sigma}(x)) = \mathbb{C}^{sct-1}(x, \boldsymbol{\varepsilon}(x))$ is the effective secant tensor which depends on the local strain $\boldsymbol{\varepsilon}(x)$ and on the local phase (solid or liquid). We evaluate the global non linear behavior on the basis of the approximate local solution: average strain and stress in the non linear heterogeneous material are considered equal to those of the linear equivalent medium. The macroscopic global strain is thus:

$$\tilde{\boldsymbol{\varepsilon}} = \tilde{\mathbb{L}} : \tilde{\boldsymbol{\sigma}} \tag{6.34}$$

where $\tilde{\mathbb{L}}(c_r, L_r^{sct}, ...)$ is the effective tensor of the linear equivalent medium. It is obtained through the secant model on the constitutive model of the non linear material and on the volume fraction of components.

According to the modified extension of the secant method we identify an effective secant tensor for each phase r as a function of the second order moment of stress tensor.

$$\forall r \quad \mathbb{L}_r^{sct} = \mathbb{L}^{sct}(\sqrt{\langle \sigma_{eq}^2 \rangle_r}) = \frac{1}{3K_r}\mathbb{J} + \frac{1}{2G_r^{sct}\left(\sqrt{\langle \sigma_{eq}^2 \rangle_r}\right)}\mathbb{K} \tag{6.35}$$

where $\mathbb{J}$ and $\mathbb{K}$ have already been defined in section 5.1.1.
When discussing the equivalent viscoplastic behavior of the homogenized medium, we evaluate the particular case in which we have a single non linear phase (the solid matrix) and liquid inclusions which can be assumed to be isotropically distributed in the solid one. It first results that the only variable to be evaluated is the secant shear modulus of the non linear solid phase. This is defined through the non linear behavior of the solid phase. Thus, after eq. (6.32) we have:

$$G_{s,i} = G_{s,i}^{sct} = \frac{1}{3H(n_i)}\langle \sigma_{eq}^2 \rangle^{(1-n_i)/2} \tag{6.36}$$

Then, the linear equivalent material can be characterized by effective properties $\{3\tilde{K}, 2\tilde{G}\}$ obtained considering that both components are incompressible and that shear modulus of the liquid $G_l \to 0$:

$$\tilde{G} = \frac{3 - 5x_{liq}}{3} G_s = \frac{3 - 5x_{liq}}{3} G_r^{sct}\left(\sqrt{\langle \sigma_{eq}^2 \rangle_r}\right) \tag{6.37}$$

Then, the second order moment of the equivalent strain and stress tensors where obtained by P. Suquet in [Bor01], simplified as both phases are incompressible:

$$\langle \sigma_{eq}^2 \rangle_s = \frac{1}{(1 - x_{liq})} \tilde{\sigma}_{eq}^2 \frac{\partial(1/\tilde{G})}{\partial(1/G_s)} \tag{6.38}$$

where $\tilde{\sigma}_{eq}$ is the macroscopic equivalent stress. Solving eq. (6.38) with respect to the effective shear modulus and secant one defined in eq. (6.37) and eq. (6.36) respectively, we obtain the model describing the mechanical behavior of the equivalent medium:

$$\dot{\tilde{\boldsymbol{\varepsilon}}}_i^{vp} = \frac{3}{2} H(n_i) \underbrace{\left(\frac{1}{1 - x_{liq}}\right)^{\frac{n_i - 1}{2}} \left(\frac{3}{3 - 5x_{liq}}\right)^{\frac{n_i + 1}{2}}}_{\beta(x_{liq}, n_i)} \tilde{\sigma}_{eq}^{n_i} \frac{\tilde{\boldsymbol{s}}}{\tilde{\sigma}_{eq}} = \frac{3}{2} H(n_i) \beta(x_{liq}, n_i) \tilde{\sigma}_{eq}^{n_i} \frac{\tilde{\boldsymbol{s}}}{\tilde{\sigma}_{eq}} \tag{6.39}$$

Figure 6.5 represents the evolution of the $\beta(x_{liq}, n_i)$ parameter describing the effect on the mechanical behavior due to the presence of the liquid fraction x_{liq}. Parameters for the two mechanisms have been discussed by Monerie and Gatt in [Mon06]: we retain that $n_1 = 1$ for scattering mechanism and $n_2 = 8$ for dislocation mechanism. Figure 6.5 shows that $\beta(x_{liq}, n_i)$ acts like a multiplier of strain rate and that dislocation-creep is the driving phenomenon leading to a rapid loss of mechanical resistance of the melting volume.

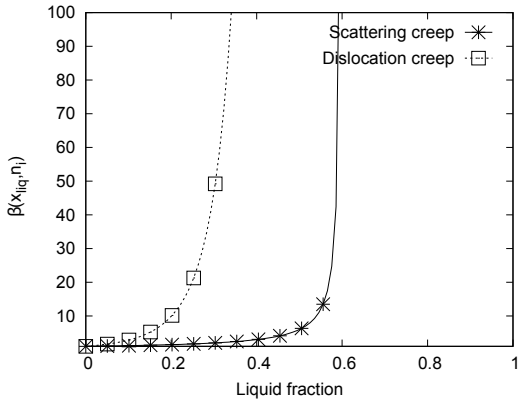

Figure 6.5 – Evolution of the β parameter as a function of liquid fraction, which acts like a multiplier of the viscoplastic strain rate. The dislocation-creep results to be the driver for the rapid loss of the mechanical resistance of the melting volume

6.5 Numerical implementation and feasibility of the measure

6.5.1 Definition of the test case

We test the model in a simple case in order to easily access and study the calculated behavior. For this we use a 2D axis-symmetric system having the geometrical characteristics of the fuel pellet. The material properties are the ones of irradiated UO_2, with stoichiometry O/M=1.98 and Bu=30 GWd/tU and null plutonium content. The problem is solved by means of the finite element code Cast3m [CEA, 2016a] while material properties are treated via MFRONT [Hel15] [CEA, 2016b].
Figure 6.6 presents geometry and boundary conditions of the problem: L0 corresponds to the central axis; LB and LH are respectively the bottom and top edge, free to move only in the radial direction. Their length corresponds to pellet radius. LR is the external edge of the pellet, which length equals pellet height.

The system is submitted to a parabolic radial temperature profile which ensures that melting first origins in the central zone and then progressively moves towards pellet periphery. At the periphery of the system the temperature is fixed. We imposed a linear rise of the thermal profile according to a constant rate.

6.5.2 Convergence test: node density

The system is modeled with a uniform radial density $n\Delta r$ with a ratio $\Delta r/R \approx 3.10^{-3}$. The reduced radial size is required as a consequence of the strong thermal gradient, to have a minimum of 2 nodes that undergo melting. Figure 6.7 shows the convergence of

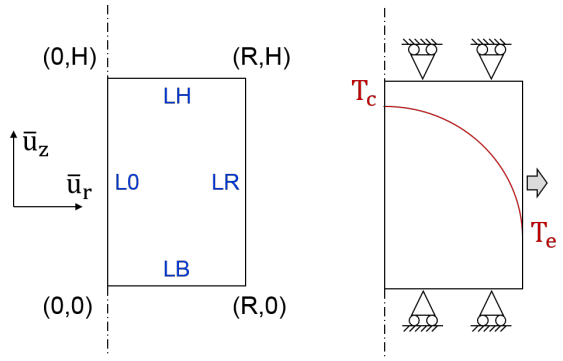

Figure 6.6 – Definition of the thermal-mechanical test case: geometry (left) and boundary conditions and thermal-loading (right)

simulation outputs as a function of the radial mesh density. Errors are calculated for the edge displacement and the equivalent stress tensor at r=R and T=3200K with respect to the highest tested density (n=6). The model converges with a residual error in the order of 10^{-4} for the displacement and 10^{-3} for stresses.

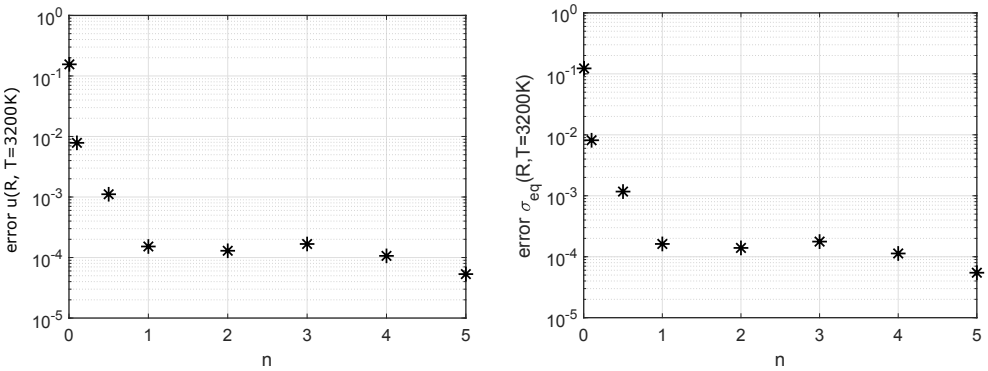

(a) (b)

Figure 6.7 – Convergency of the displacement u(r) and of the equivalent stress tensor evaluated at r=R and t=3200K, with respect to the mesh density

6.5.3 Evolution of the radial stress

We have presented in the article the evaluation of the elastic and viscoplastic behavior. Figure 6.8 illustrates the different evolution of the equivalent stress tensor σ_{eq} along the radial dimension. On the left of the figure, the equivalent stresses are evaluated according to a pure elastic behavior and on the right according to an elasto-viscoplastic one. Both are evaluated at 3200 K. The highlighted region corresponds to the melting plateau that, according to the defined thermophysical characteristics of the material, takes place between 3112 and 3141 K.
As the liquid material is modeled as incompressible, σ_{eq} is null in the melted region. In the solid region, we observe that the creep mechanisms activated at high temperature induce a strong relaxation of stresses. Toward the external side, temperature decrease and stresses increase in the system due to the absence of creep.

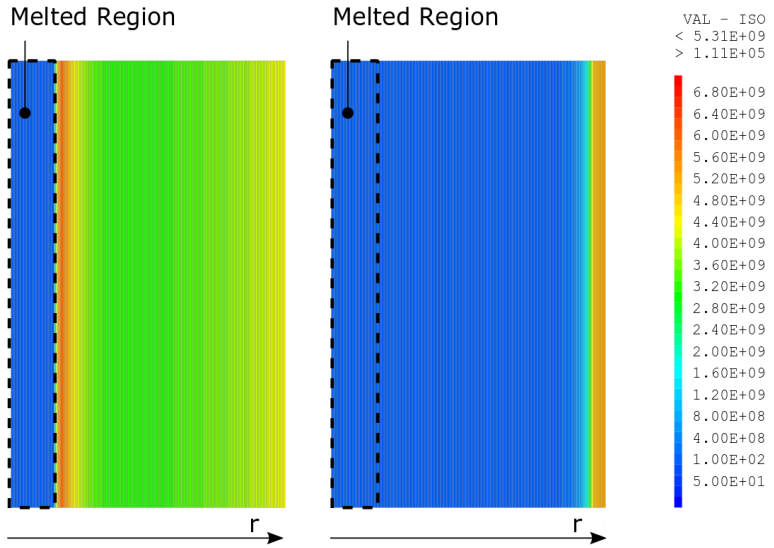

Figure 6.8 – Equivalent stress tensor as a function of the normalized radius at T(r=0) = 3200K. Comparison of the pure elastic and elasto-viscoplastic behavior: in the melted region the equivalent stresses are null because of the incompressibility of the liquid. The activation of the creep mechanisms results into a strong relaxation with respect to the elastic case. At the periphery, where the temperature is too low for the activation of creep, stresses increase

6.5.4 The resulting pellet macroscopic displacement

We are interested in evaluating how the macroscopic displacement of the system varies according to the central melted region. Figure 6.9 shows the kinetics of the modeled system edge displacement as a function of time. Δt is defined as the difference between the generic time t within the transient and the t_0 at which liquidus temperature is first reached in pellet center.
The melted fraction is defined as as the ratio of melted volume with respect to the total volume of the pellet:

$$V_f = \frac{r_{liq}^2}{R^2} \tag{6.40}$$

where r_{liq} is the radius at which the liquidus temperature is reached.

Calculation shows that once melting appears, a discontinuity in displacement kinetics is observed. This leads to an acceleration of system deformation. In the proposed problem we imposed a linear increase of temperature equal to 1 K/s and the kinetics of displacement is accelerated by a factor 3.
The implemented model shows that there is a direct relation between the calculated displacement kinetics and the increase of the melted fraction, which is the major driver to its evolution. From the figure we can conclude that the thermal-mechanical strain defined in equation (6.8) can be approximated by $\dot{\bar{\varepsilon}} \approx \dot{\bar{\varepsilon}}^m$.

6.5.5 Discussion on the measurement feasibility

From this simple case we can deduce that a strong modification of displacement kinetics is expected at central melting, whose slope will depend on the thermal properties of the

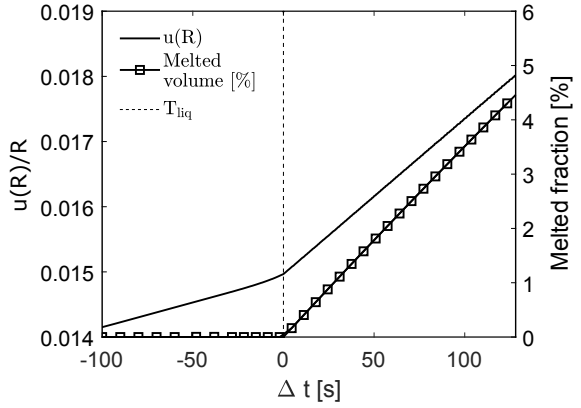

Figure 6.9 – Time evolution of the normalized displacement at r=R and of the melted volume

system and absorption of latent heat. The linear dependency between the displacement u(R) and the melted fraction is a direct consequence of the fact that the temperature is imposed to increase linearly in time, without taking into account the latent heat of melting. When solving the thermal problem instead, the latent heat of melting affects thermal history thus modifying the slope of the displacement evolution.
It is noteworthy also that this problem applies to an hypothetical power ramp test carried out in material testing reactor, where the increase rate of temperature ranges at at least 1 order of magnitude higher than the one used in our test case. Those two phenomena are expected to drive the evolution of system displacement in the real scenario.

Outcomes of Part II

One of the objectives of the thesis is to determine whether the onset of melting process in the fuel pellet induces a characteristic modification of the deformation kinetics of the cladding diameter. The principle lies on the fact that a characteristic dilatation occurs when the solid uranium dioxide becomes liquid.
At the beginning of this work, there was no thermal-mechanical model available in ALCYONE to describe the macroscopic behavior of the fuel element during a large amplitude power ramp test leading to the onset of melting in the pellet center. This lead us to propose a model to make the code evolve and take into account the progressive appearance of a liquid fraction in the fuel pellet.

In this part II, we have first discussed the thermo-physical characteristics of the PWR fuel material at melting onset. According to the radial redistribution of the oxygen from the hot central part of the pellet to the colder outer region, we have defined the melting interval for the hypostoichiometric irradiated fuel material, in terms of a solidus temperature T_{sol} and a liquidus temperature T_{liq}. For this, we assume a linear superposition of the effects due to burn-up and the deviation from stoichiometry and we consider that the plutonium content is negligible.

To enhance its integration in the thermal-mechanical models of ALCYONE, the melting model has been developed to be driven by the local temperature and it is based on the same homogenization approaches introduced in the previous part to model the thermal-mechanical behavior of the solid fuel material. A review of the theoretical approach for analytical homogenization is presented in chapter 5.

To model melting, we start from the definition of the viscous mechanical behavior of the solid porous fuel material obtained by elliptical thermal-mechanical potential as described by Monnerie and Gatt in [Mon06]. We make the fundamental assumption is made that porosity in the fuel material approaching melting temperature is on a first approximation considered negligible. Thus, the viscoplastic strain rate for the solid fuel material at melting onset is obtained from a Norton potential. Liquid inclusions progressively nucleate in the central region and, assuming that they appear in a uniform way in the volume where the local temperature overcomes the solidus threshold, they are completely described by their volume fraction x_{liq}. We evaluate the macroscopic elastic properties of the equivalent material as a function of liquid fraction, using the Self-Consistent model. We account for material density assuming that an isotropic expansion origins and thus introducing $\tilde{\varepsilon}^{\mathbf{m}}$ contribution to the macroscopic strain rate. Concerning the viscoplastic behavior, we use modified secant method to obtain the macroscopic behavior and we find out that the viscoplastic deformation undergoes strong acceleration due to dislocation creep, leading to a strong decrease in system stress.

Material properties are treated by the MFRONT code generator [Hel15] [CEA, 2016b], developed in the frame of the PLEIADES platform, and a simple case is solved by means of the finite element code Cast3m [CEA, 2016a]. This is aimed at analyzing the macroscopic output of the modeled system, discuss the calculated resulting behavior and validate the modeling principle.
We study a 2D axisymmetrical system having the radius and height of the fuel pellet, blocked at the top and bottom and free to deform in the radial direction. The modeled material properties are the ones discussed for the UO_2 material and are temperature dependent. By comparing a pure elastic resolution and the elasto-viscoplastic one we show that the creep mechanisms origin a strong relaxation of stresses with respect to the elastic case, with an increase of calculated stresses only in the external part of the pellet, as a consequence of the decrease of temperatures. Through the analysis of the macroscopic displacement it is evident that the discontinuity appearing at melting onset and the resulting kinetics are directly linked to the appearance and progression of melting in the pellet center.
Taking into account the present state of the melting model, it is untimely to evaluate the uncertainties in the calculated deformation and perform a study of uncertainties propagation.
Further work is required to integrate the melting model in ALCYONE and couple the stresses associated to the melting process with the characteristic phenomena occurring in the fuel pellet (e.g. the gaseous swelling). This takes advantage of the fact that the model is developed according to the same approaches and using the same independent variables. At this stage, we cannot conclude on the theoretical feasibility to measure a characteristic effect on the cladding deformation kinetics due to the melting onset.
From the results on the simple case, we expect that the macroscopic deformation of the fuel element will result from the tendency of the melted fraction to expand, as we have shown in figure 6.9 but also on the power history of the rod, controlling the available latent heat to melt, on the evolution of gaseous swelling at high temperature and on the reaction of the surrounding cladding to the imposed stresses.

Part III

A critical review of measurement techniques

Introduction

The previous part of this thesis has focused on the phenomenology of PCI to define the set of relevant parameters. We have also developed a thermal-mechanical model to evaluate the effects of the onset of the central melting of the fuel on the cladding deformation. By the end of the thesis, the model is not integrated in ALCYONE thus we cannot conclude on the theoretical feasibility of the detection. Nevertheless, calculated results on the macroscopic behavior of the uranium dioxide shows that melting induces an acceleration of the deformation kinetics of the system.
For the aim of the following discussion, we retain that the cladding deformation is eligible as parameter to detect the melting onset. Further studies must be carried out on the topic and we will recall them in the conclusions and perspectives of the thesis.

The relevant parameters to be detected or measured during irradiation are:

- The fuel centerline and surface temperatures and the cladding surface temperature;
- The cladding external diameter and the axial elongation of the fuel and of the cladding;
- The internal pressure of the rod.

By means of code simulations we have defined, for each of these parameters, measurement requirements expressed in terms of range, relative accuracy, spatial and temporal resolution. A first importance conclusion of previous parts is that the amplitude of the effects describing PCI imposes to minimize as much as possible the perturbation induced by the measurement itself. This results into the practical requirement that **remote measurements have to preferred**.

In this part of the work we discuss the identified technological solutions that meet all or part of the measurement requirements identified.
In this critical review we have considered:

- Present technologies developed through the years for in-pile application in material testing reactors;
- Some of the main concepts in the instrumentation field currently under development.

The investigated technological solutions are assessed in terms of their last published developments. We discuss their measurement principle, their experimental characterization, the expected perturbation of the system associated to the presence of the sensor and the level of maturity with respect to the nuclear application. This latter implies ionizing radiation, high temperature and pressure, chemical induced interaction and corrosion, operational constrains imposing high reliability and stability. The evolution and adaptation of existing technological solution to the nuclear environment constitutes indeed a challenging step in

the development of sensor for MTR application.

We group the technologies in three measurement types that correspond to the three class of dimensional parameters identified: chapter 7 for the thermal measurement, chapter 8 for the measurement of the internal rod pressure and chapter 9 for the dimensional measurements, that include the external cladding diameter, the cladding and fuel elongation and the pellet-cladding contact.

Chapter 7

Temperature measurement

In this chapter, we review different technological solutions to measure on line the temperature of a target object and discuss their advantages an disadvantages to measure PCI relevant parameters. In agreement with the purpose of the work, we do not discuss the applications of the melting wires and the SiC sensors, which measure can be investigated only after the irradiation. The considered technologies are the thermocouples in section 7.1, the expansion thermometer in 7.2, the ultrasonic thermometer in 7.3, the Johnson noise thermometer in 7.4, the fiber Bragg gratings 7.5, the optical sensor based on the scattered light in 7.6 and the optical pyrometry in 7.7. At last, we conclude with a synthesis and a comparison.

Contents

7.1 Thermocouples

Temperature has been a key parameter in most irradiation experiments carried out in MTR as it is a fundamental physical parameters to assess phenomena taking place during irradiation. One of the most developed and robust technologies are thermocouples, which have been adapted to the nuclear environment.
The fundamental physical principle is the Seebeck effect, thus the occurrence of an electromagnetic force between pairs of points in any individual electrically conducting material due to a difference of temperature between them [Web99]. For certain couple of materials the relation between the generated e and the temperature T can be approximately considered linear according to:

$$e \approx aT \tag{7.1}$$

They have a characteristic diameter of about 1 mm. A schematic view of a thermocouple and the equivalent circuit are shown in figure 7.1.

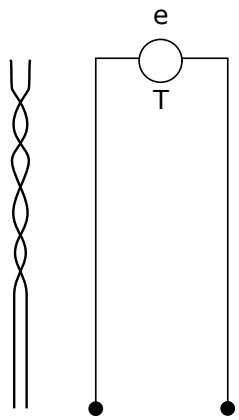

Figure 7.1 – The scheme of a thermocouple (left) and the equivalent circuit (right) [Web99]

For temperatures below 1000°C, the typical range of variation for the cladding and the pellet surface, type K (Ni-Cr/Ni-Al) and type N (Ni-Cr-Si/Ni-Si) TC show good performance, excellent reliability and stability under irradiation, even for very high integrated neutron fluences exceeding 10^{22} n/cm^2 [Vil08].
Major difficulties have been encountered through the years for the applications where temperature overcomes the 1000°C, towards the thermal range of fuel center. Indeed type K and type N TC drift at temperature T > 1000°C.
In-pile measurements in this range have generally employed Type C TC (W-Re alloys). But, they show to rapidly present a significant change in the wire composition caused by neutron induced transmutation.
To cope with the need for improvement in the in-pile high temperature measurements, INL and CEA have independently developed their thermocouples with Mo/Nb based thermoelements.
CEA has proved the higher performances of the pure Mo/Nb after extended tests on several samples in an induction furnace at 1600°C[Vil08].
INL has developed a doped Molybdenum-niobium alloy TC named High Temperature Irradiation Resistance ThermoCouple (HTIR-TC). Figure (a) of 7.2 compares the HTIR-TC performance with type K and N thermocouples at 1200°C. We observe that after 4000 h the doped TC presents limited decalibration of 20°C (2% of the imposed temperature).

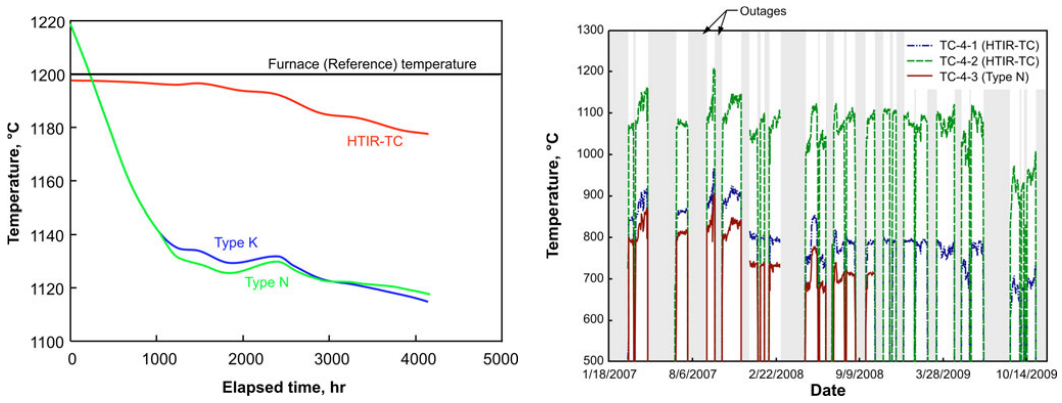

(a) (b)

Figure 7.2 – (a) Test carried out by INL on the performance of type K, N, and HTIR-TC thermocouples, submitted to 1200°C for 4000h. Out of pile tests. (b) Tests carried out by INL on the performance of HTIR-TC in the AGR-1 reactor [Rem11]

Tests were then performed under irradiation in the Advanced Gas Reactor-1 (AGD-1) at temperature up to 1200°C [Rem11]. The test lasted approximately 1 year and a half, between 2007 and 2009. Figure (b) of 7.2 illustrates the performance of two HTIR-TC, one at 1200°C(green) and the other (blue) next to the type N thermocouple (red) in a cooler region, during an experiment carried out in the Idaho National Laboratory's reactor ATR. We observe that at the beginning of the irradiation, the HTIR-TC and the type N TC in the cooler region give consistent results compared to the ones resulting from the HTIR-TC placed in the hotter region.
In the figure it is showed that during the irradiation, the type N thermocouple failed and its signal ceased.

Recent tests carried out by the INL in conjunction with the Boise State University and the Idaho Laboratories Corp have shown that the HTIR-TC have lasting results in the reactor at 1450°C and that the thermocouples could be eventually pushed to the range of 1600°C or beyond [Ski19].

In the frame of an experiment dedicated at the detection of relevant temperatures for PCI characterization, type K and N thermocouples are a robust and reliable technology to measure of the surface temperature of the cladding and of the fuel (T_c^e and T_f^e), while they cannot stand the centerline fuel temperatures, neither the ones reached at normal temperature conditions. For this range, type C and HTIR-TC show good performance.
The measurement performed via a TC is the local temperature at the TC extremity. The first consequence is that a transfer function has to be established, between the temperature of the target object and the one detected. Second, the TC has to be placed as close as possible to the target object, even in contact which involves a local perturbation the system. This perturbation varies depending on the specific application. For the measure of T_c^e, the presence of the thermocouple leads to a local modification of the cladding-coolant thermal exchange and to the origin an hot spot on cladding surface. The consequences on the local PCI phenomenon require a dedicated study. To measure the T_f^i, the thermocouple has to be introduced in the center of the pellet, drilling it. Temperatures interesting for PCI application are the ones toward the central region of the fuel rod, that leads to the

necessity to drill half of the fuel stack.
About the measurement of the pellet surface temperature T_f^e, the geometrical configuration of the fuel rod is not compatible with the introduction of a thermocouple in the gap. This means that, to locally extract the surface temperature of the pellet at a certain axial position, a grooving should be performed on the pellet surface, to host the thermocouple. This results into a local modification of the thermal-mechanical behavior of the fuel rod, a loss of axis-symmetry of the behavior and a fundamental modification of the local thermal exchange between the pellet and the cladding. We consider the resulting perturbation of the thermal-mechanical behavior not compatible with the requirement for PCI detection and measure.

7.2 Expansion thermometer

The expansion thermometer (ET) is based on the measure of the thermal expansion of a tungsten rod which passes in a central hole, drilled through the whole fuel stack. The thermal expansion of the rod is measured by means of a linear voltage differential transformer (LVDT), which operation is discussed in chapter 9 and is detailed in appendix C. The sensor has been developed by the IFE/HRP to monitor the average temperature during long time irradiation of nuclear fuel in the Halden reactor. The main advantage of this technological solution is that, with respect to thermocouples, it does not present any drift in the output signal due to neutron induced transmutation. The design of the device is represented in figure 7.3.

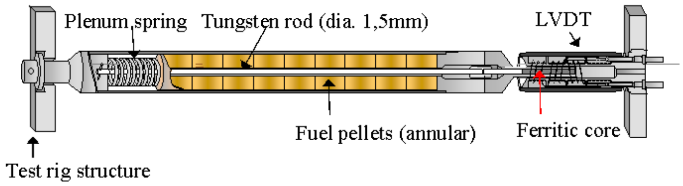

Figure 7.3 – Principle of the IFE/HRP expansion thermometer: the fuel stack heats up the tungsten rod, which is introduced in a central hole drilled in the entire fuel stack. The thermal increase makes the W rod expand. The expansion is measured by means of the LVDT fixed on the test rig structure [Nie09]

This device has showed to work well under irradiation and its design is adapted to the harsh nuclear environment. But, it results from the measurement principle that the temperature measured through the expansion of the tungsten rod is the average temperature in the tungsten rod and not the one of the fuel stack with a consequent strong source of measurement uncertainty.
In the frame of PCI behavior, the effects of a central hole performed along the entire fuel stack completely changes the thermal-mechanical evolution of the phenomenology, with a perturbation of the system that is not compatible with the aims of the experiment. This sums to the fact that the only accessible quantity is an average temperature along the fuel stack axis and make this technological solution not relevant to the study of PCI.

7.3 Ultrasonic thermometer

Ultrasonic thermometers work on the principle that the speed at which sound propagates in a material (acoustic velocity) depends on the temperature of the material itself. The most studied and thus the better developed type of ultrasonic thermometers are the ones based on the pulse echo method. By sending an ultrasonic pulse through a thin magnetostrictive rod (diameter from 0.25 to 1 mm) of known length and measuring the time between the initial pulse and its reflection from the opposite side of the rod, the average acoustic velocity can be evaluated and the average temperature in the rod derived. By introducing acoustic discontinuities in the rod, like diameter variations, a multiple point measure can be performed. For thin rods, the acoustic velocity is related to the Young's Modulus $E(T)$ and the material density $\rho(T)$ through the following formula:

$$\nu(T) = \sqrt{\frac{E(T)}{\rho(T)}} \tag{7.2}$$

Figure 7.4 extracted by [Lau10] represents the typical design of a multi-sensor ultrasonic thermometer system. As indicated, a narrow ultrasonic pulse is generated by the excitation coil in the thin rod. This pulse propagates in the sensor, where a fraction of the original pulse is reflected at each discontinuity. These reflections are collected by the excitation coil, transformed into an electrical signal, amplified and evaluated in the counter system. The time intervals obtained are compared to a calibration curve to give the average temperature of the rod segment.

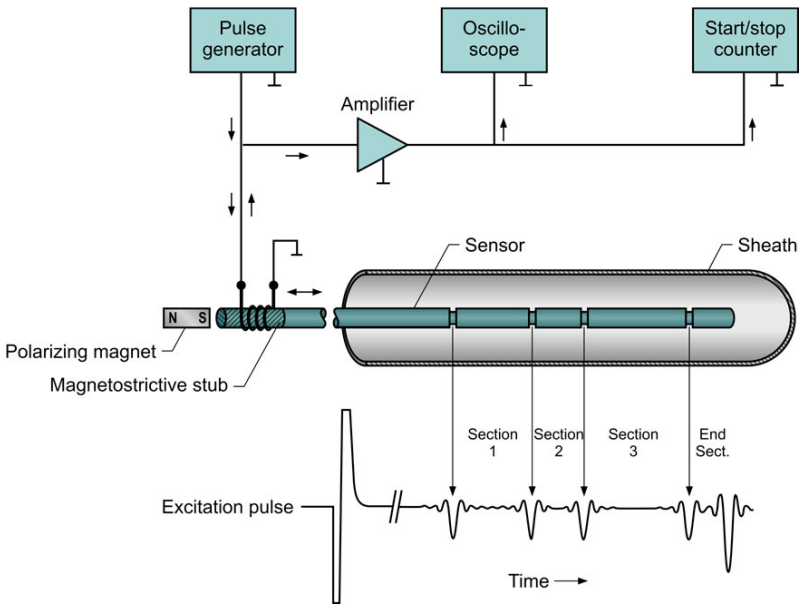

Figure 7.4 – A typical multi-sensor pulse-echo ultrasonic thermometer system [Lau10]

This type of thermometers has demonstrated to resist very high temperatures, up to 2800°C, which is in the range of the melting temperature of the uranium dioxide, during experiments carried out by CEA in the PHEBUS reactor [Phe07] and by INL to measure the centerline temperature of fuel component[Daw10].

This technological solution presents different advantages and disadvantages for application to measure the centerline fuel temperature. First of all, just like thermocouples, extensometer and as we will see in the next section, optical based sensors, this sensor requires the central drilling of a part of the fuel stack. As we said before, the local modifications of the system are expected to be not compatible with the studied mechanisms.
The technological solution is interesting to validate code calculation out of the zone concerned by the study of PCI. In this frame, with respect to the thermocouples, it allows a distributed measurement. Nevertheless, the open literature available on the experimental characterization does not specify the limits of the spatial discretization, the effects of the acoustic attenuation that occurs along the sensor length on the output signal and how to distinguish between the reflections at the discontinuity and the ones at a contact point between the sensor and its sheath.

7.4 Johnson noise thermometer

The principle of the method, that was published in the Physical Review Letters by Johnson and Nyquist [Jon28], is to use the thermal agitation of the electrons in a conductor as an indication of its temperature. An unloaded passive network always presents at its ends a voltage, fluctuating statistically around zero. The mean square of this voltage, in the range of T>100 K and for frequency f <1 GHz, has a negligible dependency of the frequency and is described by the following equation:

$$e_n^2 = 4kTR \tag{7.3}$$

where the means square of the voltage is expressed in V^2/Hz, k is the Boltzmann constant, T the temperature in Kelvins and R the resistance of the network.
For a frequency bandwidth Δf, the above expression becomes:

$$e_n = \sqrt{4kTR\Delta f} \tag{7.4}$$

The interest of this kind of technological solution lies on the fact that the measurement principle should not be affected by drift under irradiation as it is independent on the physical properties of the sensor, except for its resistance, that needs to be measured.
The main difficulty is related to the fact that the generated voltage is really small: for a bandwidth of 1 MHz and 1kΩ resistor, the RMS voltage amounts to just 1 μV, which is the limit of current precision measurement capabilities. It results that long measurements are required to obtain a good statistics of the measured temperature. Also, it is affected by the electromagnetic perturbations of the surrounding environment.
Recent development presented by the National Physical Laboratory and Metrosol Limited [Pea19] concern a proof-of-principle prototype that demonstrated an uncertainty in the measure of 0.28°C (2σ) with a measuring time of 6.5 s.

The characteristics of this sensor makes it an interesting solution to re-calibrate the other sensors during irradiation but it is not compatible with the transients of a power ramp test to study PCI.

7.5 Fiber Bragg Gratings

Fiber Bragg Gratings are one of the several Optical Fiber Sensors (OFS) which is considered a promising technological solution for measurements in the nuclear environment because of the fundamental properties characterizing the optical fiber sensors: reduced size to limit system perturbation, quasi-immunity to most electromagnetic perturbations and intrinsic high accuracy. A presentation of the Optical Fiber Sensors and the main aspects of the evolution of optical properties under irradiation are presented in appendix B.

FBG consists of a periodic perturbation of the core refractive index, associated to a period Λ typically from 0.5 µm up to a few µm, performed on a certain extension of the optical fiber. The modulation of the refractive index is realized taking advantage of the photo-sensitivity of the doped optical core (type I FBG), by focusing a UV laser light at a point of the core, locally increasing its index n and translating the laser or the optical fiber along the axis. Due to this modulation, a coupling is created between the input and the output light. Figure 7.5 represent the principle of a FBG: a white light is injected in the fiber where the FBG is realized, with a certain period Λ, and the transmitted and the reflected spectrum are showed.
They are both characterized by a specific wavelength λ_{Bragg} which depends on the modulation of the refractive index:

$$\lambda_b = 2n_{eff}\Lambda \tag{7.5}$$

where n_{eff} is the effective refractive index of the propagating core mode. We can say that the FBG work as a band pass filter in reflection and a stop-band filter in transmission.

The basic principle of spectral multiplexing applied to the FBG transducer is that by

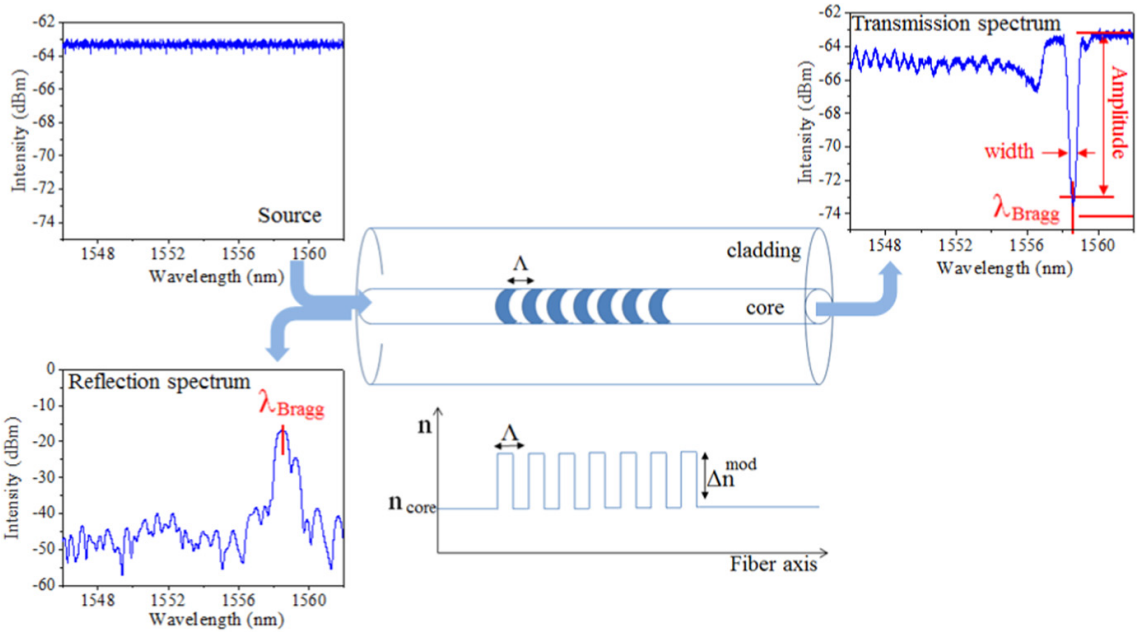

Figure 7.5 – The scheme of the FBG written on an OF. In the example the white light spectrum of the source is injected in the waveguide and the measured transmission and reflection spectra of the FBG are illustrated. At the figure center, the FBG is schematized as a modulation of the refractive index along the fiber axis [Gir18]

simply changing the grating pitch, the Bragg wavelength can be modified from one FBG to another, written on different locations of the same optical fiber.

The sensing nature of FBG lies on the fact that a temperature variation ΔT results into the offset of the Bragg wavelength $\Delta\lambda_b$ due to the coupled effect of the thermal dilatation of the optical fiber which modifies the periodicity of the modulation λ and the evolution of the refractive index with the temperature (thermal-optic effect). The relation can be expressed as follows:

$$\frac{d\lambda_b}{dT} = \lambda_b \left(\frac{1}{n_c} \frac{dn_c}{dT} + \frac{1}{L} \frac{dL}{dT} \right) \tag{7.6}$$

where n_c is the refractive index of the core and L the length of the grating.
For silica fiber, the thermal dilatation is about $5 \cdot 10^{-7}\mathrm{K}^{-1}$ and the thermal-optic coefficient $1 \cdot 10^{-5}\mathrm{K}^{-1}$. The thermal sensitivity of the FBG is linear with respect to λ_b:

$$\frac{\Delta\lambda_b}{\Delta T} \approx 7.3 \cdot 10^{-6} \lambda_b \tag{7.7}$$

In the optical range of interest for nuclear application, the thermal sensitivity range at about 10 pm/°C.
It has to be said that the Bragg wavelength is sensitive not only to temperature but also to the applied pressure and strain. The application of an FBG as a temperature transducer has to take into account these sensitivities by making the sensor insensitive to the other parameters with suitable conditioning or by compensating or correcting the measure [Gir18].
Commercially available FBG present two main technological limits for their application in the nuclear environment: weak thermal stability and radiation sensitivity. Indeed, an intrinsic feature of FBG realized by taking advantage of the photo-sensitivity of the optical core is that the realized modulation erases at high temperatures. A commercial FBG disappears after few hours at 300°C, which is lower than cladding surface temperature.
We discuss in the following the main developments in these two fields.

7.5.1 Development of high temperature FBG

Several methods have been proposed in literature to increase the thermal stability of germano-silicate photosensitive optical fiber. Nowadays the most promising ones are:

- The thermal regeneration of FBG;
- The femtosecond FBG.

The regeneration method was discovered by M. Fokine in 2002 [Fok02] during his Ph.D. works and constitute an attractive approach to increase the operating lifetime of FBGs in high temperature environment [Can09][Laf13]. It consists in taking a standard FBG which is first erased through an annealing temperature close to 900°C and subsequently a new Bragg peak appears on the spectrum. The regeneration process and the evolution of the reflectivity of the OFS are presented in figure 7.6: the original FBG is stable during the step at temperature 700°C and it is erased when the temperature approaches 900°C. Then, during the holding time at this temperature, the regeneration process takes place and the OFS reflectivity increases gradually up to a maximum level. The resulting behavior of the so called "re-generated FBG" depends on the optical fiber itself, on its chemical composition and on the regeneration protocol [Laf18].

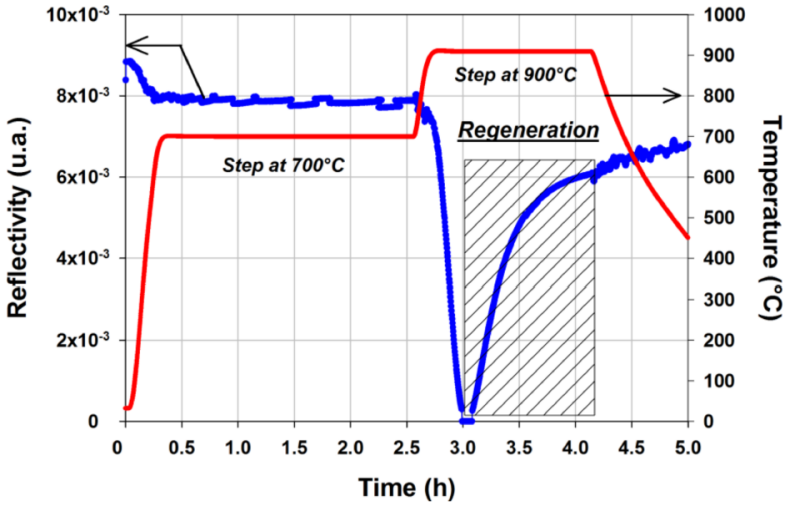

Figure 7.6 – Evolution of the FBG reflectivity during the regeneration process [Laf18]

Tests presented by Laffont in [Laf18] show that regenerated FBG can withstand a one-year long thermal aging at temperatures very close to their regeneration temperature without disappearing, even though a moderate wavelength drift has been observed.
This type of thermal treatment present some difficulties related to the chemical and mechanical reliability of regenerated FBG. Indeed, the regeneration process had to be performed over a limited region of the OFS, where the protective jacket has been removed. The unnecessary heated up regions of the fiber present cumulated defects which increases the brittleness of the unprotected fiber [Laf18].

The **femtosecond FBGs** result of an advanced photo-writing technique based on an ultra-fast laser and can operate beyond the regeneration temperature and present a greater mechanical reliability. By focusing an intense pulsed laser beam from a femtosecond near-IR laser, micro-explosions are generated in the optical core that lead to the formation of localized micro-voids. By translating the OFS in front of the pulsed laser source at a constant speed, an array of micro-voids with constant pitch is obtained along the fiber axis. This array of micro-voids origins a spectral resonance corresponding to Bragg peak. This technology has several advantages: it is not based on the photo-sensitivity of the OFS, so it presents increased thermal stability, beyond 1000°C, can be performed without the need to dope the optical core and by using pure silica fiber, which are the most adapted to nuclear environment [Laf18] and can be performed without removing the protective jacket of the OFS.
Micro-voids based FBG have been demonstrated to be operational at temperatures up to 1300°C [Laf18] in silica based optical fiber. For applications beyond 1300°C, investigations on different types of femtosecond inscription techniques are being performed.

7.5.2 FBG performance under irradiation

The radiation sensitivity of optical fibers is a first concern in the development of FBG for the nuclear field. As detailed in appendix B, three main radiation effects are observed at the macroscopic scale when the silica-based optical fiber are exposed to radiation. The first one is the Radiation Induced Attenuation (RIA) , which progressively degrades the guided signal up to its loss; the second is the Radiation Induced Emission (RIE) that is a

parasitic light that superposes on the propagated signal and decreases the Signal-to-Noise Ratio; the third effect is the Radiation Induced Refractive Index Change (RIRIC) which causes a drift of the Bragg wavelength with an increase of the measurement errors [Gir18]. On-line experiments are required as the dynamic behavior of FBG under harsh environments coupling high temperature and radiation are difficult to anticipate and predict with present knowledge [Laf18].
Preliminary studies have been carried out at CEA on regenerated FBG: an high temperature furnace has been placed in the irradiation area of a high energy linear accelerator emitting X-rays. Preliminary results show that the radiation induced error in temperature measurement decreases with the increase of the operating temperature [Laf18]. This highlights the interest in developing such devices for nuclear applications but further investigations are required, where regenerated and femtosecond FBG must be directly tested in research reactors.

7.5.3 Application of FBG to PCI detection and measurement

The intrinsic accuracy of FBG and the possibility to realize a distributed measure along the fiber length is interesting for nuclear application, in the frame of thermal measurements, and push for their further development to stand radiation and high temperatures. Compensation for the strain sensitivity has to be taken into account: this can be realized through a relative measurements using multiple optical fiber systems and a relative measurement or by isolating the optical fiber from the surrounding environment by a mini-tube as to avoid the origin of strains.
Regenerated FBG are a practical solution to obtain FBG resistant to high temperature with a thermal treatment but with strong consequences on the mechanical reliability of the device.
Femtosecond FBG are a promising solution for application at temperatures even higher than 1300°C, making it an interesting solution, meeting all the measurement requirement for temperatures in PCI detection and characterization in normal operation conditions.
A first consequence of the measurement principle of FBG is that they measure the temperature in the optical fiber which requires to establish a transfer function between the measured temperature and the target one; second, this error reduces if the two objects are in contact. As for the aforementioned technological solutions, the resulting perturbation depends on the specific application:

- For the measurement of the T_c^e: the optical fiber, or the mini-tube surrounding it, has to be attached to the fuel rod surface. By multiplexing the fibers, we obtain the thermal profile along the entire rod axis. Consequent to the contact, the thermal exchange between the cladding and the coolant is limited by the presence of the optical fiber and a local increase of temperature origins. The perturbation of the system must be estimated to judge the representativity of the measure.
- To measure the T_f^e: as for TC, the geometrical configuration and the PCI phenomenon itself make it impossible to introduce an optical fiber inside the fuel rod, between the pellet and the clad. A grooving of the pellet surface can be proposed, where the optical fiber inside a mini-tube is introduced without a modification of the encumbrance of the fuel stack, as it has been proposed for the TC. It results that the local thermal-mechanical modifications are not negligible and dedicated studies must be performed to evaluate the representativity of performed measurements.
- To measure T_f^i: the fuel stack has to be drilled to permit the introduction of the optical fiber, like for TC. Taking into account the need of a mini-tube to protect

the fiber from the mechanical stresses, the characteristic dimension of the drill is in the same order of the one required for a thermocouple. There, the optical fiber is submitted to the highest temperatures of the system, to the interaction with beta radiation and fission products. The interaction with the fiber matter can result into enhanced transmutation and an enhanced attenuation or loss of the output signal. Its resistance to these conditions must be studied.

7.6 Scattered light based distributed sensors

The laser light injected into a silica-based fiber can be transmitted, absorbed or scattered by the material. There exists two types of scattering, which are represented in figure 7.7:

- The elastic scattering: if the scattered light and the injected one have the same wavelength. This is the case for the Rayleigh scattering;
- The inelastic scattering: when the scattered light presents a different wavelength, as in the case of Raman and Brillouin emissions. When the inelastic interaction between the incident light and the fiber leads to an energy transfer to the latter, the scattered light has a frequency lower than the incident one as it is know as Stokes component. On the contrary, if energy is absorbed by the photon, the wavelength of the scattered light is shifted upward and it is known as Anti-Stokes.

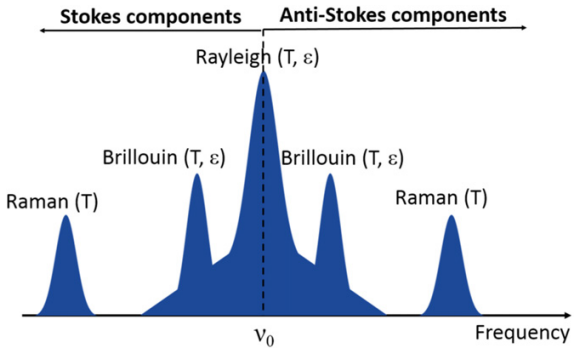

Figure 7.7 – Schematic represtnation of the spectrum of a scattered signal as a function of frequency. ν_0 is the frequency of the incident light [Gir18]

Emissions are intrinsically dependent on the optical fiber properties, which vary according to the environment surrounding the fiber. By measuring the shift of the characteristic Rayleigh, Raman and Brillouin wavelength, the evolution of externally applied stimuli can be measured (temperature and strain).
Different techniques are used to measure the backscattered emissions:

- Optical Time Domain Reflectometry (OTDR): a pulsed signal is injected at one end of the fiber. After interaction with the silica material, the back-scattered light is recorded, the time t needed by the incident signal to reach a point at a certain distance along the fiber and for the back-scattered light to be collected is:

$$t = 2v_g z \tag{7.8}$$

where $v_g = nc$ is the velocity of the propagated light in the medium, which depends on the refractive index n and the light velocity in vacuum c, and z the traveled distance. This lead to the fact that the spatial resolution of the sensor is directly related to the pulse width duration.

– Optical Frequency Domain Reflectometry (OFDR): in this case, the light of a tunable laser source is injected into the two arms of an interferometer and from the spectral analysis of the interference patterns between the measured light and the reference one it can be obtained the variation of the applied temperature (or strain) and the spatial localization of this information.

In the following we detail the different types of sensors and associated developments, focusing on the OFDR measurement techniques, as we are interested in the localization of the temperature measurement for PCI detection and characterization along the fuel rod.

7.6.1 Rayleigh-based sensors

Rayleigh scattering is an elastic phenomenon characterizing optical fibers, caused by the random fluctuation of the refractive index, due to small variations in density or dopant concentrations. Each fiber presents its own Rayleigh signature giving the back-scattered light amplitude as a function of the distance. Such a signature locally changes when an external stimulus is applied, as temperature or strain. This is the principle for the Rayleigh based optical fiber distributed sensors: a temperature and/or a strain variation applied to a segment of the fiber length can be measured by comparing the measured Rayleigh signature with the reference one.
From the spectral cross correlation of the reference and scattered Rayleigh signal, it results a peak in the spectrum. The shift of this peak is proportional to the temperature and strain variation according to the following equation:

$$\frac{\Delta\lambda}{\lambda} = C_T \Delta T + C_\varepsilon \Delta\varepsilon \tag{7.9}$$

where C_T and C_ε are the temperature and strain coefficients, respectively. For a germano-silicate fiber they amount to $6.5 \cdot 10^{-6}$ 1/°C and 0.8 $\mu\varepsilon$/°C.

7.6.2 Raman-based sensors

Raman scatterings are nonlinear effects which come from the inelastic interaction between the light and the molecular structure of the fiber that can transfer a small fraction of the incoming electromagnetic field into two other fields, which frequencies are downshifted and up-shifted by a specific amount: a Stokes component at λ_s and an Anti-Stokes wave at λ_A. Raman based sensor are not sensitive to strain and only to temperature. This technological solution operates on the ratio of the intensities of the Stokes and the anti-Stokes signals , $R(T, z)$ which depends on the the position along the fiber length z and on the local temperature T accoding to the following relation [Gir18]:

$$R(T,z) = \left(\frac{\lambda_S}{\lambda_A}\right)^4 exp\left(-\frac{h\nu_R}{k_B T}\right) exp\left(-\int_z^0 (\alpha(\nu_{AS}, u) - \alpha(\nu_S, u))du\right) \tag{7.10}$$

The first factor takes into account the different frequencies of the Stokes and the Anti-Stokes waves, the second one accounts for the dependency on temperature through h is the Planck's constant, ν_R is the Raman frequency shift, k_B is the Boltzmann's constant. The third factor includes the differential losses, due to the different attenuation α at the two frequencies of the emitted signals. This last term is non-negligible in a radiative environment.

7.6.3 Brillouin-based sensors

Brillouin scattering is the inelastic scattering of a photon from fluctuations in the density of the medium, with the creation of a Stokes and of an Anti-Stokes acoustic phonons. The frequency of the scattered light is shifted with respect to the excitation one by a quantity named Brillouin frequency ν_B and defined by the following equation, as reported by [Gir18]:

$$\nu_B = \frac{2n_{eff}V_a}{\lambda_0} \tag{7.11}$$

where n_{eff} is the effective refractive index in the propagating medium, V_a is the acoustic speed of silica (about 5800 m/s) which depends on the density, an λ_0 is the wavelength of the incident light. Brillouin frequency generally ranges between 9-13 GHz depending on its composition.
As the acoustic speed depends on temperature and applied strain, the Brillouin frequency is shifted under the coupled effect of the two parameters which leads to the necessity to compensate the measurement the dependency on strain for application as temperature sensor, or limit it by manufacturing.

7.6.4 Performance of scattered light based technologies

Scattering light based temperature sensors benefit from the intrinsic accuracy of the optical measure and permit to access the thermal profile of the target object rather than a localized temperature, with a minimum spacing occupied by the sensor. At present days, further improvement in rad-hard optical fibers are required and in-pile qualifications of sensor performance.

Several studies have been performed to investigate the performance of Rayleigh based sensors in radiation environment. As reported by Rizzolo in [Riz17], radiation hardened optical fibers associated to the OFDR sensors are able to operate up to demonstrated dose $>$ 2 MGy and to mixed neutron and γ radiations up to 10^{17}n/cm^2/s with limited drifts and measurement errors: the temperature measurement feasibility is demonstrated with an accuracy of 0.1°C over a sensing length up to ∼130 m.

A main issue in the application of Raman-based sensors in a nuclear environment is that in addition to a reduction of the sensing with the dose, the RIA affects the Stokes and the Anti-Stokes signal is two different ways. This differential RIA results in an error in the evaluation of the ratio between the two scattered emissions. This phenomenon is generally known as ΔRIA [Jen98][Fern05] and leads to a measurement error increasing with fiber length [Gir18]. A solution to this radiation induced effects consists in compensating the ΔRIA with the cost of doubling the RIA issue. Using this solution, Lecompte [Lec17] demonstrated that Raman-based sensors can be used to monitor temperature evolution around 350°C up to a few kGy.

For Brillouin-based sensors, two effects have been observed under radiation: the RIA and the Radiation-Induced Brillouin Frequency Shift (RI-BFS). Even though the origin of this phenomenon are still not completely understood, it is clear that the shift depends on the fiber composition so that both effects can be minimized by optimizing the design of the OFS. Nowadays, fluorine-doped fibers are the best candidates for these applications, as they have limited RIA levels at MGy dose level a limited RI-BFS to a temperature error of few degrees of Celsius [Gir18].

Table 7.2 resumes the performance of the discussed technologies in terms of spatial resolution, strain and temperature measurement accuracy. The table gives typical values as reported by [Gir18], that are accessible at the time at which the technologies are evaluated under irradiation. The research being really active in this field, the reported values are continuously optimized.
As reported in the table, the spatial resolution and the temperature accuracy of Rayleigh and Brillouin-based OTDR are not compatible with the characteristic dimension of the sample rod and the required accuracy of the measurement. Further assessment have to be performed on the minimum spatial resolution of Brillouin-based BOTDA (Brillouin Optical Time Domain Analysis) and Raman-based OTDR but their accuracy meets the measurement requirements [Gir18].
Rayleigh-based OFDR meets the measurement criteria but has to be compensated for the strain sensitivity while a great advantage of Raman based is that strain is not a source of error.

Type	Acquisition	Spatial resolution	Temperature accuracy	Strain accuracy
Rayleigh	OTDR	1 m	15°C	not available
	OFDR	From 1 cm to 10 µm	0.1°C	1 µε
Brillouin	BOTDR	1 m	10°C	60 µε
	BOTDA	<50 cm	1°C	20 µε
Raman	OTDR	<50 cm	1°C	not sensitive

Table 7.2 – The main characteristics of scattered light based optical sensors [Gir18]

For the application of Raman-OFDR, Brillouin-BOTDA and Raman-OTDR to the monitoring of temperatures relevant for PCI detection, the discussion is similar to the one illustrated for FBG devices: their application can be proposed to obtain the profile of the T_c^e, T_f^e and T_f^i but the modifications induced in the thermal-mechanical behavior of the fuel rod must be attentively studied.
Studies are being carried out on the attenuation of the signal-to-noise ratio of Rayleigh scattering at high temperatures: indeed high temperatures seem to induce a transformation in the silica matrix with consequences on the elastic scattered light. This constitutes a technological limits for the monitoring of high temperatures, like the centerline fuel temperature, but solutions are under investigation [Gir18].

7.7 Optical Pyrometry

Optical pyrometry is a non contact temperature measurement based on the emissivity of the object to be characterized. The basic measurement principle is the Planck's law: the radiance per unit length of the emitted radiation from a black body $R_{bb}\mathrm{W/m^2/sr/m}$, a perfect absorbing medium for all incident radiation, is a function of its temperature according to:

$$R_{bb}(\lambda, T) = c_1 \left[\frac{\lambda^{-5}}{exp\left(\frac{c_2}{\lambda T}\right) - 1} \right] \tag{7.12}$$

with $c_1 = 1.1908 \cdot 10^{-16}$W.m^2/sr, $c_2 = 0.01438$m.K, λ the measurement wavelength and T the temperature of the target object. The radiance of a real body is lower than the one of a black body and this deviation is expressed by the emissivity ε which is, in first approximation, a function of λ and T.
The thermal flux emitted by the target is collected by the optical fiber and transferred from the target object to the IR spectrometer.
Multispectral pyrometry is under development in the recent years for its application in the LORELEI (Light Water One-Rod Equipment for Loca Experiment Investigation) device, one of the irradiation devices to be installed in the JHR research reactor, dedicated to studying the loss-of-coolant accident. According to the scenario under investigation, the development focuses on air or water vapor environment and a temperature range of 700-1200°C.
In this frame, Ramiandrisoa et al. [Ram14] experimentally characterized the accuracy of pyrometry measure on cladding sample in air atmosphere up to 1000°C. This has been supported by the following studies carried out by Bouvry [Bou17][Bou18] who highlighted the influence on the measured temperature coming from a surrounding at high temperature.

In the frame of its application in an experiment dedicated to study PCI, the main interest of this technological solution is that it is the only identified sensor that allow a **remote temperature measurement**. Also, it benefits from the fact that, as it is based on optical fiber, the sensor can be miniaturized.
Optical pyrometry requires to be placed in front of the target object, which is impossible when the researched temperature is the surface temperature of pellet because the geometry of the fuel rod and the PCI phenomenon lead to the impossibility to access it.
For similar reasons, the optical pyrometry cannot be applied to measure the centerline temperature of pellets placed within the fuel stack. But, it can be applied for the purpose of code validation on the top of the fuel stack, to measure the local temperature of the top pellet with a minimum perturbation of the system. Also, by displacing the sensor, a partial or complete thermal map of the radial evolution of the pellet temperature can be obtained.

For the application of this technological solution to measure the cladding external temperature T_c^e, several main research axis have to be investigated:

- Verification of the capability of IR to pass through the surrounding water. A positive factor is that the absorption spectrum of water is low in the range of the near IR (spectral range <1.3 µm) which corresponds to the selected one by Bouvry in its studies [Bou18];
- Verification of the performances of optical pyrometry at lower temperatures: cladding external surface presents at normal operation condition a temperature around 300°C. The radiance of a body strongly decreases with temperature which makes the measure more complex;
- Development of a sensor capable to resist the corrosive water environment, high temperatures, pressure and radiation;
- Miniaturization of the sensor to fit the geometrical burdens of irradiation devices.

7.8 Concluding remarks

We have discussed in this chapter different technological solutions to measure on-line the temperatures of interest for PCI detection and characterization that are the cladding surface temperature T_c^e, the pellet surface and centerline temperatures, T_f^e and T_f^i, respectively.
The performance of the investigated technologies are resumed in table 7.3.
From a general point of view, from the previous discussion we have concluded that:

- The expansion thermometer is too intrusive and is not recommended to investigate the centerline temperature of the fuel;
- The Johnson noise thermometer is rather eligible for in-pile recalibration of thermal sensors than for monitoring of a target object as a consequence of the long acquisition time required for a single sampling.

We focus now on the target parameters to be characterized.

Monitoring of T_c^e: Among the technological solutions investigated, the design of the ultrasonic thermometer make this technology not adapted to monitor the cladding surface. Thermocouples have the advantage of being a robust technological solution, with several applications in the nuclear environment. All the reported types meet the range of investigated temperature. But they allow a single point measurement (at the bottom of the TC) and require to be in contact to the target object.
Fiber Bragg Gratings are an interesting alternative to thermocouples as they are characterized by reduced encumbrance and can perform distributed measurements. They require at present days further developments to resist to radiation. Regenerated and femtosecond FBG show promising results to extend the operating range at temperatures well above the one of the cladding surface.
In addition to temperature, FBG are sensitive to strain, which imposes compensation or correction of the measurements performed.
Just like FBG, scattered light based optical sensors are eligible for application to the distributed monitoring of T_c^e. To meet the spatial resolution, the retained technological solutions are the Rayleigh-based OFDR, that also present an accuracy of 0.1°C, the Brillouin based BOTDA and the Raman-based OTDR. Among these optical based sensor, the only one that doesn't need to be compensated for strain is the Raman sensor.
All these sensors require to be in contact with the target object: the presence of the sensor locally reduces the thermal exchange between the cladding and the coolant with a consequent modification of the unperturbed system. A dedicated evaluation of the induced perturbation must be performed.
Finally, optical pyrometry is the only technological solution identified that allows to perform the remote measurement of the target local temperature. Investigations must be done to verify the performance of this technology for temperatures in the range of 300°C.

Monitoring of T_f^e: On the basis of the investigated technological solutions, the measurement of T_f^e cannot be performed without introducing the sensor directly inside the sample rod, which induces a strong perturbation of the system: it modifies the local thermal-mechanical behavior and the local thermal exchange. These effects are not compatible with the requirements of PCI detection so that we conclude that none of the investigated technological solutions is eligible to monitor T_f^e in the frame of PCI characterization.

Monitoring of T_f^i: The range of variation of the T_f^i, from 1000°C in normal operation conditions, at about 2900°C in case of melting onset, is very complex to investigate. Also, the geometrical configuration of the system makes the point of interest in the fuel stack difficult to access. From the previous discussion is results that, except from the optical pyrometry that can be used to remotely measure the temperature of the bottom pellets, it is not possible to access the central temperature of the fuel pellet towards the mid-rod plane without drilling an important portion of the fuel stack. Among the available technologies, the only adapted to this range of temperatures are the type C thermocouples, which are limited to 2000°C and can stand radiations for a limited time, and the ultrasonic thermometer, which allows to reach temperatures up to 2800°C and perform a distributed measurement.
In the frame of PCI detection and measurement, non-negligible modifications are induced on the thermal-mechanical behavior of the pellet by the central hole and must be concerned by a dedicated study to analyze the representativity of the measured quantities with respect to the unperturbed system.
These two technologies are interesting to validate code calculation out of the zone concerned by the study of PCI. In this frame, ultrasonic thermometer also allows a distributed measurement, even though further experimental characterization in research reactor are required.

Technology	**Range (°C)**	**PCI Application**	**Design**	**Resistance to Nuclear Env.**	**Status**
Type K Thermocouple	[0:1000]	T_c^e, T_f^e	Local measure, Contact required	Technological limit at T 1000°C	Operational
Type N Thermocouple	[0:1000]	T_c^e, T_f^e	Local measure, Contact required	Technological limit at T 1000°C	Operational
Type C Thermocouple	[0:2000]	T_c^e, T_f^e, T_f^i	Local measure, Contact required	Limited resistance under radiation	Operational
High Temperature Irradiation Resistance Thermocouple	up to 1600°C	T_c^e, T_f^e, T_f^i	Local measure, Contact required	Limited sensitivity to high temperatures Good performance under neutron flux	On going commercialization [Ski19]
Expansion thermometer		T_f^i	Average temperature, Contact required, Drilling of the whole fuel stack	Qualified under irradiation	Operational
Regenerated FBG	<1000°C	T_c^e, T_f^e	Distributed measure, miniaturized, contact required	Radiation induced drift, issue on mechanical reliability	On-going developments

Technology	**Range (°C)**	**PCI Application**	**Design**	**Resistance to Nuclear Env.**	**Status**
Femtosecond FBG	up to 1300°C (possible use >1300°C)	T_c^e, T_f^e, T_f^i	Distributed measure, miniaturized, contact required	To be compensated for ε Radiation induced drift	On-going development
Rayleigh based OFDR	<1000°C	T_c^e, T_f^e	Distributed measure, miniaturized, contact required	To be compensated for ε Limited resistance under radiation (RIA)	On-going developments
Raman based OTDR	<350°C	T_c^e	Distributed measure, miniaturized, contact required	Limited resistance under radiation (RIA and ΔRIA)	On-going developments
Brillouin-based BOTDA	not available	T_c^e, T_f^e	Distributed measure, miniaturized, contact required	To be compensated for ε Limited resistance under radiation (RIA)	On-going developments
Optical Pyrometry	<1000°C	T_f^i, T_c^e	Local measure, miniaturized, remote	Radiation effects on optical fiber sensors, to be adapted to lower temperatures	On-going developments
Ultrasonic Thermometer	<2800°C	T_f^i	Distributed measure, drilling required	Qualified but few experiments	Operational
Johnson noise Thermometer	not available		Local, contact measurement	Not affected	On-going developments for recalibration of other sensors

Table 7.3 – Synthesis of characteristics of investigated technologies for temperature measurements: External Cladding Temperature (T_c^e), External Fuel Temperature (T_f^e), Internal centerline Fuel Temperature (T_f^i)

Chapter 8

Pressure measurement

We have seen in part I that the internal pressure cannot directly allow the detection and the characterization of the PCI mechanism. Nevertheless, it constitutes a fundamental parameter for its indirect description: gaseous swelling, the increase of the fuel pellet dimension due to the progressive accumulation of fission products, is one of the main mechanisms driving the pellet deformation under irradiation. This is strictly related to the fission gas behavior and the amount which is released. Information can be obtained by monitoring the evolution of the internal pressure, which directly depends on the fractional release of fission products out of the fuel pellets.
Two technological solutions have been taken into account in this chapter to compare their capability to meet the measurement criteria defined via simulations, that show good performance in the nuclear environment ensuring the minimum perturbation of the system: the counterpressure sensor in section 8.1 and the acoustic sensor in section 8.2

Contents

8.1 Counterpressure sensor

This robust, reliable and qualified sensor has been developed by CEA and is based on the drift-less counterpressure principle [Vil03].
As illustrated in figure 8.1, it consists of two gas cavities, separated by a double expanding wall. The first cavity communicates with the internal fuel rod pressure. The second cavity is connected to an external helium loop, which is called the "counterpressure" circuit.

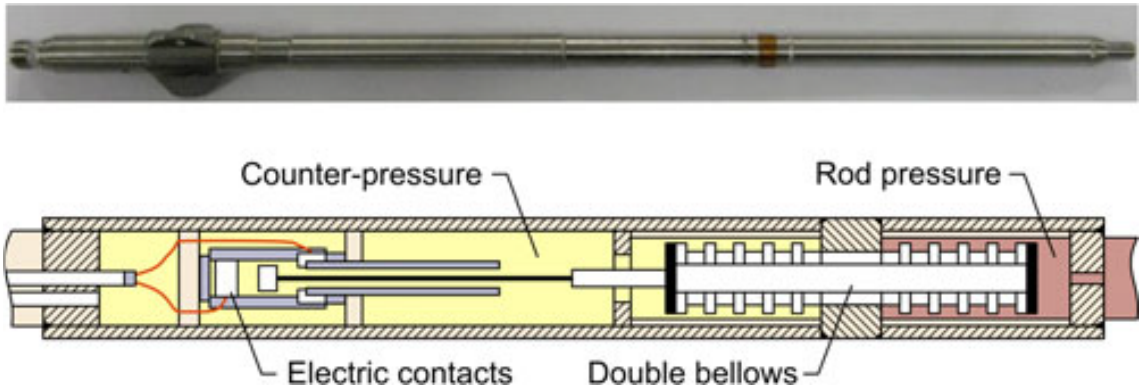

Figure 8.1 – CEA counterpressure sensor to measure the internal pressure inside the fuel rod [Kim11]

The imbalance between the internal rod pressure and the counterpressure is accurately detected by two electric contacts, activated by the motion of the double bellows, and can be compensated by inflating or deflating the counterpressure. From the simultaneous knowledge of the imbalance signal and the direct measure of the counterpressure from the helium circuit, the system permits to accurately measure the internal rod pressure.

The design of this sensor is studied to meet the needs of research reactors: to minimize its encumbrance and perturb as less as possible the system, the sensor has the same diameter of the sample rod (about 10 mm) and is roughly 25 cm long.
Its design is adapted to resist to the harsh environmental conditions of the nuclear reactor: neutron flux and gamma radiation, temperatures up to 350°C and up to 160 bars.

The qualification of the sensor has been carried out during the REMORA 3 experiment in the OSIRIS reactor: it showed no failure, thus proving its capacity to withstand the severe irradiation experimental conditions and the accuracy for the internal pressure measurement during the in-pile tests has been evaluated to amount to ± 0.325 bars (2σ) on the entire tested pressure range so up to 120 bars.
Thanks to its specific design and as it is always placed above the sample rod, out of the zone presenting the highest neutron flux, the counterpressure sensor shows no drift of the signal during irradiation.
The sensor has been successfully used during the REMORA 3 experiment with the acoustic sensor presented here below. We postpone the analysis of the instruments performance at the end of the following section.

8.2 Acoustic sensor

A dedicated acoustic sensor has been developed by CEA to measure the online fission gas release in the fuel rod during irradiation experiments. As illustrated in figure (a) of 8.2, the device presents a small cylindrical cavity, which contains the gas to be analyzed and is connected to the fuel rod upper plenum. On the upper part of the cavity, a thin stainless steel plate is welded in order to insulate the plenum volume from the outside. To this, a piezoelectric transducer is fixed, in order to generate and measure acoustic waves through the plate in the gas cavity. These acoustic waves propagate in the gas inside the cavity, where they are reflected. The signal and its echoes are recorded, measuring the time of flight of the signal and its attenuation. From the echoes attenuation it can be derived the internal pressure in the fuel rod. In addition to this, from the acoustic velocity of waves in the cavity, it can be derived the composition of the gas mixture.

The acoustic velocity depends on the molar mass and, by an accurate design of the system, it can be simply derived from the measure of the time of flight. In the case of a cylindrical cavity of length L the time of flight is:

$$\Delta t = \frac{2L}{c} \tag{8.1}$$

By the acoustic velocity c the molar mass can be obtained according to the following formula:

$$M = \frac{\gamma RT}{c^2} \tag{8.2}$$

where R is the universal gas constant 8.314 J/mol/K and γ the adiabatic index, equal to 5/3 for a monoatomic gas.

Figure (b) of 8.2 illustrates the measurement principle: the signal and its echoes are recorded, and the time of flight of the signal and its attenuation are measured. From these measurements it can be simultaneously deduced: the molar mass of the gas, from the acoustic wave velocity, and the pressure of the gas, from the echoes attenuation.

The development of this sensor to be applied in the nuclear environment has required several researches on piezoelectric components, which have the tendency to rapidly degrade under radiation. For this, CEA, IES Montepllier and SCK·CEN collaborated to identify the best performing material [Fou11]. As reported in [Gio17] a full scale device with Lead Zirconate Titanate piezoelectric ceramic was successfully tested during a two year exposure in a hot cell in the CEA research center. The acoustic method is validated by using calibrated gas mixtures and gives and accuracy of ±5 bars and ±0.3% on pressure and gas composition measurement respectively.
The in-pile performance of the acoustic sensor has been proved to operate up to 0.25 MGy and an operating temperature in the cavity of 144°C[Gio17].
Further improvement are under analysis to increase the thermal resistance of the device up to 300-400°C. In this frame, on-going developments focus on the technique to fix the piezoelectric transducer to the stainless steel [Ver15].

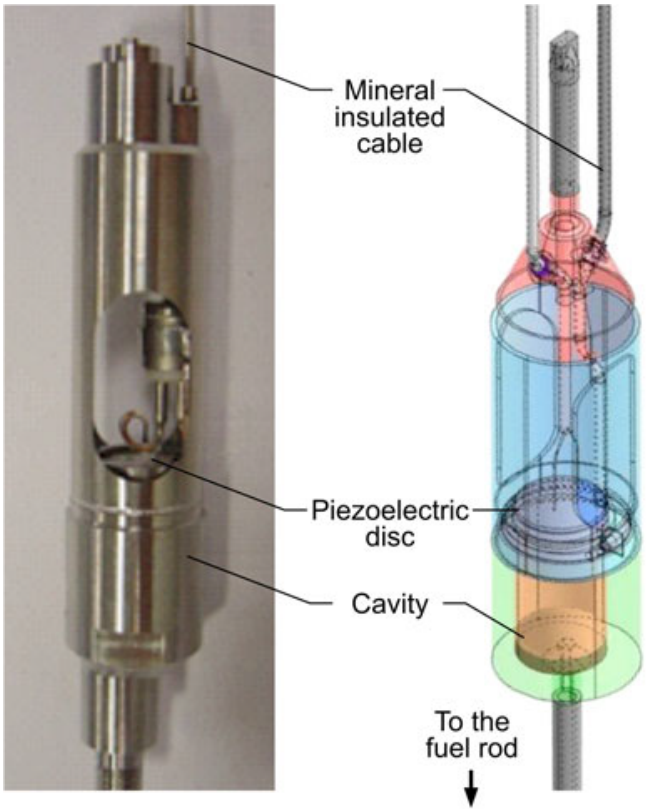

(a)

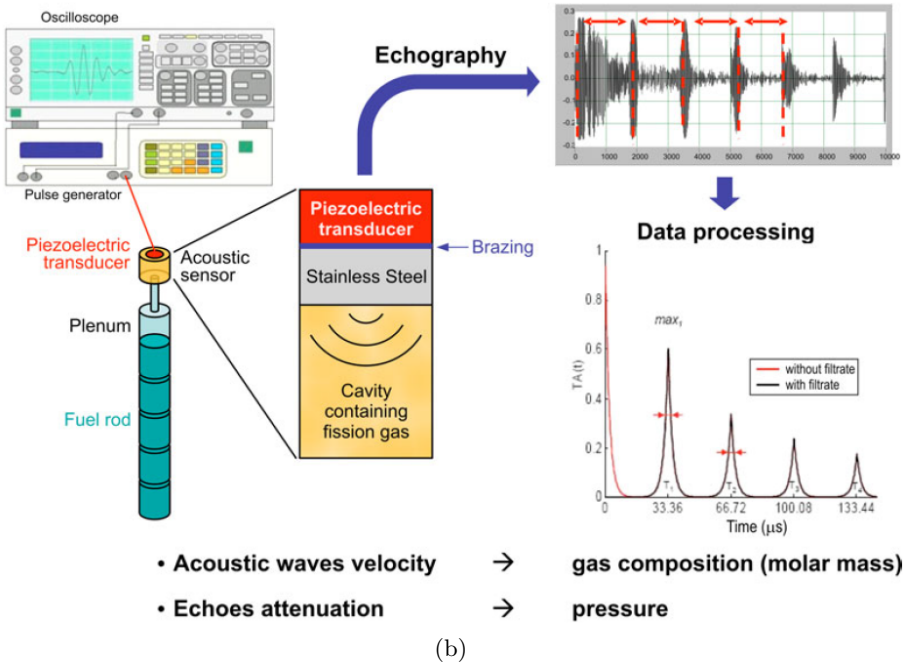

(b)

Figure 8.2 – (a) Acoustic sensor designed to be implemented on sample fuel rod to be irradiated in research reactor. (b) Principle of acoustic sensor for fission gas release measurement [Kim11]

8.3 Performance of the presented sensors in REMORA 3

In 2010 the acoustic and the counterpressure sensors have been used in the REMORA 3 experiment in the OSIRIS reactor to achieve the online measurement of the fission gas release from the fuel stack. The instrumented sample rod is showed in figure 8.3: the instrumentation is connected to the end plugs that are welded to the sample rod cladding. Previous to the irradiation, a thermal mock-up has been performed to validate the ability of the acoustic sensor to operate under temperatures representatives of the REMORA 3 irradiation.
During the test, the total thermal fluence acquired by the irradiation test at the level of the acoustic sensor was about $3.5{\cdot}10^{19}$ n/cm^2. On the basis of the available published results, the acoustic sensor is operational for what concerns the online monitoring of the fission gas release while it is not clear its performance to measure the pressure, that is monitored without failures by the counterpressure device.

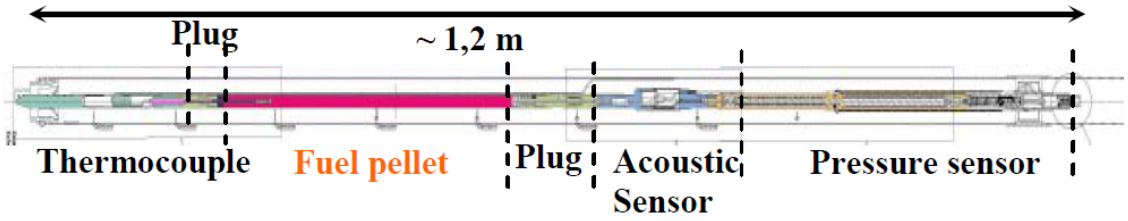

Figure 8.3 – Instrumented sample rod in the REMORA 3 experiment in the OSIRIS reactor [Lam11]

8.4 Concluding remarks

We have discussed in this chapter the selected technological solutions eligible to measure the evolution of the internal pressure inside the fuel rod, during normal operation conditions and during power ramp test.
The counterpressure sensor results to be a robust and reliable device, eligible to be used for PCI dedicated experimental sequences. It indeed meets the measurement criteria identified concerning the internal pressure: it permits to measure online the evolution of the internal rod pressure up to 120 bars with a demonstrated accuracy of ± 0.325 bars (2σ). Also it has been designed and qualified to operate in the nuclear environment with a minimum perturbation of the system and with no drift of the collected signal.

The acoustic sensor instead constitute an interesting development as theoretically allows to double the information collected from a single measurement: the internal pressure evolution and the modification of the gas composition. The developed device proves to perform well under irradiation for what concerns the online monitoring of the composition of the released fission gasses but further experimental characterization and investigation are required to verify the pressure measurement. This is indeed based on the analysis of the amplitude of the signal and its attenuation that has to be distinguished from the attenuation due to the interaction radiation-matter at the piezoelectric transducer.

The performance and main characteristics of the two sensors are summarized in table 8.2

Technology	**Range (°C)**	**PCI Application**	**Design**	**Resistance to Nuclear Env.**	**Status**
Counterpressure sensor	≤120 bars	p_{int}	Adapted to the sample rod geometry	qualified adapted to MTR application	Operational
Acoustic Ultrasonic sensor	not available	p_{int}, Fission gas composition	Adapted to the sample rod geometry	T<200°C Sensitivity to radiation of the PZT component	On-going development

Table 8.2 – Synthesis of the main characteristics of investigated pressure sensors

Chapter 9

Dimensional measurement

In this chapter we investigate the technological solutions eligible for use in the nuclear context to measure the dimensional parameters of interest for PCI detection. In section 9.1 we investigate the LVDT and Fabry-Perot extensometer as possible technologies to follow the evolution of the cladding and fuel elongations. Section 9.2 is dedicated to the Michelson type Interferometer based sensor, the diameter gauge, the strain gauge and the confocal microscopy to measure the effects of strong PCI on the deformation kinetics of the cladding external diameter. In section 9.3 we present the acoustic microscopy and the physical principle of using vibrations to detect and characterize the weak PCI

Contents

9.1 Elongation measurement of the fuel rod components

9.1.1 Linear Variable Differential Transformer

The linear variable differential Transformer (LVDT) consists of a transformer with a single primary winding, activated by a constant current generator and two secondary coils connected in series opposing manners. The general object to be measured is physically attached or corresponds to the central iron core of the transformer, so that the mechanical movement affects the balance of the signal from the secondary coil and the corresponding signal is linearly correlated to the change in position. Further details on the physical principle of LVDT are reported in appendix C.
This type of detector has been adapted to the nuclear environment and it has been used in several experimental sequences. Many MTRs nowadays rely on the LVDTs fabricated by the Norwegian Institute for Energy Technology (IFE) as part of the Halden Reactor Project (IFE/HRP) [Nie09], which are **designed to stand the light water reactor conditions**. Its geometry has been studied **to fit the geometrical constraints of the research reactor and to minimize its perturbation of the system**: aligned to the fuel rod, it presents a diameter equivalent to the fuel rod itself and occupies a length of about 50 mm.
Figure 9.1 illustrates its typical design: (a) the primary coils, (b) the secondary ones, (c) the ferritic core and (d) the signal cables.

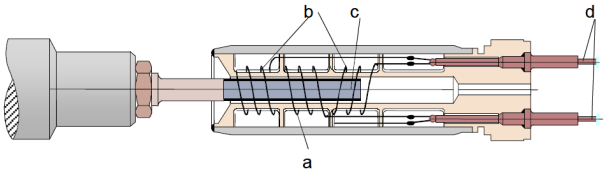

Figure 9.1 – General design of an IFE/HRP LVDT detector [Nie09]

The cables permit to extract the evolution of the signal corresponding to the the position of the magnetically permeable core, attached to one of the fuel element components: the fuel stack or the cladding.

IFE/HRP has invested through the years in making in-core measurements and more than 2200 different types of LVDTs have been installed in the Halden reactor. **The reported failure rate of this system is lower than** 10% **after 5 years of operation under irradiation**. In figure 9.2 are presented two different available designs, (a) is adapted to the detection of Cladding Elongation and (b) to the detection of Fuel Elongation.

In the presented design (a), to measure the cladding elongation, the magnetically permeable core is fixed to the fuel rod end-plug, which is welded to the cladding. A fixed support structure is needed to extract the cladding elongation: only the side attached to the core has to be free to move inside the LVDT coils whereas the other side of the cladding has to be fixed to the support plate. Also, the LVDT coils have to be fixed on another grid plate of the support structure.
In the presented case (b), to measure fuel elongation, the magnetic core is placed inside the test rod, attached to a plate located at the end of the fuel stack, through the upper spring. The bottom side of the fuel stack has no possibility to expand so its elongation is measured by the upper located LVDT.

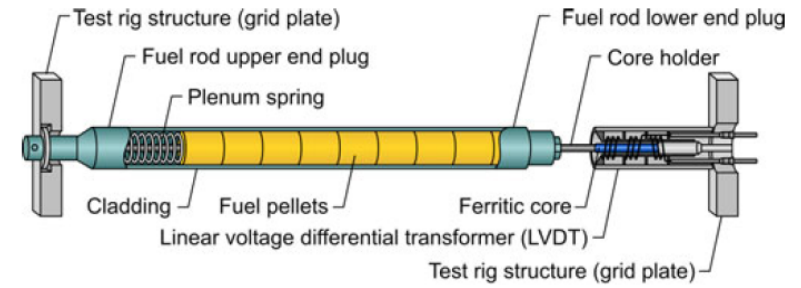

(a)

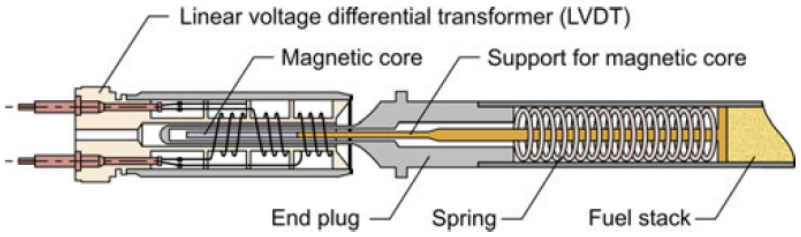

(b)

Figure 9.2 – IFE/HRP design to detect cladding elongation (a) and fuel stack elongation (b) [Kim11]

A technological limit of these devices is defined by the Curie point of Nickel[1]. Indeed for higher temperature than 356°C to 358°C there is strong modification in the output signal and a change in the sensitivity of the detector.
To avoid the sensitivity change of the detector when temperature overcomes this point, IFE/HRP evaluated different materials for LVDT coils, such as oxidized aluminium or insulated silver alloy wire. In collaboration with INL, silver alloy wire were tested and showed a very stable output signal for the entire test sequence of 1000 h at 500°C. From 2007, CEA with the collaboration of IFE/HRP has worked to enhance the temperature range, to maximize the measurement range and detection performances. It resulted from this collaboration the "5-wire" or "self-compensating electronic setup" [Vil09]. The two electronic schemes are compared in figure 9.3.
In the four wire configuration, only the voltage difference at the two secondary coils is measured and the voltage output is then proportional to the core displacement. In the improved configuration, the additional wire is connected to a zero reference between the two secondary coils. The resulting signal is a ratio:

$$x \propto \frac{(V_a - V_b)}{V_a + V_b} \tag{9.1}$$

This configuration allows to get rid of the evolution of magnetic and electrical properties taking place during irradiation and that affect in the same way the output voltage at the primary and secondary coil. This lead to a reduced sensitivity of output signal from temperature and radiation effects.
Extensive out-of-pile experiments showed that this setup permits to achieve:

[1]The Curie point of a material is the temperature at which a ferromagentic material looses its properties and is no more ferromagnetic

- Improved linearity to a range of ±2 mm and a usable measurement range is enhanced to ±7.5 mm;
- in the linear range, the sensitivity is 1.7 V/mm and the resolution amounts to 0.5µm, corresponding to the 0.012% of the linear range;
- Improved accuracy and repeatability: the measured accuracy amounts to 9 µm and repeatability to 3µm, for a measurement range of 1 mm (2σ).

It is also observed that this setup presents:

- Suppression of temperature sensitivity;
- Suppression of aberration in the central area which characterized the measured signal in the four wire configuration;
- Reduced influence of Curie point;
- Suppression of signal shift due to irradiation;

Enhanced LVDT have been implemented in the instrumented sample holder MELODIE, tested in OSIRIS in 2015 to follow on-line the cladding elongation. This test permitted to evaluate the in-pile performance of this improved design [Gui15].

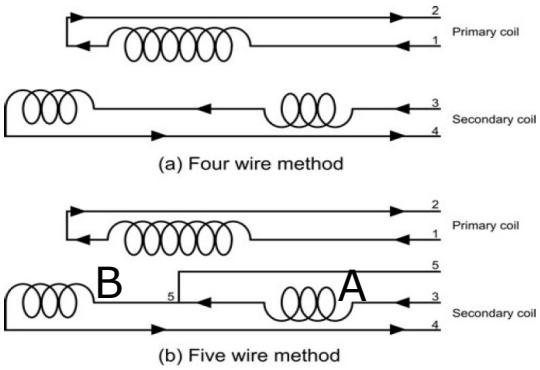

Figure 9.3 – Wiring scheme for LVDT design: the original 4-wire configurations (a) and the improved one (b)

9.1.2 Fabry Perot extensometer

The Fabry Perot extensometer developed by CEA and SCK·CEN is based on the classical Fabry Perot interferometer [Cau12]. Figure 9.4 presents its principle [Che11]: a source of light and a spectrometer are connected by an optical fiber to a low-finesse cavity, located at the bottom of the fiber itself. In the presented design, each side of the cavity have to be connected to a localized are of the target object to be characterized. The gauge length L_g is defined as the length of the fiber between the fixing points. Any variation of the sample length leads to a similar variation of the gauge one with result into the modification of the cavity extension L_c. The input beam reflects on both faces of the cavity and the state of interference generated by the two reflected beams depends on the ratio L_c/λ with λ being the wavelength of the injected beam. From the interference pattern it can be retrieved the variation of the cavity length.

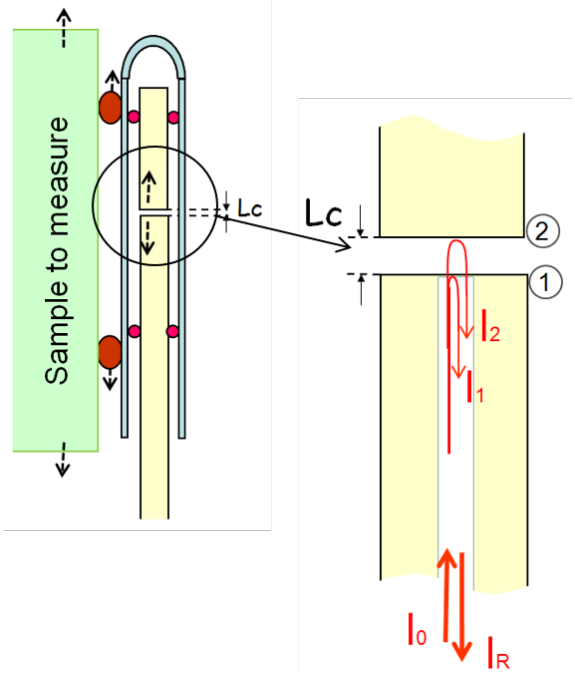

Figure 9.4 – Principle of a Fabry-Perot extensometer

A first adaptation has concerned the problem of the radiation-induced compaction of the optical fiber: under fast neutron flux, a phase transition is induced in the fiber with a resulting increase in its density with respect to the initial state. This variation in density is associated to a modification of 0.5% in the optical index. This leads to a huge measurement error: as the compaction of the optical fiber results into a sensible enlarging of the optical cavity, this may can be wrongly associated to the modification of the sample length.
Investigations lead to develop a Fabry Perot sensor adapted to operate in a reactor core up to 400°C which consists of a single-mode radiation-hardened optical fiber, a stainless steel rod insensitive to radiation, a metallic housing including a bellow which isolates the cavity from the external environment and which enhances the welding of the sensor on the metallic sample rod [Che19]. The modified design has been verified during an irradiation test [Che14], which proved the limitation of the radiation-induced compaction drift.
Recent work has focused on the verification of the sensor performances at high temperature: out-of-pile tests demonstrated that in the thermal range of 300-400°C the measurement error is limited to 1 µm and it can reach some µm in the range within the specifications of the sensor (1% to 2% of the length of the sample) [Che19]. More precise results are not available at the moment.

According to the measurement requirements in an experiment to characterize PCI, the Fabry-Perot can be used to measure the total elongation of the cladding, just like the LVDT, but also to access the local elongation of a portion of the cladding. In this frame, the sensor benefits from the reduced characteristic dimensions of the optical fiber systems and requires to be placed in parallel to the sample rod.
Because of the geometrical configuration of the fuel rod, the Fabry-Perot cannot be applied to measure the elongation of the fuel stack.

9.2 Measurement of the external cladding diameter

We have seen in the first part of this work that the cladding diameter constitutes one of the most important parameter that permits the characterization of the origin and evolution of the strong PCI, in both normal and off-normal operation conditions.
The modifications induced by PCI on the deformation kinetics of D_c^e implies the formation of primary ridges and secondary ridges, which amplitudes are in the range of the tens of µm.
According to modeling, the phenomenology requires remote measurements, to minimize theirs perturbation, an accuracy in the measurement of the relative evolution of the D_c^e of at least 1 µm and the investigation of the central zone of the fuel rod, with a spatial resolution of 0.5 mm.

Among the possible solutions to measure the deformation of the cladding diameter during irradiation, we have considered the Michelson type interferometer sensors, the diameter gauge, the strain gauge and the confocal microscopy.

9.2.1 The Michelson type Interferometer

In a Michelson type Interferometer, the same pattern of Fabry-Perot systems can be obtained by the interferences between two reflections on surfaces beyond a beam-splitter, as shown in figure 9.5. With respect to the Fabry-Perot, it is more flexible allowing to measure larger displacement. In the Fabry-Perot, the diverging beam outside the fiber (in the gauge cavity) and the small dimensions of the optical fiber result into a rapid decrease of the intensity of the re-injected signal in the fiber when the cavity length increases (larger that 200 µm). In the Michelson type interferometer, the diverging beam can be focused by a lens that allows to extend the maximum measurable displacement (order of 1 mm).

A miniature sensor has been developed by the CEA dedicated to the on-line monitoring of the fuel rod swelling during irradiation test in MTR [Che13]. Figure 9.6 illustrates the scheme of the sensor. The sensor presents a mechanical probe in contact with the fuel rod cladding that allows to perform an optical measurement of its displacement. The body of the sensor provides a mechanical protection to the fiber from the environmental conditions. The total encumbrance of the optical module is about 2 mm. Out-of-pile tests

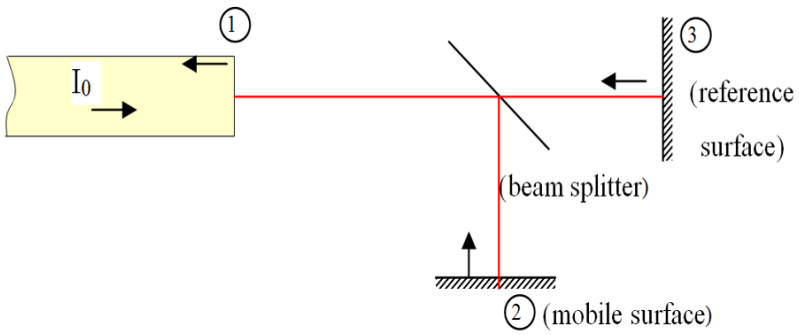

Figure 9.5 – Principle of a Michelson type Interferometer: the beam (1) guided by the fiber propagates outside the fiber, it is split by the beam-splitter and it is reflected on the mobile surface (2) and on the reference surface. Once returned to the fiber, the two beams interfere depending on the displacement of the mobile surface [Che13]

showed that the sensor is capable to measure displacement in the range of ~ 0.5 mm with an absolute accuracy of $\sim$10 µm.

Further tests must be carried out to evaluate the performance of the sensor at the operating conditions of the nuclear research reactor. It must be analyzed the performance of the sensor to operate at the temperature of the cladding surface, about 300°C and, as all the optical fibers,the resistance to irradiation of the fiber. For its application in the frame of PCI characterization, the disadvantage of this sensor is that it requires the contact with the cladding. This contact is achieved by means of the mechanical probe. Its capability to meet the axial resolution required to follow the formation kinetics of the ridges on the cladding (0.5 mm) has to be verified. Also, the contact has to be guaranteed against the flow induced vibrations of the sample rod. To obtain this, a force of some Newtons has to be applied by the mechanical probe to the cladding.

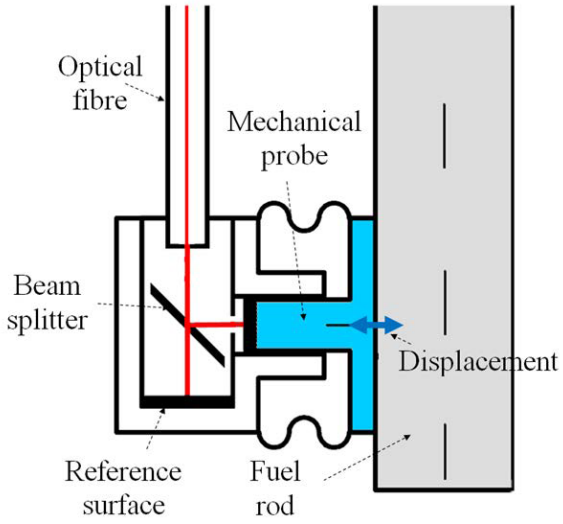

Figure 9.6 – Scheme of the sensor based on the Michelson type Interferometer for the measurement of the rod real-time swelling. The mechanical probe is in contact with the cladding and is displaced according to the local deformation. The motion is measured at the opposite face of the mechanical probe by optical interference [Che13]

9.2.2 The Diameter Gauge

The diameter jauge (DG) is a rotary core differential transformer [Web99] and it is based on the same principle of the LVDT. The adapted principle is illustrated in a schematic view in figure 9.7: it presents two primary and two secondary coils which are wound on a U-shape ferromagnetic structure. Separated by two symmetric gap, a ferritic arm constitutes the moving part of the magnetic circuit, which rotation axis is presented as a cross in figure 9.7. When an external force moves the armature from its equilibrium position, the reluctance of the magnetic circuit decreases at one secondary coil and increases at the opposite one. The generated electromagnetic force in the secondary coils, which are equal in the balance position, differs in magnitude and in phase as a result of the imposed displacement. The output signal results modified and the modification can be correlated to the displacement.

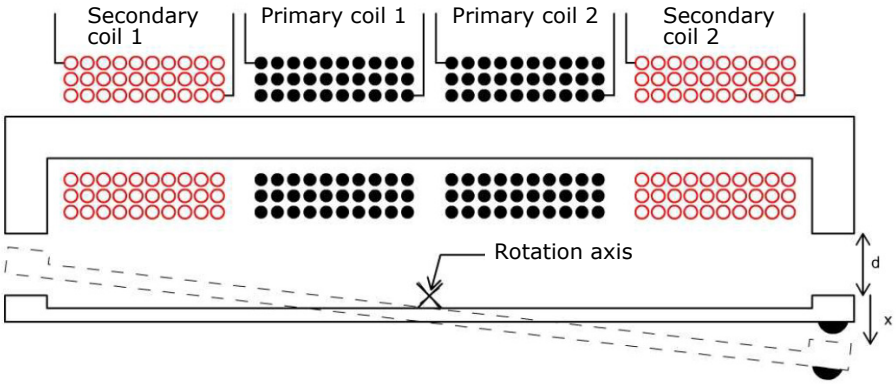

Figure 9.7 – Principle of a DG detector: when an external forces moves the armature from its equilibrium position, the reluctance increases at one secondary coil and decreases at the other one. From the modification of the output signal it can be obtained the displcament of the object [Web99]

The IFE/HRP has designed and fabricated a DG detector adapted to measure the fuel rod profile. The design and the characteristic dimension of the device are shown in figure 9.8. According to the design, the detector is installed parallel to the fuel rod, the latter being in contact with the DG feelers. One of this sensing probes is fixed on the moving arm of the DG. The contact between the sample rod and the feelers is ensured by a set of springs. The modification in the diameter of the fuel rod induces the rotation of the arm around the pivot, which is measured by the output signal.

DG test supports developed by IFE/HRP also present a mechanical system to move the detector along the sample rod. This permits to carry out a profilometry over a portion or the whole sample rod. On each end of the rod, several calibration steps (V-grooves) are incorporated in the end plugs as reference diameters. The DG movers over these calibration steps before and after each diameter trace, to check and correct the DG sensitivity.

As for the LVDT technology, **the five-wire electrical scheme allowed to reach comparable improvements**. Tests carried out on the enhanced DG system operated on

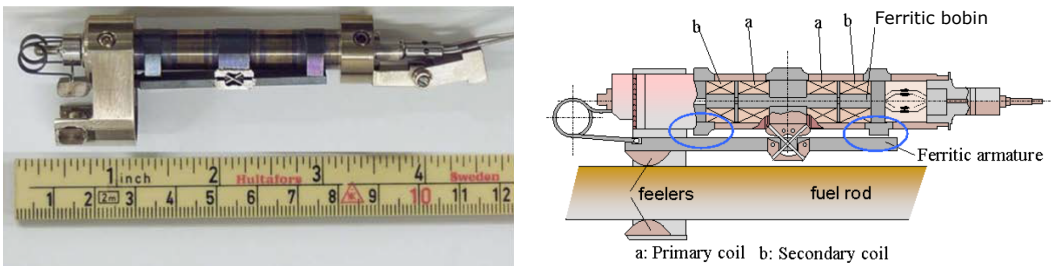

(a) (b)

Figure 9.8 – IFE/HRP design of the DG: (a) presents the overall dimension of the detector, (b)permits to identify the main components: a. the primary coils, b. the secondary coils, c. the ferromagnetic arm, d. the moving bra, e. the pivot allowing arm rotation, f. the feelers, g. the sample fuel rod [Kim11].

a self-compensating mode, show that the linear response is enhanced over a range of ±900 µm, 3 times larger that the required range identified for PCI application. The accuracy in the measure amounts to 2 µm.

A completely different design has been proposed by CEA in the frame of the MUSICA experiment, to make the DG design compatible with the geometrical constraints of OSIRIS system, where the experiment was carried out [Gui15]. The main problem of the original design is that the internal diameter of material testing reactor like OSIRIS and JHR is tight, about 20-25 mm which makes it impossible for the DG to be located parallel to the fuel rod.
The designed system presents the body of the DG placed on the bottom end of the fuel rod, aligned with it. From a single arm configuration, this presents three long arms, at 120° each other: two out of the three are fixed to the DG body, the third free to rotate. The resulting design of the MELODIE sample holder used in MUSICA is shown in figure 9.9.

As in the standard design, the feelers have to stay in contact with the sample rod for the measure to be performed. This is realized by means of two systems:

1. The DG body is not perfectly fix but slightly moves to accommodate the possible motion or not alignment of the sample. This is obtained by a flexible stalk which connects the DG to the bottom support;

2. The springs in the original design are replaced by counterweights made of tungsten, attached to an Inconel wire as to maintain the three feelers in contact with the sample. This way we get rid of the spring, which has the tendency to relax

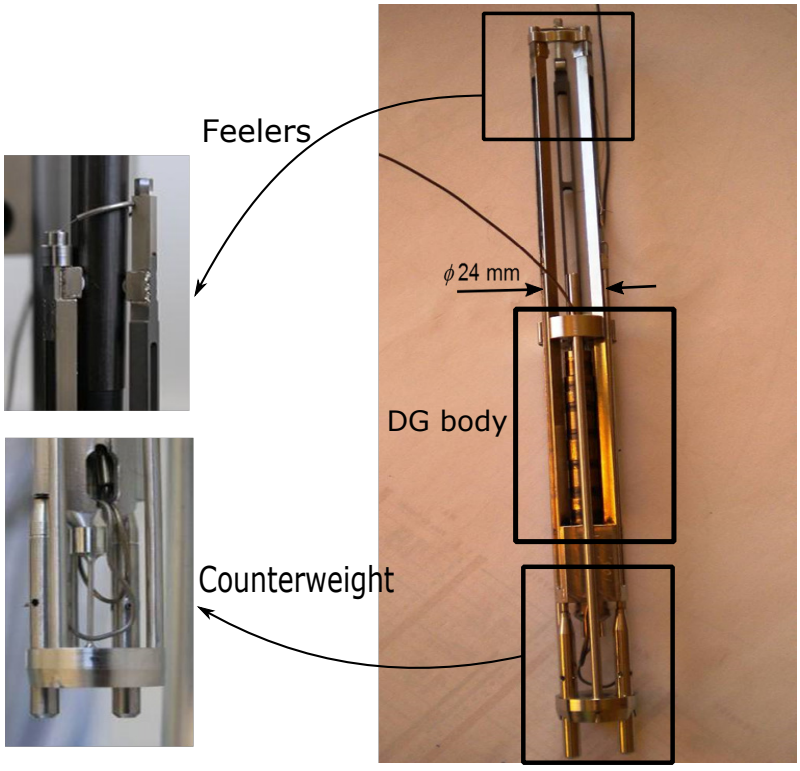

Figure 9.9 – Adapted and improved design to meet the geometrical burdens of OSIRIS reactor in the frame of the MELODIE experimental sample holder [Gui15]

under irradiation and it can be found the minimal force which ensures contact with a minimum perturbation in the sample deformation, unavoidable in this kind of detector.

Extensive out-of-pile characterization has permitted to obtain the following characterization for the improved DG design:

- Measurement range: diameters from 8.8 to 10.3 mm. The range can be modified by adjusting the position of fixed feelers;
- Sensitivity of 0.85 mV/µm;
- Resolution of 1 µm;
- The standard deviation form linearity amounts to 0.8 µm and the repeatability to 1 µm. Uncertainties are given at 2σ.

In the frame of its application to the measurement of the deformation kinetic of the cladding diameter during irradiation, the DG meets the measurement requirements in terms of accuracy and spatial resolution, with the possibility to investigate a portion of the sample rod surface. But, the contact with the target object is required, which is not foreseen for PCI application. The device requires to be calibrated as to apply the optimized pressure on the cladding surface that ensures a constant contact to perform cladding profilometry and guarantees no scratches are formed on its surface.

9.2.3 Strain gauge

The use of strain gauges in the nuclear environment has been the subject of several researches to investigate their tendency to degrade under radiation [Nop93]. Experimental evidence showed modification of their response due to several physical phenomena: lattice damage and transmutation in the gauge grid metal under neutron radiation, loss of electrical insulation and mechanical embrittlement of the grid carrier, mechanical degradation. Weldable gauges were identified as the best performing under radiation and have been further investigated.
Electrical resistance strain gauges can be used to measure deformation and vibration. Michel Pettigrew in [Pet13] describes several in-reactor experiments featuring the use of axial and circumferential weldable strain gauges to measure the fuel element vibration and its axial and circumferential deformation. Figure 9.10 illustrates a sample fuel element instrumented with the strain gauges. From a detailed discussion about the effects of radiation, temperature and intense neutron fluxes on strain gauges parameters (sensitivity, electrical resistance, insulation and mechanical integrity). The reported experiments study the strain gauges performance up to 300°C, 10 MPa and for a high neutron flux (fast flux up to 10^{17} n/cm^2/s and thermal flux up to 10^{18} n/cm^2/s). The results lead him to conclude that the irradiation effects can be corrected, under the assumption that they are well understood and quantified.

Strain gauges allow to detect the local deformation of the cladding surface but contact is required and cannot perform a profile as only discrete measurements are possible, leading us to conclude that this technological solution is not eligible for use in a measurement method devoted to PCI characterization.

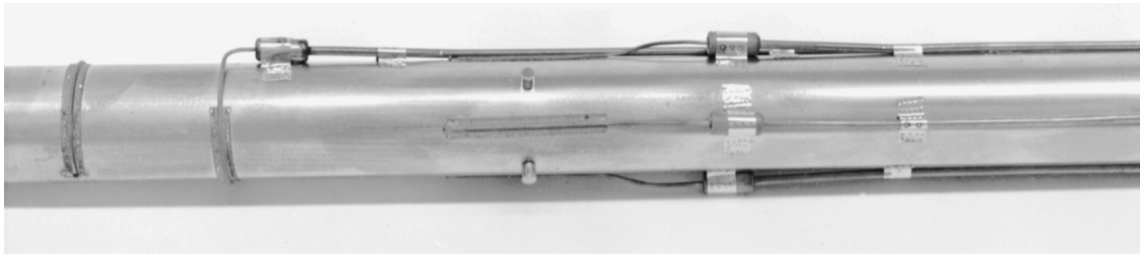

Figure 9.10 – Nuclear fuel elements instrumented with axial and circumferential weldable strain gauges [Pet13]

9.2.4 Confocal Microscopy

Confocal microscopy is an contact-less optical technique to measure the displacement of an object. The technology is based on the physical phenomenon of chromatic aberration of a lens, which consists in its failure to focus a white length to a single point. This is due to a dispersion of the lens: its refractive-index depends on the wavelength of incident light and the focusing length depends of the refractive-index thus leading to the aforementioned aberration.

The principle of the measure is illustrated in figure 9.11: the system consists of a white light source passing through a chromatic lens and focused, depending on the wavelength, at different position on the optical axis. The back-scattered light by the target object is deflected through a filtering pinhole towards the detector. Only the light coming from the focused point passes through the pinhole. The light collected by the spectrometer presents a maximum at the wavelength corresponding to the focal distance between the lens and the surface. Therefore, at each point of the surface, the axial coordinate can be determined from the maximum intensity on the spectrometer.

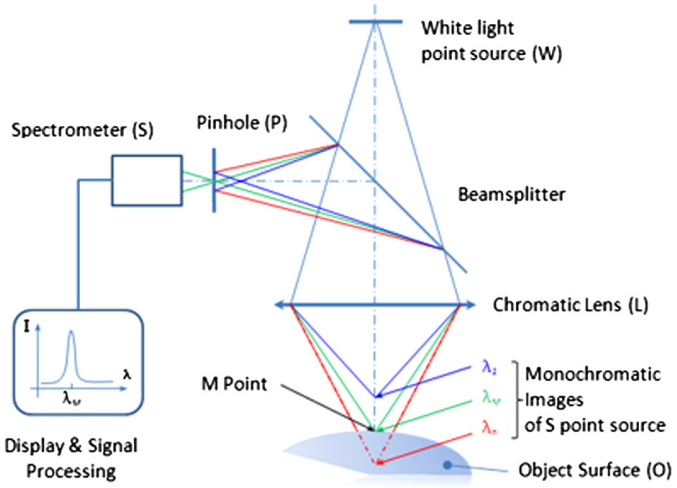

Figure 9.11 – Principle of a chromatic confocal microscope: the white light source passes through a lens and by aberration it focuses at different axial locations depending on the wavelength. The back scattered light from the target object is deflected through a pinhole towards the detector. The light collected by the spectrometer has a maximum at the wavelength corresponding to the focal distance between the lens and the surface [Stil]

A device based on this principle has been developed by the STIL French company [Stil95] and is commercially available in different configurations for a wide variety of applications [Stil]. To optimize the design, the device makes use of an optical fiber as waveguide. The modification of the focal length permits to vary the measurement range with an axial resolution that can decrease to the order of 10 nm and a lateral one of few µm. By moving the object or the optical head it is possible to scan the target object, along a single direction to produce a profilometry, or in two directions to reconstruct a 3D image. This technological solution is currently used at CEA to characterize the manufacturing quality of fuel rod to be irradiated with an accuracy in the order of the µm and it is also used to measure the erosion on components of the fusion machine in Tore Supra which are submitted to the plasma [Gau13] .

The solution is promising as it is the only technology leading to a remote characterization of the fuel rod diameter evolution during irradiation and meeting the identified measurement requirements. However, the present system has been developed for industrial application but several improvements are required to foreseen its application in in-pile irradiation tests: improvement of its capability to operate at higher temperatures and resistance to radiation. This latter challenge takes advantage of the researches carried out in the last years on the development of radiation-hardness optical fibers [Gir18].

9.3 Detection of the pellet-cladding contact

We have said several times in this work that the closure of the gap (weak interaction) is the necessary condition for the strong PCI to occur. According to the axial profile of the linear power production, this contact origins first at the Mid-Core plane and then progresses towards the extremities of the fuel rod. By simulation, an estimation of the time at which the first contact origins can be evaluated. But, this evaluation is based on present knowledge of the phenomenology, thus it is obtained from post irradiation examinations and residual deformations. The accuracy of the code estimation cannot be clearly identified as it is not validated by on-line measurements.
The strong PCI can be directly detected and measured by monitoring the kinetics of the external cladding surface and of the primary ridges formation during the irradiation. From an experimental point of view, this measurement results into the need to periodically perform an axial investigation of the fuel rod, by confocal microscopy or one of the others identified technologies, to access the initiation or not of strong PCI. With a consequent increase of the cumulated dose on this first importance sensor, the rise of failure risk of its displacing device and an increase perturbation of the system.
To optimize the use of this instrumentation and reduce system perturbation, the detection of the pellet-cladding contact has great importance.

In our review we consider two solutions under investigations to detect it: the acoustic microscopy and the analysis of sample rod vibrations.

9.3.1 Acoustic microscopy

In the system, a piezoelectric transducer is electrically excited and produces an acoustic signal. This signal propagates through a coupling liquid that ensures the transmission of the acoustic wave and interacts with the target object. At the interface, the signal is partially reflected back to the transducer, where it is converted to electric signal, and

partially transmitted. The principle is illustrated in figure 9.12. The portion of the pulse that is reflected is determined by the acoustic impedance Z of each material that the wave meets at the interface according to the following formula:

$$R = \frac{Z_2 - Z_1}{Z_2 + Z_1} \tag{9.2}$$

where R is the fraction of reflected acoustic wave and Z_i the acoustic impedance of each material, given by the density times the speed of sound in the i^{th} material. If there are several internal interfaces at different depths, the echoes arrive at the transducer at different time.

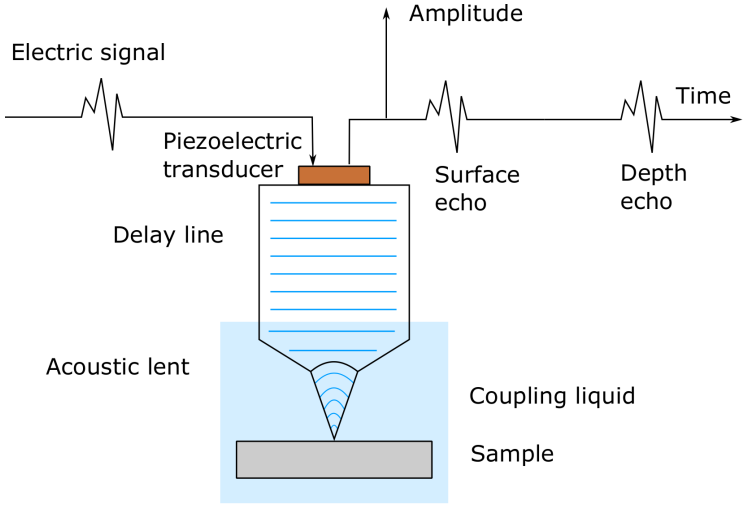

Figure 9.12 – Principle of an acoustic microscope

The technology is already used in the nuclear field to qualify the irradiation induced damage of materials after irradiation and to investigate the elastic properties of fuel materials. Recently, a research has been carried out to develop and qualify this technology as a non destructive post irradiation examination in hot cell, to investigate the internal state of the cladding surface [Sai18]. By analyzing the depth echo of the reflected acoustic wave, the principle is to identify whether the internal cladding surface interacts with the pellets or not.
The research showed encouraging results: it is possible to investigate cylindrical interfaces placed at a depth representative of the cladding thickness (570 µm) and to discriminate if the internal surface of the cladding interacts with the air or with a representative material in terms of acoustic impedance (a glue).

The constraints for its possible future application in the characterization of the weak PCI implies the need for the sensor to be placed in front of the target object to allow the detection of the local contact. This leads the sensor to be submitted to the flow induced vibrations generated by its interaction with the surrounding turbulent flow rate. The impact of the variable distance between the sensor and the sensor on the axial resolution of the acoustic micrometer must be investigated.
Also, it must be further studied its capability to recognize if the local contact is the result of PCI or if it is due to a lack of alignment or a fragment of pellet locally in contact with the cladding.

9.3.2 Vibrations: the measurement principle

In all systems where structures are submitted to an axial turbulent fluid flow rate, so also in fuel rods cooled by water in the nuclear reactor, Flow Induced Vibrations (FIV) origin from the interaction of the structure with the surrounding fluid.
According to Paidoussis [Pai04] [Pai81],Axisa [Axi01] and [DeS17], flow induced transverse vibrations in industrial structures are generally of small amplitude: their amplitudes are in the range of $y/D \approx 10^{-3}$, where y is the root mean square amplitude of vibrations and D the characteristic rod dimension, which leads to about ≈ 1 µm.
These small amplitude vibrations are caused by random pressure fluctuations present in the flow field surrounding the structure and as reported by Chen [Che70]. The vibrations of the cylindrical structures are characterized by two aspects: (i) the system responds according to its first mode, while the contribution of higher modes are negligible at low flow velocities; (ii) the excitation mechanism is random and generally treated in terms of a power spectral density.

Even if vibrations analysis are widely used in industrial engineering for various scopes (e.g. investigation of internal defects, effects of fatigue on loop components), in the nuclear domain they are mostly studied for fatigue and when thigh spacing is involved. This is the case for fuel elements undergoing fretting with the supporting grid spacers and in the case of heat exchanger tubes [Pai81].
The dynamic response of the fuel element in the axial fluid flow is governed by the external soliciting mechanisms and by the characteristics of the structure, in terms of mass, stiffness and damping:

$$[M]\{\ddot{x}\} + [C]\{\dot{x}\} + [K]\{x\} + \{fnl\} = \{F_e\} \tag{9.3}$$

Where $[M]^{N,N}$ is the total mass matrix, $[C]^{N,N}$ the total damping matrix, $[K]^{N,N}$ the total stiffness one and F_e is the externally applied force. Part of the energy dissipated in the structure is due to the non linear mechanisms activated inside the fuel rod and it depends on the pellet-clad relative motion: pellet-pellet friction and pellet-clad shock in the transverse direction.
The progressive closure of the gap and the pellet-cladding contact along the rod axis lead to the gradual disappearance of this relative motion, with a consequent reduction in the dissipated energy.
The non linear vibration of fuel rod has been recently studied by Ferrari et al. [Fer18]: his study concerned a 900 mm zircaloy clad, clamped at both extremities, eventually fulfilled with cylindrical tungsten carbide pellets modeling uranium fuel pellets in terms of dimensions and density. The interesting fact is that he studied the dynamics of an empty rod, of a rod fulfilled with pellets but freely moving inside as no spring was placed at the top of the fuel stack, and a rod fulfilled with pellets axially constrained bu the spring. The research was performed in air and in quiescent water and it was observed that:

- Pellets decrease natural frequencies of the rod;
- Axial constriction increases natural frequencies and reduces damping with respect to freely moving configuration, both in air and in water.

Indeed the non linear mechanisms induced by the presence of pellets, that are the dry friction arising at the interface between moving pellets and shocks as pellets shake against the internal clad wall, depend on the relative motion of pellets with respect to cladding: the axial limitation due to the presence of the spring lead to a decrease of the dissipated

energy and thus a reduction of the damping ratio associated to the fuel rod.

We propose to investigate the fuel rod vibrations, induced by its interaction with the surrounding turbulent flow rate, to inspect the initiation and the axial progression of the pellet-cladding contact.
The use of vibration in this frame is an innovative proposal. We have performed a study to state of the feasibility to measure a modification on the fuel rod vibrations induced by the local weak interaction and its progression along the rod axis. This under the passive excitation imposed by the flow induced vibrations.
The feasibility study is presented and discussed in the following Part IV, in the application frame of the JHR irradiation devices.

Vibrations can be measured both with contact or remote sensors. Contact instruments (like displacement probes and accelerometers) are based on piezoelectric, piezoresistive and capacitive components that are commonly used to convert the object motion into an electrical signal. When remote monitoring is instead required, as in our case, as we want to reduce as much as possible the perturbation of the system, one of the most used devices in industrial engineering is the laser vibrometer. These devices are based on the Doppler effect, represented in figure 9.13: a single wavelength laser beam is pointed on the vibrating object, from which it is scattered back. The velocity and the displacement amplitudes of the target generate a frequency or a phase modulation, respectively.
Other solutions can be proposed. For example, the use of a LVDT, modified in order to make it sensitive to the transverse motion of the sample rod.

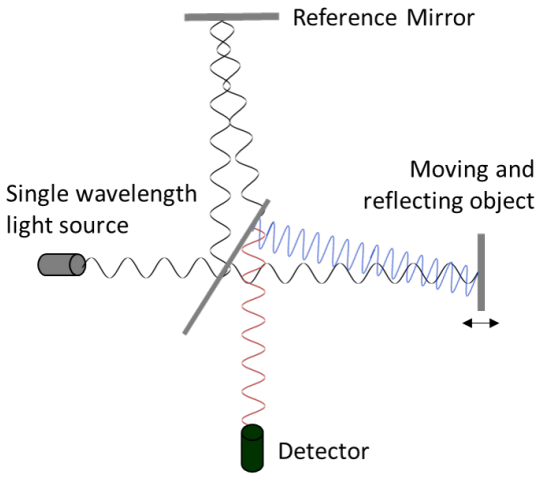

Figure 9.13 – Principle of a laser doppler vibrometer

9.4 Concluding remarks

We have discussed in this chapter different technological solutions, to measure or detect the geometrical evolution relevant for PCI detection and characterization.

LVDT sensor are a robust and reliable technological solutions for in-pile applications, with available designs adapted to follow the integral evolution of cladding and fuel elongation

during irradiation. They proved to operate under continuous irradiation in the Halden reactor with a reduced failure rate and meet the identified measurement requirements for PCI application.
The recent development of the self-compensating LVDT has permitted to further improve its performance, with increased linear range and reduced influence of the Curie temperature and radiation induced drift of the signal and with enhanced accuracy of 9 µm in the measurement range of 1 mm.
The Fabry-Perot extensometer constitutes a promising complementary technology to LVDT: they can indeed assess the local elongation of a portion of the cladding. At the moment the performance of the technological solution at high temperature and under irradiation has to be confirmed but intermediate result give positive results. A radiation resistant device has been developed and high temperature measurements have showed a resolution in the order of the µm. Due to the geometrical configuration of the sample rod, this technology is not adapted to measure the fuel stack elongation.

One of the most important parameters to be characterized during irradiation is the deformation kinetic of the cladding external diameter. For this, we have discussed four technological solutions: the Michelson Interferometer based sensor, the Diameter Gauge, DG, the strain gauge and the confocal microscopy. The Michelson based Interferometer permits an optical measurement of the cladding defromation through a mechanical probe in contact with the target object. From out-of-pile characterization is shows good absolute accuracy, even if it is a little high with respect to the one required for PCI measurement. Information on the relative accuracy is not available but could meet the requirements. The critical point is that this sensor requires to be in contact with the cladding, which has to be ensured against the flow induced vibrations.
The DG benefits from the several experimental feedback from irradiations in the Halden reactor, where the system allowed to perform cladding profilometry. The design has been modified by the CEA to meet the geometrical constraints of the OSIRIS and the JHR reactor . Few tests are available to qualify this device. Fundamental features is that it meets the measurement requirements for what concerns resolution and the possibility to investigate a portion of the sample rod. But, it requires to be in contact with the cladding and its measurement is noised by the flow induced vibrations of the sample rod.
Weldable strain gauge allow to follow the the deformation of the cladding but requires to be in contact and allow a local measure, which does not meet the PCI criteria defined.
Finally, confocal microscopy is the only technological solution identified that allows to investigate a portion or the whole sample rod by a remote measurement. Also, it benefits from the use of optical fiber system to permit miniaturization of the sensor. Nowadays used in the industrial field, the feasibility to perform the measurement in the nuclear field, under irradiation and through the flow rate surrounding sample rod, is being investigated.

Concerning the detection of the pellet-cladding contact, we have presented two technological solutions that are both at a feasibility study. First, the acoustic microscopy has showed interesting results with representative materials in laboratory conditions. Further investigations must be perform on its capability to perform the measurement under turbulent flow rate in the frame of an application in the nuclear research reactor, and to distinguish the weak PCI from a local contact caused by a lack of alignment or local fragment.
Second, we have proposed to investigate whether the progressive pellet-cladding contact and the decrease of the relative motion along the fuel stack axis induces a measurable effect on the fuel rod vibrations caused by its interaction with the surrounding liquid.

For this, we have performed a feasibility study, designed to study the effects of the local weak PCI on the rod FIV. As the experiment is designed to be a simplified version of the ADELINE irradiation device of the JHR reactor, the study is discussed in chapter 11, after having introduced the environment in chapter 10.

Table 9.2 summarizes the characteristics of previously discussed technologies.

Technology	**PCI Application**	**Design**	**Resistance to Nuclear Env.**	**Status**
5 wire-LVDT	Cladding and Fuel elongation	Adapted to MTR application	qualified	Operational
Fabry-Perot extensometer	Cladding Elongation	Miniaturized device, measurement parallel to the rod, can be applied to a portion of the clad	Limited resistance under radiation, in-pile tests required	On-going development
Michelson Interferometer based sensor	Cladding External Diameter	Miniaturized device, Local contact measurement	To be tested at high temperature and under irradiation. Effects of vibrations to be investigated	On-going development
5 wire-DG	Cladding External Diameter	Contact measurement	Few experimental characterizations	Quasi-operational
Confocal microscopy	Cladding External Diameter	Miniaturiza-tion possible by means of optical fibers	Sensitivity of optical fibers to radiation to be place in the axial flow	Feasibility study
Acoustic microscopy	Pellet-Cladding Contact	PZT transducer in front of the target, local measurement	To be characterized	Feasibility study
Vibrations	Pellet-Cladding Contact	Discussed in chapter 11	To be characterized	Feasibility study

Table 9.2 – Synthesis of the main characteristics of the technological solutions investigated for dimensional measurements

Outcomes of Part III

In this part we have focused only on the technologies that allow the on-line monitoring of the parameter evolution and performed a critical review of the main technological solutions and on-going developments that meet all or part of the previously defined technical specifications. The discussion has been structured according to the three types of physical parameters: thermal, pressure and dimensional measurements. We have discussed their measurement principles, their experimental characterizations, the expected perturbations of the system associated to the presence of the sensor and the level of maturity with respect to the nuclear application. We summarize hear the conclusions of this part that are the basis for the selection, that is performed in the next part in the frame of application to the ADELINE irradiation device in the JHR.

Thermal measurements

Melting wires and SiC sensors are not discussed in this review because they permit the measurement of the local temperature after the irradiation and is out of scope for the PCI characterization.
Two technologies have been considered not adapted to the studied phenomenology:

- The expansion thermometer, because it is too intrusive;
- The Johnson noise thermometer, which is rather eligible for in-pile recalibration of thermal sensors.

Monitoring of the External Cladding Temperature T_c^e: Among the technological solutions investigated, the design of the ultrasonic thermometer makes this technology not adapted to monitor the cladding surface. Thermocouples have the advantage of being a robust technological solution, with several validated applications in the nuclear environment. All the reported types meet the range of investigated temperature. But they allow a single point measurement (at the bottom of the TC) and require to be in contact to the target object or to establish a transfer function between the measured temperature and the one of interest.
Fiber Bragg Gratings are an interesting alternative to thermocouples as a single sensor can perform distributed measurements. They require at present days further developments to resist to radiation. Regenerated and femtosecond FBG show promising results to extend the operating range at temperatures well above the one characterizing cladding surface in this study. In addition to temperature, FBG are sensitive to strain, which imposes compensation or the use of a mini-tube to protect it.
Just like FBG, scattered light based optical sensors are eligible for application to the distributed monitoring of T_c^e. To meet the spatial resolution, the retained technological

solutions are the Rayleigh-based OFDR, that also present an accuracy of 0.1°C, the Brillouin based BOTDA and the Raman-based OTDR. Among these optical based sensor, the only one that doesn't need to be compensated for strain is the Raman sensor. The performance of these sensors at high temperature and under radiation must be investigated. All these sensors require to be in contact with the target object: the presence of the sensor locally reduces the thermal exchange between the cladding and the coolant with a consequent modification of the unperturbed system. A dedicated evaluation of the induced perturbation must be performed.
At last, optical pyrometry seems the only technological solution identified that allows to perform the remote measurement of the target local temperature. Investigations have to be done to verify the performance of this technology for temperatures in the range of 300°C.

Monitoring of Fuel External surface Temperature T_f^e: On the basis of the investigated technological solutions, the measurement of T_f^e cannot be performed without introducing the sensor directly inside the sample rod, which induces a strong perturbation of the system: it modifies the local thermal-mechanical behavior and the local thermal exchange. These effects are not compatible with the requirements of PCI detection so that we conclude that none of the investigated technological solutions is eligible to monitor T_f^e in the frame of PCI characterization.

Monitoring of Fuel Centerline TemperatureT_f^i: The range of variation of the T_f^i, from 1000°C in normal operation conditions, to about 2900°C in case of melting onset, is very complex to investigate. Also, the geometrical configuration of the system makes the point of interest in the fuel stack difficult to access. From the previous discussion is results that, except from the optical pyrometry that can be used to remote measure the temperature of the bottom pellets, it is not possible to access the central temperature of the fuel pellet towards the mid-rod plane without drilling an important portion of the fuel stack. Among the available technologies, the only adapted to this range of temperatures are the type C thermocouples, which are limited to 2000°C and can stand radiations for a limited time, and the ultrasonic thermometer, which allows to reach temperatures up to 2800°C and perform a distributed measurement.
In the frame of PCI detection and measurement, non-negligible modifications are induced on the thermal-mechanical behavior of the pellet by the central hole and must be concerned by a dedicated study to analyze the representativity of the measured quantities with respect to the unperturbed system.
These two technologies are interesting to validate code calculation out of the zone concerned by the study of PCI. In this frame, the transfer function has to be established to evaluate the temperatures at the point of interest.

Pressure measurement

The counterpressure sensor results to be a robust and reliable device, eligible to be used for PCI dedicated experimental sequences. It indeed meets the measurement criteria identified concerning the internal pressure: it permits to measure online the evolution of the internal rod pressure up to 120 bars with a demonstrated accuracy of ± 0.325 bars (2σ). Also it has been designed and qualified to operate in the nuclear environment with a minimum perturbation of the system and with no drift of the collected signal.

The acoustic sensor instead constitute an interesting development as theoretically allows to double the information collected from a single measurement: the internal pressure evolution and the modification of the gas composition. The developed device proves to perform well under irradiation for what concerns the online monitoring of the composition of the released fission gasses but further experimental characterization and investigation are required to verify the pressure measurement.

Dimensional measurement

The axial elongation: LVDT sensor are a robust and reliable technological solutions for in-pile applications, with available designs adapted to follow the integral evolution of cladding and fuel elongation during irradiation. Also, the recent development of the self-compensating LVDT has permitted to further improve its performance with enhanced accuracy of 9 µm in the measurement range of 1 mm.
The Fabry-Perot extensometer constitutes a promising complementary technology to LVDT: they can indeed assess the local elongation of a portion of the cladding. At the moment the performance of the technological solution at high temperature and under irradiation has still not be validated but intermediate results give positive results. A radiation resistant device has been developed and high temperature measurements have showed a resolution in the order of the µm. Due to the geometrical configuration of the sample rod, this technology is not adapted to measure the fuel stack elongation.

The Cladding External Diameter: It is one of the most important parameters to be characterized during irradiation is the deformation kinetics. For this, we have discussed four technological solutions: the Michelson Interferometer based sensor, the Diameter Gauge (DG) the strain gauge and the confocal microscopy.
Weldable strain gauges allow to follow the the deformation of the cladding but requires contact and allow a local measure, which does not meet the PCI criteria defined.
Michelson Interferometry based sensor is under-development to follow cladding swelling under irradiation in the environment of the MTR. For PCI application, it presents an absolute accuracy a little higher than required but in relative terms it could meet the measurement criterion of 1 µm. The measurement can only be performed if the mechancial probe is in contact with the cladding, that has to be ensured against the flow induced vibrations of the two systems. The DG benefits from the several experimental feedback from irradiations in the Halden reactor, where the system allowed to perform cladding profilometry. The design has proposed by the CEA allows to have a sensor aligned to the sample rod but requires three long arms to assess the sample rod profile. Few tests are available to qualify this device and the in-pile performance of the sensor has to be studied. As the Michelson Interferometry based sensor, for the measurement the feelers have to stay in contact with the vibrating object.
Finally, confocal microscopy is the only technological solution identified that allows to investigate a portion or the whole sample rod by a remote measurement. Nowadays, it is at a feasibility study but developments are being studied.

Pellet-Cladding Contact: Concerning the detection of the pellet-cladding contact, we have presented two technological solutions that are both at a feasibility study.
First, the acoustic microscopy has showed interesting results with representative materials in laboratory conditions but investigations must be perform on its capability to distinguish the weak PCI from a local contact caused by a lack of alignment or local fragment.
Second, we have proposed to investigate whether the progressive pellet-cladding contact and the decrease of the relative motion along the fuel stack axis induces a measurable effect on the fuel rod vibrations induced by its interaction with the surrounding liquid. For this, we have performed a feasibility study, designed to study the effects of the local weak PCI on the rod FIV. As the experiment is designed to be a simplified version of the ADELINE irradiation device of the JHR reactor, the study is discussed in chapter 11, after having introduced the environment in chapter 10. In this study, we use Laser Doppler Vibrometry to measure the transverse vibrations of the rod but different technological solutions can be developed, like a modified version of the LVDT to measure the radial motion of the sample rod.

Part IV

On-line measurement method for PCI and melting onset detection and characterization in the JHR

Chapter 10

The JHR environment

The objective of this chapter is to select, from the discussed technological solutions in the previous part, the eligible measurement prospects adapted to the JHR irradiation device. For this, in section 10.1 we introduce the main features of the JHR reactor facility and discuss in detail the configuration of the irradiation device that will be dedicated to the study of PCI under irradiation, ADELINE. In section 10.2 we use the geometrical and environmental constraints imposed by the ADELINE device to select the most suitable technological solutions to detect and measure the PCI and to identify the effects of melting onset in the fuel center on the cladding deformation.

Contents

10.1 The Jules Horowitz Reactor

The Jules Horowitz Material Testing Reactor (JHR) is an international user's facility[1] on the site of CEA Cadarache (France) designed for the field of material and fuel behavior studies under neutron flux and for medical applications to produce radio-isotopes. Currently under construction, it will operate by the mid 20's. [rjh-cea].
The JHR is a 100 MWth pool type reactor having a compact core cooled by a slightly pressurized primary circuit, at about 10 bars. The reactor core tank is located in the reactor pool. It has the dimensions of a washing machine: the fissile length amounts to 60 cm and the core diameter to 70 cm. The reactor shall operate for 25 days/cycle, for a total of 10 cycles per year.
The JHR core is designed to achieve high experimental performances and to exploit a twofold neutron spectrum [Gai09]:

- The fast neutron flux (E>1 MeV) has a maximum at about 1.10^{15} n/(cm^2/s) that exponentially decreases with the distance from the core axis as illustrated in figure 10.1. It allows to create the ideal conditions to test structural materials, like claddings and in-vessel components submitted to high dpa rates;
- The maximum of the thermal neutron flux (E≈0.025 eV), about 5.10^{14} n/(cm^2/s) takes place in the Be reflector (c.f. Figure 10.1), where there are the right conditions to test fuel materials.

The axial profile of the JHR power production has a maximum at the mid-core plane and decrease towards the extremities. As a consequence we observe in figure 10.1 that the values of neutron fluxes decrease as a larger region around the mid-core plane is considered: there is an approximately 20% reduction of the maximum value between the 20 cm centered region and the 80 cm centered region.

[1]CEA, EDF, FRAMATOME (France); JRC (European Commission); CIEMAT (Spain); VTT (Finland); UJV (Czech Republic); Studsvik (Sweden); NNL (UK); DAE (India); IAEC (Israel).

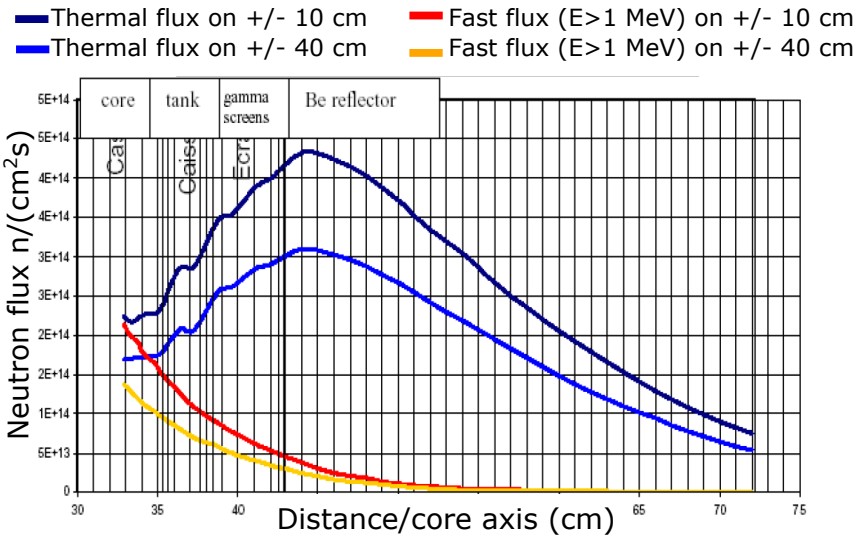

Figure 10.1 – Neutron flux spatial evolution as a function of the distance from the JHR core axis[OECD18]

The specific conditions created in the research reactor permit to fasten the aging of materials with respect to a power reactor, so to be able to study the behavior of new type of fuel rods, to test in safe conditions extended operation protocols and qualify them before their use in an industrial power reactor.
To allow a large range of irradiation conditions, the facility presents several irradiation locations, as illustrated in figure 10.2 [Gon17]:

- Ten experiment locations located inside the core tank, where the aging rate is the highest;
- Ten positions in the Beryllium reflector zone surrounding the core;
- Six channels for water loops, depending on the neutron flux produced in the core, and installed on displacement devices, allow to various irradiation tests, as the power ramp sequences for PCI characterization [Gon17].

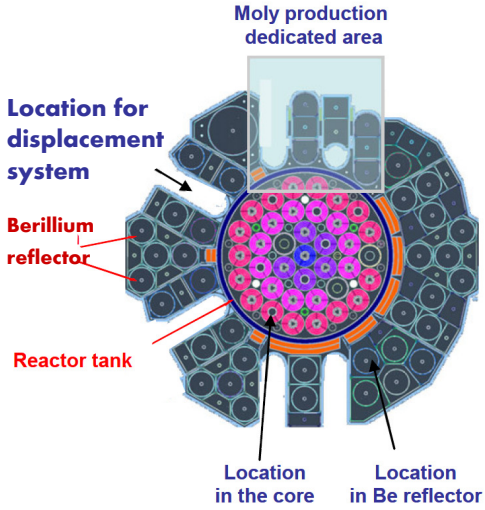

Figure 10.2 – Cross section view of the JHR core and surrounding components[OECD18]

Three fuel test devices are currently under development to study the behavior of light water reactor materials and fuels (e.g. PWR):

- the **MADISON** loop: the Multi-rod Adaptable Device for Irradiation of experimental fuel Samples Operating in Normal conditions will allow testing the behavior of several experimental fuel rods under normal operating conditions of a power plants [Gon17];
- the **LORELEI** loop, dedicated to accidental situations, the reference irradiation sequence being the Loss of the primary Coolant accident (LOCA) [Fer14];
- the **ADELINE** loop: the Advanced Device for Experimenting up to Limits Irradiated Nuclear fuel Elements will allow testing a single sample rod up to its operating limits and during some incidental sequences. This is the loop where PCI studies concerned with the operational limits are to be carried out, by performing dedicated power ramp tests.

In our study, we consider the application frame to be the ADELINE irradiation device. Indeed its design is nowadays the most developed and presents the strongest constraints in terms of geometry, as we detail in section 10.1.1.

The JHR experimental capacity is designed to include non-destructive examinations benches (NDE) located in the reactor pool: a coupled gamma scanning and X-ray tomography bench and a neutron imaging system. They can be used to:

- Check the experimental set-up and the sample rod before irradiation;
- Eventually adjust the experimental protocol or control the calibration parameters after a first irradiation run;
- Perform inter-cycle examinations without the need to move the sample rod to the hot cells laboratories.

The underwater Gamma and X-ray scanning device can be used to detect cracks and characterize corrosion spots on the cladding surface, with a spatial accuracy in the order of 100 µm. The neutron imaging system allows to access complementary information on the presence of water or coolant withing the cladding to detect a failed rod and neutron absorbing materials.
Hot cells laboratories will be available for the preparation of the sample rod and the performance of pre and post-irradiation examinations, of the same kind as detailed in chapter 2.1.

We present in the following section the specific geometrical and environmental characteristics of the ADELINE device. This constraints are then applied to the pre-selected technologies to identify the ones most adapted to characterize PCI and detect fuel melting in this irradiation system.

10.1.1 The ADELINE loop

ADELINE loop presents a single fuel rod test section, where UO_2 or MOX fuels, fresh or previously irradiated in a power reactor, with standard PWR geometry, will be irradiated. The objective is to study the fuel performance up to limit conditions and incidental scenario, including rod over-pressurization, permanent irradiation in a failed mode (loss of cladding integrity) and fuel pellet central melting conditions approach. The loop can indeed operate with a possible contaminated coolant: the fission products and possible actinides released are monitored by on-line gamma spectrometry and delayed neutron detection techniques and a permanent purification radiological controls are performed.
The loop consists of two main parts: the in-pile part, subjected to the flux in the reactor pool, and the out-of-pile part, a grounded section including the fluid circuit, the conditioning and auxiliary components. The layout of the loop is illustrated in figure 10.3.

We focus on the in-pile part. As illustrated in figure 10.4, the sample rod is supported in the test section by a sample holder. Its middle plane is aligned with the middle plane of the JHR core thus the axial profiles are the same: the maximum linear power is obtained at the mid-rod plane and a 20% decrease occurs at both the extremities.

The double containment guarantees the isolation of the loop from the rest of the reactor environment. In the section, the thermal-hydraulic conditions representative of the PWRs are induced and the coolant at 155 bars is injected from the out-of-pile- part, enters the inner tube from the bottom and cools the sample rod by an up-streaming flow. The inner tube diameter is about 20 mm at the sample rod and the allowed dimensions for the sample rod are: cladding diameter of 9.5 mm and length between 200 and 600 mm.

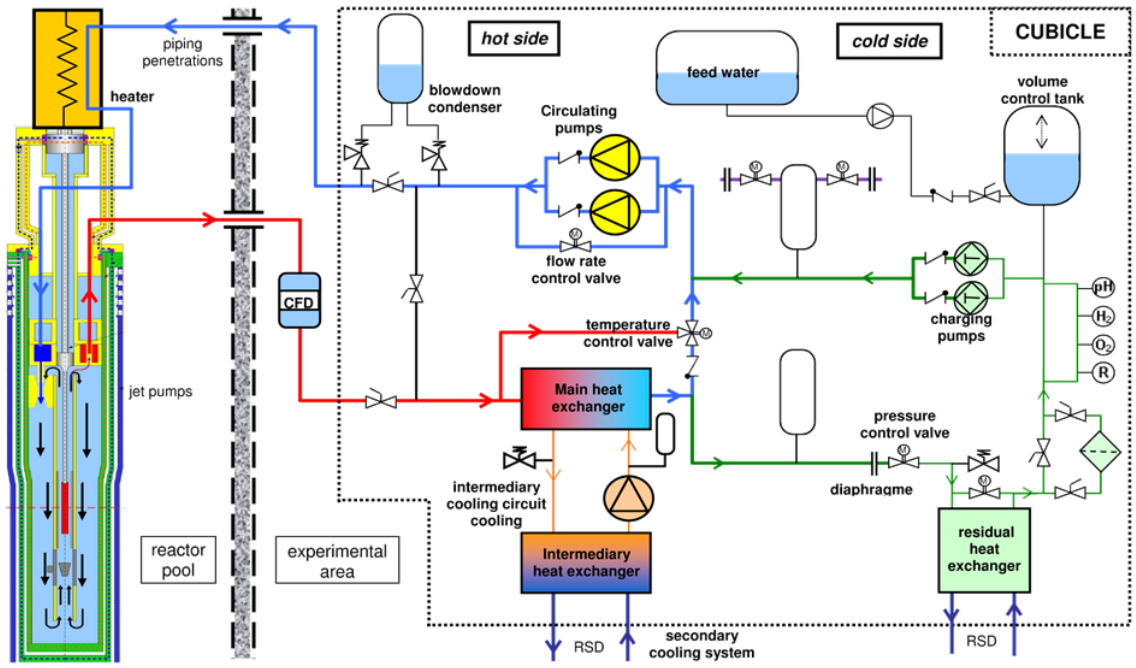

Figure 10.3 – Layout of the ADELINE loop [Gon17]

The instrumentation holder contains the environment sensor and the "jet-pumps", that permit to amplify the flow rate at the sample rod, optimizing the fluid flow managed by the out-of-pile part.
The instrumentation to be placed in the in-pile part to permit the on-line monitoring of interest parameters for PCI detection and characterization, can be supported by this component and, when the investigation requires to point directly the surface of the sample rod, the sensor has to be introduced in the test section, between the inner tube and the sample rod cladding. The geometrical configuration of the irradiation device leave a narrow available spacing, with a radial gap of about 5 mm.

In order to perform, in a simple and controlled way, the quick linear power variations in the sample rod required by the power ramp sequence, the device in loaded on a displacement system, as shown in figure 10.5: by means of the "X" arms, the device can be moved closer or further from the JHR core, depending on the irradiation sequence requirements, with a linear power rate from 10 to 660 W/cm/min. The performance of the designed power ramp kinetics is guaranteed with an accuracy lower than 10 W/cm at the maximum linear power.
To accommodate the displacement of the device, all connections between the in-pile section and the out-of-pile part of the device have to be flexible.

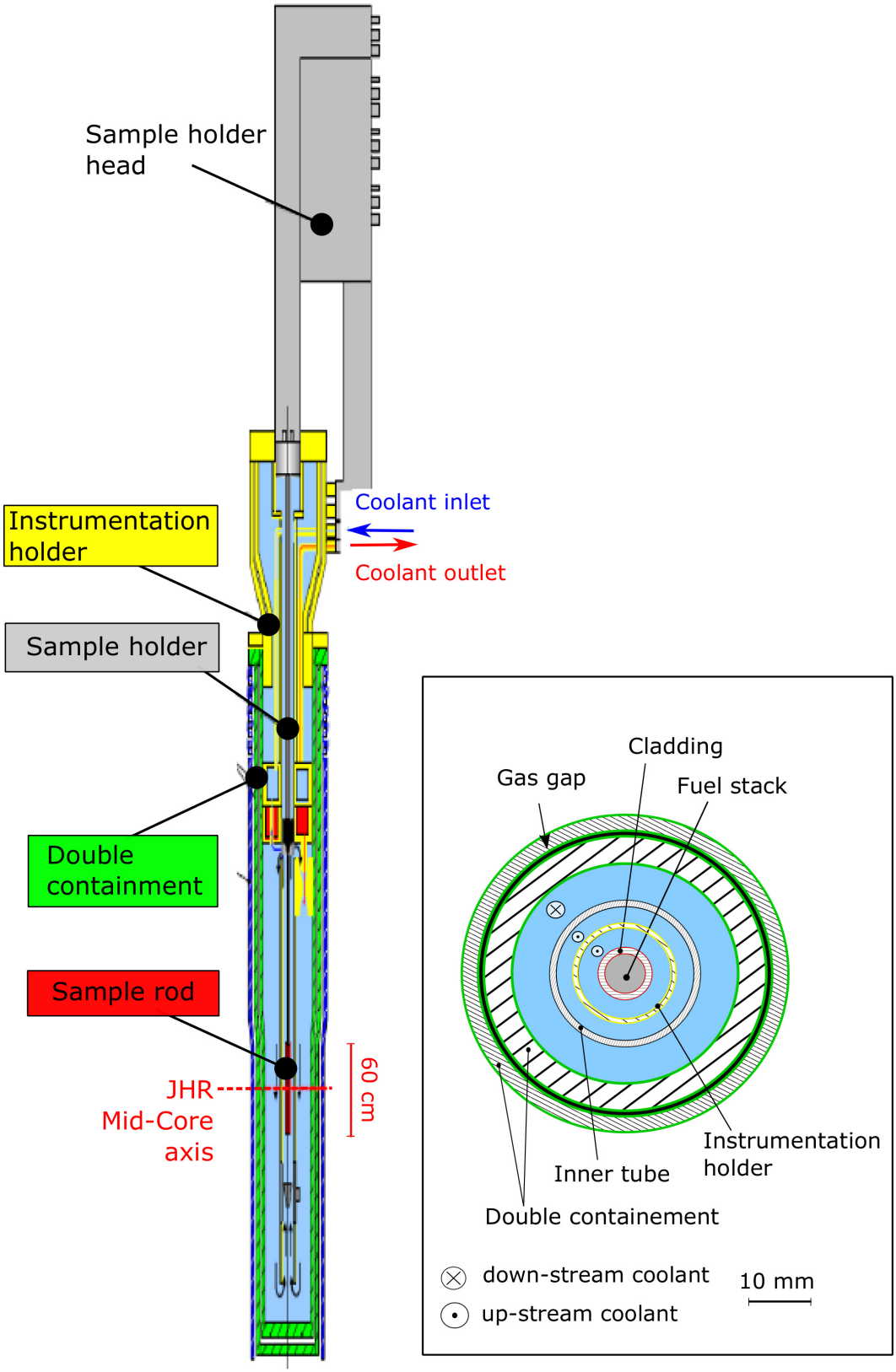

Figure 10.4 – Schematic view of the in-pile section of the ADELINE irradiation loop [Gai09]

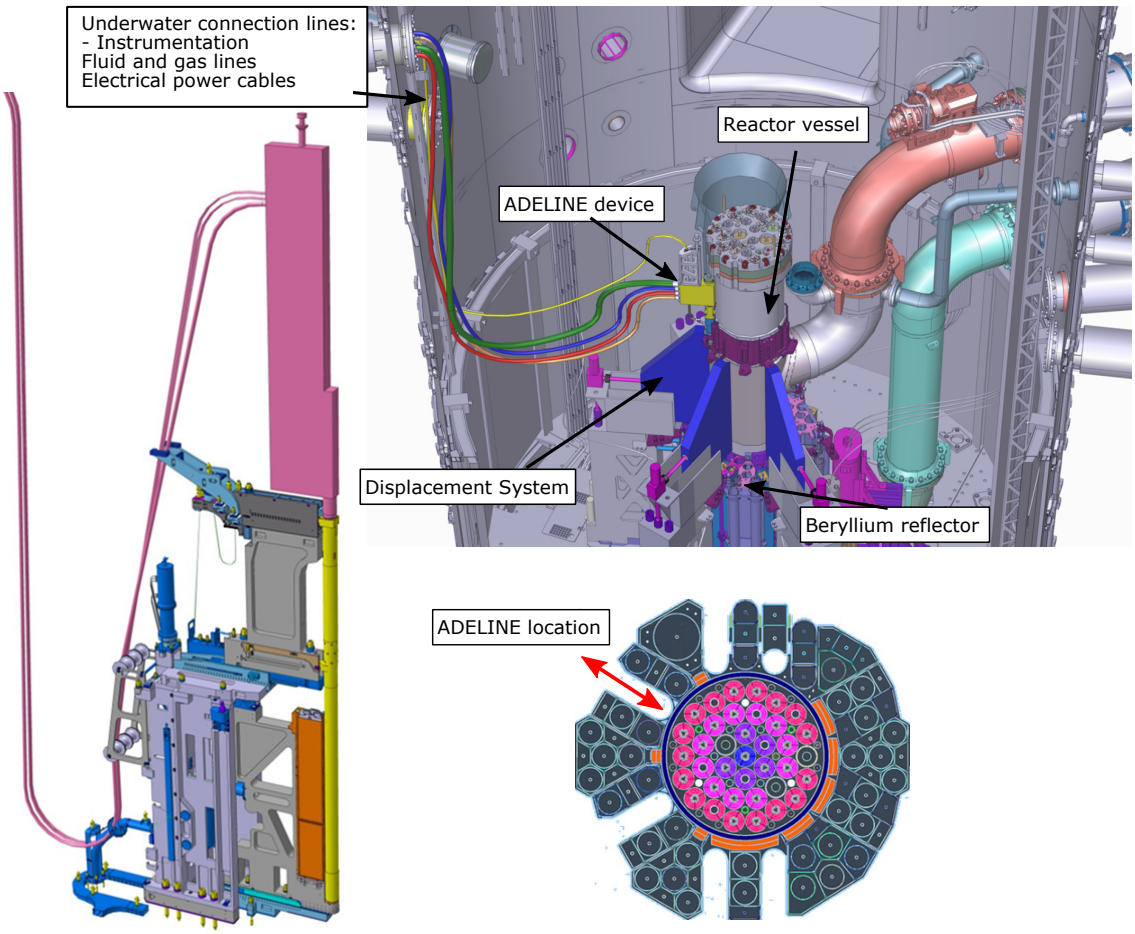

Figure 10.5 – The ADELINE device installed on the part of the device that permits its displacement (left); a picture of the 3D design of the reactor pool where we highlight the location of the reactor vessel, the one of the ADELINE in-pile part (right) [Gai09]

10.2 Eligible measurement prospects

In the previous part, we discussed present technological solutions and innovative ones and pre-selected the ones that meet the measurement criteria of relevant parameters for the PCI detection and characterization during normal and incidental operation conditions. It has to be clear since the beginning that all the aforementioned technological solutions have to be optimized to meet the ADELINE specifications. We recall the main features of retained technologies in table 10.2.

The environment and the design of the ADELINE irradiation device [Gai09] impose the following specific constraints to the instrumentation set-up to be implemented:

- The environment is characterized by high neutron and gamma fluxes, with a maximum of thermal neutron flux of 5.10^{14} n/cm^2/s;
- Neutron fluxes, and consequently temperature, are strongly anisotropic and axial and radial gradients establish. Due to the exponential decrease of the neutron flux with the distance from the reactor core, the sample rod presents a hot size (facing

the core) and a cold size in the opposite direction, as schematically illustrated in figure 10.6. Depending on the location of the sample rod with respect to the core axis, between the sample rod internal and outer side there is variation up to 10%.

Thermal measurement			
Parameter	**Technology**	**Measurement type**	**Status**
Cladding Surface Temperature	Scattering based OFS	Contact - distributed	Feasibility study
	FBG	Contact - distributed	On-going developments
	Optical Pyrometry	Remote - Local	To be characterized at 300°C
Fuel Centerline Temperature	Type C-TC (up to 2000°C)	Contact - Local	Operational
	UTs (up to 2800°C)	Contact - distributed	Operational
Dimensional measurement			
Parameter	**Technology**	**Measurement type**	**Status**
Cladding External Diameter	Michelson Interferometry based sensor	Contact - Local	On-going developments
	DG	Contact - Local	Operational
	Confocal microscopy	Remote - Local	Feasibility study
Cladding Elongation	LVDT	Contact - Integral	Operational
	Fabry-Perot	Contact - Integral/Local	On-going developments
Fuel Elongation	LVDT	Contact - Integral	Operational
Pellet-Cladding Contact	Acoustic microscopy	Remote - Local	Feasibility study
	Vibrations	Remote - Integral	Feasibility study
Pressure measurement			
Parameter	**Technology**	**Measurement type**	**Status**
Internal Rod Pressure	Acoustic sensor	Remote - Integral	On-going developments
	Counter pressure sensor	Remote - Integral	Operational

Table 10.2 – Synthesis of pre-selected technological solutions to measure the relevant parameters for PCI detection and characterization: Fiber Bragg Gratings (FBG), Ultrasonic Thermometer (UTs), Diameter Gauge (DG), Linear Variable Differential Transformer (LVDT)

Due to the axial profile of the neutron production by the JHR core, the maximum linear power production is approximately at the sample rod mid-plane, where fuel T_f and cladding T_c temperatures are the highest, as schematically represented in figure 10.7. The sensors, depending on their design and location, can be submitted to differential thermal dilatation.
Also, high temperatures and strong gradient are present in the system: along the radial direction, when the linear power imposed to the sample rod is in the order of 200 W/cm (normal operation conditions), the fuel center is approximately at 1100°C and the temperature decreases to 300°C at the coolant, with a thermal gradient of 800°C in a few millimeters. This gradient increases with the linear power, as we have discussed in the previous chapters;

– Imposed environmental conditions are meant to rapidly vary in the loop as a direct consequence of the characteristic irradiation scenario foreseen with the power ramp test: thermal shocks are imposed to all components submitted in the irradiation device, their amplitudes varie from several hundreds of degree Celsius to some tens depending on the specific location;

– The sample rod is externally cooled by a turbulent axial flow rate. As the sample rod itself, the instrumentation located in the test section undergoes flow induced vibrations;

– It results from the geometrical configuration of the device (c.f. figure 10.4) that the central region of the sample rod is hard to access: there are approximately 3 m from the head of the sample holder and the radial distance between the sample rod and the inner tube confining the up-streaming coolant is in the order of 5 mm (at the mid-core plane), as illustrated in figure 10.7.

In the following sections, we apply those criteria to identify the eligible prospects for the physical measurements in ADELINE.

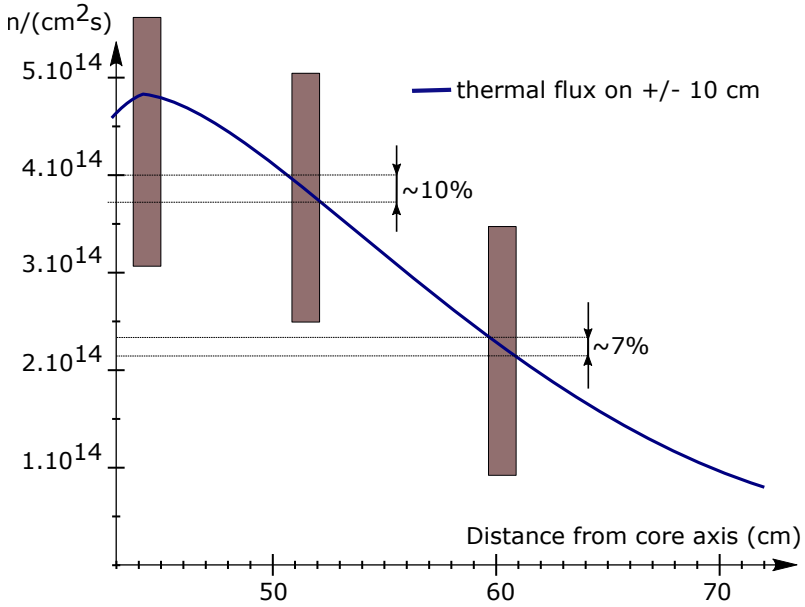

Figure 10.6 – Simplified thermal neutron flux profile on the sample rod depending on its distance from the core axis.

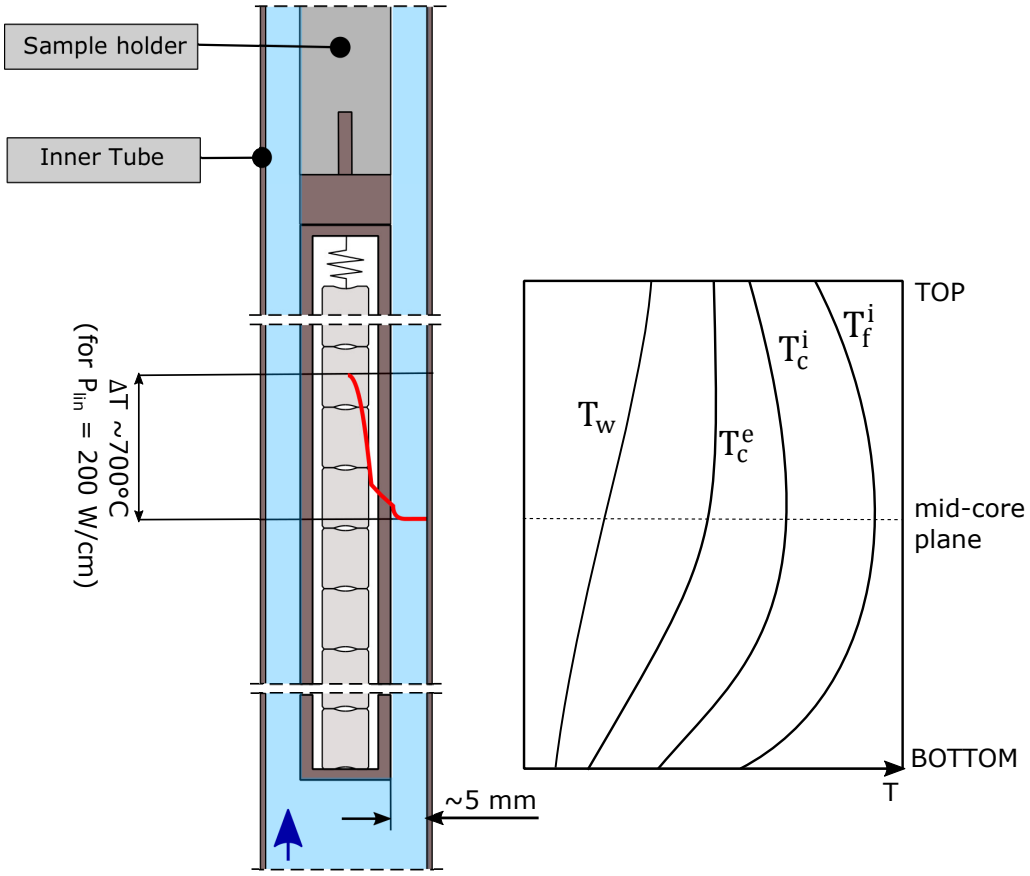

Figure 10.7 – Schematic view of the geometrical constraints and thermal gradients in the axial and radial direction in the ADELINE device

10.2.1 Thermal sensors for ADELINE

Cladding external surface: The first direct consequence of the ADELINE configuration is that the dependency of PCI phenomenology on the thermal range, as detailed in part I, origins a preferential circumferential location for the measurement of the cladding thermal profile, that is the one facing the reactor core.
According to the measurement criteria defined in part I, we have selected two suitable technological solutions, the optical pyrometry and the FBG. The first is a remote but local measurement device, the second allows a distributed monitoring but requires contact. Both technologies are currently under-development for the nuclear environment

The implementation of an optical pyrometry device in ADELINE presents two main technological challenges due to the fact that the measurement principle requires that the optical fiber is placed in front of the cladding:

- Required minimization of the sensor with respect to the characteristic dimension of the test section (5 mm in the radial direction), to reduce the local thermal hydraulic perturbation of the system;
- Need of a moving support, to locate the sensor along the rod axis and perform a monitoring of the rod temperature profile.

Leaving the sensor in front of the cladding is not required (the phenomenology of weak

PCI in normal operation conditions is slow, the sampling frequency is in the order of 10^{-5} Hz) neither convenient (higher dose received by the optical fiber with a consequent degradation of the output signal and perturbation of the environment). So, the sensor has to be coupled with a displacement device, that permits to keep the sensor out of the harsh region and to locate it along the rod axis at the time of interest or with a fixed sampling frequency.

The other identified solution, the FBG, allows a distributed measure, which implies that a displacement system is not required. The absence of the moving support implies that there is no risk of a failure of this device, with a positive increase in the reliability of the system and reduced need for maintenance. But, the measurement principle requires the fiber, or the mini-tube in which the fiber is introduced, to be in contact with the target object, the cladding, which has two consequences:

- The FBG is submitted to the highest neutron fluence, about 10^{20}n/cm^2, during the entire irradiation sequence, as it is located on the hot side and cannot be removed when measurements are not required. This results into an enhancement of the aging and faster deterioration of the optical fiber;
- The presence of the optical fiber reduces the thermal exchange between the coolant and the cladding and origins a hot spot exactly where the measurement is carried out.

Even though the continuous on-line monitoring is possible, the optical fiber is expected to rapidly degrade and the sensor cannot be replaced at inter-cycles without the risk of a degradation of the cladding surface.

The permanent perturbation and the unavoidable degradation of the optical fiber under irradiation involved with the use of FBG lead us to consider the optical pyrometry as more suited to the measure of the cladding surface temperature, keeping in mind the technological challenges required for its correct implementation in the irradiation device.

Centerline fuel Temperature It is a direct indicator of the complete closure of the gap along the pellet so of the establishing of a strong PCI. Also, it is a clear indicator of the approaching and onset of the localized melting onset, considering that a dedicated experimental characterization of the melting threshold in irradiated fuel is performed, as proposed at the end on Part II.
In the previous discussion of the technological solutions, we could not identify one permitting a remote monitoring of the central fuel temperature at different locations along the rod axis. The best performing contact-thermometers are the **type-C thermocouples**, reliable under radiation, and the **ultrasonic thermometers**, that allow a distributed measurement up to very high temperatures, approaching the melting threshold of uranium dioxide.

The strongest concern in the use of this device is that it requires to perform a central drilling of the fuel stack to introduce the sensor at its sheath, with a not-negligible perturbation of the system. The presence of the central hole along the entire fuel stack modifies the thermal-mechanical behavior of the system, with consequences on PCI phenomenology. Also, it reduces the volume of fuel material: the characteristic dimension of the sensor to be used ranges from 0.25 to 1 mm which reduces the pellet volume by approximately 0.1 to 2%. The impact the PCI phenomenology has to be studied to evaluate the relevancy and

representativity of the obtained measure with respect to the unperturbed phenomenology.

This type of sensor can be used to validate the code rather than measure the local PCI. For this, the central drilling has to be performed over a limited length, as it has been carried out in the REMORA 3 experiment [Lam11]. In this frame, it is fundamental to establish the transfer function that allows to evaluate from the measured temperature the ones of interest for the code.

10.2.2 Pressure sensors in ADELINE

The rod internal pressure: It is a relevant information for the indirect characterization of PCI, during normal and incidental conditions. Its variation ranges from 60 bars (hot conditions), for a fresh fuel rod submitted to normal irradiation conditions, to about 120 bars for ramped rods. We have identified and discussed two technological solutions: the counter-pressure sensor and the acoustic one.

Counterpressure sensor have the advantage that they are designed to perform in a radiative environment, qualified to operate up to 120 bars and optimized to meet the geometrical constraints of research reactors [Vil09]. The acoustic sensor is also designed to fit the geometry of the sample rod in the research reactor. It demonstrated, during the REMORA 3 experiment, its performance to characterize the molar mass of release fission gasses during the irradiation demonstrated. But, it is not qualified to measure the internal pressure evolution. In the mentioned experiment indeed, the counter-pressure sensor is the reference device to measure pressure. Also, the sensitivity to radiation of the PZT material in the acoustic sensor makes it less resistance at present days for an application at high neutron fluxes for long periods, like the case of an irradiation sequence to characterize PCI origin and evolution during normal operation. In such scenario, the use of robust and drift-less counter-pressure sensor appears to be much more reliable.
Different is the case of a power ramp test scenario eventually pushed to the melting threshold. As illustrated and discussed in Part I, in this case the released fraction of fission products increases strongly, rising the interest to investigate the composition of the gas mixture. The reliability of the acoustic sensor should to be further investigated to verify its performance in these specific conditions.

10.2.3 Dimensional measurements in ADELINE

Cladding external diameter: Its evolution in normal and incidental operation condition is a direct effect of the strong PCI interaction and constitutes a fundamental parameter to be characterized. The range of variation of this parameter is in the order of the 0.3 mm with respect to the fabrication value and the modifications induced by the PCI are in the order of the tens of micrometers, imposing a relative accuracy in the order of $\sim 1\mu m$.
We have discussed in the previous part, the features of pre-selected three technological solutions: the Michelson Interferometry based sensor, the diameter gauge and the confocal microscopy, the first two being contact and local measurement systems, developed and more or less qualified in the nuclear environment, the second is a remote and local measurement device, used in civil application and under development for application in the nuclear field.

We have presented two geometrical configurations for the diameter gauge: the IFE/HRP design in figure 9.8 and the CEA one in figure 9.9. The IFE/HRP design presents a sensor coupled to a moving support, which is approximately 11 cm long (axial direction) and 3 cm large (radial encumbrance). Its geometry is thus not compatible with the design of the ADELINE device.
The CEA design is better adapted to the constraints of the JHR irradiation devices, which are coherent with the ones of ADELINE: the test section was 25 mm in diameter in the OSIRIS irradiation system and is about 20 mm in ADELINE, with the same radial encumbrance of the tested rod. But, the design of the device presents three arms placed along the rod axis. In the ADELINE device this lead to the fact that these are submitted to differential deformation due to the axial thermal profile. This deformation not only induces a measurement error but also imposes further constraints in the calibration applied by the feelers to maintain the contact. This constitutes a critical aspect for the application of DG to the characterization of the cladding diameter and sums up to the fact that the contact has to be also ensured against the flow induced vibrations of the sample rod. The applicable pressure has to be optimized to guarantee that the cladding is not deformed by the feelers and it has to be managed with respect to the pressure of the coolant during the different operational phases.

In a similar manner, the Michelson type Interferometry based sensor requires that the mechanical probe is maintained in contact with the cladding, with similar challenges for the calibration of the applied force and its management during the operation of the device to not deform the cladding and preserve the sensor performance.
To reduce as much as possible the impact of the measurement on the PCI phenomenology, remote measuring should be preferred.
In the frame of remote investigation, we discussed the confocal microscopy. Already applied in the industrial field, it is currently under-development for nuclear application. This technological solution is particularly interesting as the optical physical principle guarantees a measurement with an accuracy in the order of the µm, meeting the measurement criteria. Also, the optical fiber sensor can be used to drive the wavelength to the target point: the reduced characteristic dimension guarantees the possibility to miniaturize the sensor, fitting the geometrical configuration of ADELINE.
Two main technological challenges add to the required developments for the application of confocal microscopy in ADELINE discussed in part III:

- The development of a moving support to allow the investigation by confocal microscopy of a portion or of the whole sample rod. The need to move the sensor has the advantage of reducing the dose received by the sensor, limiting its degradation, but with a consequent increase in the risk of a failure of this moving support and the failure of the entire measurement system. Sampling frequency has thus to be defined to permit the correct characterization of the studied phenomenology and to limit the support wear;
- The sensor, to investigate the cladding, has to be placed in the turbulent axial flow so that the efficiency of the measure through the fluid flow has to be investigated contribution.

The flow induced vibrations should not constitute a problem for the confocal microscopy: the performed measurement has a time constant far smaller than the frequency of vibration of the sample rod.
The measurement of the rod profile along a single axis can be affected by the possibility

that the sample rod is not perfectly centered in the section. A relative measurement performed along three generatrices allows to get rid of this issue.

Axial elongation: For the measurement of the cladding and the fuel elongation, we have identified and discussed two possible technological solutions, the Linear Variable Differential Transformer (LVDT) and the Fabry-Perot extensometer (FP).

The Fabry Perot extensometer is an optical based sensor that allows to measure the elongation of a component by analyzing the interference pattern generated in an optical cavity which is joint to the target. In the presented configuration in part III, the sensor is designed to be placed in parallel with the cladding. To measure the total elongation of the cladding, the aligned configuration is preferable, so the present design should has to be adapted, creating an optical cavity on top of the fuel stack or at the bottom of the sample rod. The development would be motivated by the advantages of the optical measure: the simple and miniaturized design, the insensitivity to the electromagnetic perturbations and the accuracy of the optical measure.
An interesting feature of the Fabry Perot is that is can be applied to measure the local elongation of a portion of the cladding (one or more pellets), parameter that cannot be assessed by means of the LVDT.

The LVDT are a robust and reliable technology, that showed good performance in the nuclear environment. They operate in harsh environment with a reduced drift of the measurement thanks to the 5 wire configuration. The design presents the sensor aligned to the sample rod, with an equal radial encumbrance that enhance its easy implementation in ADELINE. According to the IFE/HRP design showed in 9.1, the modifications required for its implementation:

- To measure the cladding elongation: fixed at the top of the sample holder, the cladding can elongate towards the bottom of the test section, where the LVDT is to be placed. The bottom plug is modified to host a ferritic core that is introduced in the LVDT coils. This way, the measure accounts for the contribution to the axial elongation of the other parts of the sample holder. For this, a second LVDT is required, mounted on the top plug of the sample rod;
- To measure the fuel elongation, a support for the magnetic core is joint to the fuel stack top and passing through the top spring is integrated in the top plug, free to be displaced by the elongation of the fuel stack. As the top plug is introduced in the LVDT coils, the displacement is collected. Water-tightness has to be ensured.

LVDT results to be a valid technological solution for the measure of the axial elongation of components, meeting all the measurement criteria and having a design adapted to the ADELINE geometrical configuration and resisting the harsh environment, which make it a valid choice for PCI application. Fabry Perot is an interesting solution to achieve measurements with higher accuracy but their performance for long applications has to be qualified.

Pellet-Cladding Contact: Pellet cladding contact is the necessary condition for strong PCI to occur.
The possibility to detect the first Pellet-Cladding contact at the Mid-rod plane and its progression toward the extremities of the rod with a not intrusive technological solution is a fundamental information to optimize the whole measurement method that has been

discussed in the previous section. Optical pyrometry for the investigation of the cladding thermal profile and the confocal microscopy for the evolution of cladding diameter both require the use of a moving support. Their displacement is defined by a sampling frequency that is chosen to maximize the amount of useful information and limit to risk to wear the device. The direct consequence for the detection of the weak PCI by vibrations is to dispose of a technological solution allowing continuum measurements.
Nowadays, there is no technological solutions available to detect the local closure of the gap along the rod axis. We have discussed in the previous critical review two possible technologies that can respond to this need, the acoustic microscopy and the analysis of sample rod vibrations. In our study, we dedicate to the investigation of the feasibility to measure the effect of the local Pellet-Cladding contact on the dynamic response of the fuel element in a passive way. The next chapter is devoted to this topic. The discussion of the technological solution adapted to the ADELINE environment is postponed at the end of the feasibility study.

10.3 Concluding remarks

The constraints associated to the ADELINE environment and configuration lead us to identify the most suitable technological solutions available and under development for PCI detection and measurements. Conclusions from previous discussion are summarized in the following table 10.4.

Concerning the measurement of the internal rod pressure, we have indicated the counter pressure sensor as the eligible technology recommended for application in the characterization of PCI under irradiation. We want to stress that the acoustic sensor is a valid technological alternative. It presents indeed the unique feature of measuring on-line the gas composition but its application is better adapted in scenarios involving stronger release of fission products (study of high burn-up fuels).

We have not indicated any eligible sensor for the measurement of the fuel centerline and surface temperature, considering the analyzed technological solutions not compatible with the ADELINE constraints and the induced thermal-mechanical perturbations related to the introduction of these sensors. These recommendations can be reconsidered on the basis of dedicated modeling of the impact of the sensor on the researched phenomena. Nevertheless, it is important to have a measure of the central fuel temperature to validate code calculation.

Parameter	**Type**	**Eligible technologies**	**Comments**
Cladding surface temperature	Measure	Optical Pyrometry	Under development Local measure, requires a moving support
Fuel surface temperature	Measure	None	Technological solutions exist but none compatible with ADELINE configuration and PCI phenomenon
Feel centerline temperature	Validation	Type C-TC and UTs	Limited by the maximum temperature and intrusivity of the sensor.
Internal rod pressure	Measure	Counter pressure sensor	Qualified and adapted to the ADELINE configuration.
Pellet-Cladding contact	Detection	*see chapter 11*	Feasibility test prior further investigation of technological solutions.
Cladding elongation	Detection	LVDT/ Fabry-Perot	LVDT: Qualified and adapted to the ADELINE configuration FP under-development
Fuel elongation	Detection	LVDT	Qualified and adapted to the ADELINE configuration
Cladding external diameter	Measure	Confocal microscopy	Under-development Remote measurement, miniaturization possible by optical fiber Moving support required

Table 10.4 – Synthesis of the eligible technological solutions meeting measurement criteria

Chapter 11

PCI detection in ADELINE by vibrations: feasibility study

In this chapter we focus on the investigation of vibrations as technological solution to measure the local establishing of the weak pellet-cladding interaction along the fuel stack axis, from the Mid-rod plane, where temperatures are the highest, towards the extremities. In section 11.1 we define the objectives of the experiment. In section 11.2 we discuss the design of the experimental bench, based on the geometrical configuration of ADELINE and representative of the hydraulic excitation mechanism. In section 11.3 we illustrate the experimental campaign, the post processing of measured data and the obtained results on the measurement feasibility. In section 11.4 we discuss the results and define the development axis for possible further investigations on the subject.

Contents

11.1 Objectives

The presence of the local pellet-cladding gap and the excitation of the sample rod induced by the flow induced vibrations, origin a relative motion between the two components of the sample rod: pellet-cladding shocks and pellet-pellet friction, that are dissipation mechanisms. These dissipation mechanisms contribute to the total energy dissipated in the structure and damp the system vibrations.
The establishing of the weak interaction reduces relative motions, with the consequent reduction of the dissipated energy. The objective of the experimental campaign is to verify the feasibility to measure an effect on sample rod dynamic due to the local gap closure. The investigated parameters are:

- Frequencies of the system. We have focused on the first mode frequency, that is the one that is excited under turbulent flow rate;
- Viscous damping ratio, which is the parameter associated to the energy dissipated in the system.
- For a system submitted to forced excitation, the amplitude of vibrations informs on the energy dissipated in the system: the higher the dissipation, the smaller the system oscillations with respect to the same external excitation.

11.2 Design of the test bench IMPIGRITIA

The IMPIGRITIA[1] test bench is designed and realized during this Ph.D. thesis to investigate the feasibility of measuring the impact of a local weak pellet-cladding interaction on the dynamic behavior of the fuel rod system in the chosen application frame of the ADELINE device. The geometrical configuration is developed on its basis and the hydraulic circuit is designed to submit the sample rod to the equivalent flow induced excitation of the ADELINE test section.
The final aspect of the test bench is illustrated in figure 11.1.

The environment: IMPIGRITIA is designed to operate at room temperature (20° C) and low pressure. The high pressures and temperatures of the real device as well as the neutron irradiation, modify the thermal-mechanical properties of the system. For a first investigation of the measurement, we study the phenomenon in a simple environment. Theoretical and experimental correlations are available, to evaluate the evolution of material properties with the environment [Fin00] and predict the expected behavior. In practical terms, the in-pile qualification remains a required step, which is out of the scope of this work.

Hydraulic design: Hydraulics is designed in order to reproduce the external solicitation in terms of the axial turbulent flow and pressure fluctuation in the flow. We identified a range of representative flow rate, imposing two principles:

- The conservation of wall pressure fluctuations [Axi01]: random wall pressure fluctuations are the driver for the origin of small amplitude vibrations in structures submitted to the axial flow rate [DeS17].As the turbulent excitation is not a deterministic process, a statistical approach is generally necessary to evaluate the pressure

[1] Acronym form "**I**nteraction **M**écanique **P**ast**I**lle **G**aine :**R**éal**I**sation du **T**est v**I**br**A**toire", from *latin* impigritia, impigritiae; means "zeal, dedication"

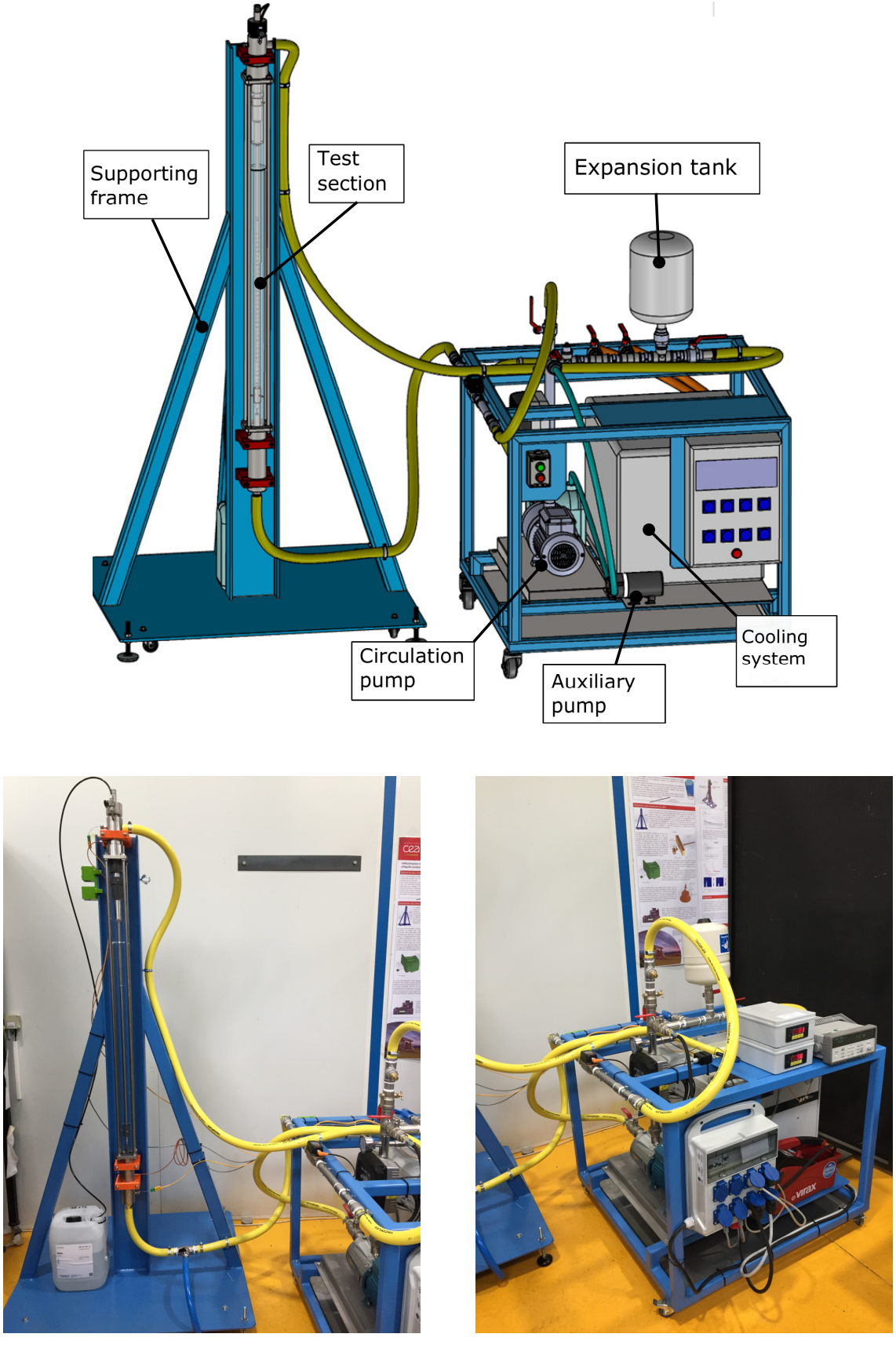

Figure 11.1 – Illustration of the final aspect of the designed test bench IMPIGRITIA

forces applied on the tube wall, based of the use of Power Spectral Density (PSD). The envelop PSD obtained from Clinch data [Cli69] can be applied to have an idea of the fluid solicitation. The conservation of the wall pressure fluctuation p_{rms} is imposed according to the definition proposed by Axisa in [Axi01] which its reported in equation (11.1):

$$p_{rms} = 0.003(\rho v^2) \tag{11.1}$$

where p_{rms} is the root mean square of pressure fluctuations, the ρ is fluid density and v is the average flow velocity.

– The Burgreen principle [Pra11]: the criterion, established by Burgreen, has been recently used by De Paw et al. in [DeP15] to study flow induced vibrations in a prototype representative of the MYRRHA system. The criterion is reported in equation (11.2).

$$v_{exp} = v\frac{\rho^{0.5}\mu^{-0.33}E^{-0.33}M^{0.165}}{\rho_{exp}^{0.5}\mu_{exp}^{-0.33}E_{exp}^{-0.33}M_{exp}^{0.165}} \tag{11.2}$$

Subscript 'exp' stands for prototype, μ the fluid dynamic viscosity, E the elastic modulus and M the mass of the sample rod at operating temperature.

The described criteria in our test conditions define a range of representative flow rate. Fluid flow velocity ranges between 0.9 to 2.6 times the fluid velocity at the sample rod in ADELINE.

$$\frac{v_{exp}}{v} \in [0.9 : 2.6] \tag{11.3}$$

From the definition of the desired flow rate at the sample rod and the geometrical configuration of the loop, we designed a conditions system to supply the required flow rate to the test section.

Geometrical configuration: Geometry and fixation conditions strictly impact the dynamics of a structure and its response under flow rate excitation. In IMPIGRITIA we keep the fixation conditions of ADELINE sample, represented on the right of figure 11.2: the sample holder is fixed at the top of the test section by a locking nut. A ring shape joint ensures the water-tightness. Coherently with ADELINE design, four elements center the sample holder in the test section.
Concerning the geometrical configuration, mechanical similarity and scale reduction cannot simply be applied to ADELINE due to the reduced L/D ratio and a 1:1 scale system was not compatible with exploitation issues. We decided to limit our study to the lower part of ADELINE sample holder, where the sample rod is located. The decision leads to an experimental system of about 1.3 m, as illustrated in figure 11.2, that is fixed at the top of the experimental section and centered in the section by means of four annular elements. The minimum radial gap between the rod and the internal diameter of the annular elements is 250 µm.
The configuration has two main consequences on the feasibility study: on one side, the shortening of the sample holder strengthens the relative impact of a local pellet-clad interaction on the global dynamics of the structure. This enhances the possibility to measure the impact of the local closure on the global rod dynamics. On an other side, it increases the stiffness of the structure. As a consequence, the same excitation mechanism results is smaller vibration amplitudes, making it more difficult to measure the studied phenomenon.
The modification in the geometrical configuration and the increase in the stiffness of the system increase the frequencies of the system with respect to ADELINE. Table 11.1 resumes the first six expected eigen-frequencies $f_{i,l}$ for ADELINE and IMPIGRITIA, obtained according to the linear modeling of the system detailed in appendix D.

The test section presents a central part manufactured in optical quality PMMA to permit the collection of data on transverse rod displacement by Laser Doppler Vibrometry, (LDV): the laser beam is pointed on the vibrating object and scattered back from it. The velocity and displacement amplitudes of the studied object generate a frequency or a phase modulation respectively, due to Doppler effect. The laser used is a class 2 Helium-Neon type, having a wavelength of 633 nm and a cavity length of 204 ±1 mm. Located at about 0.5 m from the moving rod, the spot on the rod is about 50 µm. The test section is isolated from the environment by means of a dedicated frame (in blue in the photo (a) of figure 11.1).

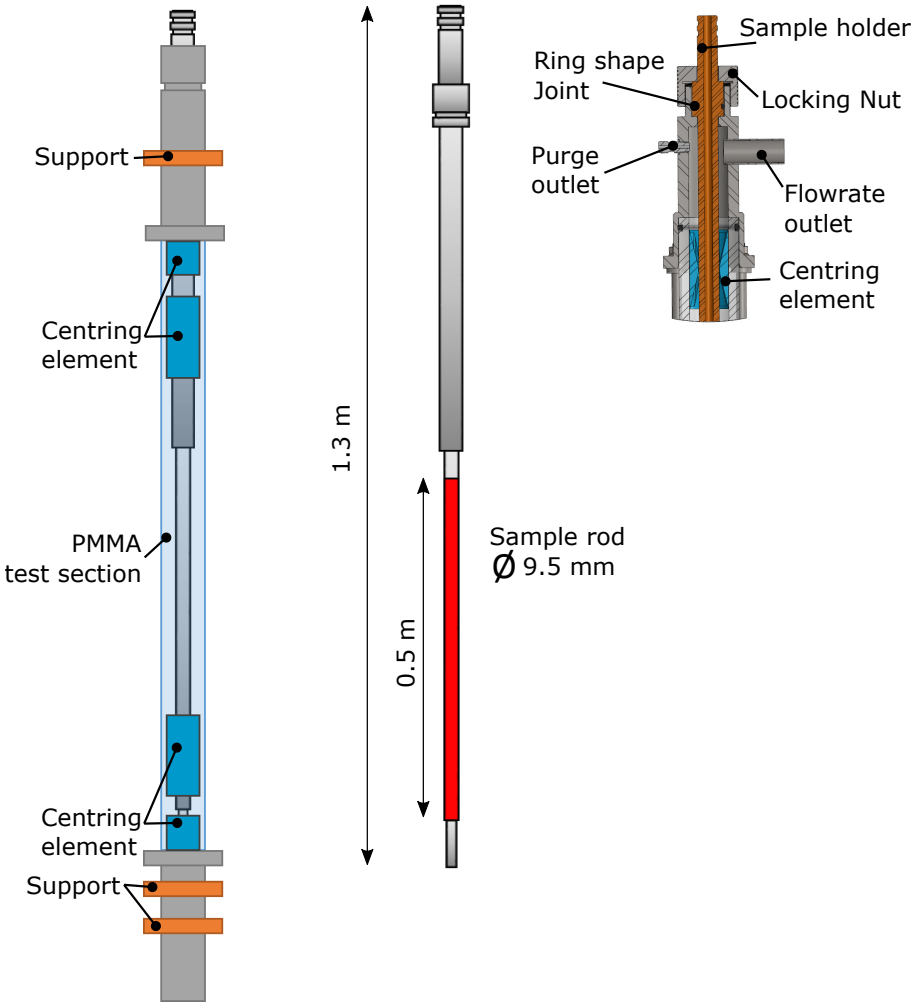

Figure 11.2 – Design of the IMPIGRITIA sample holder: on the left the assembled test section, in the middle the sample holder and on the right the sample holder fixation

Device	$f_{1,l}$	$f_{2,l}$	$f_{3,l}$	$f_{4,l}$	$f_{5,l}$	$f_{6,l}$
ADELINE	1.5	7.6	13.0	21.6	42.6	65.1
IMPIGRITIA	6.2	29.0	79.9	170.2	261.9	343.0

Table 11.1 – Eigen-frequencies of ADELINE and IMPIGRITIA devices by linear approximation. Frequencies are reported in Hz.

The sample rod 33 pellets, for a total length of 495 mm, are placed within a standard zircaloy cladding having internal diameter $D_i = 8.36$ mm and external diameter $D_e = 9.5$ mm. Pellet diameter is imposed at $D = 8.2$ mm which corresponds to a fabrication gap of 80 µm of radial gap. UO_2 is replaced by molybdenum, the most representative material in terms of density. Coherently with the design of a PWR sample rod, a spring is located at the top of the "fuel" stack.

To fulfill the fabrication gap existing between pellets and clad and remotely control PCI, a dilatation system capable of local expansion is used. It has been developed for stent implantation in the medical domain and it is made of an elastic balloon which expands once inflated. The system is remotely controlled by a connection tube, which permits to inflate and deflate the balloon, and so to locally close and open the gap, respectively, without the need to disassemble to system. A general assembly scheme is presented in figure 11.3.
In order to introduce the dilatation system, the top plug that is welded to the clad and the sample holder itself are centrally drilled.

The dilatation system is thus introduced from the top of the sample holder, through centrally drilled pellets and the balloon is placed in the region where gap closure wants to be induced. There, pellets are replaced by two half pellets, which are displaced by means of the inflated balloon, leading to pellet-cladding contact.

In order to identify the minimum number of pellets that have to be in contact with the cladding to obtain a measurable impact on the investigated parameters, we use commercially available balloons of different length to recreate weak PCI along different axial extension: we manufactured 4 rods (C2 to C5) where the weak interaction is established over different axial extensions by remotely inflating the balloon. The configurations are detailed in table 11.2. We have also manufactured three more rods for the qualification of the model used to design the system:

– C0 the empty rod is used to characterize the dynamic response of the strucutre without the extra unknown induced by the presence of pellets;

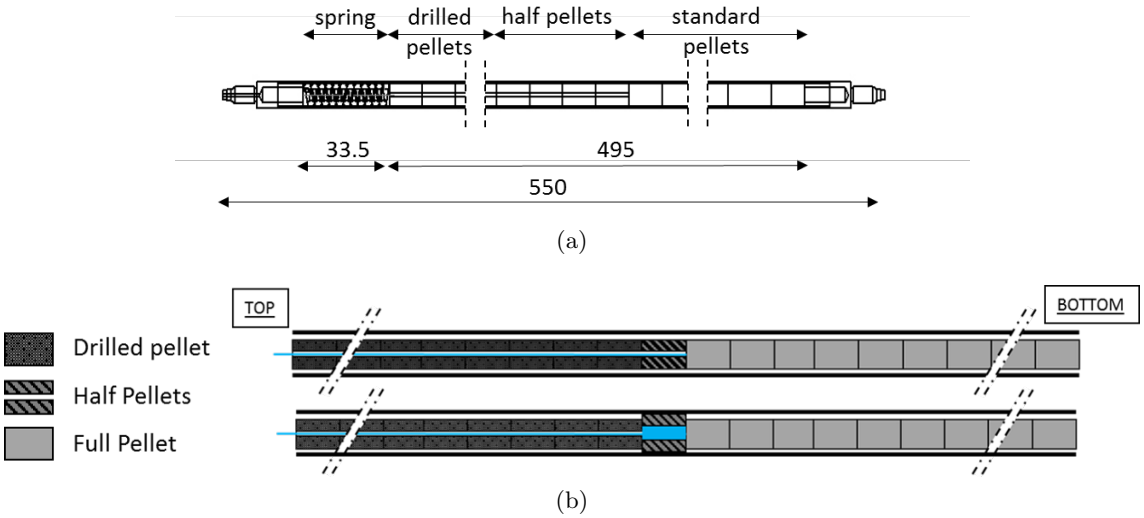

Figure 11.3 – Schematic view of the sample rod

– C1 is a standard rod with 33 pellets and open gap along the entire fuel stack. It is used to analyze the experimental bias induced by the presence of the inflating system;

– C6 corresponds to C1 but with closed gap along the entire fuel stack. It is realized by fulfilling the radial gap with a specific glue. It is realized to obtain an upper bound for the effects by the local Pellet-Cladding contact.

Rod identifier	N° of full pellets	N° of half-pellets	N° of drilled pellets	L of PCI [mm]
C0	0	0	0	-
C1	33	0	0	-
C2	15	2x1	17	15
C3	14	2x3	16	45
C4	13	2x5	15	75
C5	11	2x9	13	135
C6	33	0	0	-

Table 11.2 – Characteristics of the fuel rods used during the experiment. In blue the rods where the dilatation system is introduced to study the weak interaction, in black the other rods used for the aforementioned scopes.

11.3 The experimental campaign and its results

IMPIGRITIA is designed in two phases: a first one in air, where the system is studied in controlled free vibrations tests. This phase permits to characterize the system and verify the feasibility to detect a modification on rod dynamics resulting from a local weak interaction.
The first phase giving positive results on feasibility, we move to the second phase, where the structure is immersed in water and submitted to the representative excitation of the ADELINE device. The only excitation mechanisms are the flow induced vibrations. The objective of this phase is to state on the technological feasibility to measure the impact of weak PCI interaction with a passive system without the need to actively excite it.
For both experimental phases, the imposed fixation condition is the same but, in air tests, centering elements are removed.

11.3.1 Controlled environment: air measurements

Methodology

According to scientific literature, the system submitted to turbulent flow rate responds according to its first mode [Pai81] For this, air tests are carried out in order to characterize the first mode of system vibration.
An initial displacement is imposed to the rod and when released, the decay of free oscillations is measured in the direction of transverse displacement. Measurements are collected at the bottom of the sample rod, where vibration amplitudes are the highest.

The test is repeated 10 times for each rod configuration (type of rod, open gap and closed gap) and the sampling frequency is imposed at 10 kHz, that is much higher than the first mode frequency of the IMPIGRITIA system, evaluated by linear approach and amounting

to 6 Hz. It thus permits an accurate sampling of the researched signal.

In the following we discuss the evolution and behavior of the rod configuration C3, in which the weak PCI is induced over the 3 central pellets in the rod, for a total length of 45 mm of the whole "fuel" stack. We discuss its time evolution and the modification of the local closure on the viscous damping ratio. Then, we report some comments on the behavior of the other rods and the results on the analysis of the first mode frequency.

Analysis of the damping ratio

From the measured velocity of displacement, we calculate the spatial decay of free oscillations by direct interaction. Figure 11.4 illustrates in light blue a sample evolution for the C3 rod and in red are highlighted the peaks used to evaluate the viscous damping ratio by logarithmic decrement.

For a linear, single degree of freedom system, the displacement can be written in the following form:

$$x(t) = exp(-\zeta\omega_0 t)\,(Acos(\omega_d t) + Bsin(\omega_d t)) \tag{11.4}$$

where $\omega_0 = 2\pi f_0$ is the natural frequency of the SDOF system, $\omega_d = \omega_0\sqrt{1-\zeta^2}$ is the pseudo-angular frequency which is directly measured by the pseudo-period T_d, A and B depend on the initial conditions of the problem.
The term $exp(-\zeta\omega_0 t)$ describes the decay of free oscillations. In this case, to obtain the viscous damping ratio ζ it is sufficient to consider two different local maxima: considering the peak displacement x_i occurring at time t and the peak displacement x_{i+n} at time $t + nT_d$:

$$\frac{x_i}{x_{i+n}} = \frac{exp(-\zeta\omega_0 t)}{exp(-\zeta\omega_0(t+nT_d))} = exp(\zeta\omega_0 nT_d) \tag{11.5}$$

When the system presents a non linear behavior, the viscous damping ratio depends on the amplitude of system vibrations and to the LCM is preferred the Consecutive Linear Logarithmic Method, C-LDM: two successive local maxima are considered, the viscous damping ratio is considered linear between these two peaks and evaluated N times along the decay of system oscillations. As the dissipation mechanisms due to the presence of the internal gap in the rod are non linear, we apply the C-LDM method.

A minimum amplitude has been identified, amounting to $\mathrm{A_{min}} = 0.2$ mm, below which the presented approach cannot be applied. For smaller amplitudes, the oscillations of the rod are no more centered in zero, as illustrated in figure 11.5. This possibly results form the coupled effect of the curvature of the rod and the non unidirectional motion that establishes, which make a single point measurement not sufficient in this range.
For each test of a rod in the same configuration, we extract the evolution of the viscous damping ratio as a function of the amplitude of rod oscillations. We make the hypothesis of a linear relation between the viscous damping ratio and the amplitude of oscillations for the i^{th} experiment of the j^{th} rod configuration is expressed in terms of:

$$\zeta_i = a_i + b_i x \tag{11.6}$$

where a_j and b_j are the coefficients of the linear regression. Under the hypothesis that the measurements have a normal distribution, an average evolution is obtained from the N tests, $\bar{\zeta}^j$ associated to its variance $\sigma^2_{\bar{\zeta}^j} = \dfrac{1}{N}\sum \sigma^2_{\zeta_i^j}$.

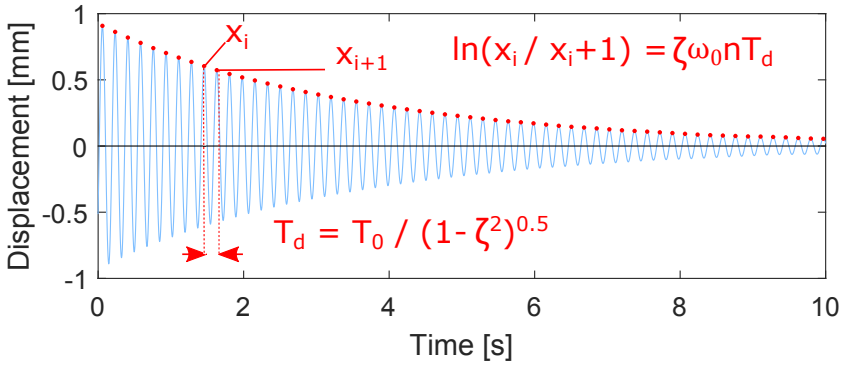

Figure 11.4 – Measured displacement for C3 and methodology for the evaluation of the viscous damping ratio

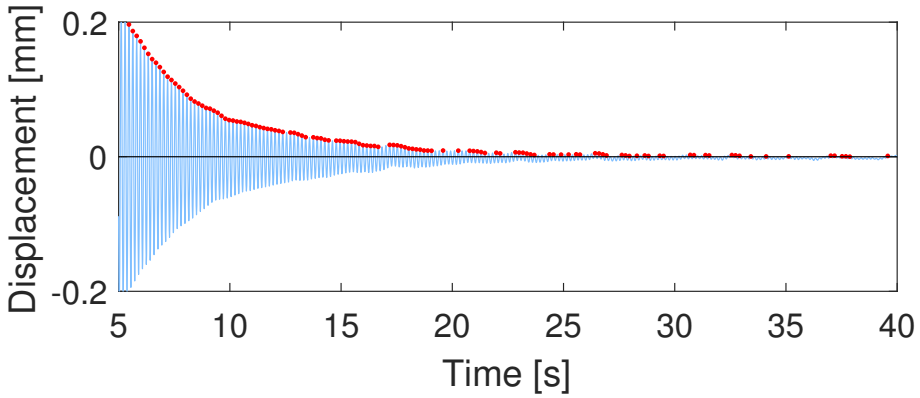

Figure 11.5 – When oscillation amplitudes are smaller than A_{min}, the decay of free vibrations is no more centered in zero and the C-LDM method cannot be directly applied. The measurement system may be sensible to the non-unidirectional motion of the rod and the curvature of the rod.

Figure 11.6 illustrates the average evolution of the viscous damping ratio $\bar{\zeta}^j \pm 1\sigma_{\bar{\zeta}^j}$ of C3 rod, in blue when the gap is open, in red when the balloon is inflated and the local contact is induced. The evaluation is performed in the range of oscillations amplitude 0.2-1 mm.

We are interested in characterizing the confidence associated with the feasibility to detect the weak PCI depending on the range of oscillations: indeed, as illustrated in figure 11.6, the variance of measured evolutions is larger near the minimum threshold. For this, we evaluate the first order (α) and the related second order risk (β) associated to the detection of the weak PCI, in the different ranges of oscillation amplitudes. Under the hypothesis that the measurements have a normal distribution, the first order risk is evaluated at the intersection of the two Gaussian distributions and the beta value is consequently deduced. Figure 11.7 graphically illustrates the meanings of the confidence level and β risk.

We report in table 11.3 the results of the analysis.
First of all, **we observe that in all ranges of oscillations amplitudes, the weak PCI reduces on average the damping ratio of the structure because of the local disappearance of the dissipation mechanisms induced by the relative pellet-cladding motion.**

The general approach used in measurements is to impose a maximum acceptable value of first order risk α of 5%. As expected the first order risk is not acceptable in the region below the value of A_{min} (0.1-0.2) and the detection can be considered feasible for oscillations which amplitude is higher than approximately 0.3 mm.

Even though the highest confidence is between 0.7-1.0 mm, in the ADELINE system the amplitudes of oscillations have to be limited, for neutronic and safety reasons. So, we are more interested to the fact that the detection is feasible in the range of 0.3 mm.

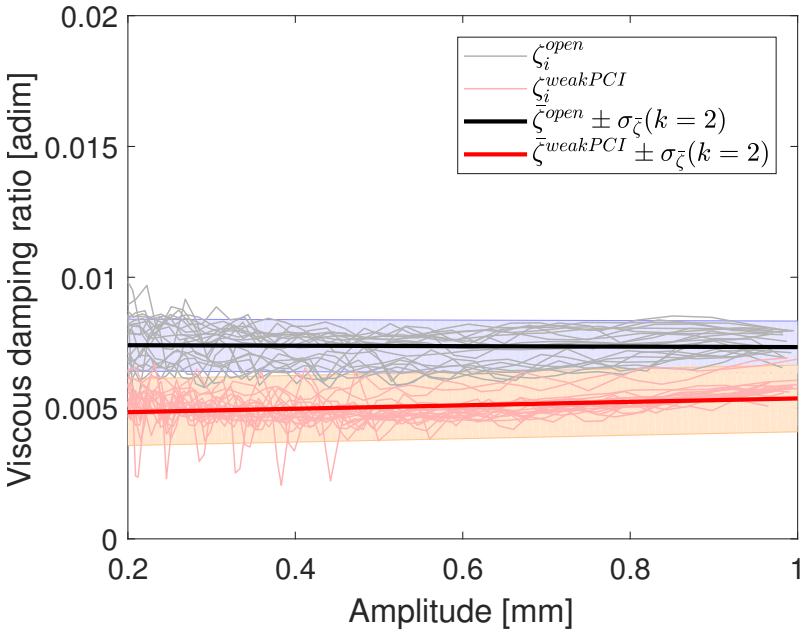

Figure 11.6 – Viscous damping ratio evolution as a function of the amplitude of oscillations for the C3 sample rod: the i^{th} calculated evolutions are represented in light grey for the open gap configuration and in light red for the closed gap one (induced weak PCI). In black and red are illustrated the linear models calculated in the highlighted interval, with the associated range of standard error at k=2.

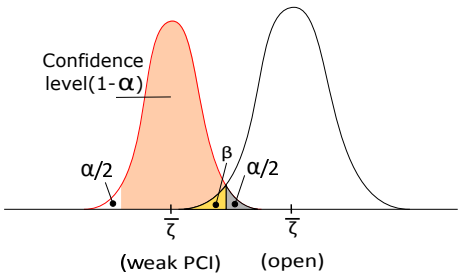

Figure 11.7 – Illustration of the first order risk α and the related confidence level and second order risk beta

Amplitude	Open gap			Weak PCI			$\alpha/2$	$\beta(\alpha/2)$
range [mm]	$\bar{a}$	$\bar{b}$	$\sigma_{\bar{\zeta}}$ (k=1)	$\bar{a}$	$\bar{b}$	$\sigma_{\bar{\zeta}}$(k=1)	risk (I)	risk (II)
0.1 - 0.2	6.5e-3	6.9e-3	1.4e-3	5.8e-3	-2.6e-3	1.6e-3	32.8%	24.4%
0.2 - 0.3	8.2e-3	-2.7e-3	7.1e-4	5.8e-3	-3.0e-3	7.9e-4	5.5%	4.8%
0.3 - 0.4	8.2e-3	-2.4e-3	5.1e-4	5.7e-3	-2.4e-3	7.4e-4	2.7%	1.71%
0.4-0.5	7.7e-3	-1.1e-3	5.4e-4	5.4e-3	-1.4e-3	7.2e-4	3.2%	2.3%
0.5-0.6	7.3e-3	-2.3e-4	5.5e-4	4.6e-3	4.4e-4	4.1e-4	0.7%	1.0%
0.6-0.7	6.0e-3	1.8e-3	4.5e-4	4.3e-3	1.1e-3	4.0e-4	0.3%	0.4%
0.7-1.0	6.5e-3	1.1e-3	3.3e-4	3.1e-3	2.8e-3	2.6e-4	0.1%	0.1%
0.1 - 1	7.5e-3	-1.5e-3	9.0e-4	5.2e-3	-1.2e-3	1.0e-3	13.1%	10.9%
0.2 - 1	7.4e-3	-9e-5	5e-4	4.7e-3	6.6e-4	6.4e-4	4.8%	3.5%
0.3 - 1	7.1e-3	3.07e-4	4.1e-4	4.3e-3	1.2e-3	5.3e-4	2.5%	1.8%

Table 11.3 – Results of the analysis on the confidence of the detection of the weak PCI for the C3 fuel rod during air tests

Comments on the other rods

We could not assess all the manufactured rods. Indeed, during the experiment, some water entered the C4 and C5 rods, where the weak PCI is induced over 5 and 9 pellets. This resulted from a loss of water-tightness occurred during previously qualification tests performed under imposed flow rate. **The presence of water has completely modified the pellet-pellet and pellet-cladding interactions making these rods not reliable for further analysis.**
In order to recover these rods, they were heated up to induce water evaporation (T>100°C) but this process caused the oxidation of Molybdenum pellets. Molybdenum indeed undergoes strong oxidation when it reacts with water at a temperature above 80°C. A fine dust was produced in the oxidation, depositing on the internal surface of the clad leading to the impossibility to further exploit them to detect PCI.

We have investigated the behavior of the C2 sample rod, where a single pellet is replaced by 2 half that are locally put in contact with the clad. The evolution of the damping ratio as a function of the oscillation amplitudes is illustrated in figure 11.8: its damping ratio strongly varies with the amplitude of oscillations showing that C2 has a stronger non linear behavior than C3. Data variance in the sub-interval 0.2-0.6 is too large and the two behaviors cannot be distinguished. In the subinterval 0.6-1 mm, the weak PCI decreases the average damping ratio but the confidence level is much lower than for the C3 sample rod.
To investigate this behavior the methodology has to be improved in order to cope with the non linearities of the system. This should involve 2D measurements and the development of a model to describe internal mechanisms and support the understanding of measured phenomena.

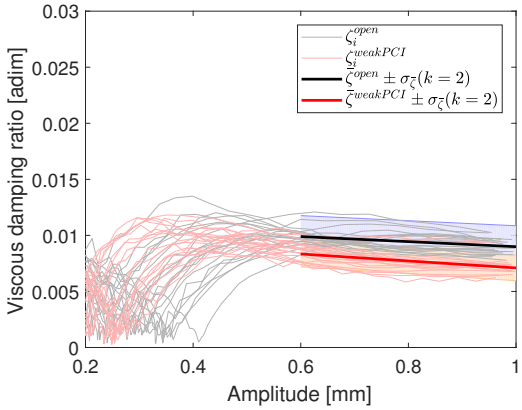

Figure 11.8 – Viscous damping ratio evolution as a function of the amplitude of oscillations for the C2 sample rod: the i^{th} calculated evolutions are represented in light grey for the open gap configuration and in light red for the closed gap one (induced weak PCI). In black and red are illustrated the linear models calculated in the highlighted interval, with the associated range of standard error at k=2.

Analysis of first mode frequency

Table 11.4 summarizes the experimental results about first mode eigen-frequency for the water-tight rod configurations defined in table 11.2. All results are measured with an uncertainty of ±0.1 Hz (2σ).
C0 presents a first mode frequency at 8.2 Hz, higher than the other rod, which is due to its lower mass, as there are no pellets inside the cladding.
C6 shows a slightly higher frequency for the first mode than the others, which can be found by modeling the rod as a linear system where the mass is equal to the mass of the "fuel" stack and the stiffness is the one of a full rod having external diameter the one of the cladding, as detailed in appendix D.
By comparing the first mode frequency of C1 with the rod configurations C2, C3, C4 we observe that:

- **The local closure of the gap induces no measurable variation in the tested rods;**
- The failure in the water-tightness of the C4 and C5 does not modifies the frequency of the first mode in a measurable way, thus leading to the impossibility to detect it without disassembling the device;
- The modifications imposed to the rods to introduce the dilatation system and to locally induce the weak PCI do not modify in a measurable way the first mode frequency.

11.3.2 Passive representative excitation: turbulent flow rate

Methodology

Supported by the positive results obtained in the first experiments in air, we focus this experimental phase on the research of an effect due to the modification of dissipated energy in the system on the rods that showed positive results in air tests: C3 and C2. For this, each rod is submitted to the turbulent flow rate designed to be representative of ADELINE device. By Laser Doppler Vibrometry (LDV), the velocity of system motion

	C0	C1	C2	C3	C4	C5	C6
f_1,open [Hz]	8.2	5.7	5.8	5.7	5.8	6	6.7
f_1,closed [Hz]	-	-	5.8	5.7	5.8	6	-

Table 11.4 – Experimental frequencies for the different rod configurations: C0 is the empty rod, C1 is a standard rod, with open gap; C2 is manufactured to induce weak PCI on one pellet, C3 on 3 pellets, C4 on 5 pellets, C5 on 9 pellets. C6 is the closed gap rod configuration, where the relative motion is prevented by fulfilling it with glue.

is measured. The excitation mechanism is random, long measures are thus performed to improve the statistics. The sampling frequency is 10 kHz as for the air measurements. The experiments are conducted at four different flow rates within the identified representative interval of ADELINE device. Tested conditions are summarized in table 11.5.

Flow rate [l/min]	$\boldsymbol{u}$ **[m/s]**
13.5	0.82
20	1.21
30	1.82
41.5	2.51

Table 11.5 – Flow rate conditions imposed in the passive representative tests

As previously mentioned, according to scientific literature [Pai81], the system, submitted to flow induced vibrations, responds according to its first mode. For this, measurements have been collected at the bottom of the sample rod, where oscillation amplitudes are the highest.
The vibration amplitude is an indicator of the energy dissipated by the system: for the same excitation mechanisms, the more energy is dissipated by the system, the lower the vibration amplitude is. Absolute values of the vibration amplitude at a certain time are not meaningful since the excitation mechanism is a random phenomenon. Given the random nature of the external force, and the central limit theorem, the displacement of the structure adhere to a normal Gaussian distribution, for a sufficiently high number of samples. In appendix E are reported the histograms of the measured displacements showing the validity of this assumption.
We evaluate the root mean square value of the displacement, here after defined effective amplitude or simply amplitude A, in the time and frequency domain. In the time domain it results form the following definition:

$$A = x_{rms} = \sqrt{\frac{1}{n}\sum_{j=1}^{n} x_j^2} \tag{11.7}$$

In the frequency domain, it corresponds to the square root of the area below the PSD of the signal. Considering $x(t_i)$ the corrected displacement signal of the system and $S_{xx}(f)$ its power spectral density, the x_{rms} can be obtained by the following:

$$A = x_{rms} = \int_0^{f_a} S_{xx}(f)df \tag{11.8}$$

where f_a is the Nyquist frequency, half of the sampling one.

Cylinders respond to the pressure fluctuations in the flow field at all flow velocities, as shown in the figure 11.9. For a Strouhal number smaller that 0.2, like in this experiment, Chen [Che70] and Paidoussis [Pai04] show that the vibration amplitude are proportional to $u^{1.5}$. In figure 11.9 we observe that the amplitude of oscillations presents a peak when the structure is parametrically excited by the flow and oscillates at one of its resonant frequencies. Above a certain critical velocity, the structure undergoes fluidelastic instability and the amplitude of oscillations exponentially increases.

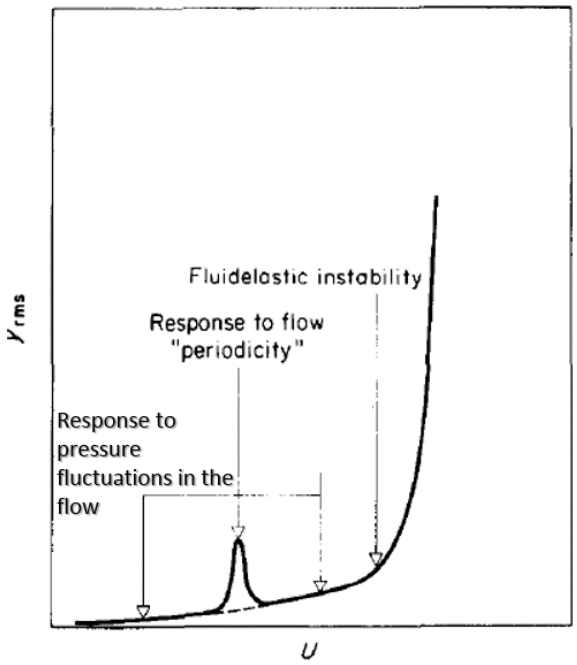

Figure 11.9 – Idealized response of a cylinder in axial flow [Pai81].

Data treatment

The velocity of transverse motion of the sample rod under flow rate excitation is measured with a typical resolution of 0.5 µm/s. Collected signal is noised by the presence of optical dropouts: the non perfect rod surface diffuses the incident light, the collected signal from the LDV is amplified or decreased depending on the fact that the phase of the direct and diffused contribution is synchronized or not. This phenomenon results into an instantaneous saturation, a Dirac in the time signal, which leads to an increase in the noise level. We clean the signal from dropouts: as shown in figure 11.10, we identify the range of variation of the collected signal (red). Once identified all the single measures out of this range (green), they are replaced by a linear interpolation between the previous and following valid measurement points. The resulting signal is shown in magenta in the figure (b).
From the corrected velocity signal, the displacement is obtained by direct integration.

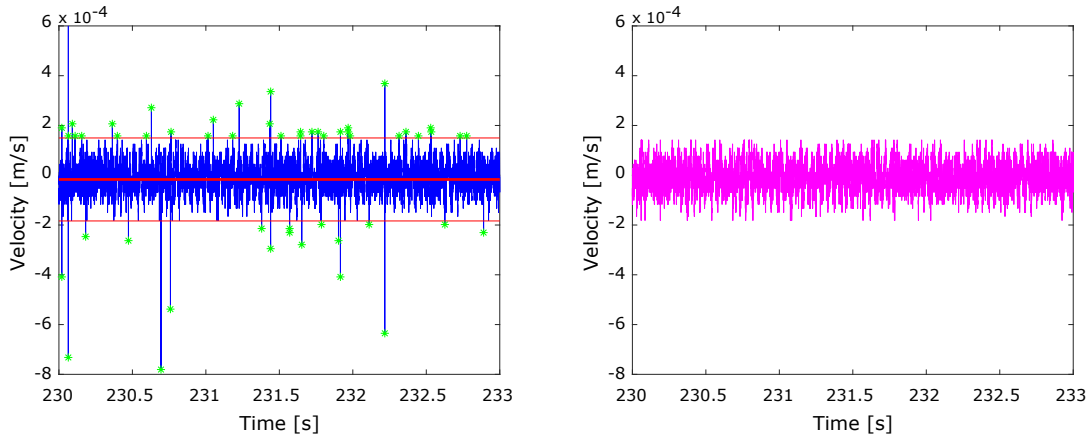

Figure 11.10 – Identification of optical dropouts and correction of the signal: from the raw signal (blue) we identify the optical drop-outs (green) and clean the signal (magenta)

Analysis of the amplitude of oscillations

Figure 11.11 shows the amplitude of the sample rod oscillations in µm as a function of the fluid velocity in [m/s]. In black are reported the measurements for the open gap configuration and in red when the weak PCI is locally induced on the 3 central pellets by inflating the dilatation system. Data from the graph are reported in table 11.6, with k=1. When the fluid flow exciting the sample rod is below 1.8 m/s, the sample rod barely moves: the oscillation amplitudes are lower than 1 µm and the standard errors are of the same order. It is not possible to distinguish any modification induced by the local pellet-cladding contact. The amplitude of oscillations increases when we impose a fluid velocity of 1.8 m/s at the sample rod (30 l/min in the loop): we measure an effective amplitude of 4.6 µm with a standard error of 1.2 µm when the gap is open and the amplitude decreases to 2.3±0.9 µm when the dilatation system is inflated to induce the local weak PCI.
We apply the same approach used with the air measurements to evaluate the confidence level associated to the detection of the weak PCI. From experimental results we evaluate that the detection can be performed with a maximum confidence level of 80% (k=1.3) and a risk of a false detection of about 17%.

Fluid velocity [m/s]	**Open gap** $\bar{A} \pm \sigma_{\bar{A}}$ (k=1) [µm]	**Weak PCI** $\bar{A} \pm \sigma_{\bar{A}}$ (k=1) [µm]	**Confidence** (1-α)	**II Order** Risk β
0.8	0.4±0.4	0.5±0.4	∼0%	∼100%
1.2	0.5±0.4	0.5±0.4	∼0%	∼100%
1.8	4.6±1.2	2.3±0.9	80%	17%
2.5	96.1±5.5	93.1±5.4	24%	40%

Table 11.6 – Results of the analysis on the confidence of the detection of the weak PCI for the C3 fuel rod under representative flow rate excitation

When the sample rod is submitted to a fluid velocity of 2.5 m/s, the amplitude of oscil-

lations strongly increases to an average value of 96 µm with a standard error of 5.5 µm. The local contact shows to induce no detectable modification in the amplitude. The two are not statistically distinguishable at this excitation level.

The experiment shows that the weak PCI can be detected by measuring the amplitude of oscillations under flow rate excitation.
We have applied in IMPIGRITIA a passive measurement: the system is excited only by the flow rate and we measure the induced vibrations. From the results it appears that the feasibility of the detection is related to a precise range of amplitudes induced by the corresponding flow rate. This indicates that the application of **an active excitation, forcing the system to vibrate in the optimum range of oscillations, would enhance the probability to detect the weak PCI.**

From the experiments we observe other facts of interest for further analysis.
First of all, we observe that the local contact leads to the decrease of the oscillations amplitude of C3, while we expected an increase resulting from the reduction of the dissipation mechanisms, in agreement with the measurements on the first experimental phase. A possible explication can be related to the characteristic radial gap size in the fuel rod: as we previously said, the pellet-cladding gap has a radial dimension of 80 µm. At 1.8 m/s, when we detect the weak PCI, the system oscillates in a range of amplitudes that is one order of magnitude smaller than the gap. So, we can think that, when the gap is open, the external force is too low to create a relative motion between pellets and cladding, thus there are no shock neither friction mechanisms dissipating energy. When the dilation system is inflated instead, some energy is dissipated in the contact and results into a macroscopic reduction of amplitudes.

Second, when the external excitation mechanism rises, the amplitude increases to about 100 µm but the weak PCI cannot be detected. We identified two possible explanations for

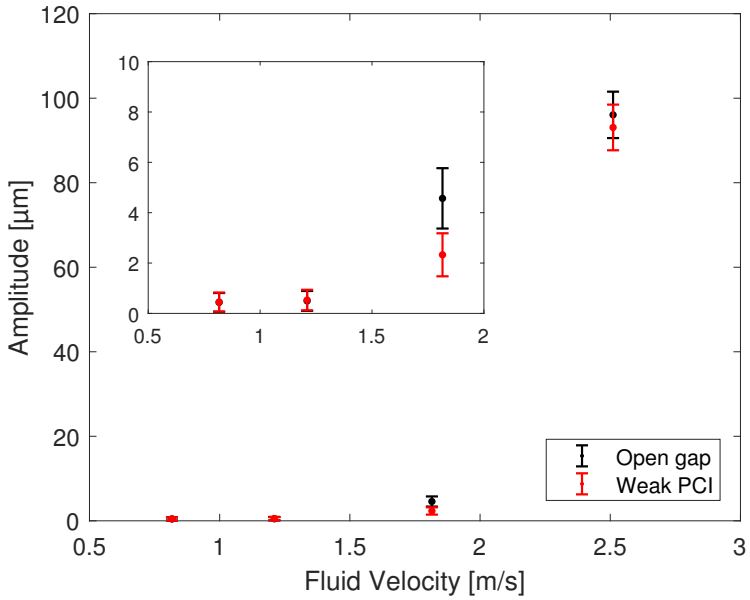

Figure 11.11 – Root Mean Square amplitude of flow induced vibrations for the C3 fuel rod, k=1

this result, that constitutes interesting research axes for future works:

- The amplitude of oscillations are in the same order of the gap existing between the rod and the bottom annular element introduced in the test loop to center the rod in the section (cf figure 10.4). Excited by the flow rate, the sample rod hits the annular elements, the boundary conditions are completely modified, with negative consequences on the feasibility of detection. To further investigate this possibility, the power spectral densities of the tested rods should to be studied and the analysis supported by a complete modeling of the system;
- The strong increase in the amplitude of oscillations may result from a resonant effect between the fluid and the structure (see figure 11.9). The fluid-interaction mechanisms of the rod is to be analyzed by a complete model of the structure.

Comments on the other rods

Figure 11.12 presents the measured RMS amplitude for the watertight sample rods: C1, C2, C3 and C6.

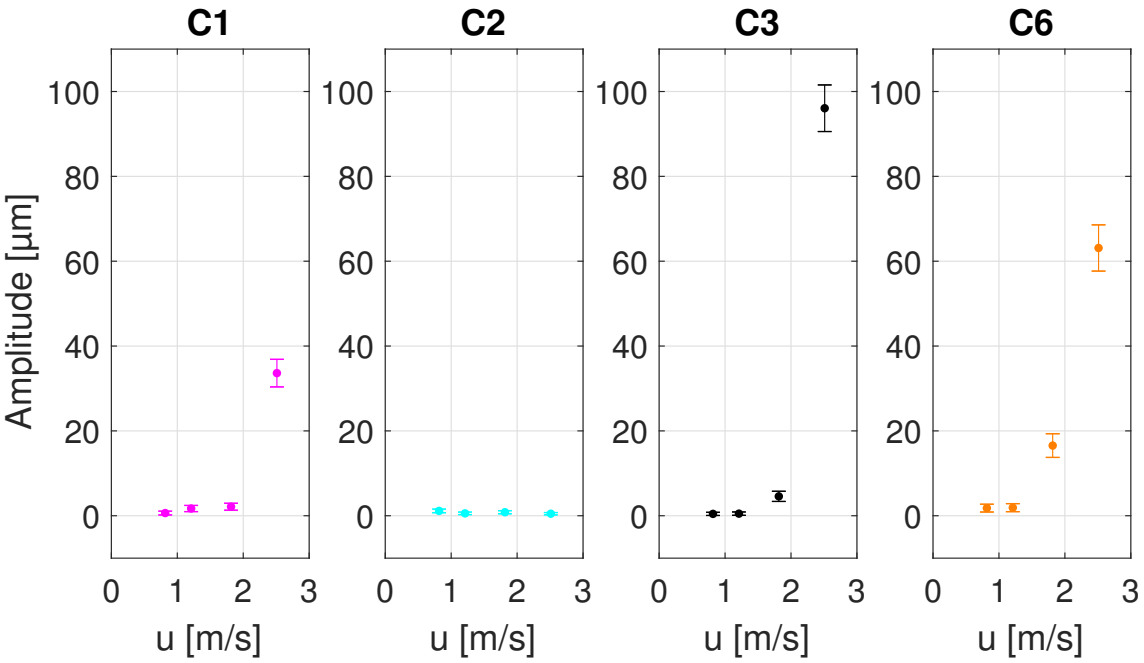

Figure 11.12 – RMS amplitude of vibrations for all tested rod configurations at different flow rates in the representative range of variation (k=1)

For a single tested rod, we find that the increase in the imposed flow rate induces an increase in the vibration amplitudes. For all except C2, which vibrations amplitudes show approximately no dependency on fluid flow rate excitation.
We also observe that different rods submitted to the same flow rate excitation present different oscillation amplitudes, with a dispersion that ranges from 1 to 2 orders of magnitude. These two facts lead us to conclude that **a lack of repeatability characterizes the experiments on different rods under flow rate excitation.**
This may come from a dependency of the rod response on the way it is assembled: for the

tests we used two sample holders, each composed of several pieces, tightened together, and each sample holder has its own joint. In further investigations, the use of a single sample holder, which is assembled monitoring the tightening torque or welding the different parts, can enhance the possibility to compare the different rods.
Figure 11.12 also shows that the strong increase in vibration amplitude that characterizes C3 at u = 2.5 m/s, occurs for all the other rods, except C2 that is not reliable. Figure 11.13 illustrates the power spectral densities evaluated for the performed tests. From the PSD we observe that the spectral response completely changes when the rods are submitted to higher flow rates: this can be caused by a fluidelastic instability, a resonant phenomenon or can origin from the interaction of the sample rod with the annular elements that center it in the test section. Further investigation shall be performed to understand the causes of these modifications.

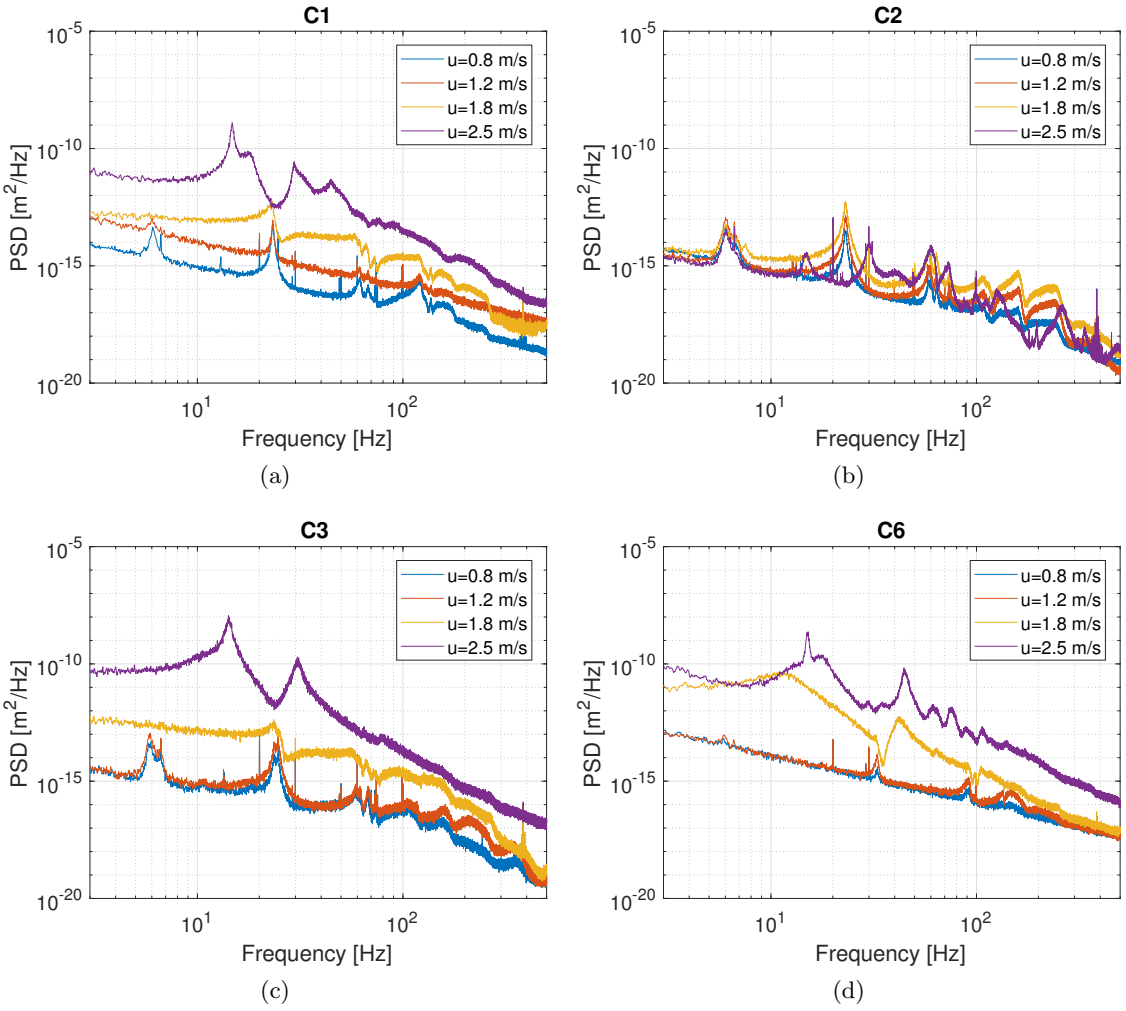

Figure 11.13 – Power spectral density of the sample rod displacement, obtained integrating the corrected velocity signal and imposing an Hanning window of 60 s with an overlapping ratio of 0.5 [BP10]

11.4 Conclusions and further investigations

We have presented in this chapter the IMPIGRITIA experiment to study the feasibility to detect the local contact between the pellets and the cladding through the dynamic response of the sample rod. It constitutes a first of its kind experiment to recreate at low temperature, at low pressure and out of neutronic flux a progressive and local contact between pellets and the surrounding cladding.
The test bench and the experimental program have been completely designed and realized during the Ph.D. thesis in order to be a simplified version of the ADELINE device, similar in terms of geometrical configuration and excited by a representative hydraulic flow rate. The experimental campaign has been carried out in two phases, distinguishing between the global feasibility to detect PCI through vibrations and the feasibility of the detection under representative excitation.

We showed that the weak PCI can be detected analyzing the dissipated energy while it has no measurable effects on the first mode frequency of the rod.

Indeed, from the analysis of the C3 sample rod, where the three central pellets are replaced by 3 couples of half-pellets, remotely attached to the surrounding cladding when the dilatation system is inflated, we obtained positive results on the feasibility of the detection, both in air measurements and under flow rate excitation. In air, the results are associated to a high confidence level while larger uncertainties are associated to the measurements under flow rate excitation.

The experiment highlights that the feasibility of the detection is strictly related to the excitation force. Under flow rate excitation indeed, the weak PCI induces a measurable effects only for one out of the four flow rates imposed to the sample rod.

We have showed that a **lack of repetability** characterizes the different tested rods. This can be caused by slight differences in the assembling of the sample holder or a variability in the interaction of the sample rod with the boundary conditions (the centering elements), induced by a lack of straightness of the sample holder or of alignment of the sample rod in the test section. This variability is likely to occur in ADELINE, where the pre-irradiated sample rods shall present different state of deformation depending on their irradiation history.
In this frame, the active excitation can improve the management of the sample rod vibrations, forcing it where the confidence of detection is the highest.

This implies that an active excitation should be considered for further investigations and for application in ADELINE, in order to force the system to vibrate in the range where the feasibility is enhanced.

We have identified three axes for the further investigations:

- **Modeling**: To support the understanding of the physical phenomena occurring inside the sample rod and its behavior depending on the applied force, it is necessary to develop a dynamic model for the system, that takes into account the internal dissipation and the fluid-structure interactions. A basis for the modeling has been proposed but further developments are required (see appendix D).
  This model can be validated by means of the experimental results of IMPIGRITIA

and it can be used to provide elements to improve the design of the ADELINE irradiation device;

- **Experiment:** A second experimental campaign should be performed. This should aim at validating and characterizing the interest of an active excitation of the structure.
  Also, IMPIGRITIA has proved the feasibility of the detection with mock-up pellets in Molybdenum, which is representative of the uranium dioxide density but presents a different friction coefficient. A test should be thus performed using depleted UO_2 pellets;
- **Instrumentation:** The instrumentation used in IMPIGRITIA is the laser Doppler Vibrometer, which showed to perform really well in the designed operational conditions, leading us to measure displacements in the order of 0.5 µm. But, it is not adapted for use in the ADELINE device. First, the measurement principle is strongly affected by the unwanted motion of the sensing head with respect to the target object. Second, the instrumentation set-up requires the system to be placed at a certain distance form the object to maximize the reflected signal. For the used instrumentation, the minimum optimal distance is of about 200 mm, which is not compatible with the geometrical configuration of the ADELINE test section. Over all, the LDV uses an Helium-neon laser having wavelength of 633 nm. According to the attenuation of the spectrum under irradiation proposed by Cheymol in [Che11], this wavelength is strongly attenuated under irradiation.
  A possible identified solution is the use of a modified LVDT, placed at the bottom of the sample rod, to measure the transverse displacements of the sample rod. The system can be adapted to measure the displacements along different circumferential angles to verify the position of the sample rod in the test section and verify the axisymmetry of the rod vibrations. This device shall allow to investigate the rod behavior in continuum, with a sensor that is placed out of the region of the highest neutron flux and aligned to the sample rod, which limits the perturbation of the system.

Chapter 12

Proposal of an irradiation scenario to measure PCI and melting onset

The objective of this chapter is to apply the results of the previous parts of this work to propose the principles of an irradiation scenario and the related measurement method to detect and to characterize Pellet-Cladding Interaction and to detect the onset of melting in the fuel pellet. In this frame, we recall in section 12.1 the target parameters to be characterized and the selected technological solutions. In section 12.2 we define the sample rod to be used and, in section 12.3, the irradiation scenario considered. Finally, in 12.4, we propose the measurement method related to the different experimental phases.

Contents

12.1 Objectives

We want here to sum up all the results of the presented work to propose a principle of irradiation scenario and the related measurement method that permits to detect and characterize the Pellet Cladding Interaction and the melting onset through the deformation induced on the external cladding.
In the following we consider as available and reliable the technological solutions that have been previously selected but are currently under development and we do not consider any limitations in the number of sensors to be integrated in the instrumentation set up.

According to the analysis developed in the part I and II of this thesis, the identified relevant parameters to be measured are the following:

- **The evolution of the cladding external diameter** : this parameter allows to detect the origin and development of the strong PCI that results into the formation of primary and secondary ridges on the cladding surface. Also, by modeling the onset of melting in the fuel pellet, we have showed that we expect the acceleration of the pellet deformation kinetics, with a probable consequent impact on the kinetics of the cladding.
  Due to the axial power profile of the JHR reactor, the highest temperatures origin at mid rod plane, where the phenomenology is enhanced. But, a local measure is not sufficient to measure the deformation kinetics and an in-pile profilometry is required, over different axial extension depending on the phase of the irradiation scenario. This imposes the use of a reliable moving support for the sensor;
- **The axial elongation of sample rod components**: modeling shows that a discontinuity occurs when the PCI is sufficiently strong along the fuel stack that the fuel elongation drives the cladding one. Since this moment, the two objects deform in the axial direction according to a mutually influenced kinetics. It has to be recalled that the whole sample holder is expected to elongate as a consequence of the local thermal range. For this, the axial elongation of the cladding and of the fuel have to be corrected by the elongation of the rest of the sample holder;
- **The pellet-cladding contact**: indicator of the origin of the weak PCI, the contact is the initiator of the strong PCI. According to the axial profile of the linear power in the reactor, the contact is expected to start at the mid rod plane and propagate along the extremities. We assume in this frame that vibrations have proved to allow the identification of the first pellet-cladding contact;
- **The temperature of cladding surface**: the cladding thermal profile is the boundary condition for the whole thermal-mechanical calculation that allows to model the origin and evolution of PCI;
- **The fuel centerline temperature**: calculations show that it allows to detect the local complete closure along the pellet length and it is thus a direct indicator of the strong PCI. As the cladding surface temperature, it is of great interest also for code validation;
- **The evolution of the internal pressure**: it is not directly impacted by the origin and evolution of the PCI: the local gap closures does not affect the global variation of the internal rod pressure. Nevertheless, the reopening of the gap can result into the sudden release of fission gasses and induce the increase of the internal pressure. The parameter is important for code validation.

We have identified in part III and in the previous chapters of this part IV the measurement principles and the instrumentation sensors better adapted to fit the measurement criteria imposed by modeling and by the geometrical and irradiation constraints of the ADELINE device. We have selected the following ones:

- **The LVDT** to measure the axial elongation, that is a robust and reliable technological solution, meeting the measurement criteria and fitting the geometrical and environmental constraints of the ADELINE system;
- **A modified version of the LVDT** to measure the transverse vibrations of the sample rod along different angles. We assume that the same device periodically actively excites the system, which ensures the capability to manage its vibrations and optimizes the possibility to detect the first pellet-cladding contact ;
- **The optical fiber based confocal microscope sensor** to perform a remote investigation of the cladding diameter evolution. It is mounted on a specifically developed displacement system to perform a profilometry. The application of optical fiber ensures the minimization of the sensor dimensions;
- **The counter pressure sensor**: based on the same measurement principle than LVDT, it is a reliable technological solution to measure the evolution of the internal rod pressure during irradiation and its design fits the geometrical constraints of ADELINE. Nevertheless, the acoustic sensor is an alternative to be taken into account depending on its development to improve its capability to follow the pressure evolution and the capability to discriminate different types of releases fission gasses;
- **The optical pyrometer sensor** to perform the remote monitoring of the local thermal evolution of the cladding surface. As the confocal microscopy, it requires the development of moving support and makes use of optical fibers to minimize sensor encumbrance;
- **The ultrasonic thermometer**, introduced in the fuel by drilling its center along a limited axial length, allows to measure the centerline fuel temperature. The ultrasonic thermometer is preferred to the type-C thermocouples to benefit from the possibility of a distributed measurement.
  The aim of the measurement is not to detect PCI but to obtain on-line data for code validation. For this, it is necessary to establish the transfer function between the measured temperature and the one of the unperturbed system, which is used for code validation.

12.2 The sample rod

We consider a sample rod made of UO_2 fuel pellets, having standard length 13.5 mm, surrounded by a zircaloy based cladding that has external diameter of 9.5 mm and internal diameter 8.36 mm. The total length of the sample rod is about 50 cm, compatible with the geometrical constraints of ADELINE.
In order to reduce the phenomena activated during the test that contribute to the formation of PCI mechanism, we propose to use a fresh sample rod, that has not been previously irradiated in a power reactor. According to a separate effect approach, this ensures no uncertainties in the behavior laws of the material constituting the rod and limited effects due to irradiation and solid or gaseous swelling to be considered. Also, the melting onset of a quasi stoichiometric fuel rod is far better characterized than the one of an irradiated

fuel.
In our case, we consider that the PCI mechanism purely results from the thermal dilatation and creep mechanisms of the two components.

12.3 The irradiation scenario

To study the PCI mechanism and approach the fuel melting using a fresh fuel rod and minimizing the risk of loss of integrity of the cladding, a stair-case power ramp sequence appears to be the most suitable irradiation scenario. Indeed, the solid and gaseous swelling are negligible in the fuel and the time for the cladding to undergo inward creep under differential pressure is limited by the maximum duration of the irradiation sequence, 25 days based on the constraints of the JHR environment. Under these hypothesis, the PCI is driven by the stronger thermal dilatation of the pellets with respect to the cladding. It results that the PCI origins during the transient phase of the power ramp while relaxation through creep takes place during the holding period. A staircase ramp allows to control the origin and evolution of PCI in the sample limiting the stresses induced on the cladding, ensured during the holding periods.
The target linear power is the power to melt of the fresh sample rod. Figure 12.1 shows a schematic view of the irradiation scenario proposed. Before to undergo the stair-case phase of the ramp, a "densification" phase is recommended, at a normal linear power, to induce the occurrence of the thermal-elastic phenomena taking place during the first couple of days of irradiation: the differential thermal expansion and cracking of the fuel pellet, with the consequent hourglass shape and the fuel densification phenomenon.
In the proposed scenario, the linear power is initially increased by steps of 50 W/cm and a power rate of 100 W/cm/min which involves a duration of the transient of approximately 30 s. The duration of the holding period at constant linear power has to allow the system to relax internal stresses: the duration can vary between 12 and 24 h depending on the level of linear power.
A fundamental advantage that comes from the availability of on-line measurements is that the scenario can be updated and optimized during the irradiation. Specifically, the power ramp can be stopped and the linear power kept constant when the first pellet-cladding contact is detected and when the power to melt is reached and melting onset detected, the irradiation sequence can be rapidly concluded by moving the ADELINE device far from the reactor core.

We have pointed on the graph the indicative instants at which occur relevant phenomena for the definition of the measurement method: the first pellet-cladding contact, the discontinuity in the axial elongation kinetics of the cladding and the onset of fuel melting.

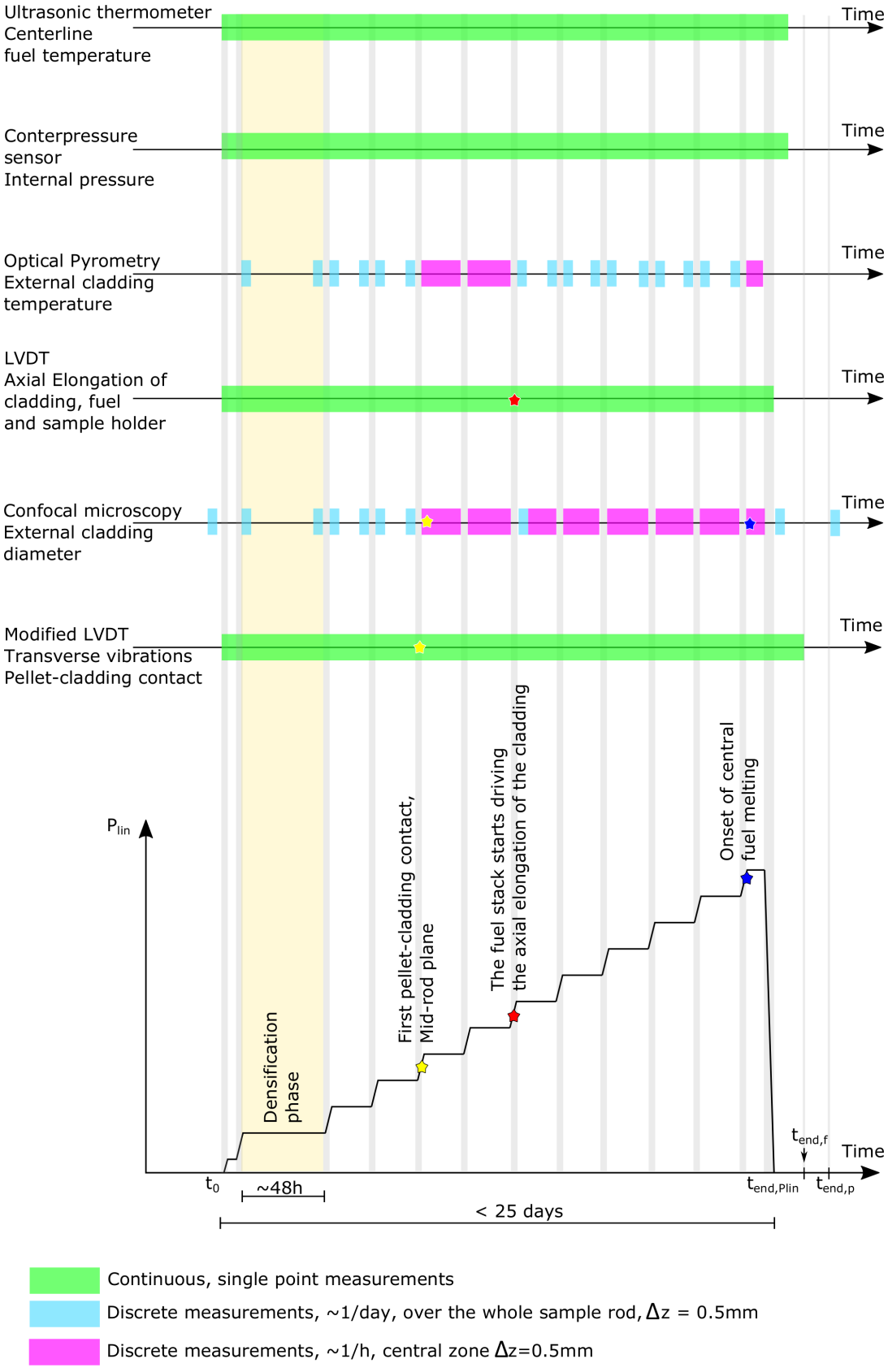

Figure 12.1 – Proposed scheme of irradiation scenario and associated measurement method to detect and characterize PCI and detect the melting onset on the cladding deformation

12.4 The measurement method

12.4.1 Before the beginning of the ramp

It is convenient to perform a profilometry of the whole sample rod by means of the confocal microscopy sensor. This allows to verify the measurement system with respect to the manufacturing characteristics, as we consider the use of a fresh fuel, or with respect to the optical profilometry performed in hot cell on a pre-irradiated sample rod, in the general case, and to have a reference diameter before and during the irradiation sequence.

12.4.2 During the power ramp test

Measurements that are locally performed along the sample rod axis, have to be focused on the hot side of the sample rod, the one facing the JHR reactor as the main studied mechanisms are temperature dependent. In the ideal case, the monitoring of the diameter evolution along several generatrices allows to get rid of the local effects on the measurement induced by the flow induced vibrations of the sensor and lack of alignment of the sample rod in the test section.

Continuous measurements They are performed to follow the evolution of the internal rod pressure, the cladding kinetics, the fuel centerline temperature, the fuel, the cladding and the sample holder axial elongation and the transverse vibrations. The periodic excitation of the sample rod allows the investigate the internal modification of the energy dissipated due to the pellet-cladding weak interaction and permits to detect the first contact. The discontinuity in the axial elongation of the sample rod components is detected by the LVDT and further characterization should be available by the analysis of the transverse vibrations, to define the number of pellets in contact with the cladding related to this discontinuity. Fuel centerline measurement allows to validate code calculations.

Discrete measurements During the transient phase, the local linear power rapidly varies and it is extremely difficult to relate a performed measurement to the exact local power at a precise instant, which makes it comparable with the corresponding calculated value. Also, the time required to investigate a portion of the cladding, which is required for the discrete measures, is too long with respect to the rate of power increase. This implies that each point is collected at a different local power, making the axial investigation ineffective. For these reasons, all the discrete measurements are performed at constant linear power.
The discrete measurements evolve in terms of sampling frequency and spatial discretization depending on the phase of the irradiation. Up to the detection of the first pellet-cladding contact, the evolution of the cladding external diameter is measured before and after each variation in the linear power, with a sampling frequency in the order of 1/day, as the expected kinetics is slow in this range of linear power, as discussed in the first part of this manuscript. Measurements are performed along the entire fuel rod, with a spatial discretization of at least 0.5 mm. This allows to have a sufficiently high number of points along a single pellet. The investigation has to be performed sufficiently fast with respect to the time constant of creep mechanisms at P_{lin} during the holding period, as to consider the measurements at different axial locations as synchronized.
In the same phase, the monitoring of the external cladding temperature is performed to validate code simulation. Measurements should be synchronized with the monitoring of

the cladding diameter.

Once the first pellet cladding contact is detected through vibrations, the monitoring of the cladding diameter has to be focused on the mid-rod plane, with a higher sampling frequency in the range of 1/h, to follow the deformation of the cladding as it accommodates the pellet shape and characterize the formation of ridges.
Cladding temperature is, as before, synchronized with the cladding diameter.

When the discontinuity in the axial elongation is detected, an examination of the whole fuel rod is recommended, to relate it with the state of cladding deformation. Then, the monitoring has to be focused back to the central region, to characterize the deformation kinetics during the holding time at higher linear power productions.
In this phase, the monitoring of the cladding temperature is used to validate the code, so it is performed only before and after the power transient and on the whole fuel rod.

The consequences of the accelerated kinetics of fuel deformation after the onset of melting process should be detected during the holding period by confocal microscopy measuring the modified relaxation kinetics of cladding diameter.
In this phase, the synchronized measurements with the cladding temperatures allow to detect the possible thermal effects induced by the central melting.

12.4.3 After the end of the ramp

The monitoring of the internal rod pressure is performed up to equilibrium, reached after the t_{end} of the irradiation sequence, to characterize the consequences of the reopening of the pellet cladding gap, the diffusion of the locally released gases from the reopening of the pellet-cladding gap and the pellet cracking, to the upper plenum, where the sensor is placed, which could be not instantaneous. The measured quantities are then compared to the one resulting from puncturing test performed after the power ramp test in the hot cell laboratory.
The transverse vibrations are induced and monitored up to the stop of the circulation pump ($t_{end,p}$) to measure the effects of the reopening of the gap.
Confocal microscopy is used to perform a profilometry of the whole sample rod after the end of the irradiation $t_{end,Plin}$, under flow induced vibrations and a second one after the stop of the circulation pump and the depressurization of the loop, in order to compare them with the optical microscopy profile obtained after the ramp in the hot cell laboratory.
After the power ramp tests, during post irradiation examinations, the optical microscopy performed on the cross section of the central pellets shall allow to measure the percentage of melted volume by analyzing the consequences on the microstructure of the fuel.

12.5 Concluding remarks

We have presented in this chapter a principle of irradiation scenario and the related measurement method to detect and measure on-line the evolution of the PCI mechanism and detect the onset of fuel central melting through its effects on the cladding deformation kinetic. We stress the fact that this is a simplified study, which configuration and details have to be defined by dedicated studies about the expected behavior of the sample rod.
In this scenario, a fresh sample rod is used, according to a separated effects approach, to avoid the uncertainties due to the effects of irradiation and the solid and gaseous swelling.

We have defined a stair-case power ramp test, where confocal microscopy and optical pyrometry are used to perform discrete measurements along the sample rod axis. Meanwhile, continuum measurements are performed by the counter pressure sensor, of the internal rod pressure, by the LVDTs, of the cladding, fuel and sample rod elongation, and by a modified LVDT to measure the transverse vibrations of the sample rod and detect the pellet cladding contact.
All these collected data, measured during the irradiation sequence and describing the evolution of relevant observable parameters, constitute a huge source of information that can be compared to the simulation outputs to validate the code.

Outcomes of Part IV

In this fourth and final part of the thesis, we have focused on the proposal on an on-line measurement method to detect and characterize the PCI mechanisms and to identify the onset of the melting process in the fuel pellet by its effects on the deformations of the cladding.
In the previous part we have reviewed the existing and currently under development technological solutions that allow to detect the identified relevant parameters to be measured. Here, we take into account the specific application frame that is the ADELINE irradiation device of the Jules Horowitz material testing reactor: pressurized single rod test section, approximately 3 m in length and the hydraulic diameter at the sample rod is 1.15 cm where the turbulent coolant (water) passes at 155 bar and 280°C, submitted to quick, up to 660 W/cm/min, and large, up to power to melt, power transient.
The environment and the specific geometrical configuration of the device impose specific constraints in the definition and design of the instrumentation set-up. These constraints are related to the strong ionizing radiation and high neutron flux, variable in the space surrounding the reactor core, which causes radiation induced damages and transmutations of structural components, to the axial and the radial thermal gradients, to the thermal shocks imposed by the irradiation scenarios realized in the device. All the structures are submitted to the interactions with the surrounding pressurized coolant, with consequent flow induced vibrations and corrosion. Concerning the design, a tiny space is available in the radial for the instrumentation and the sample rod is difficult to access due to the axial extension of the sample holder.
Considering these conditions, we have selected the most adapted technological solutions:

- **The confocal microscopy** for the measure of the cladding external diameter, which further development for use in the nuclear environment is highly recommended;
- **The LVDT** for the axial elongation of the fuel and the cladding, operational and reliable;
- **The optical pyrometry** is a good solution to measure the the cladding external temperature, which performance at about 300°C has to be characterized.
- **The type-C thermocouple or the Ultrasonic thermometer**: the integration of thermal sensors to detect PCI through its local effects on the fuel centerline and surface temperature is not recommended because we consider the induced thermal-mechanical perturbation related to the introduction of the sensor not compatible with PCI measurement criteria. The use of these sensors is instead proposed in the frame of code validation, under the hypothesis that a transfer function is established to obtain the temperature of interest from the measured one.

We have introduced in the previous part the interest of to investigate dynamic response of the sample rod submitted to flow induced vibrations to detect the pellet-cladding contact origin and evolution, from the mid-rod plane toward its extremities. For this we

have designed on the basis of the ADELINE environmental and geometrical conditions, the IMPIGRITIA test bench. Here, we have recreated at low pressure, low temperature and out of neutron flux the local mechanical interaction. This is realized by means of a local dilatation system: several sample rods are manufactured, in each a different number n of centrally located pellets are replaced by two half-pellets. The dilatation system is introduced in the sample rod through the driller upper pellets and remotely inflated to move the half-pellets in contact with the cladding.
We have realized the experimental campaign in two phases, the first one in air, with the aim to investigate the general possibility to measure an effect of the local contact on the frequency and damping characteristics of the sample rod; the second one under representative flow rate excitation, to state on the feasibility of the passive measurement.

During the experiment, we showed that it is possible to detect the local weak PCI by means of its impact on the energy dissipated in the system, that modifies the viscous damping ratio and the amplitude of oscillations.
We conclude that the measurement principle has a concrete interest for the PCI detection in ADELINE, but further investigations are required. First of all, the test has to be performed with UO_2 pellets. For IMPIGRITIA we used mock-up pellets in Molybdenum, which have a different friction coefficient that UO_2 ones. The active excitation of the system is recommended, to manage the lack of repetability of the measurement with respect to different rods and to force the system to vibrate in the range where the probability of the detection is the highest.
A complete model of the system is required. This shall support the understanding of the mechanisms activated and the interaction of the sample rod with the surrounding medium. It shall also allow to optimize the boundary conditions as to give elements for the improvement of the ADELINE design.

The Laser Doppler Vibrometry used in IMPIGRITIA to measure transverse vibrations is not adapted for use in ADELINE. Here, we have proposed the development of a modified sensor based on the LVDT measurement principle, placed at the bottom of the sample rod, that performs a continuum monitoring of the rod displacement along different angles and actively excites the system.

The selected technologies are applied in the final chapter 12 to propose the principles of a simplified stair-case power ramp test and the related measurement methods to investigate the PCI and identify the onset of central fuel melting. Here, we have assumed that the technological developments required for each of the identified technology and the related moving support has been achieved, that the performances of the sensors are qualified and that they meet the required measurement accuracy.
In the proposed irradiation scenario, we take advantage of the on-line measurements of the relevant parameters, to update and to manage it depending on the observed phenomena. The huge amount of measured data can be then compared to calculated outputs to validate and improve present modeling.

Conclusions and Perspectives

This thesis aims at stating the feasibility and giving the elements for the development of a measurement method dedicated to the on-line characterization of the PCI kinetics as well as the detection of the onset of central fuel melting.
Dedicated power ramp tests could be performed in the ADELINE irradiation device (Jules Horowitz Reactor, Cadarache, France) to improve the present knowledge of the phenomena related to PCI under transient conditions and to the onset of central fuel melting. On-line measurements about the evolution kinetics of these mechanisms will allow to extract fundamental information that are not available at the moment, as the majority of measurements has been performed before and after the irradiation, giving only the initial and final state of the system.

Conclusions

Observable parameters for the detection and the measurement of PCI and fuel melting onset

The first part of this thesis has focused on the identification and characterization of the relevant set of parameters to measure the PCI evolution and to detect the onset of central fuel melting in the PWR fuel rod. The analysis of the thermal mechanical behavior of the solid fuel element has been performed by simulating several normal operation conditions and power ramp tests. For this, we relied on the fuel performance code ALCYONE, co-developed by CEA, EDF and FRAMATOME. Calculations have shown that the weak PCI can be directly detected by:

- The local pellet-cladding contact;
- The local fuel surface temperature;

From the weak PCI, the strong PCI origins and evolves. In the latter, the mutual influence between the fuel pellets and the cladding modify the thermal-mechanical behavior of the rod. This induces observable direct consequences on:

- The external cladding diameter, that evolves to accommodate the pellet shape with the consequent formation and evolution of the primary ridges during normal operations and of secondary ridges during power ramp;
- The axial elongation of the cladding. Its kinetics presents a discontinuity when the mechanical interaction with the fuel stack is so strong that its axial deformation results to be accelerated and driven by the fuel;
- The fuel centerline temperature, that increases under the effect of the thermal degradation of the fuel material under irradiation.

The internal pressure and the fuel elongation have been identified as indirect indicators of the effects of the weak PCI, integrated along the rod axis.
The temperature of the cladding surface is a fundamental input parameter to model the

origin and evolution of PCI.

The lack of a model to account for the onset of fuel melting in the ALCYONE code required its development prior to the evaluation of the effects on the cladding deformation kinetics of the characteristic fuel expansion that appears at the solid-liquid transition of the uranium dioxide. We thus proposed a thermal-mechanical model to describe the behavior of the fuel at the melting onset, under the hypothesis of ensured cooling of the external surface of the cladding. To enhance its integration in ALCYONE, the model has been developed to be driven by the local temperature and we have applied the homogenization approaches already used to model the behavior of the solid fuel. Before its integration in the multi-physics ALCYONE code, the modeling principle had to be validated. This has been done through the analysis of a simple case, coded in MFRONT and solved by means of the finite element code Cast3m. From the analysis on the simple case, we concluded that we expect a discontinuity and an acceleration in the macroscopic deformation kinetics of the uranium dioxide, which is directly related to the portion of melted material.

Vibrations for the detection of the weak PCI in ADELINE

Part of this thesis has concerned an experimental research performed to state on the feasibility to detect the weak PCI by analyzing the flow induced vibrations of the sample rod, under passive excitation representative of the ADELINE system. For this, we have designed and realized the IMPIGRITIA experiment. Here, the weak PCI is remotely induced in the manufactured sample rods by a local dilatation system that makes the relative motion between pellets and cladding disappear. Mock-up pellets are manufactured in Molybdenum, representative of uranium dioxide in terms of mass density.

We have been able to prove the feasibility to detect the local weak PCI through the analysis of the energy dissipated in the system and the study of the viscous damping ratio of the structure.

Controlled tests in air under imposed initial displacement have shown positive results on the capability to detect the local pellet-cladding contact on approximately the 10% of the fuel stack length (45 mm out of the 495 mm). The contact reduced the dissipated energy and the viscous damping ratio of the structure is modified and can be detected.
Investigations have been performed under the flow rate excitation representative of the one imposed to the sample rod in the ADELINE device. Results are positive but affected by larger uncertainties.
All the tests showed that the local contact cannot be detected by analyzing the characteristic frequencies of the structure.

On-line measurement method for PCI and melting onset detection and characterization

We have reviewed the technological solutions already used in the nuclear field and those under-development to measure the set of relevant identified parameters. Then, we have taken into account the characteristics constraints of the JHR environment and the ADELINE configuration and we have selected the technologies that seem to be better adapted to detect and characterize the PCI and the melting onset during a power ramp test.
We foreseen the use of three LVDTs, one to measure the integral elongation of the fuel, one to measure the cladding one and one to remove the contribution of the other components of the sample holder. To measure the internal rod pressure, we recommend the use of a

counter pressure sensor.
The use of sensors based on the confocal microscopy and the optical pyrometry to measure on-line the deformation kinetics of the external cladding and the cladding external temperature, respectively, require further technical developments in both fields. They also require the design of a dedicated displacement device to allow the investigation of a portion or of the whole sample rod.
The use of thermal sensors in the fuel to detect the local effects of PCI is not recommended because of the strong impact of the sensor on the local thermal-mechanical behavior of the fuel. But, thermal measurements are extremely important to validate the code simulation and can be performed for this purpose sufficiently far from the region where PCI is investigated. In this frame, we need to establish the transfer function between the measured temperature and the one of the unperturbed system and we need to obtain by modeling the temperatures at different axial positions in the fuel stack.
The selected technological solutions are the type-C thermocouples and the ultrasonic thermometers, the first because of its robust application in previous experiments, the second because of its capability to reach high temperatures and the possibility of distributed measures.

At the end of this thesis, we have proposed an irradiation scenario to detect and characterize PCI and eventually detect fuel melting through the fuel rod deformations. The application of a dedicated on-line measurement method allows to rearrange and optimize the irradiation scenario depending on the observed phenomena. It also provides experimental results that can be compared with calculated outputs to validate and improve modeling capability.

Perspectives

We structure the perspectives of this thesis along three research axis: modeling, instrumentation and irradiation device.

Modeling

Further work is required for the integration of the melting model in ALCYONE and to couple it with the phenomena in the fuel. This step is necessary to evaluate the effects on the cladding due to the expansion taking place in the fuel and thus state on the theoretical feasibility to detect melting onset by the deformations induced to the cladding.
An important topic to be investigated is the role of gaseous fission products present in the fuel at melting onset, especially how the melting onset impacts their release kinetics and their consequent contribution to the macroscopic deformation of the system. For this, we could foreseen a dedicated test, performed in the VERDON facility [Pon17]. A test performed in VERDON would allow to investigate the behavior of fission gasses in a sample rod with an integer cladding and validate the modeled evolution of the geometrical deformation of the system.

From a general point of view, in order to quantitatively compare the simulation results with experimental ones, it is important to improve the degree of confidence of the fuel performance code by quantifying the uncertainties of calculated quantities. Calculated parameters are affected by several sources of uncertainty: material properties, model parameters, experimental conditions (especially the ones related to the linear power at which the rod is irradiated and the thermal measurements), uncertainties of the experimental results that are used to validate the code (like fission gas release measurement) and mod-

eling uncertainties. The propagation of this uncertainties can be performed by means of the URANIE framework and a Monte-Carlo technique, as detailed in [Bou12] and [Bou19].

In the frame of using vibrations to detect PCI, further researches are foreseen, on the basis of the work done in this thesis on the IMPIGRITIA feasibility test.
It is recommended to develop a model of the dynamic behavior of the rod that accounts for the internal dissipation mechanisms in the sample rod and its interaction with the surrounding fluid. The model can be validated by means of the measured evolutions and shall allow to improve the understanding of the phenomena observed during IMPIGRITIA and provide elements for the optimization of the ADELINE design to enhance the detection of PCI.

Instrumentation

All the selected technological solutions require developments and/or adaptations for their application in ADELINE. They also require the evaluation of the measurement uncertainties and the definition of the specific calibration procedure.

The design of the LVDT and the counterpressure sensor could require some adaptation to meet the geometrical configuration of ADELINE, but they are almost operational for application in the JHR.
Before to apply the ultrasonic thermometer in the system, further investigations are needed, to characterize its performance in terms of spatial discretization of the measurements. Type-C thermocouples are reliable for use in the research reactor.
The sensor based on confocal microscopy has to undergo extended technical developments. It has to be tested in a highly radiative environment, at high temperature and pressure and its performance through a layer of turbulent flow rate has to be characterized. Its capability to measure the cladding surface with a relative accuracy of 1 µm has to be verified. The sensor itself has to be designed to fit the geometrical configuration of the ADELINE test section and to resist to its environment.
The sensor based on optical pyrometry to measure the cladding temperature has to be developed too and its performance has to be verified in the range of the cladding operating temperature (300°C).
The confocal microscopy and the optical pyrometry both require the development of a dedicated displacement device, remotely controlled during the irradiation sequence to perform the discrete investigations along the sample rod axis.
Technical developments are required to design and develop a modified version of LVDT, capable to measure the rod transverse vibrations along multiples angles and to provide an active and controlled excitation of the sample rod.

ADELINE irradiation device

The development of the model on the basis of the experimental results collected during IMPIGRITIA can provide elements for the optimization of the ADELINE device to detect PCI: the design and location of centering elements and the application of an active excitation to control rod vibrations and enhance the possibility to detect PCI.
Further experiments seem to be required, to validate the feasibility of the detection with real fuel pellets and to characterize the proposed improvements before their implementation in ADELINE. Part of these tests can be carried out on the IMPIGRITIA test bench but their validation on a full-scale prototype shall be performed. The TOTEM platform (CEA Cadarache) can be used for this purpose. The prototype can be also used to check the design of the instrumentation set-up and to test its out-of-pile performance.

Bibliography

[Ada85] M. Adamson, E. Aitken, and R. Caputi. Experimental and thermodynamic evaluation of the melting behavior of irradiated oxide fuels. *Journal of Nuclear Materials*, 130:349–365, 02 1985.

[Ait68] E. Aitken and S. Evans. A thermodynamic data program involvig plutonia and urania at high temperatures. *General Electric, U.S. Atomic Energy Commission, Contract AT(04-3)-189 Project agreement 53*, 1968.

[All85] C. Allison, G. Berna, and L. Siefken. Draft preliminary report for comment: Scdap/mod1 theory and models. *Idaho National Engineering Laboratory informal report*, 1985.

[ASN] `https://www.asn.fr/Professionnels/Installations-nucleaires/Guides-de-l-ASN/Guides-de-l-ASN-n-22-Conception-des-reacteurs-a-eau-sous-pression`. [Online; version of 18/07/2017].

[Axi01] F. Axisa. *Modélisation des systèmes mécaniques : Vibrations sous écoulements*, volume 4. Hermes, 2001.

[Bai06] M. Baichi, C. Chatillon, G. Ducros, and K. Froment. Thermodynamics of the O−U system: III − Critical assessment of phase diagram data in the U−UO2+x composition range. *Journal of Nuclear Materials*, 349:57–82, 2006.

[Bai96] C. P. H. Bailly, D. Ménessier. *Le combustible nucléaire des réacteurs à eau sous pression et des réacteurs à neutrons rapides, Conception et comportement*. EYROLLES, 1996.

[Ben04] F. Bentjac and N. Hourdequin. Toutatis, an application of the cast3m finit element code for pci three dimensional modelling. *Proceedings of Pellet-clad Interaction in Water Reactor Fuels, Aix-En-Provence*, pages 496–506, 2004.

[bilan16] `https://rte-france.com/fr/article/bilans-electriques-nationaux`.

[Bor01] M. Bornert, T. Bretheau, and P. Gilormini. *Homogénéisation en mécanique des matériaux 2 : Comportements non linéaires et problèmes ouverts*, volume 1. HERMES Science Europe Ltd, 2001.

[Bou12] A. Bouloré, C. Struzik, and F. Gaudier. Uncertainty and sensitivity analysis of the nuclear fuel thermal behavior. *Nuclear Engineering and Design*, 253:200–2010, 2012.

[Bou17] B. Bouvry, G. Cheymol, R. Ramiandrisoa, B. Javaudin, C. Gallou, H. Maskrot, N. Horny, T. Duvaut, C. Destouches, L. Ferry, and C. Gonnier. Multispectral pyrometry for surface temperature measurement of oxidized zircaloy claddings. *Infrared Physcs and Technology*, 83:78–87, 2017.

[Bou18] B. Bouvry, G. Cheymol, C. Gallou, H. Maskrot, C. Destouches, L. Ferry, and C. Gonnier. Theoretical and experimental analyses of the impact of high temperature surroundings on the temperature estimated by an optical pyrometry technique. *TNS Transactions on Nuclear Science*, 65, 2018.

[Bou19] A. Bouloré, C. Struzik, and F. Gaudier. Importance of uncertainty quantification in nuclear fuel behaviour modelling and simulation. *Nuclear Engineering and Design*, 253:200–2010, 2019.

[BP10] J. Bendal and A. Piersol. *Random Data, Analysis and Measurement Procedures*. John Wiley & Sons, Inc., Hoboken, New Jersey, 2010.

[Bre90] W. Breitung and K. O. Reil. The Density and Compressibility of Liquid (U,Pu)-Mixed Oxide. *Nuclear Science and Engineering*, 105(3):205–217, 1990.

[Cam87] W. Camp, M. Young, J. Tomkins, J. Kelly, P. Maudlin, and R. Henninger. Melprog-pwr/mod0: A mechanistic code for analysis of reactor core melt progression and vessel attack under severe accident conditions. Technical report, Sandia National Labs., Albuquerque, NM (USA); Nuclear Regulatory Commission, 1987.

[Can09] J. Canning, D. Bandyopadhyay, S. M., P. Biswas, J. Fenton, and M. Aslund. Regenerated gratings. *J. Eur. Opt. Soc. Rapid Publ.*, 4, 2009.

[Car01] J. J. Carbajo, G. L. Yoder, S. G. Popov, and V. K. Ivanov. A review of the thermophysical properties of MOX and UO2 fuels. 299(3):181–198, 2001.

[Cau12] C. Caucheter. Introduction aux capteurs á fibre optique. *Techniques de l'ingenieur*, page 14, 2012.

[CEA, 2016a] C. W. CEA, 2016a. URL `http://www-cast3m.cea.fr/`.

[CEA, 2016b] M. W. CEA, 2016b. URL `http://www.tfel.sourceforge.net/`.

[CEA09] CEA. *Nuclear Fuels*. Editions le Moniteur, 2009.

[CEA18] CEA. *L'instrumentation et la mesure en milieu nucl''eaire*. Editions le Moniteur, 2018.

[Che08] G. Cheymol, H. Long, J. Villard, and B. Brichard. High level gamma and neutron irradiation of silica optical fibers in cea osiris nuclear reactor. *IEEE Transactions on Nuclear Science*, 55:2252–2258, Aug.2008.

[Che11] G. Cheymol, B. Brichard, and J. Villard. Fiber optics for metrology in nuclear research reactors - applications to dimensional measurements. *IEEE Transactions on Nuclear Science*, 58:1895–1902, 2011.

[Che13] G. Cheymol, A. Gusarov, S. Gaillot, C. Destouches, and N. Caron. Dimensional Measurements under High Radiation with Optical Fiber Sensors based on White Light Interferometry - Report on Irradiation Tests. *IEEE Transactions on Nuclear Science*, 2013.

[Che14] G. Cheymol, A. Gusarov, S. Gaillot, C. Destouches, and N. Caron. Dimensional measurements under high radiation with optical fiber sensors based on white light interferometry - report on irradiation tests. *IEEE Transactions on Nuclear Science*, 61:2075–2081, 2014.

[Che19] G. Cheymol, A. Verneuil, P. Grange, H. Maskrot, and C. Destouches. Report of high temperature measurements with a fabry-perot extensometer. In *Proceedings of ANIMMA 2019*, 2019.

[Che70] Y. Chen. Turbulence-induced vibration of tube bundle heat exchangers with cross and parallel flow. part 1: Parallel flox. *Flow Induced Vibration in Heat Exchangers*, pages 57–66.

[Cli69] J. M. Clinch. Measurements of the wall pressure field at the surface of a smooth-walled pipe containing turbolent water flow. *Journal of Sound and Vibration*, 9:398–419, 1969.

[Daw10] J. Daw, J. Rempe, and J. Crepeau. Ultrasonic thermometry for in-pile temperature detection. In *Seventh American Nuclear Society International Meeting on Nculear Plant Instrumentaiton, Control and Human Machine Interface Technologies NPIC & HMIT*. American Nuclear Society, 2010.

[DeB10] F. De Bruycker, K. Boboridis, D. Manara, and P. Poml. Reassessing the melting temperature of puo2. *Materials Today*, 13(11):52 – 55, 2010.

[Del16] C. Delafoy and I. Arimescu. Developments in fuel design and manufacturing in order to enhance the PCI performance of AREVA NP's fuel. In *Proceesings of the NEA Workshop on PCI in Water-Cooled Reactors. Lucca (Italy)*, 22-24 June 2016.

[DeP15] B. De Pauw, W. Weijtjens, S. Vanlanduit, K. Van Tichelen, and F. Berghmans. Operational modal analysis of flow-induced vibration of nuclear fuel rods in a turbulent axial flow. *Nuclear Engineering and Design*, 284:19–26, 2015. doi:10.1016/j.nucengdes.2014.11.040.

[DeS17] D. De Santis and A. Shams. Numerical modeling of flow induced vibration of nuclear fuel rods. *Nuclear Engineering and Design*, 320:44–56, 2017. doi:10.1016/j.nucengdes.2017.05.013.

[Dro81] W. Drotning. In *Proc. of the Eighth Symposium of Thermophysical Properties, Gaithersburg, MD, National Bureau of Standards 1981*, 16-18 June 1981 1981.

[Esh57] J. Eshelby. The determination of the elastic field of an ellipsoidal inclusion, and related problems. *Proceedings of the Royal Society A.*, 241:376–396, 1957.

[Fer14] L. Ferry, D. Parrat, C. Gonnier, C. Blandin, Y. Weiss, A. Sasson, , and al. The LORELEI Test Device for LOCA Experiments in the Jules Horowitz Reactor. In *Proceedings of the WRFPM 2014, Sendai, Japan*, number 100094, Sept. 14-17 2014.

[Fer18] G. Ferrari and P. Balasubramanian. Non-linear vibrations of nuclear fuel rods. *Nuclear Engineering and Design*.

[Fern05] E. Fernandez, P. Rodeghiero, B. Brichard, B. F., A. Hartog, P. Hughes, K. Williams, and A. Leach. Radiation-tolerant raman distributed temperature monitoring system for large nuclear infrastructure. *IEEE Transactions on Nuclear Science*, 52:2680–2694, 2005.

[Fin00] J. Fink. Thermophysical properties of uranium dioxide. *Journal of Nuclear Materials*, 279(1):1 – 18, 2000.

[Fin81] J. Fink, C. Chasanov, and L. Leibowitz. *Journal of Nuclear Materials*, 102:17, 1981.

[Fok02] M. Fokine. Formation of thermally stable chemical composition gratings optical fibers. *J. Opt. Soc. Am. B 19*, pages 1759–1765, 2002.

[Fou11] D. Fourmentel, J. Villard, J. Ferrandis, F. Augereau, E. Rosenkrantz, and M. Dierckx. Acoustic sensor for in-pile fuel rod fission gas release measurement. *IEEE Transactions on Nuclear Science*, 58:151, 2011.

[Fro82] H. Frost and M. Ashby. *Deformation-Mechanism Maps, The Plasticity and Creep of Metals and Ceramics*. Pergamon Press, 1982.

[Gai09] S. Gaillot, D. Parrat, G. Laffont, C. Garnier, and C. Gonnier. The ADELINE irradiation loop in the Jules Horowitz MTR: Testing a LWR fuel rod up to the limits with a high quality level experimental process. In *Proceedings of the 12th International Group on Research Reactor (12th IGORR), CIAE-Beijing, P.R. China*, October 28-30 2009.

[Gat05] J.-M. Gatt, Y. Monerie, D. Laux, and D. Baron. Elastic behavior of porous ceramics: application to nuclear fuel materials. *Journal of Nuclear Materials*, 336(2-3):145–155, 2005.

[Gau13] E. Gauthier, C. Brosset, H. Roche, E. Tsitrone, B. Pégourié, A. Martinez, P. Languille, X. Courtois, Y. Lallier, and M. Salami. Confocal microscopy: A new tool for erosion measuremnts on large scale plasma facing components in tokamaks. *Journal of Nuclear Materials*, 438:S1216–S1220, 2013.

[Ger15] M. Géradin and D. J. Rixen. *Mechanical Vibrations, Theory and Application to Structural Dynamics.* Wiley, third edition edition, 2015.

[Gio17] M. Giot, L. Vermeeren, A. Lyoussi, C. Reynard-Carette, C. Lhuillier, and et al. Nuclear instrumentaion and measurement: a review based on the animma conferences. *EPJ N - Nuclear Sciences Technologies, EDP Sciences*, 3:33, 2017.

[Gir18] S. Girard and *al.* Recent advantages in radiation-hardenerd fiber based technologies for space applications. *Journal of Optics*, 20:Art. no. 093001, Aug.2018.

[Gon17] C. Gonnier, J. Estrade, G. Bignan, and B. Maugard. Experimental devices in jules horowitz reactor and first orientation for the experimental programs. In *IGORR*, 2017.

[Gue08] C. Guéneau, C. Chatillon, and B. Sundman. Thermodynamic modelling of the plutonium−oxygen system. *Journal of Nuclear Materials*, 378(3):257–272, 2008.

[Gue11] C. Guéneau, N. Dupin, B. Sundman, C. Martial, J.-C. Dumas, S. Gossé, S. Chatain, F. D. Bruycker, D. Manara, and R. J. Konings. Thermodynamic modelling of advanced oxide and carbide nuclear fuels: Description of the U−Pu−O−C systems. *Journal of Nuclear Materials*, 419(1):145–167, 2011.

[Gue85] Y. Guérin. Le comportement mécanique du combustible nucléaire sous irradiation. *Ann. Chim. Fr.*, 10:405–414, 1985.

[Gui15] P. Guimbal, S. Huotilainen, S. Taehtinen, G. Thellier, and J. Villard. Status of the MeLoDIE experiment, an advanced device for the study of the irradiation creep of LWR cladding with full online capabilities. In *Conference: ANIMMA 2015: 4. International Conference on Advancements in Nuclear Instrumentation Measurement Methods and their Applications, Lisboa (Portugal), 20-24 Apr 2015; Other Information: Country of input: France.*

[Har89] J. Harding, D. Martin, and P. Potter. Thermophysical and thermochemical properties of fast reactor materials. *Harwell Laboratory UKAEA Report EUR 12402*, 1, 1989.

[Has63] Z. Hashin and S. Shtrikman. A variational approach to the theory of the elastic behavior of multiphase materials. *Journal of the Mechanics and Physics of Solids*, 11:127–140, 1963.

[Hel04] T. Helfer, P. Garcia, J.-M. Ricaud, D. Plancq, C. Struzik, F. Sidoroff, and L. Bernard. Modelling the effect of oxide fuel fracturing on the mechanical behaviour of fuel rods. In *NEA international Seminar on Pellet-Clad Interaction in Water Reactor Fuels, Aix en Provence*, 9-11 March 2004.

[Hel15] T. Helfer, B. Michel, J.-M. Proix, M. Salvo, J. Sercombe, and M. Casella. Introducing the open-source mfront code generator: Application to mechanical behaviours and material knowledge management within the PLEIADES fuel element modelling platform. *Computers & Mathematics with Applications*, 70:994–1023, 2015.

[IAEA05] IAEA International Atomic Energy Agency. Thermophysical properties database of materials for light water reactors and heavy water reactors. Report IAEA-TECDOC-1496, IAEA, 2005.

[IRS17] IRSN. Avis irsn/2017-00168. `https://irsn.fr/FR/expertise/avis/2017/Documents/mai/Avis-IRSN-2017-00168.pdf`, 22 mai 2017.

[Jen98] F. Jensesn, E. Takada, M. Nakazawa, T. Kakuta, and S. Yamamoto. Consequences of radiation effects on pure-silica-core optical fibers used for raman -scattering-based temperature measurements. *IEEE Transactions on Nuclear Science*, 45:50–58, 1998.

[Jom14] G. Jomard and *al.* CARACAS: an industrial model for the description of fission gas behavior il LWR-UO_2 fuel. In *Proc. WRFPM, 2014, Sendai, Japan*, number 100154, September, 14-17 2014.

[Jon28] J. Johnson. *Phys. Rev*, 32:97, 1928.

[Jos88] J. Joseph, J. Royer, and M. Grosgeorge. Transient behaviour of fregema fuel rods previously irradiated under commercial conditions. *ANS-Williamsburg*, 1988.

[Jul08] J. Julien. *Modélisation multi-échelles du couplage physico-chimie-mécanique du comportement du combustible à haute tempÃ©rature des réacteurs ´a eau sous pression.* PhD thesis, Université de Provence - Aix-Marseille, 2008.

[Kim11] B. Kim and J. Rempe. Reveiw of instrumentation for irradiation testing of nuclear materials. *Nuclear Technology*, 2011.

[Kom88] J. Komatsu. The melting temperature of irradiated oxide fuel. *Journal of Nuclear Materials*, 154(1):38 – 44, 1988.

[Kon19] P. Konarski, J. Sercombe, C. Riglet-Martial, L. Noirot, I. Zacharie-Aubrun, K. Hanifi, M. Frégonèse, and P. Chantrenne. 3d simulation of a power ramp including fuel thermochemistry and oxygen thermodiffusion. *Journal of Nuclear Materials*, 519:104–120, 2019.

[Kon99] K. Konno and T. Hirosawa. Melting temperature of simulated high-burnup mixed oxide fuels for fast reactors. *Journal of Nuclear Science and Technology*, 36:596–604, 1999.

[Laf13] G. Laffont, R. Cotillard, and P. Ferdinand. Multiplexed regenerated fiber bragg gratings for hight temperature measurement. *Meas. Sci. Technol.*, 24, 2013.

[Laf18] G. Laffont, R. Cotillard, N. Roussel, R. Desmarchelier, and S. Rougeault. Temperature resistant fiber bragg gratings dor on-line and structural health monitoring of the next-generation of nuclear reactors. *Sensors*, 18:1791, 2018.

[Lai18] M. Lainet, B. Michel, J. Dumas, M. Pelletier, and I. Ramiére. GERMINAL, a fuel performance code of the PLEIADES platform to simulate the in-pile behaviour of miwed oxide fuel pins for sodium-cooled fast reactors. *Journal of Nuclear Materials*, 516:30–53, 2018.

[Lam11] T. Lambert, E. Muller, E. Federici, E. Rosenkratz, J. Ferrandis, X. Tiratay, V. Silva, D. Machard, and G. Trillon. REMORA 3: the First Instrumented Fuel Experiment with On-Line Gas Composition Measurement by Acoustic Sensor. In *2011 2nd International Conference on Advancements in Nuclear Instrumentation, Measurement Methods and their Applications*, pages 1–6, June 2011.

[Lau10] M. Laurie, D. Magallon, J. Rempe, C. Wilkins, J. Pierre, C. Marquié, S. Eymery, and R. Morice. Ultrasonic high-temperature sensors: Past experiments and prospects for future use. *International Journal of Thermophysics*, 31:1417–1427, 2010.

[Lec17] P. Lecompte. *Mesure haute temperature en environnement irradié par fibre optique utilisant l'effet Raman*. PhD thesis, Université de Perpignan, 2017.

[Lec98] S. Leclercq. Modelling of the fuel mechanical behavior: from creep laws to internal variable models. *Nuclear Engineering and Design*, 185:221–228, 1998.

[Lem01] J. Lemaitre and J. Chaboche. *Mécanique des matériaux solides*. Dunod, Paris, 2001.

[Lyo67] W. Lyon and W. Baily. The solid-liquid phase diagram for the uo2-puo2 system. *Journal of Nuclear Materials*, Volume 22, Issue 3:332–339, 1967.

[Man05] D. Manara, C. Ronchi, M. Sheindlin, M. Lewis, and M. Brykin. Melting of stoichiometric and hyperstoichiometric uranium dioxide. *Journal of Nuclear Materials*, 342(1):148 – 163, 2005.

[Man07] D. Manara, C. Ronchi, M. Sheindlin, and R. Konings. On the present sate of investigation of thermodynamic properties of solid and liquid uo_{2+x}. *Journal of Nuclear Materials*, 362:14–18, 2007.

[Mar17] V. Marelle, P. Goldbronn, C. Introini, S. Bernaud, A. Bouloré, M. Casella, C. Fillaux, J. Julien, K. Mer-Nkonga, and L. Noirot. Validation of pleiades/alcyone 2.0 fuel performance code. *Water Reactor Fuel Performance Meeting*, 2017.

[Mar88] D. Martin. Thermal expansion of UO_2 and $(U,Pu)O_2$ mixed oxides - a review and recommendations. *Journal of Nuclear Materials*, 152:94–101, 1988.

[Mar89] D. G. Martin. Elastic constants of polycrystalline uo2 and (u, pu) mixed oxides: a review and recommendations. *High Temperatures - High Pressures*, 21(1):13–24, 1989.

[MicB13] B. Michel, J. Sercombe, C. Nonon, F. Michel, and V. Marelle. Simulation of Pellet-Cladding Interaction with the PLEIADES Fuel Performance Software Environment. *Journal of Nuclear Technology*, 182:124–137, 2013.

[MicJC92] J.-C. Michel and P. Suquet. The constitutive law of nonlinear viscous and porous materials. *Journal of the Mechanics and Physics of Solids*, 40(4):783–812, 1992.

[Mon06] Y. Monerie and J.-M. Gatt. Overall viscoplastic behavior of non-irradiated porous nuclear ceramics. *Mechanics of Materials*, 38(7):608 – 619, 2006.

[Mor73] T. Mori and K. Tanaka. Average stress in matrix and average elastic energy of materials with misfitting inclusions. *Acta Metall. Mater.*, 21:597–629, 1973.

[Nak81] M. Nakatuska. *Journal of Nuclear Materials*, 96:205–207, 1981.

[Nie09] R. Van Nieuwenhove and S. Solstad. In-core fuel performance and material characterization in the halden reactor. *Transactions on Nuclear Science*, 57:2683–2688, 2010.

[Noi11] L. Noirot. Margaret: A comprehensive code for the description of fission gas behavior. *Nuclear Engineering and Design*, 241:2099–2118, 2011.

[Non03] C. e. Nonon. Impact of fuel microstructure on pci behavior. In *IAEA Technical Committee Meeting on Advanced Fuel Pellet Materials and Deisgns for Mater Cooled Reactors, Brussels*, 20-24 October 2003.

[Non04] C. e. Nonon. Pci behaviour of the chromium oxide doped fuel. In *NEA international Seminar on Pellet-Clad Interaction in Water Reactor Fuels, Aix en Provence*, 9-11 March 2004.

[Nop93] N. Noppe and Decréton. Strain gauges in nuclear environment. *Materials & Design*, 14(6), 1993.

[Nuc15] Nuclear Science Committee. State-of-the-art report multi-scale modelling of nuclear fuels. Report, OECD Nuclear Energy Agency, 2015.

[OECD18] OECD/NEA. State-of-the-art report on light water reactor accident-tolerant fuels. Technical report, Nuclear science, 2018.

[Pai04] M. Paidoussis. *Fluid-Structure Interactions, Slender Structures and Axial Flow*, volume 2. ELSEVIER, 2004.

[Pai81] M. Paidoussis. Fluidelastic vibration of cylinder arrays in axial and cross flow: State of the art. *Journal of Sound and Vibration*, 76(3):329–360, 1981.

[Pea19] J. Pearce, P. Bramley, and D. Cruickshank. Development of a driftles johnson noise thermometer for nuclear applications. In *Proceedings of ANIMMA 2019*, 2019.

[Pet13] M. Pettigrew. The beahaviour of weldable strain gauge under nuclear reactor core conditions. *Nuclear Engineering and design*, (263):350–361, 2013.

[Phe07] Preliminary report FPT3. Doc. Phébus IP/06/569, March 2007.

[Pir17] M. Piro, S. Sunderland, J. Sercombe, W. Revie, A. Quastel, K. Terrani, and C. Judge. A review of pellet-clad interaction behavior in zirconium alloy fuel cladding. *Reference Module in Materials Science And Materials Engineering, Elsevier*, 2017.

[Pon17] Y. Pontillon, E. Geiger, C. Le Gall, S. Bernard, A. Gallais-During, P. Malgouyres, E. Hanus, and G. Ducros. Fission products and nuclear fuel behaviour under severe accident conditions part 1: Main lessons learnt from the first VERDON test. *Journal of Nuclear Materials*, 495:363–384, 2017.

[Pop00] S. Popov, J. Carbajo, V. Ivanov, and G. Yoder. Thermophysical properties of mox and uo2 fuels including the effects of irradiation. Report ORNL/TM-2000/351, Oak Ridge National Laboratory, 2000.

[Pra11] V. Prakash, M. Thirumalai, M. Anandaraj, P. A. Kumar, D. Ramdasu, G. Pandey, G. Padmakumar, C. Anandbabu, and P. Kalyanasundaram. Experimental qualification of subassembly design for prototype fast breeder reactor. *Nuclear Engineering and Design*, 241(8):3325–3332, 2011.

[Ram14] L. Ramiandrisoa. *Etude et développement d'une mesure pyométrique en coeur de réacteur pour le suivi de la température d'une gaine de combustible : Application à l'étude des accidents de perte de réfrigérant (APRP) au cours d'essais de simulation dans le réacteur expérimental Jules Horowitz (RJH).* PhD thesis, Université de Reims Champagne−Ardenne, 2014.

[Ran78] M. Rand, R. Ackermann, F. Gronwold, F. Oetting, and A. Pattoret. *Rev. Int. Des Hautes Temperatures et des Refractories*, 355:15, 1978.

[Rem11] J. Rempe, M. Meyer, D. Knudson, K. Condie, J. Daw, and S. Wilkins. ATR NSUF instrumentation ehancement efforts. *Nuclear Technology*, 173:66, 2011.

[Rig16] C. Riglet-Martial, J. Sercombe, J. Lamontagne, J. Noirot, I. Roure, T. Blay, and L. Desgranges. Experimental evidence of oxygen thermo-migration in pwr uo2 fuels during power ramps using in-situ oxido-reduction indicators. *Journal of Nuclear Materials*, 480, 2016.

[Riz17] S. Rizzolo, A. Boukenter, T. Marin, E. andRobin, M. Cannas, A. Morana, J. Périsse, and al. Evaluation of distributed ofdr-based sensing performance in mixed neutron/gamma radiation environments. ***IEEE transactions on nuclear science*** , 64:61–67, 2017.

[rjh-cea] `https://www-rjh.cea.fr`.

[Sai18] H. Saikouk. *Imagerie par microscopie acoustique haute résolution en profondeur de la surface interne d'une gaine de crayon combustible de type REP.* PhD thesis, Université de Montpellier, 2018.

[Ser07] J. Sercombe. Introduction dans ALCYONE du modèle couplé fissuration-fluage "Gatt-Monerie". Note Technique SESC/LSC 06-052 - PLE 06-025 - Indice 0- Février 2007.

[Ser13] J. Sercombe, J. J., F. Michel, B. Michel, and E. Fédérici. *TopFuel 2013*, 2013.

[Shc84] V. Shchavelin, A. Kostochka, A. Bolobolichev, A. Kuznetsov, I. Golovnin, and Y. Bibilashvili. [translated]. *Atomnaya Eneriya*, 56(3):134–136, 1984.

[Shc86] V. Shchavelin, A. Kostochka, A. Bolobolichev, A. Kuznetsov, I. Golovnin, and Y. Bibilashvili. [translated]. *Atomnaya Eneriya*, 61(3):175–178, 1986.

[Sil79] H. Sills. Eloca: fuel element behaviour during high temperature transients. Technical report, Atomic Energy of Canada Ltd., 1979.

[Ski19] R. Skifton, J. Palmer, K. Davis, P. Calderoni, D. Corbett, and E. Sikorski. Summary of high temperature irradiation resistant thermocouple standarization tests. *INL/CON-18-51789-Revision-0*, 2019.

[Stil] `http://stilsas.stil-sensors.com`.

[Stil95] J. C. Sabban. Dispositif de microstatigraphie optique. Brevet 95 10401, 30th August 1995.

[Suq95] P. Suquet. Overall properties of nonlinear composites: a modified secant method theory and its link with Ponte Castañeda's non linear variational procedure. *Compte Rendu de l'Académie des Sciences Paris II*, (317):1512–1522, 1995.

[Tor02] S. Torquato. *Random Heterogeneous Materials, Microstructure and Macroscopic Properties*. Springer, New York, 2002.

[Ver15] F. Very, E. Rosenktratz, D. Fourmentel, C. Destouches, J. Villard, P. Combette, and J. Ferrandis. Acoustic sensors for fission gas characterization in mtr harsh environment. *Physics Procedia*, 70:292–295, 2015.

[Vil03] J. Villard, G. Lemaitre, J. Chaussy, and F. Lefevre. High accuracy sensor for online measurement of the fuel rod internal pressure during irradiation experiments. In *7th Int. Topl. Mtg. Research Reactor Fuel Management (RRFM 2003), Aix en Provence, France*, March 9-12, 2003.

[Vil08] J. Villard, S. Fourrez, D. Fourmentel, and A. Legrand. Improving high-temperature measurements in nuclear reactors with mo/nb thermocouples. *International Journal of Thermophysics*, 29:1848–1857, 2008.

[Vil09] J. Villard. State-of-the-art and improvement of online measruements in present and future research reactors. presented at INL, Idaho Falls, Idaho, September 15,2009.

[Web99] J. Webster. *The measurement instrumentation and sensors handbook*. CRC press LLC, 2000 Corporate Blvd., N.W., Boca Raton, FL 33431, 1999.

[Wel09] M. Welland, W. Thompson, B. Lewis, and D. Manara. Computer simulations of non-congruent melting of hypertoichiometric uranium dioxide. *Journal of Nuclear Materials*, 385:358–363, 2009.

[Wij08] T. Wijnands, L. De Jonge, J. Kuhnhenn, S. Hoeffgen, and U. Weinard. Optical absorption in commercial single mode optical fibers in a high energy pjysics radiation field. *IEEE Transactions on Nuclear Science*, 55:2216–2222, Aug.2008.

[Wri06] P. Wriggers. *Computational Contact Mechanics*. Springer Berlin Heidelberg New York, second edition edition, 2006.

[Yam88] S. Yamanouchi, T. Tachibana, K. Tsukui, and M. Oguma. Melting Temperature of Irradiated UO2 and UO2-2wt%Gd2O3 Fuel Pellets up to Burnup of about 30 GWd/tU. *Journal of Nuclear Science and Technology*, 25(6):528–533, 1988.

Appendices

Appendix A

Investigation of the radial deformation mechanisms

The evolution of the radial deformation during base irradiation and power ramp test is extracted from the 3D simulation of the modeled sample rod. The radial dimensions which are used in this section are schematized in figure A.1: the External Diameter of the Fuel, at the Inter-Pellet plane ($D^{e}_{f,IP}$) and at the Mid-Pellet plane ($D^{e}_{f,MP}$), the Internal Cladding Diameter, at the IP plane ($D^{i}_{c,IP}$) and at the MP plane ($D^{i}_{c,MP}$) and the External Cladding Diameter, at the IP plane ($D^{e}_{c,IP}$) and at the MP plane ($D^{e}_{c,MP}$).

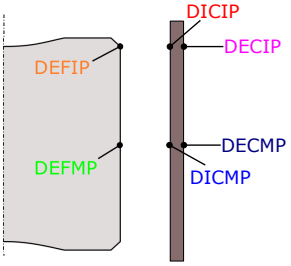

Figure A.1 – Schematic view of considered radial dimension

Base irradiation

For each of the three base irradiation profiles, we present on the left of figure A.2 the evolution of the Internal Cladding Diameter at the Inter-Pellet plane ($D^{i}_{c,IP}$) and at the Mid-Pellet plane ($D^{i}_{c,MP}$), the evolution of the External Fuel pellet Diameter at the Inter-Pellet plane ($D^{e}_{f,IP}$) and at the Mid-Pellet Plane ($D^{e}_{f,MP}$). On the right of the figure, are presented the gap thicknesses at the Inter-Pellet Plane (gap_{IP}) and at the Mid-Pellet plane (gap_{MP}), for the three studied cases.

We first focus on the pellet deformation kinetics: at the beginning of the irradiation the pellet undergoes instantaneous thermal dilatation and as a consequence of the strong thermal gradient and the fragile nature of the material, the hourglass shape origins in the system: the $D^{e}_{f,IP}$ (orange) is higher than the $D^{e}_{f,MP}$ (green). The hourglass shape is enhanced by the increase of the linear power produced in the system.
After the initial dilatation, pellet diameter decreases as a consequence of the densification process occurring in the component.
Once densification ends, the pellet undergoes solid and gaseous swelling, which progressively increases the radial dimension of the pellet.

Meanwhile, the cladding undergoes an instantaneous thermal dilatation, largely smaller than the one in the pellet. This is due to the lower temperatures established in this component. Initially, the inward creep is not linear as the differential pressure is not constant due to gap thickness increases as a consequence of the pellet densification, This is showed

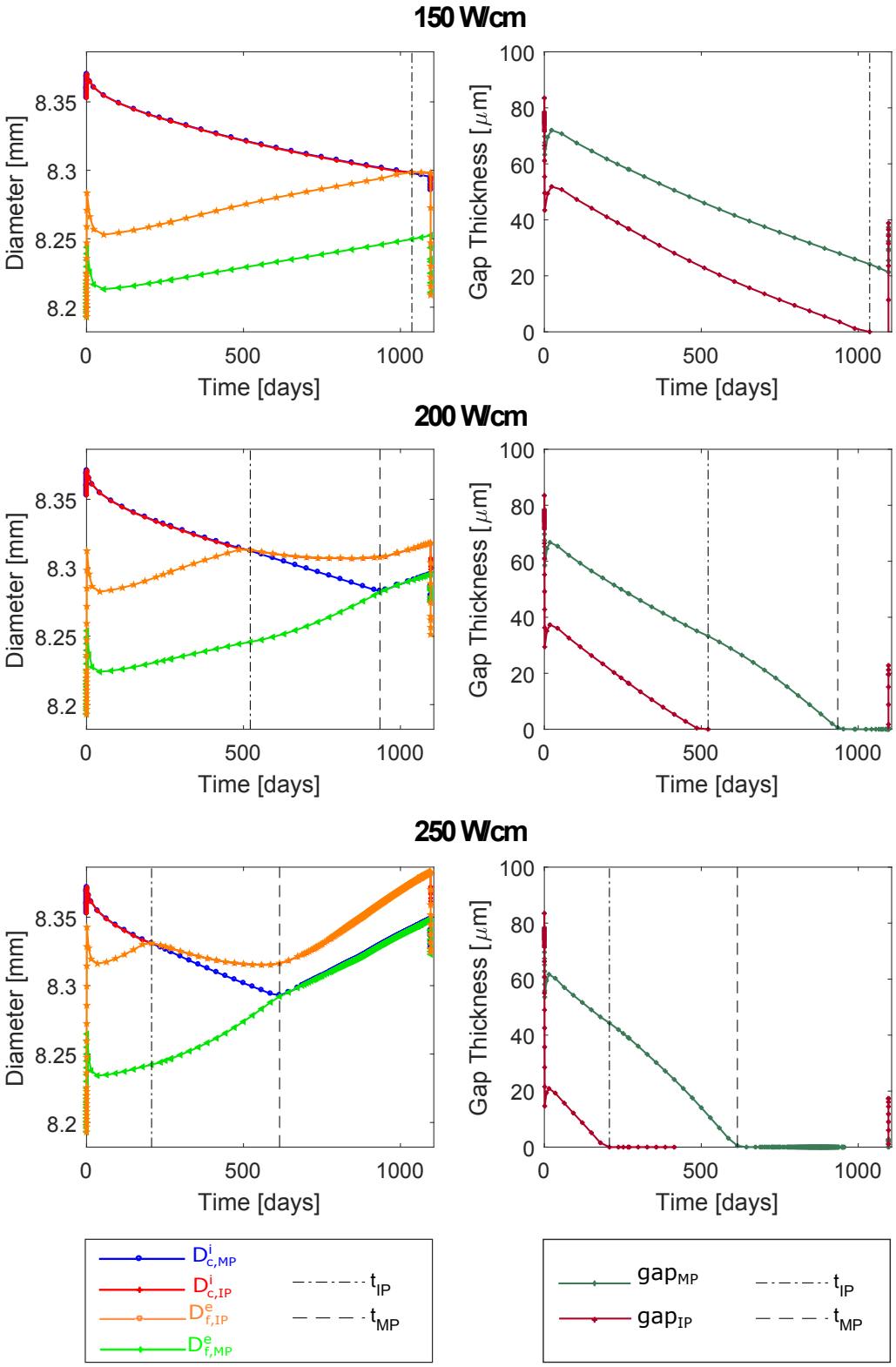

Figure A.2 – (left) Time evolution of the internal surface of the cladding and of the external one of the pellet, at the Inter-Pellet plane and at the Mid-Pellet plane. (right) Time evolution of gap thickness, at the Inter-Pellet plane and at the Mid-Pellet plane

in the graphs on the right side of figure A.2. When the densification process ends, the inward creep proceeds at an approximately constant rate and the gap thickness linearly decreases.
As a consequence of the hourglass shape, the gap thickness goes to zero first at the IP, where the weak PCI first establishes. In the interaction, the deformation kinetics of both the $D^{e}_{c,IP}$ and the $D^{e}_{f,IP}$ are modified: as we can see in the irradiation cases at 200 W/cm and 250 W/cm, the two components deform in the same way: the inward creep prevails in this phase on pellet swelling and the radial dimension decreases at the IP but the creep rate is decreased in the interaction.
At the Mid-Pellet plane, the calculated $D^{i}_{c,MP}$ and the $D^{e}_{f,MP}$ are not influenced by the contact established at the IP plane and they maintain their deformation kinetics up to the moment when the opposite deformation mechanisms lead to the closure of the gap at the MP plane. For symmetry reasons, this corresponds to the complete gap closure along all the pellet surface.
Since the instant of the complete closure (t_{MP}), the deformation of the cladding is driven by the dilatation of the pellet, and the radial dimension increases. We talk about strong PCI.
From the comparison of the three plots we observe that the linear power produced in the system has a strong influence on the deformation kinetics of the pellet: first a stronger thermal dilatation takes place at the real beginning of the irradiation, leading to a partial closure of the gap. Second, the enhanced hourglass shape contributes to locally reduce the gap_{IP} since the beginning of the irradiation. Third, solid and gaseous swelling, which directly result from the fission events, is enhanced by the increase of the linear power.
The superposition of these three effects leads to the fact the increase of the linear power produced in the rod moves up the gap closure.
The cladding deformation is much less impacted by the increase of the power produced. A slightly higher temperature on the internal surface leads to a stronger thermal dilatation, but this event has a negligible effect on the gap closure kinetics with respect to the thermal dilation of the pellet.
The deformation mechanism of the cladding is driven by the inward-creep under differential pressure. It has to be said that this deformation mechanism is enhanced under irradiation. This means that inward creep is accelerated by a stronger linear power, which also contributes to an earlier closure of the gap.

These phenomena, that occur inside the sample rod, modify the deformation kinetics of the external surface of the cladding. In the following, we focus only on the base irradiations at 200 W/cm and 250 W/cm, where the complete gap closure is achieved.
Figure A.3 shows the time evolution of the External Cladding Diameter at the Inter-Pellet ($D^{e}_{c,IP}$) and the Mid-Pellet plane ($D^{e}_{c,MP}$).
Consistently with the internal mechanisms, the cladding creeps inward, under the effect of the differential pressure. This is not linear at the beginning due to the increase of pellet-cladding gap as a consequence of pellet densification. When the gap locally closes at the IP plane, the creep rate locally reduces as a consequence of the pellet-cladding interaction. Meanwhile, at the MP plane, the cladding keeps on contracting. When the gap closes at the MP plane and thus along the entire length of the pellet, pellet deformation drives cladding behavior and the rod diameter starts to increase.

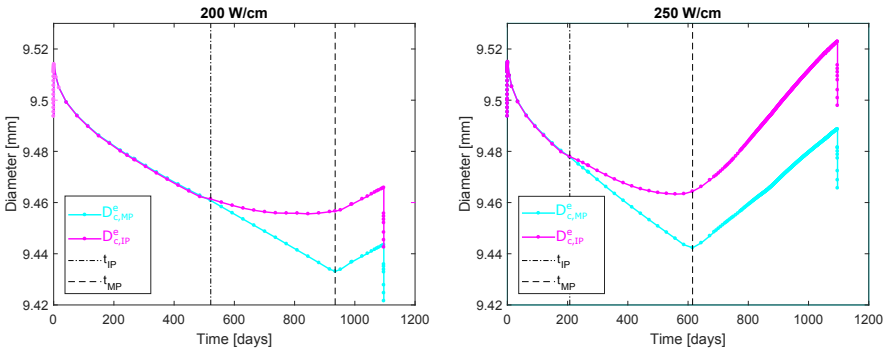

(a) (b)

Figure A.3 – Time evolution of the external diameter of the cladding at the Inter-Pellet and at the Mid-Pellet plane, for the case at 200 W/cm (a) and at 250 W/cm (b)

We focus on the time of local closure. Figure A.4 shows a comparative view of the time of gap closure at the IP and MP plane for the two studied case. To compare them, we shift the x-axis of the time of each gap closure (t_{IP} and t_{MP}) and the y-axis of the value of the external cladding diameter evaluated at the time of gap closure ($D^e_{c,IP}(t_{IP})$ and $D^e_{c,MP}(t_{MP})$).
First, we focus on the contact at the IP plane, figure A.4(a). Calculations show that before the gap closure, inward creep has a constant velocity of contraction. Since the gap closes, the velocity decreases. In the studied cases, the local interaction with the pellet leads to a a decrease of a factor 2 in the cladding creep rate. Figure A.4(b) shows the local deformation kinetics of the cladding at the MP plane: the calculated cladding behavior switches at t_{MP}. Since the complete closure, the expanding pellet imposes an expansion to the contracting cladding.

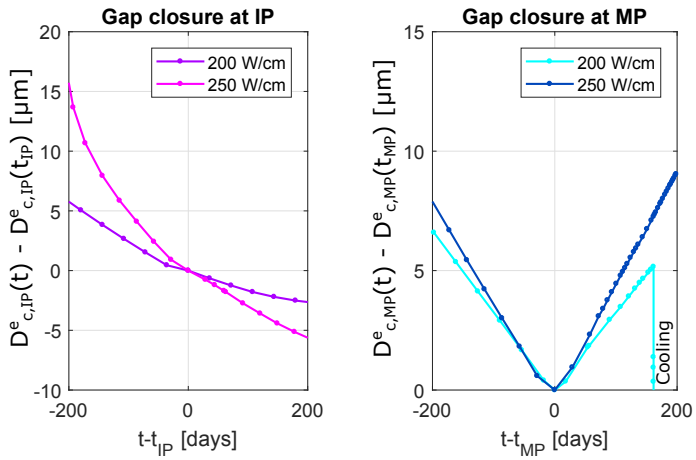

(a) (b)

Figure A.4 – Evolution of the external cladding diameter at the IP plane (a) and the MP plane (b), for the studied case at 200 W/cm and 250 W/cm. X-axis and Y-axis origin have been translated for (a) with respect to $(t_{IP}, D^e_{c,IP}(t_{IP}))$, for (b) with respect to $(t_{MP}, D^e_{c,MP}(t_{MP}))$.

One of the main consequences of the PCI phenomenon during base irradiation is the formation of primary ridges on the cladding surface. Figure A.5 shows the calculated formation kinetics of the $H_{r,IP}$ during base irradiation for the three study cases. The irradiation at 150 W/cm is reported even though it gives really few information.
Calculations show that for the cases at 200 W/cm and 250 W/cm the $H_{r,IP}$ starts forming since the gap closure at the Inter-Pellet plane. Before the complete gap closure, the deformation kinetics for the two cases is similar. Indeed the kinetics is driven by the inward creep of the cladding. Thus, the hourglass shape of the pellets defines the time at which a first contact is induced but has a negligible impact on the formation kinetics of the HRIP.
The height of the primary ridge during base irradiation has an amplitude in the order of the tens of µm. This imposes a relative accuracy for the measurement in the order of 1 µm.
Calculations show that the $H_{r,IP}$ presents a region where it is approximately constant along time: this coincides with the complete closure of the gap, when cladding has deformed to arrange pellet shape.
Lastly, calculations for the studied case at $P_{lin} = 250$ W/cm show that the $H_{r,IP}$ increases again from about 700 days within the irradiation, which corresponds to a burn-up of about 40GWd/tU. This could be due to a calculated enhancement of the gaseous swelling. Noteworthy is the fact that this approximately coincides with the strong increase of the released fraction of fission gasses, as shown in figure 3.7.

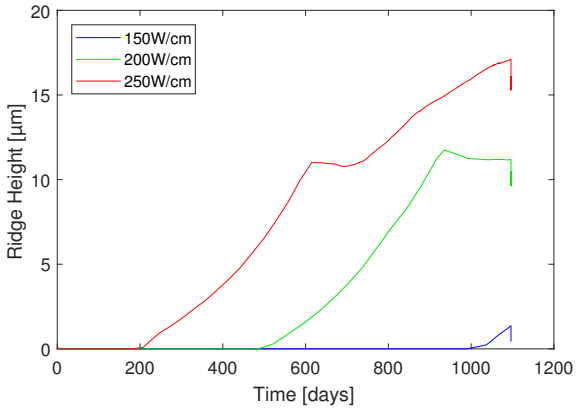

Figure A.5 – Time evolution of the Primary Ridge Height at the IP plane for the three study cases.

Figure A.6 shows the heights of primary ridges for the three studied cases after the end of their base irradiation, at room temperature and pressure. The height of the primary ridge strongly depends on the pellet deformation during irradiation: we observe that the $H_{r,IP}$ in cold conditions is the highest for fuel rod irradiated at the highest linear power. This is mainly due to two mechanisms:

- The fact that pellet hourglassing is exacerbated due to the stronger thermal gradient;
- The increase in fuel swelling under stronger neutron flux.

The plastic deformation of the cladding evolves of several µm/mm along the axial direction. To characterize the height of the primary ridge, it is important to characterize the local cladding deformation at the Inter-Pellet plane and to obtain the minimum cladding radius, on the same generatrix. Figure A.6 shows that the location of the $R^{e}_{c,min}$ varies

depending on deformation at the IP plane.
It results that, to characterize the formation kinetics of the primary ridge, several measurements have to be performed along the pellet length. During the GONCOR experiment, the cladding diameter has been measured each 0.5 mm, sufficient to reconstruct the ridge shape and identify the location of the minimum cladding radius.

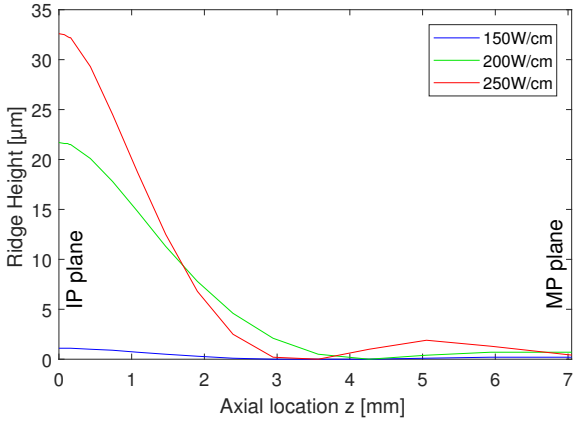

Figure A.6 – Plastic deformation of the cladding in cold condition: ridge height

Ramp Test

We focus on the characteristic radial deformation of the system components during off-normal conditions. In chapter 1 we have introduced that the characteristic phenomenon occurring during power ramp test is the formation of the secondary ridges at the MP plane on the cladding surface. Those are observed during Post Examination Investigations and their formation and evolution kinetics is related to the creep mechanism and to the gaseous swelling the fuel pellet.
Just like the primary ridge, its amplitude and form and its evolution during irradiation depends on the local external cladding diameter at the MP plane $D^{e}_{c,MP}$ and the out-of-ridge radial dimension of the cladding $D^{e}c, min$. From this we can conclude on the basis of the previous discussion that, to characterize the ridge formation and evolution, multiple measurements along the cladding surface are required.

In the following, we first detail the radial cladding deformation during a single power ramp test, for example the one having an Ramp Terminal Level (RTL) at 450 W/cm. We analyze the radial deformation of the system, the formation and evolution of the primary and secondary ridges and discuss the internal mechanisms activated during the transient which influence their behavior.
Then, we discuss how the linear power reached during the RTL impacts the activated internal mechanisms and how this modifies the resulting rod deformation kinetic.

Power ramp with RTL at 450 W/cm

Figure A.7(a) presents the evolution of the cladding external diameter during the power ramp test and the evolution of gap thickness in A.7(b). Time t = 0 is imposed at the beginning of the transient phase. Figure A.7(a) shows that the external diameter of the cladding, which is stable during the conditioning phase, is suddenly increased by the

transient and then decreases during the holding period as a consequence of stress relaxation through creep mechanism. The gap, as presented in figure A.7(b), is locally closed at the IP plane and a residual gap is thus present at the MP plane. The complete closure occurs during the transient phase. It reopens after the end of the power ramp test.
We focus on the holding time at the Ramp Terminal Level: figure A.8 illustrates the time evolution of the external cladding diameter at the IP and MP plane during the holding time at the RTL. In order to enhance the comparison of the deformation kinetics, the evolution of the $D^e_{c,IP}$ and of the $D^e_{c,MP}$ in A.7(a) have been normalized by their value at the end of the condition phase.

The calculated relative deformation reached at the end of the transient phase is the same for the two diameters. This means that no gaseous swelling neither creep mechanism are activated during the transient phase and that the system deforms according to a pure thermal expansion.
During the holding time at the RTL level, the relaxation of stresses through creep occurs with a non uniform cladding deformation along the axial direction: creep is stronger at the Mid-Pellet plane with respect to the Inter-Pellet plane.
This is important because the deformation kinetics of the external cladding defines the formation and coupled evolution of primary and secondary ridges.

In figure A.9 we illustrate the resulting calculated time evolution of the height of primary and secondary ridges during the power ramp test. As expected, during the conditioning phase there is no secondary ridge, coherently with the cladding status at the end of a base irradiation. It is during the transient phase that the secondary ridge forms, while the primary one increases its height. During the holding period at the RTL, each ridge presents its own kinetics because of the non uniform evolution of the cladding external surface.
During the holding time at the RTL level, figure A.8 shows that the relaxation is stronger at the Mid-Pellet plane with respect to the Inter-Pellet plane and the "slower" relaxation of the radial dimension at the IP leads to an increase of the height of the primary ridge

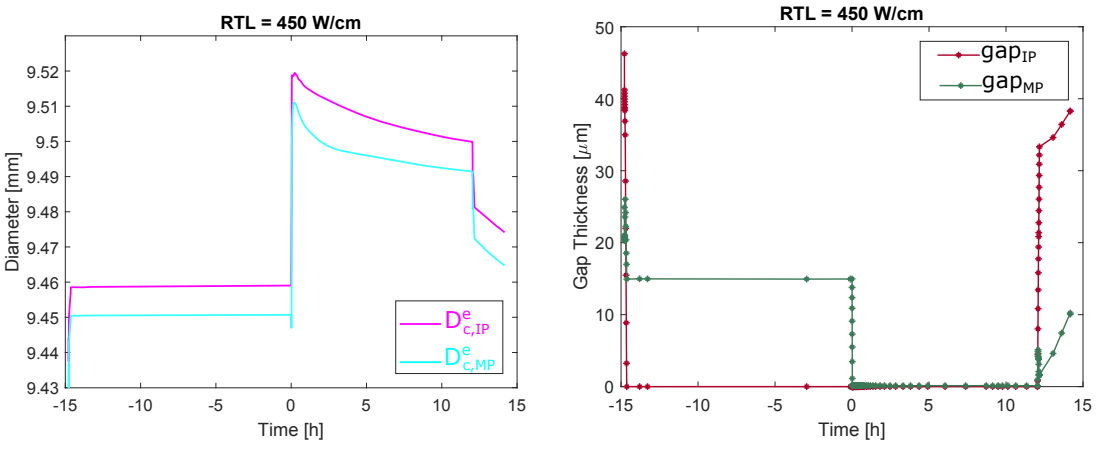

(a) (b)

Figure A.7 – (a) Evolution of the cladding external diameter at the IP (red) and MP(blue) plane during the power ramp test with RTL = 450 W/cm. (b) Evolution of hte gap thickness during the same power ramp test, at the IP plane and at the MP plane.

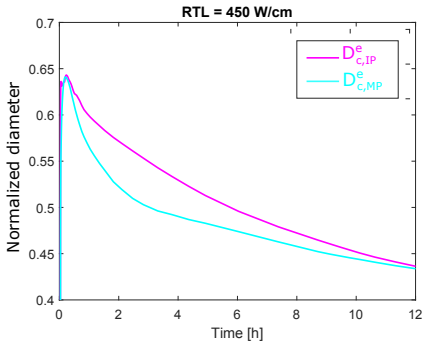

Figure A.8 – Evolution of the normalized deformation kinetics at the IP and MP planes during the power ramp test with RTL = 450 W/cm.

and a decrease of the height of the secondary one.

The calculated different evolution of the primary and secondary ridges during the holding period at the RTL depends on the coupled mechanisms of gaseous swelling and creep mechanisms in the fuel pellet and on how these mechanisms impact the progressive dish fulfillment.

Figure A.10 shows the evolution of the fuel pellet strain that is induced by gaseous swelling. It is illustrated for relevant times extracted during the holding period. We observe that in the first hour within the holding time, the gaseous swelling induces a peak in strain at the Inter-Pellet plane, where the dishing is eased in the pellet. Figure A.11 shows the calculated shape of the dishing and the percentage of fulfillment for the same instants in the holding period.
We observe that the dishing is barely modified during the transient phase: the fulfillment percentage is about 10% at the end of the transient and increases to 26% after 8 min. The dishing constitutes a reservoir for fuel deformation and in the presented case, it accommodates the fuel deformation. Part of this deformation is caused by the gaseous swelling and part is due to the creep mechanism that relaxes internal stresses. These effects result into a non uniform deformation kinetics of the cladding and in this case, into a slowing down of the Inter-pellet kinetics with respect to the Mid-Pellet one.

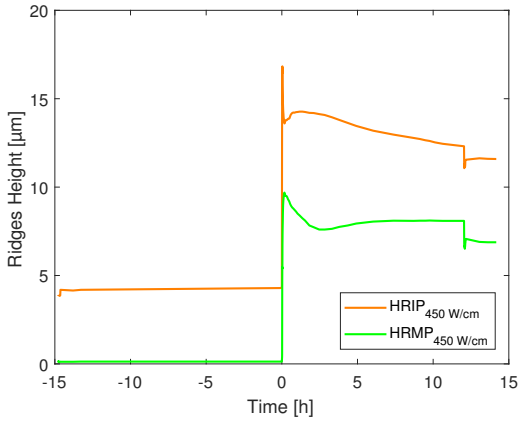

Figure A.9 – Evolution of the height of the primary (orange) and secondary (green) ridges during the power ramp test with RTL = 450 W/cm.

We evaluate now the effect of an increase in the maximal linear power reached during the RTL on the described kinetics. For this, we discuss the two other presented cases, having the RTL respectively at 550 W/cm and at 665 W/cm.

Effect of an increase in the RTL imposed during the ramp

Figure A.12 presents the calculated evolution of the cladding profile during the holding time at the RTL for the previously discussed case at 450 W/cm, at 550 W/cm and for the highest RTL tested: 665 W/cm.
The first observation is that the increase in the linear power reached at RTL leads to a stronger thermal dilatation of the system. Depending on the imposed RTL, the maximal diameter variation between the end of the conditioning plateau and the RTL ranges from 100 µm for the RTL at 450 W/cm and 200 µm at 665 W/cm.
From the comparison of the three cases, we observe that the cladding submitted to 450 W/cm expands during the first minutes in the holding period at the RTL. The blue curve corresponding to the beginning of the holding period, is not the maximum diameter, as it is for the others presented cases. As we previously showed, simulation calculates a peak of gaseous strain during the holding period (figure A.10). This gaseous strain is partially

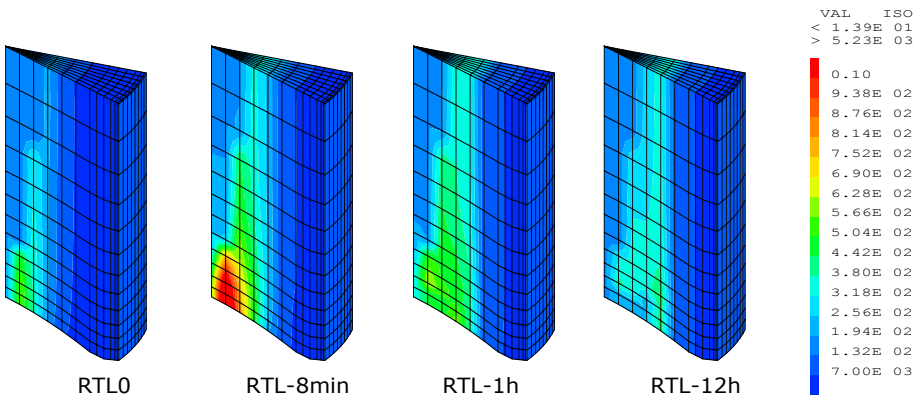

Figure A.10 – Strain due to gaseous swelling for specific times during the 12h holding time at RTL=450 W/cm. Results are extracted from 3D simulation

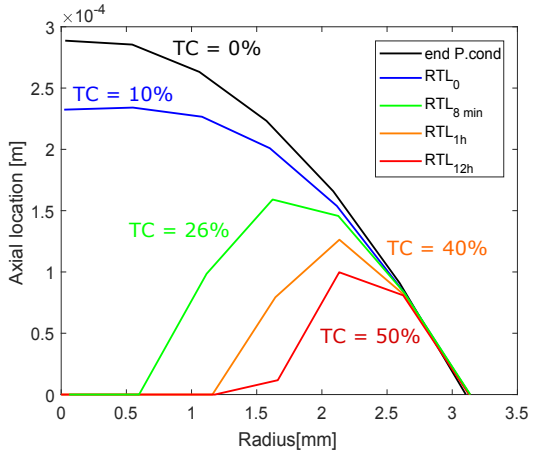

Figure A.11 – Evolution of the dish fulfillment during the 12h holding time at RTL=450 W/cm. Results are obtained by 1D and 3D simulation

accommodated at the IP by the fulfillment of the dishing. It results that the cladding external diameter at MP increases more than at the IP plane.
In the other two presented cases, the figure shows that the cladding diameter decreases during the holding period due to the stresses relaxation. For these ramp tests indeed the transient phase lasts more than the case at 450 W/cm because the RTL is reached with a fixed power rate. The gaseous swelling induces the fulfillment of the dishing during the transient phase and the pellet surface deforms in a rather uniform way.

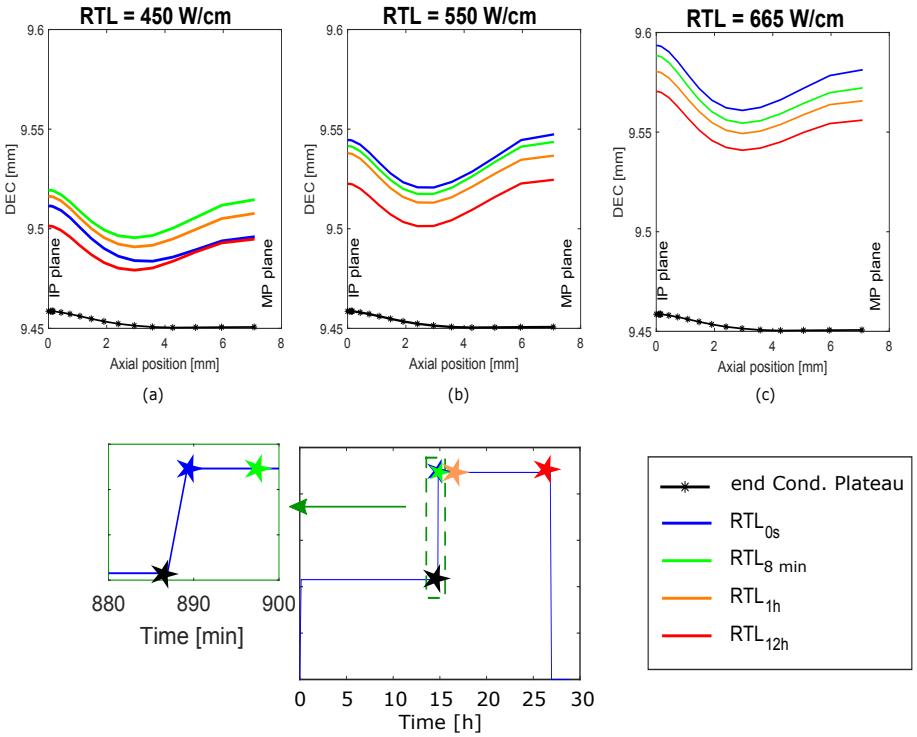

Figure A.12 – Evolution of the cladding external profile during the transient and the holding period at RTL, for three different power ramps: RTL = 450 W/cm (a) and RTL = 665 W/cm (b)

This shows that the deformation kinetics of the cladding during the power ramp tests strongly depends on the activation and the coupling of the thermal activated mechanisms in the fuel pellet. A first importance role is played by the dishing: by accommodating the fuel deformation towards the inside, it modifies the effects of the pellet-cladding interaction on the formation and evolution of ridges. Dish fulfillment decreases the pellet expansion due to gaseous swelling and slows down the relaxation kinetics. As its effect is local, this results into an non uniform deformation of the cladding surface and into a non homogeneous evolution of the primary and secondary ridges. For this, it is important to characterize the evolution of the cladding along a certain axial elongation. Considering the profile of the cladding, a spacing of 0.5 mm or less is sufficient to reconstruct the cladding profile.
The superposition of those phenomena and their coupling during the power transient leads to a non trivial behavior of the system in the first minutes in the holding period at the RTL, which results to be the most interesting for measurements to be carried out. After the first hour in the holding period, the major mechanisms governing the kinetics of deformation is creep, which takes place over longer periods, releasing the requirement in the sampling frequency of measurements.

Appendix B

Optical Fiber Sensors under irradiation

We give here some details about optical fibers, that have been discussed in part III. For an extensive study about the current state of the art of optical fiber sensors and their application under irradiation we remit to the reference artible [Gir18]. The Optical Fibers (OF) are waveguides generally of cylindrical shape, They are made of an optical core and an optical cladding. The ones interesting for nuclear application are the monomode silica based one (melting temperature higher than 1700°C), which present a central core between 4-12 µm in diameter which is surrounded by a cladding of 125 µm in diameter. The core is doped with specific chemical element (Ge, P, Al, N_2) to increase its refractive-index with respect to the surrounding glass, as represented in figure B.1. This allows OF to guide light by total internal reflection.

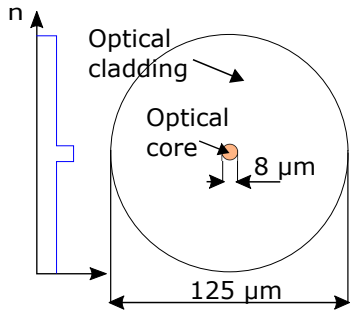

Figure B.1 – Schematic view of an optical fiber and qualitative representation of the refractive-index [Cau12]

To ensure the mechanical hardness of the waveguide and protect it from external corrosion, silica material is generally embedded into a coating, which material is chosen depending on the range of temperatures of the application environment.

Optical Fiber Sensors (OFS) present several advantages: small, insensitive to electromagnetic perturbations and can permit distributed measures. A preliminary condition for the development of OFS has been the verification of their behavior under radiation. When the OF is irradiated, the optical properties are modified: indeed the energy deposited by the radiation during its interaction with the material origins three major affects:

- The Radiation Induced Attenuation;
- The Radiation Induced Emission;

– The Radiation Induced Compaction.

The **Radiation Induced Attenuation (RIA)** consists in the augmentation of the linear attenuation in the optical fiber due to the increase of losses that appears under irradiation. The RIA depends on the dose D and on the wavelength λ according to:

$$RIA(\lambda, D) = -\frac{10}{L} log\left(\frac{I(\lambda, D)}{I(\lambda, 0)}\right) \tag{B.1}$$

where L is the length of the irradiated fiber, $I(\lambda, 0)$ the intensity of the transmitted signal before the irradiation at the λ wavelength and $I(\lambda, D)$ signal intensity after an irradiation leading to a dose D in the fiber.
The important fact about RIA is that it affects the signal transmission. Results of the COSI experiment, performed in the OSIRIS reactor in 2006 [Che08] showed that in the interval of wavelengths 800-1100 nm, the RIA remains limited, as presented in figure B.2.

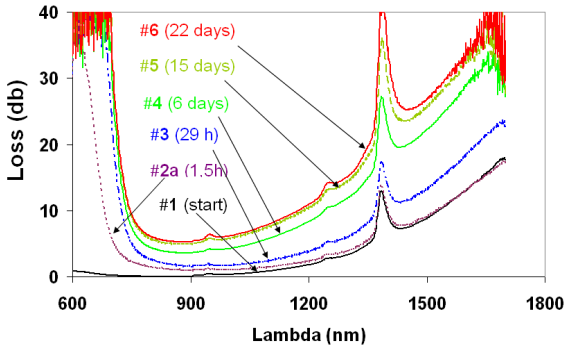

Figure B.2 – Attenuation spectrum for a monomode optical fiber made of pure silica under irradiation. Between 800 and 1100 nm the RIA is limited [Che08]

Also studies carried out to try to limit the RIA effect showed that the best performing optical fiber present a cope doped with Fluorine [Wij08] [Gir18]. Following tests carried out by CEA in collaboration with the SCK·CEN showed that the RIA is largely influenced by the operating temperature. Specifically, it was observed that the RIA shoots in the temperature range 200°C- 400°C, as shown in figure B.3. This is positive in our study as it corresponds to the application range of the cladding external surface temperature.

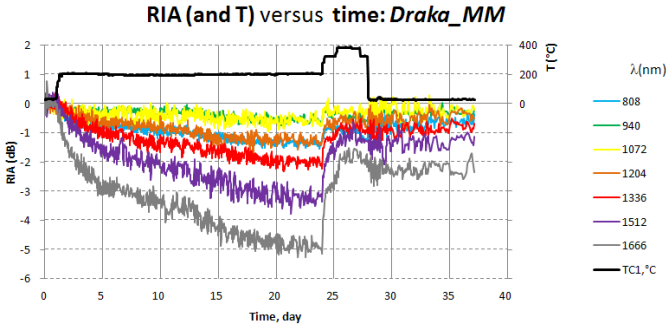

Figure B.3 – Effect of the operating temperature on the attenuation induced in the optical fiber for different wavelength. We observe a reduction of the RIA for all wavelength in the range of temperature 200°C- 400°C

Appendix C

Physical principle of the Linear Variable Differential Transformer

Figure C.1 shows a simplified electrical scheme where M' and M'' are the mutual inductance of secondary coils. L_1 corresponds to the primary coil and L'_2 and L''_2 are the secondary coils; e_1 is the applied tension to the detector; i_1 and i_2 are the current injected in the primary and secondary loop, respectively. The current extracted at the measurement system is i_2; R'_2 and R''_2 are the equivalent resistances of secondary coils and R_i is the resistance associated to the measurement system.

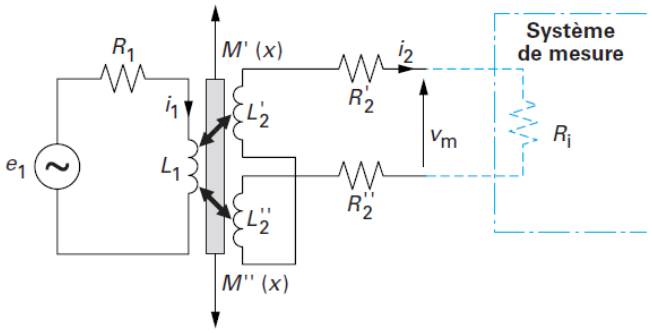

Figure C.1 – Simplified scheme of an LVDT [Web99]

The tension at the measurement system is $V_m = R_i i_2$ and from the scheme we know that:

$$e_1 = (R_1 + jL_1\omega)i_1 + j\omega\left[M'(x) - M''(x)\right] i_2 \tag{C.1}$$

$$\left[R_i + R_2 + j\omega L_2\right] i_2 + j\omega\left[M'(x) - M''(x)\right] i_2 = 0 \tag{C.2}$$

The output tension v_m can be described in terms of e_1:

$$v_m = \frac{j\omega R_1\left[M''(x) - M'(x)\right] e_1}{D} \tag{C.3}$$

with $D = R_1(R_2 + R_i) + j\omega\left[L_2R_1 + L_1(R_2 + R_i\right] - \omega^2\left[L_1L_2 + (M'(x) - M''(x))^2\right]$ and $L_2 = L'_2 + L''_2$ and $R_2 = R'_2 + R''_2$.
The linear relation between v_m and the mutual inductance and its independence from the value of R_i is obtained by imposing a really high value for this latter parameter so that equation C.3 becomes:

$$v_m = \frac{j\omega\left[M'(x) - M''(x)\right]}{R_1 + jL_1\omega} \tag{C.4}$$

According to a specific design and in a limited range, the difference between mutual inductance linearly depends on the displacement of the core of the transformer $M'(x) - M''(x) = -2ax$ with a being parameter of the system.
The measured tension is a linear function of the displacement to be measured x:

$$v_m = Ax \tag{C.5}$$

with $A = \dfrac{-2aj\omega e_1}{R_1 + j\omega L_1}$. This variation is symmetric with respect to the mid plan of the detector and generally associated to a null displacement.
At the acquisition system, the signal is amplified and the effective value and the phase of the signal are evaluated. Comparing the measured phase with the reference one, we can determine the orientation of core displacement.

Appendix D

Model IMPIGRITIA and verification of the linear approach

Presentation of the system

We have proposed a model to describe the behavior of the system, which requires further development and improvements to be applied to study the measured mechanisms. We report here some information on the identified approaches which wants to be starting point for further developments.
The sample holder and the empty clad can be modeled as a cantilevered Euler-Bernulli beam by a 2D finite element model. Each node of the clad can move along the radial (u_x) and the axial direction (u_y) and can rotate (θ_z). Pellets are considered as discrete masses m_p interacting along the radial direction with corresponding clad nodes through the non linear mechanism of dissipative shock and with each other by Coulomb friction. The equation of motion to be solved is:

$$[M]\{\ddot{x}\} + [C]\{\dot{x}\} + [K]\{x\} + \{fnl\} = \{F_e\} \tag{D.1}$$

Where $[M]^{N,N}$ is the total mass matrix, $[C]^{N,N}$ the total damping matrix, $[K]^{N,N}$ the total stiffness one, are obtained according as follow.

$$[M] = \begin{bmatrix} [M_c] & 0 \\ 0 & [M_p] \end{bmatrix} \qquad [C] = \begin{bmatrix} [C_c] & 0 \\ 0 & [C_p] \end{bmatrix} \qquad [K] = \begin{bmatrix} [K_c] & 0 \\ 0 & [K_p] \end{bmatrix} \tag{D.2}$$

where $[M_c]^{n,n}$ is the tridiagonal mass matrix for the clad and $[M_p]^{m,m}$ is the diagonal mass matrix for the pellets, with $N = m + n$. In the same way the total stiffness matrix and the total damping one depends on clad and pellets ones.
While mass and stiffness matrices characterizing the sample holder and the clad are obtained by modal analysis of the system, for the pellets modelled as discrete masses having $[M_p]$, we assume they do not contribute to the stiffness of the system, thus the $[K_p]$ is the null matrix. We use Rayleigh damping to estimate the damping matrix [C]:

$$[C] = \alpha[M] + \beta[K] \tag{D.3}$$

Assuming proportional damping, the dissipation in the structure can be described by two parameters α and β. Those parameters are not a priori known, but can be obtained experimentally measuring the first two eigen-frequencies of the system in air and by comparing the C0 and the C1 configuration. Indeed it can be shown that [Ger15]:

$$\zeta = \frac{1}{2}\left(\frac{\alpha}{\omega_i} + \beta\omega_i\right) \tag{D.4}$$

where ζ is the modal damping, which can be recovered by logarithmic decrement from free damped vibrations of the system, and ω_i are the eigenfrequencies.
The {fnl} in equation D.1 are the non linear forces applied on specific nodes of the system: in this case the dry friction and the shock interaction. They shall be detailed in section D and D.
The presence of external water plays a role in the external solicitation $\{F_e\}$ but it also induces an additional viscous damping to the structure: as described by Prank in [DeP15] the effects of flowing fluid on the spectral response of the structure is described by an added mass m_a, corresponding to mass of displaced fluid, and a dynamic amplification factor C_m such that:

$$f = \frac{1}{2\pi}\sqrt{\frac{K}{M + C_m m_a}} \tag{D.5}$$

where K and M are the structural stiffness and mass of the system. The dynamics amplification factor is equal to 1 for quiescent water thus the two parameters can be experimentally obtained by comparing the oscillation frequencies of the system in air, in quiescent water and in fluid flow. Indeed:

$$\frac{f_{air}^2}{f_{c=0}^2} = \frac{M + m_a}{M} \tag{D.6}$$

and the mass of the displaced fluid becomes:

$$m_a = \left(\frac{f_{air}^2}{f_{c=0}^2} - 1\right) M \tag{D.7}$$

Instead by comparing the frequencies in stagnant water $f_{c=0}$ and in fluid flow f we can obtain the amplification factor depending of the fluid flow rate imposed to the system:

$$C_m = \left[\left(\frac{f_{c=0}^2}{f^2} - 1\right)\frac{M + m_a}{m_a}\right] + 1 \tag{D.8}$$

The form of $\{F_e\}$ for our application is modelled by taking the PSD from Axisa [Axi01] and applying an arbitrary stochastic phasing.
Due to the non linearity of the problem, direct time integration is essential [Ger15] and to solve the equation explicit Newmark integration scheme is necessary in order to avoid strong dependencies of results on integration time step. Direct integration has been implemented in Matlab to solve the discrete problem. Attention has to be paid to the fact that when using this scheme, the time step must satisfy the condition:

$$dt \leq \frac{2}{\omega_{max}} \tag{D.9}$$

Where ω_{max} is the highest frequency included in the model (also named critical frequency). A schematic view of the system is proposed in figure D.1.

Pellet-pellet interaction: dry friction:

One of the non linear mechanisms is the dry friction mechanism arising at contact interfaces between neighbour pellets. This dissipative phenomenon is characterized by a force opposing to the relative motion of objects. To describe the mechanism we consider three pellets and we define the positive transversal displacement as $\bar{u}_x$. In the following subscript x will be neglected as we suppose pellets can only move along the x direction.

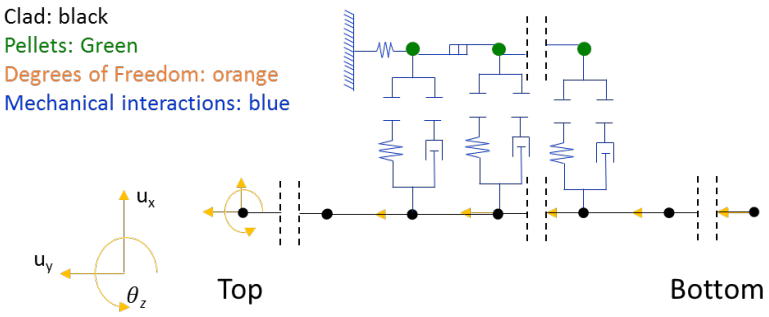

Figure D.1 – Modelling IMPIGRITIA: schematic view of the configuration

We first focus on pellets 1 and 2: when a relative motion appears between the two, we have

$$\dot{\bar{u}}_2 - \dot{\bar{u}}_1 \neq 0 \tag{D.10}$$

We can define the force imposed by pellet 1 on 2 as:

$$F_{1\to 2} = -\mu N_1 sign(\dot{\bar{u}}_2 - \dot{\bar{u}}_1) \tag{D.11}$$

where μ is the friction coefficient between the two, N_1 the normal force associated to pellet 1. The generated force is oriented in the opposite direction with respect to relative velocity. If for example pellets 1 is moving faster than 2, pellet 2 is pushed to move is the same direction while 1 is slowed down by 2.

In our application case, if we identify the generic pellet as "j" and $j = 1...NbPellets$ we have:

$$j \in [1, NbPellets - 1] \quad F_{j\to j+1} = -\mu N_j sign(\dot{\bar{u}}_{j+1} - \dot{\bar{u}}_j) \tag{D.12}$$

$$j \in [2, NbPellets] \quad F_{j+1\to j} = \mu N_{j+1} sign(\dot{\bar{u}}_{j+1} - \dot{\bar{u}}_j) \tag{D.13}$$

Clad-pellet interaction with open gap: dissipative shock

Mechanical interaction between pellets and clad is submitted to contact condition. We define d_n the distance between the generic solid S1 with respect to S2, whose direction is normal to the surface S1, positive if internally directed. We assume that the two interacting objects, in our case pellets and clad, respect the non interpenetration condition which can be written as:

$$d_n \leq 0 \tag{D.14}$$

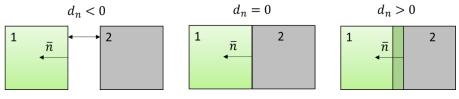

Figure D.2 – Inter-penetration condition

When contact occurs, a force generates at the interface: if we define $\bar{R}^{21}$ the general force density imposed by the solid 2 to 1, we can identify the normal and tangential components:

$$\bar{R}^{21} = R_n^{21}\bar{n} + \bar{R}_t^{21} \tag{D.15}$$

The system of equation to describe contact is expressed as follows as it is known as the unilateral normal contact low by Hertz-Signorini-Moreau [Wri06].

$$\begin{cases} d_n \leq 0 \\ \bar{R}_n^{21} \leq 0 \\ d_n \bar{R}_n^{21} = 0 \end{cases} \tag{D.16}$$

The first expression clearly corresponds to the non interpenetration condition, the second implies that the force imposed by Solid 2 on 1 is a compression and the third corresponds to complementarity principle: if contact is not established ($d_n \leq 0$) the normal contact effort is zero ($\bar{R}_n^{21} = 0$); if instead the effort contact is different from zero ($\bar{R}_n^{21} \leq 0$), contact has been established and thus $d_n = 0$. To model this phenomenon by finite elements, it is generally used a penalisation method which corresponds to replace non interpenetration condition with the following:

$$\bar{R}_n = -K_c F_{HEAV}(d_n) d_n \tag{D.17}$$

where F_{HEAV} is Heaviside function expressed as follows:

$$F_{HEAV} = \begin{cases} 1 & if \quad d_n \leq 0 \\ 0 & if \quad d_n > 0 \end{cases} \tag{D.18}$$

Where K_c is the penalisation parameter. It corresponds to define a contact stiffness which has of course no physical meaning but it is useful for numerical resolution.

In our case, considering that contact establishes for the generic clad and pellet nodes located at the same axial position we define:

$$F_n^{p \to g} = K_c d_{pg} sign(\bar{x}_p - \bar{x}_g) \tag{D.19}$$

$$F_n^{g \to p} = -F_n^{p \to g} \tag{D.20}$$

where d_{pg} corresponds to:

$$d_{pg} = \mid \bar{x}_p - \bar{x}_g \mid -j \geq 0 \tag{D.21}$$

where j is the width of radial gap. If $d_{pg} < 0$ no contact is established between the two nodes.
In order to take into account the fact that shock is a dissipative phenomenon, we define a viscous damping C_c in parallel to the contact stiffness. The resulting effort is proportional to the relative velocity.

Investigation of parameters: an empirical model

From previous discussion it comes out that a large number of parameters characterize the model and strongly modify the resulting dynamic response of the system. Mentioned parameters are resumed in table D.2.
As previously mentioned, the dependence of the model on those parameters lead to the necessity to experimentally characterize the structure to fit the model.
For what it is concerned with shock parameters, they will impact the transverse displacement of the generic open gap configuration Ci and can be fitted from experimental curves.

Parameter	Description	Experimental calibration
K_p	Pellet Stiffness	assumed zero
ζ	Modal damping	by eq. D.4 knowing ω_i for C0 and C1
m_a	added mass	by eq. D.7 knowing ω_i for C0 in air and in quiescent water
C_m	Dynamic amplification factor	by eq. D.8 knowing ω_i C0 in quiescent water and in fluid flow
K_c	Contact Stiffness	displacement data fitting
C_c	Contact viscous dissipation	displacement data fitting
μ	Pellet-Pellet Friction Coefficient	previously calibrate by tribometer on Mo samples

Table D.2 – Model parameters

The linear approximation for system design

A simplified approach can be used to dimension the heterogeneous system behavior in terms of expected frequencies and modes of vibration. The linear system is described solving the following motion equation:

$$[M_{eq}]\{\ddot{x}\} + [C_{eq}]\{\dot{x}\} + [K_{eq}]\{x\} = \{F_e\} \tag{D.22}$$

In this case we assume the bending stiffness to be given only by the geometry and inertia of the clad and the sample holder $[K_{eq}] = [K_c]$. Pellets contribute instead to the linear mass of the system $[M_{eq}]$. The damping matrix of the simplified system is a function of the equivalent mass, of sample holder and clad stiffness through Rayleigh damping (eq. D.3):

$$[C_{eq}] = \alpha[M_{eq}] + \beta[K_{eq}] \tag{D.23}$$

Section D presents a comparison of calculated and measured results showing the possibilities and limits of the proposed approximation.

Verification of the linear approach: the empty rod (C0) and the closed gap rod (C6)

We compare collected data for the C0 and C6 rod with the linear approximation of the system. The absence of the dissipation mechanisms coming from the gap presence and relative motions of the pellets with respect to the clad is expected to lead to a linear behavior of the two rod configurations.
For the specific case of C0, the mass and the stiffness of the system are completely due to material properties, geometrical characteristics and fixation conditions of the sample holder and the cladding.

$$[M_{eq}] = [M_c] \qquad [C_{eq}] = [C_c] \qquad [K_{eq}] = [K_c] \tag{D.24}$$

In the case of C6 instead, we assume that only pellets contribute to the mass of the sample rod while the stiffness of the clad is the one of a full rod having the external diameter of the original clad, thus 9.5 mm.

The viscous damping matrix is experimentally obtained: as described in section 11.3, we evaluate the linear model $\bar{\zeta}(A)$ as a function of the amplitude of oscillations. In the linear model of the system, we impose a constant value of the viscous damping ratio ζ corresponding to $\bar{\zeta} = \bar{a} + \bar{b}A_{min}$. For the empty rod we obtain the evolution showed in figure (a) of D.3 and for the closed gap rod C6 the evolution of the viscous damping ratio is illustrated in figure (b) of D.3

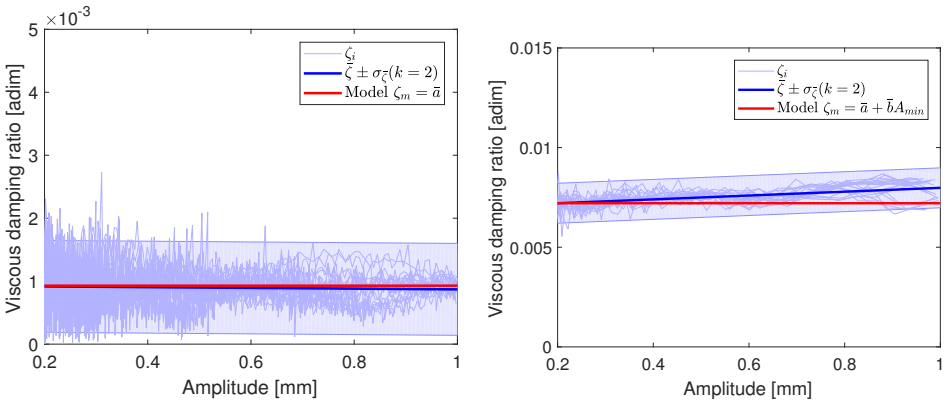

(a) (b)

Figure D.3 – Viscous damping ratio evolution as a function of the amplitude of oscillations for the C0 sample rod (a) anf for the C6 sample rod (b): the i^{th} calculated evolutions are represented in light blue, in blue is illustrated the linear model calculated in the highlighted interval, with the associated range of standard error at k=2. In red is the linear constant value of the viscous damping ratio used in the linear model

We observe that both the modeled evolutions are withing the the range of standard error at k=2 so that the model is statistically equivalent to the measured behavior of the sample rod.
We compare the first-mode frequency obtained for the calculated C0 empty rod and the C6 sample rod with the experimental value obtained from the spectral analysis of the measured motions. Figure D.4 shows that the model permits to find the correct first mode frequency, with an uncertainty lower than the instrumentation precision (0.1 Hz).

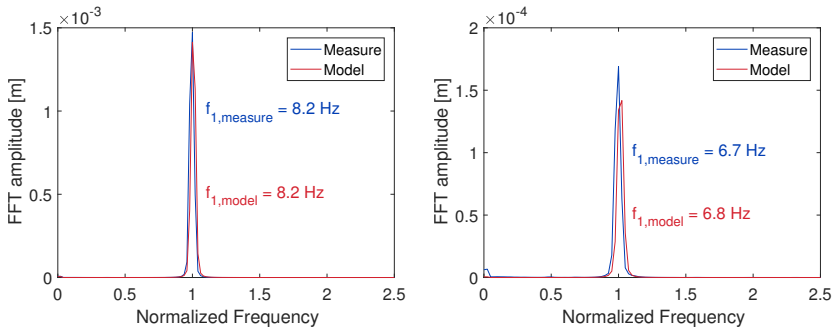

(a) (b)

Figure D.4 – Calculated first-mode eigenfrequency with the linear approach in red and experimentally evaluated one in blue for C0 (a) and C6 (b)

Appendix E

Statistical distribution of the displacement amplitudes of the tested rods

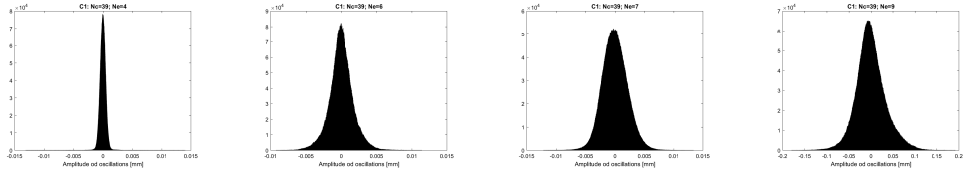

(a) (b) (c) (d)

Figure E.1 – Distribution of measured displacement for the C1 sample rod under increasing flow rate excitation: (a) u=0.8 m/s; (b) u=1.2 m/s; (c) u = 1.8 m/s and (d) u = 2.5 m/s

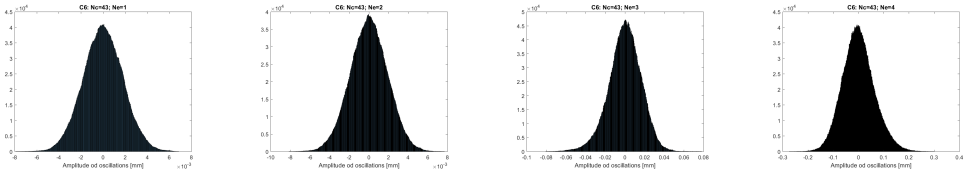

(a) (b) (c) (d)

Figure E.2 – Distribution of measured displacement for the C6 sample rod under increasing flow rate excitation: (a) u=0.8 m/s; (b) u=1.2 m/s; (c) u = 1.8 m/s and (d) u = 2.5 m/s

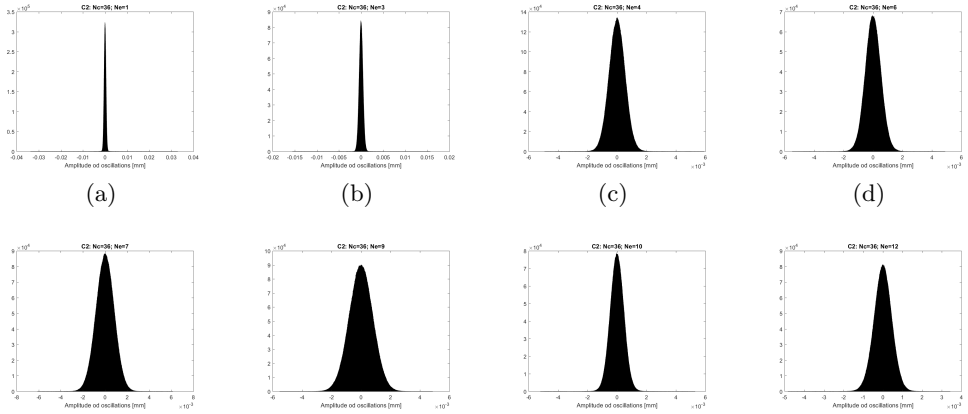

(a) (b) (c) (d)

(e) (f) (g) (h)

Figure E.3 – Distribution of measured displacement for the C2 sample rod under increasing flow rate excitation, on the left open gap, on the right closed gap on 1 pellet: (a) and (b) u=0.8 m/s; (c) and (d) u=1.2 m/s; (e) and (f) u = 1.8 m/s and (g) and (h) u = 2.5 m/s

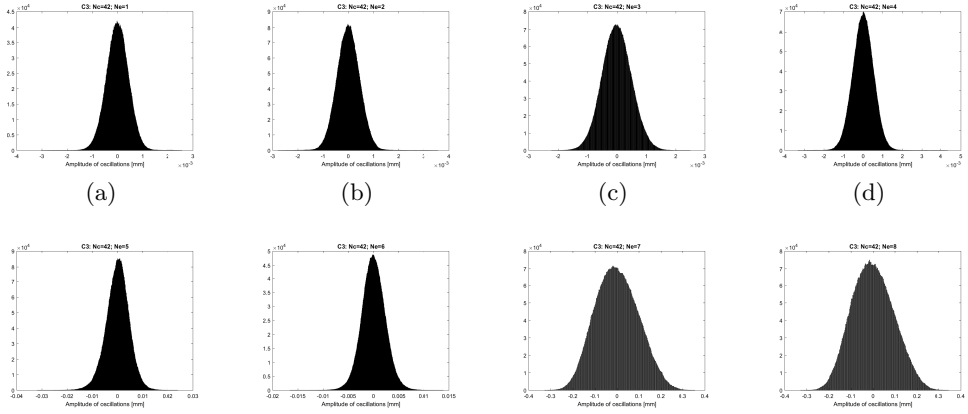

(a) (b) (c) (d)

(e) (f) (g) (h)

Figure E.4 – Distribution of measured displacement for the C3 sample rod under increasing flow rate excitation, on the left open gap, on the right closed gap on 3 pellets: (a) and (b) u=0.8 m/s; (c) and (d) u=1.2 m/s; (e) and (f) u = 1.8 m/s and (g) and (h) u = 2.5 m/s

List of Acronyms

BOTDA	Brillouin Optical Time Domain Analyzer
BOTDR	Brillouin OTDR
C/M	Calculated/Measured
DG	Diameter Gauge
$D^{e}_{c,IP}$	External Cladding Diameter at the Inter-Pellet plane
$D^{e}_{c,MP}$	External Cladding Diameter at the Mid-Pellet plane
$D^{e}_{f,IP}$	External Fuel Diameter at the Inter-Pellet plane
$D^{e}_{f,MP}$	External Fuel Diameter at the Mid-Pellet plane
EPMA	Electron Probe MicroAnalyzer
ET	Expansion Thermometer
FBG	Fiber Bragg Gratings
FIV	Flow Induced Vibrations
FPs	Fission Products
HBWR	Halden Boiling Water Reactor
$H_{r,IP}$	Height of Primary Ridges (Inter-Pellet plane)
$H_{r,MP}$	Height of Secondary Ridges (Mid-Pellet plane)
HTIR-TC	High Temperature Irradiation Resistance ThermoCouple
IP	Inter-Pellet
JHR	Jules Horowitz Reactor
LDV	Laser Doppler Vibrometer
LOCA	Loss Of Coolant Accident
LVDT	Linear Differential Voltage Transformer
MOX	Mixed OXides fuel
MP	Mid-Pellet
MTR	Material Testing Reactor
O/M	Ratio oxygen/metallic actinides
OFDR	Optical Frequency Domain Reflectometry
OFS	Optical Fiber Sensors
OTDR	Optical Time Domain Reflectometry
PCI	Pellet-Cladding Interaction
PIE	Post-Irradiation Examinations
p_{int}	Internal pressure
P_{lin}	Linear power (W/cm)
PWR	Pressurize Water Reactor
PZT	Lead Zirconate Titanate piezoelectric material
$R^{e}_{c,IP}$	Minimum External Cladding Radius
$R^{e}_{c,min}$	External Cladding Radius at the Inter-Pellet plane
$R^{e}_{c,MP}$	External Cladding Radius at the Mid-Pellet plane

RIA	Radiation Induced Attenuation
RI-BFS	Radiation Induced Brillouin Frequency Shift
RIE	Radiation Induced Emission
RIRIC	Radiation Induced Refractive Index Change
RTL	Ramp Terminal Level
SCC-I	Stress Corrosion Cracking in presence of Iodine
SEM	Scanning Electron Microscope
SIMS	Secondary Ion Mass Spectrometry
TC	ThermoCouple
T^{e}_{c}	External Cladding Temperature
$T^{e}_{c,IP}$	External Cladding Temperature at the Mid-Pellet plane
$T^{e}_{c,MP}$	External Cladding Temperature at the Inter-Pellet plane
$T^{e}_{f,IP}$	External Fuel Temperature at the Mid-Pellet plane
$T^{e}_{f,MP}$	External Fuel Temperature at the Inter-Pellet plane
T^{i}_{f}	Centerline Fuel Temperature
$T^{i}_{f,IP}$	Centerline Fuel Temperature at the Inter-Pellet plane
$T^{i}_{f,MP}$	Centerline Fuel Temperature at the Mid-Pellet plane
T_{liq}	Liquidus Temperature
T_{sol}	Solidus Temperature
UT	Ultrasonic thermometer